EXPERIMENTAL AND NUMERICAL INVESTIGATION OF AN AUGMENTED SPARK IGNITER AND EVALUATION OF IGNITER'S EFFECTIVE FLAME LENGTH AS A PERFORMANCE PARAMETER

A THESIS SUBMITTED TO
THE GRADUATE SCHOOL OF NATURAL AND APPLIED SCIENCES
OF
MIDDLE EAST TECHNICAL UNIVERSITY

BY

LEVENT ÇAĞATAY ÖZ

IN PARTIAL FULFILLMENT OF THE REQUIREMENTS
FOR
THE DEGREE OF MASTER OF SCIENCE
IN
MECHANICAL ENGINEERING

SEPTEMBER 2019

Approval of the thesis:

EXPERIMENTAL AND NUMERICAL INVESTIGATION OF AN AUGMENTED SPARK IGNITER AND EVALUATION OF IGNITER'S EFFECTIVE FLAME LENGTH AS A PERFORMANCE PARAMETER

submitted by **LEVENT ÇAĞATAY ÖZ** in partial fulfillment of the requirements for the degree of **Master of Science in Mechanical Engineering Department, Middle East Technical University** by,

Prof. Dr. Halil Kalıpçılar
Dean, Graduate School of **Natural and Applied Sciences** _____

Prof. Dr. M. A. Sahir Arıkan
Head of Department, **Mechanical Engineering** _____

Prof. Dr. Abdullah Ulaş
Supervisor, **Mechanical Engineering, METU** _____

Examining Committee Members:

Prof. Dr. Hüseyin Vural
Mechanical Engineering, METU _____

Prof. Dr. Abdullah Ulaş
Mechanical Engineering, METU _____

Prof. Dr. İbrahim Sinan Akmandor
Aerospace Engineering, METU _____

Assist. Prof. Dr. Özgür Ekici
Mechanical Engineering, Hacettepe University _____

Assist. Prof. Dr. Sıtkı Uslu
Mechanical Engineering, TOBB University of Economics and Technology _____

Date: 05.09.2019

I hereby declare that all information in this document has been obtained and presented in accordance with academic rules and ethical conduct. I also declare that, as required by these rules and conduct, I have fully cited and referenced all material and results that are not original to this work.

Name, Surname: Levent Çağatay Öz

Signature:

ABSTRACT

EXPERIMENTAL AND NUMERICAL INVESTIGATION OF AN AUGMENTED SPARK IGNITER AND EVALUATION OF IGNITER'S EFFECTIVE FLAME LENGTH AS A PERFORMANCE PARAMETER

Öz, Levent Çağatay
Master of Science, Mechanical Engineering
Supervisor: Prof. Dr. Abdullah Ulaş

September 2019, 156 pages

In the scope of this thesis, the impact of operating conditions on the performance of an augmented spark igniter in means of effective length of the flame developed by the igniter and thermal energy output of it, by using numerical and experimental techniques, is examined. The igniter uses gaseous oxygen as oxidizer and gaseous hydrogen as fuel. Tests were carried out for 3 different oxygen mass flow rate to fuel mass flow rate ratios, and at each ratio with four different total mass flow rates. Experimental data were collected by schlieren imaging of the plume, thermocouples at different points in the plume and pressure transducer that is connected to the combustion chamber of the igniter. A numerical model was constructed and three dimensional numerical analyses for flow and combustion with detailed reaction mechanism were conducted for all test points. Later, the numerical model is validated using experimental data. Lastly, the performance parameters were defined and evaluated by the numerical model.

Keywords: Augmented Spark Igniter, Torch Igniter, Spark Torch Igniter, Ignition, Liquid Propellant Rocket Engine

ÖZ

PÜRMÜZ TİPİ BİR SIVI YAKITLI ROKET MOTORU ATEŞLEYİCİSİNİN DENEYSEL VE SAYISAL YÖNTEMLERLE İNCELENMESİ İLE BİR PERFORMANS PARAMETRESİ OLARAK ETKİN ALEV BOYUNUN ELDE EDİLMESİ

Öz, Levent Çağatay
Yüksek Lisans, Makina Mühendisliği
Tez Danışmanı: Prof. Dr. Abdullah Ulaş

Eylül 2019, 156 sayfa

Bu çalışma kapsamında, farklı çalışma koşullarının pürmüz tipi bir sıvı yakıtlı roket motoru ateşleyicisinin etkin alev boyu ve termal enerji çıktısı üstündeki etkisi deneysel ve sayısal yöntemlerle incelenmiştir. Ateşleyici oksitleyici olarak gaz oksijen, yakıt olarak ise gaz hidrojen kullanmaktadır. Testler, dört farklı toplam gaz debisinde ve her debide üç farklı oksitleyici debisinin yakıt debisine oranı kullanılarak icra edilmiştir. Deneysel veriler, oluşan görünmez alevin schlieren görünteleme yöntemi ile görüntülenmesi, alev içerisindeki farklı noktalardan sıcaklık bilgisi toplanması ve ateşleme sırasında ateşleyicinin yanma odasındaki basınç verilerinin ölçülmesi ile elde edilmiştir. Ateşleyicinin test edilen çalışma koşullarında; oluşturulan sayısal bir benzetim modeli (hesaplamalı akışkanlar dinamiği) ile üç boyutlu akış ve yanma analizleri yapılmıştır. Sayısal model deneysel veriler kullanılarak doğrulanmış ve çalışma kapsamında tanımı yapılan performans parametreleri model sayesinde elde edilmiştir.

Anahtar Kelimeler: Arttırılmış Kıvılcımlı Ateşleyici, Pürmüz Tipi Ateşleyici, Kıvılcımlı Pürmüz Tipi Ateşleyici, Ateşleme, Sıvı Yakıtlı Roket Motoru Ateşleyicisi

To my family…

ACKNOWLEDGMENTS

Firstly, I would like to thank my advisor, Prof. Dr. Abdullah Ulaş, for his guidance. I am much obliged to him for having patience with me.

Also, I'd like to thank Dr. Bülent Sümer, Ali Can Özer and all TÜBİTAK SAGE employees who helped me throughout my study.

And a special thanks goes to Mr. Burak Söğütcü and Mr. Caner Ekin Kiper for their great contributions to schlieren imaging experiments. They didn't leave me alone on cold winter nights.

TABLE OF CONTENTS

LIST OF TABLES

TABLES

LIST OF FIGURES

FIGURES

LIST OF ABBREVIATIONS

ABBREVIATIONS

ASI	Augmented Spark Igniter
CFD	Computational Fluid Dynamics
GCH_4	Gaseous Methane
GH_2	Gaseous Hydrogen
GO_x/GO_2	Gaseous Oxygen
EDC	Eddy Dissipation Rate
LCH_4	Liquid Methane
LES	Large Eddy Simulation
LH_2	Liquid Hydrogen
LO_x	Liquid Oxygen
LPRE	Liquid Propellant Rocket Engine
NASA	National Aeronautics and Space Administration
O/F	Ratio of Oxidizer Mass Flow Rate to Fuel Mass Flow Rate

LIST OF SYMBOLS

SYMBOLS

A	pre-exponential factor, area
c_p	specific heat capacity at constant pressure
c_v	specific heat capacity at constant volume
D	mass diffusion coefficient
D_T	thermal diffusion coefficient
D_t	turbulent diffusivity
E	energy
E_a	activation energy
G_b	generation of turbulent kinetic energy by buoyancy
G_k	generation of turbulent kinetic energy by the mean velocity gradients
h_j	sensible enthalpy
h^0	enthalpy of formation
I	unit tensor
J	diffusion flux
k	Gladstone-Dale coefficient, thermal conductivity, turbulent kinetic energy
l	length
k_{eff}	effective conductivity
M	molar mass, Mach number
$\dot{m}$	mass flow rate
M_w	molecular weight
n	refractive index
P	pressure
R	net rate of production of a species
$\mathcal{R}$	volumetric rate of creation
R_u	universal gas constant
S	source term, modulus of the mean rate-of-strain tensor

S_h	heat of chemical reaction
Sc_t	turbulent Schmidt number
T	temperature
u	Cartesian component of velocity
V	velocity, volume
Y	mass fraction
Y_m	fluctuating dilatation in compressible turbulence

Greek Symbols:

γ	specific heat ratio
ε	turbulent dissipation rate
$\varepsilon_{x,y}$	angular deflection of light rays
μ	molecular viscosity
μ_t	turbulent viscosity
ν	kinematic viscosity
ξ^*	length fraction of the fine scales
ρ	density
σ	turbulent Prandtl number
τ	stress tensor
τ_{flow}	characteristic flow time
τ_{chem}	characteristic chemical time
∅	scalar quantity
Ω_{ij}	rate of rotation tensor

CHAPTER 1

INTRODUCTION

1.1. Motivation

For more than 60 years, liquid propellant rocket engines (LPREs) are utilized as thrust source for missiles, sounding rockets and space vehicles. They are favored over other propulsion machinery, simply because of their higher specific impulse values and flexible thrust range [1].

There are several types of LPREs. According to fuel type, they are categorized into monopropellant and bipropellant. Monopropellant LPREs are mostly utilized in satellite systems. They can directly expand the highly pressurized gas or use a catalyst to heat the gas and then eject it. Thrust from bipropellant LPREs is obtained by expanding highly pressurized hot combustion gases to ambient. The hot combustion gases are products of a reaction between oxidizer and fuel in combustion chamber in bipropellant LPREs. To start the combustion (ignite the propellants) in combustion chamber LPREs need an igniter. A simplistic schematic of an LPRE can be seen in Figure 1-1. Only hypergolic type propellants, that ignites as soon as contact occurs between propellants, don't need an igniter. Consequently, igniters must deliver significant amount of energy to the combustion chamber for a successful ignition. Igniter failure is responsible for lots of unsuccessful missions (e.g. no ignition or hard start). In the beginning of an LPRE development program, ignition is dealt as one of the primary risk source, and taken care in early stages [2], [3].

Igniters can be defined as energy (mostly in heat form) releasing equipment that uses external energy source to start combustion. They can directly deliver the energy to propellants or utilize the energy to ignite small portions of propellant flow then eject resulted hot gases into combustion chamber. There are numerous types of igniters.

Some of them are used in historic or current systems, while some of them are only studied experimentally. These types are explained in detail in the next section.

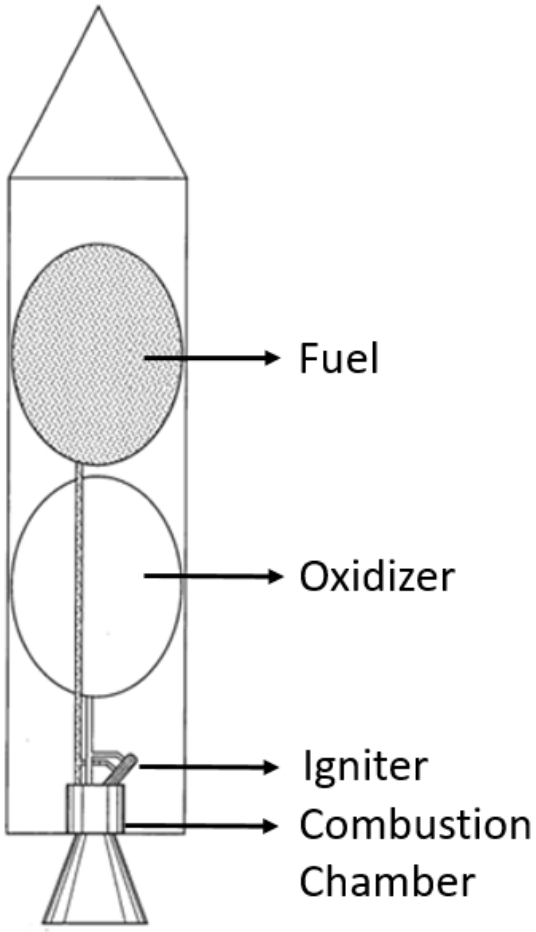

Figure 1-1. Simplified Schematic of an LPRE

1.2. Igniter Types

The selected system must ensure rapid and reliable ignition in the combustion chamber. Therefore, the choice depends on the parameters such as; reaction environment and phase of propellants, working environment (state of the combustion chamber) and the requirements in means of reusability. Compatibility of the ignition system with whole engine architecture like the source of external energy, weight and space capacity also plays an important role upon selection.

1.2.1. Catalytic Ignition

Catalytic ignition occurs by directing some portion of propellant flow through a catalyst bed. When the propellants get together with the catalyst, ignition occurs, and the resulting hot gases are directed to the combustion chamber. This system is also used in monopropellant systems with hydrazine [4]. Solid catalyst technology is used in Redstone rocket engine's steam generator and in AR-1 rocket engine both as main igniter and steam generator for turbine [5]. They can be used until the catalyst material is consumed. A schematic of an example can be seen in Figure 1-2.

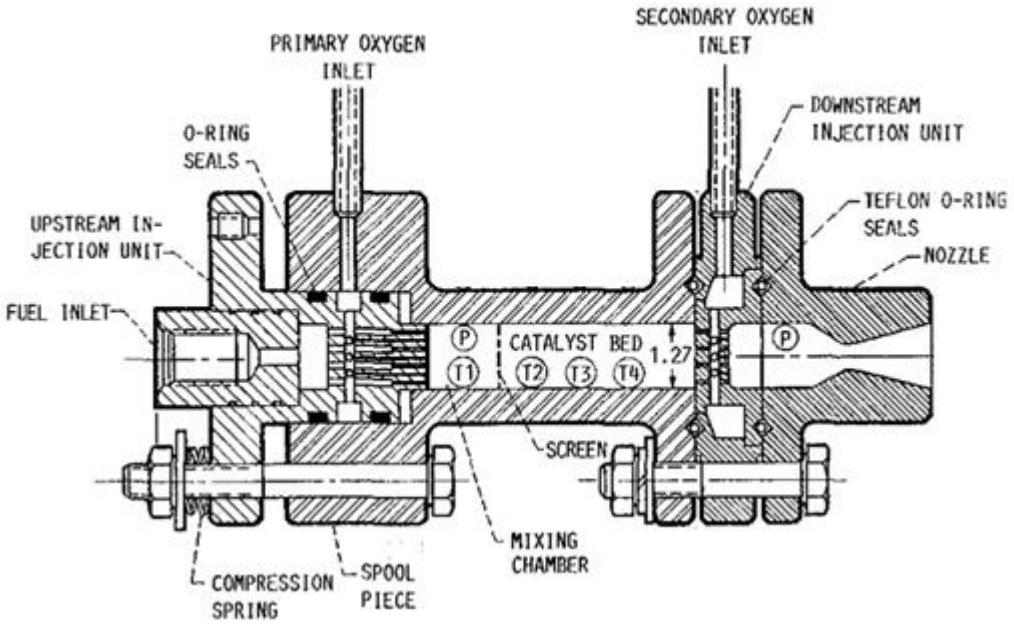

Figure 1-2. A schematic of an experimentally studied catalytic igniter [6]

1.2.2. Combustion Wave Igniter

This highly complex concept provides ignition point at multiple locations on injector face. It has a precombustor where small amount of propellants flow into it and spark plugs that start the combustion in this precombuster. After the flow is established from precombustor till injector face, the spark plugs initiate combustion. The resulting combustion wave produces compression and shock, therefore leads to detonation wave and it moves through distribution network, finally creating multipoint ignition.

Its highly complex nature and requirement for lots of specialized hardware is its primary disadvantage [5]. X-33 Aerospike engine utilizes such an ignition system. A schematic can be seen in Figure 1-3.

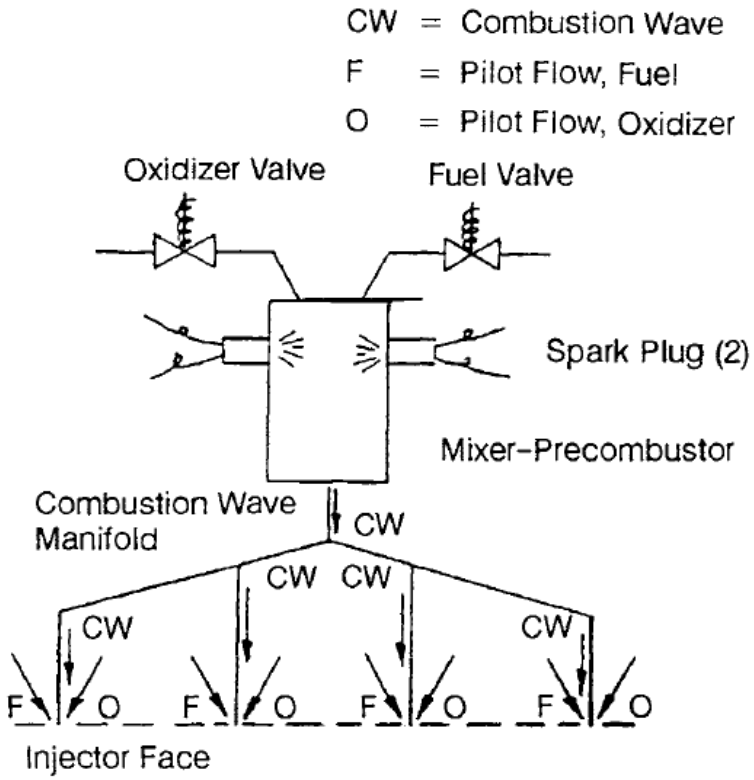

Figure 1-3. A schematic of a combustion wave ignitor [5]

1.2.3. Pyrotechnic Igniters

They are electrically triggered devices which usually include one or more pyrotechnic charges. The initial mass of pyrotechnic charge determines firing time. After pyrotechnic charge is ignited, they provide a sheet of flame which is at high temperatures. Mostly, a filament that conducts electric current is embedded in the pyrotechnic charge. They are considered to be very reliable because of their primitive design, however they are one shot devices. Beside igniting the main combustion chamber, they can be used to start the turbine that will derive the turbo-pump in LPREs. This type is used as igniter almost in every solid rocket motors. An example

of a pyrotechnic igniter is shown in Figure 1-4. Known examples of LPREs that made use of this type are Atlas, Delta, F-l, H-l, J-2, Redstone, and Thor engines [5], [7].

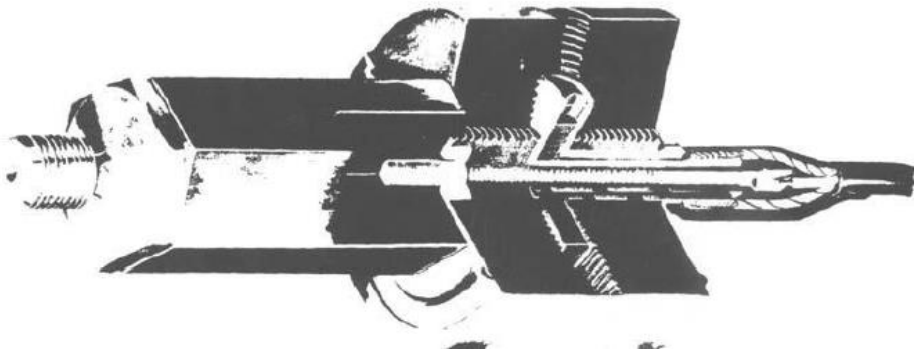

Figure 1-4. Radially outward firing pyrotechnic igniter [5]

1.2.4. Resonant Igniters

Resonant igniters use pressure resonances of unstable shock waves in an open tube with one side being closed, and a resonant tube attached to it perpendicularly, to increase the propellant's temperature above its ignition point. Unstable shock wave is achieved by directing propellant gases through a sonic nozzle, expanding them across a small chamber, and compressing the flow into the resonant tube [4]. This type doesn't require an energy input from an external source, like electrical current. A schematic of the resonance igniter is shown in Figure 1-5.

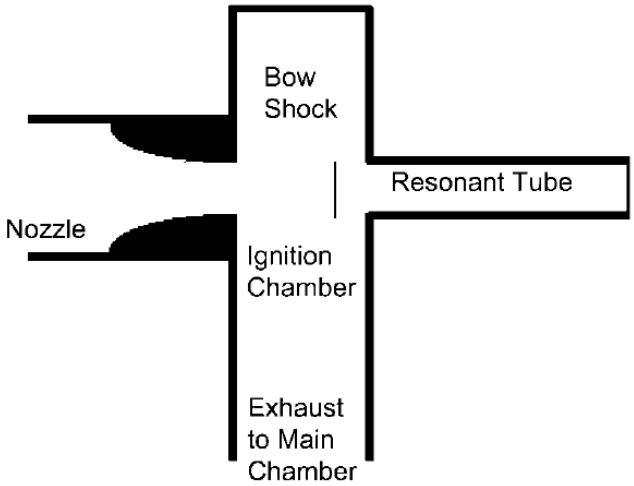

Figure 1-5. Schematic of resonance igniter[4]

1.2.5. Spark Plug

Besides of their common usage in internal combustion engines, highly reliable spark plugs and their supplementary electronics were developed for LPREs. The system uses repetitive discharge resulting very hot regions between electrodes. This arc heats the propellant and ignites it. Direct spark ignition must be designed carefully to ensure ignition and to avoid electrode deterioration and damaging the combustion chamber from pressure spikes.

1.2.6. Thermal Ignition Devices

1.2.6.1. Glow Plugs and Electrical Wires

This application type uses simply electrical current to heat a conductive metal, which is placed in propellant stream, to the ignition point of propellant.

1.2.6.2. Laser Heating

In laser heating, laser heats a target material (e.g. aluminum) to the ignition temperature of propellant. Apart from academic studies, one prototype is developed for Space Shuttle's Reaction Control System Engine which utilizes GH_2/GO_2 [4]. Another type of laser ignition system ignites propellant directly. Laser-initiated spark ignition uses high-power density laser beams for ignition. Photochemical laser ignition system creates laser beams in certain wavelengths to excite molecular bonds of one of the propellants such that the excited molecules produces reactive radicals and ignition occurs [4].

1.2.7. Torch / Spark-Torch / Augmented Spark Igniter

In addition to direct spark ignition that is placed directly in the combustion chamber, spark plugs can be mounted in a precombuster which is the combustion chamber of the igniter. To this precombuster small amounts of propellants (usually 0.1-0.3% of propellant mass flow rate) is fed and the mixture is ignited by using a spark plug. Then the resulting hot combustion gases (flame) are directed to the main combustion chamber via a tube. The directed flame ignites the main propellant flow in the

combustion chamber of LPRE [5]. This type of ignitor system called torch igniter, spark-torch igniter or augmented spark igniter (ASI).

The lack of ability of withstanding spark-quenching operating conditions in the main combustion chamber of direct spark systems has led to development of ASI systems. They have an extended service life, they can operate numerous starts over a wide range of propellant mixture ratios and mass flow rates and survive harsh environments. After the ignition is accomplished in combustion chamber of ASI, the spark plug can be turned off to protect electrodes, without stopping operation of the torch. This is highly beneficial, because the torch can be started before the propellant injection to the LPRE's combustion chamber and minimizes igniter's valve timing requirements. Also, it prevents a backflow of main propellants of the LPRE to the igniter [5]. Their reliability in means of repeatability, makes them a good choice for the LPRE applications that need to restart and reuse such as Space Shuttle and space tourism [2], [3], [8].

They can come in different designs, sizes and be placed in different sections of the main combustion chamber such as through the injector face or perpendicular to propellant flow. Two exemplary representations are shown in Figure 1-6 and Figure 1-7. Known examples of LPREs that use this type of igniter are Space Shuttle's main LPRE, XCOR Ez LPRE and Vinci upper stage engine [2], [8], [9].

While conventional spark plugs can be used in some experimental cases [10], specially designed spark plugs are commonly used in ASI systems to eliminate deficiencies of conventional ones to harsh conditions and also specialize the spark source to specific requirements. The spark plug that is developed for Space Shuttle's main LPRE can be seen in Figure 1-8.

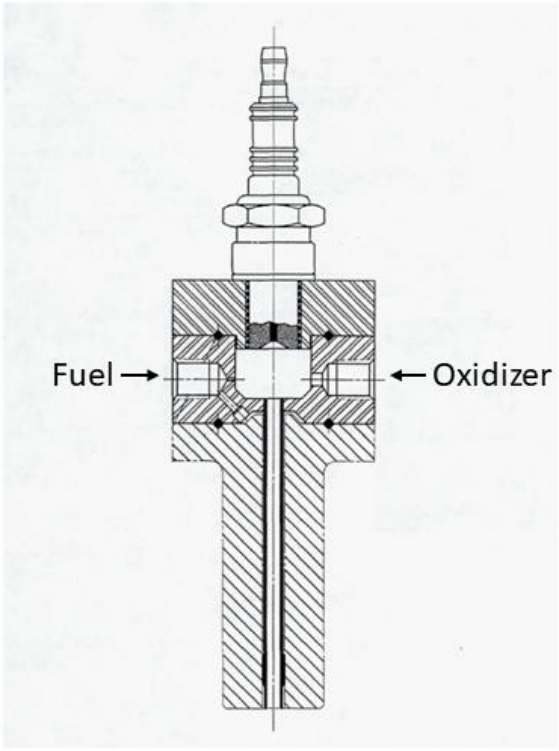

Figure 1-6. A Schematic of an Augmented Spark Igniter [10]

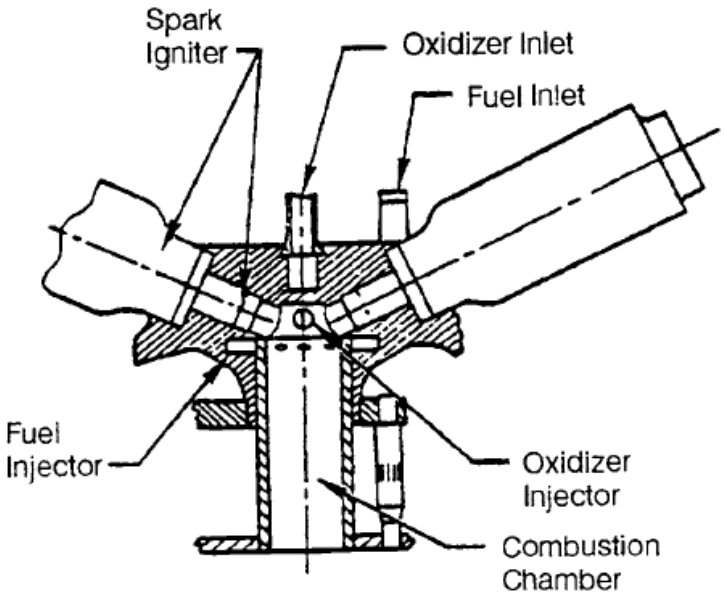

Figure 1-7. A Schematic of an Augmented Spark Igniter [5]

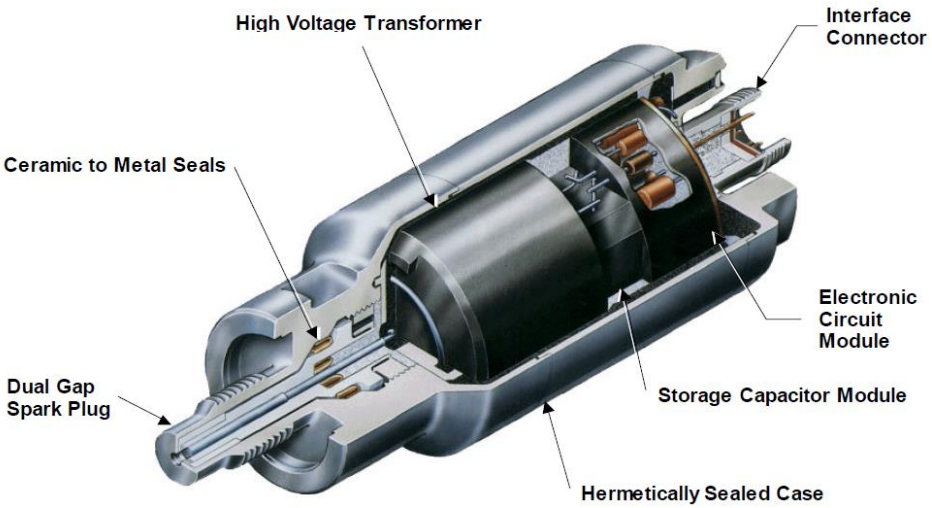

Figure 1-8. Spark Plug Design of an ASI [9]

1.3. Literature Survey

In literature, there are limited studies that focus on ASI topic. Mostly engineers from the institutions where LPRE development programs takes place, have worked on the topic. In this heading, a chronological review of the studies will be given.

One of the earlier studies was done by Lawver and Rousar [11] in 1984. In their study, they worked on ignition characterization of GOx/Ethanol propellant combination by using an ASI and showed that a previous igniter design for LOx/LH_2 and LOx/RP-1 engine was successfully utilized for the GOx/Ethanol engine. They tested the igniter over a wide range of operating conditions and concluded that it is reliable. They worked with a special design that has cooling channel around tube that purges flame through injector face. The coolant fuel (ethanol) reacts with the core flame and results as fuel-rich torch exhaust that later ignites the combustion chamber. The test variables for the ASI were propellant temperature (163.7 K to 299.8 K), cold flow pressure (0.23 to 4 bar), chamber diameter of the ASI (3.81 mm and 7.62 mm), spark energy (10-50 mJ) and mixture ratio oxidizer and fuel (0.4 to 40).

In 1986, Dexter and McCay [12] examined the shutdown detonations in Space Shuttle's main engine's fuel preburner ASI. During engine cutoff, detonations

initiated in the ASI's oxidizer line with residual oxygen and back-flowing hydrogen. Highly risky damages (rupture of line) was observed after flights. They predicted that helium purge system didn't function correctly and proposed a few solutions. From the proposed solutions, usage of a larger orifice in the helium purge line and a graphite-epoxy wrap for the line were implemented and solutions seemed to work out.

Reed and Schneider [13] made a survey for hydrogen/oxygen auxiliary and low thrust propulsion systems. In the paper they also reviewed ignition concepts and concluded that ASI type igniters are highly reliable, due to their capability of igniting liquid, two-phase and gaseous propellants and as a concept they are good and reliable choice for hydrogen/oxygen thrusters.

In a NASA Technical Memorandum, Repas [10] gave a working schedule for an ASI that is used as an ignition source for a variety of propellants. It is stated that the ASI ignitor is "inexpensive, simple to operate and has demonstrated very good reliability". This design also uses a cooling channel around the flame tube with hydrogen as coolant. The coolant fuel reacts with core flame at the exit and produces a flame which is about 300 mm long. However, author doesn't give an information about how they measured the flame length.

In a review paper for the development status of the ignition system for Vinci engine, Vermeulen, et al. [2] explain the design steps and decisions that took place on development of an ASI igniter. They decided on a few different design points. After the development stage, it is concluded that the ASI igniter has shown reliable ignition on all design points.

Schneider, John and Zoeckler [14] performed tests for designed LOx/LCH_4 igniter for a reaction control system at NASA. They designed a test matrix to examine the ignitibility of LOx/LCH_4 over a range of mixture ratio, and durability of sparking system hardware. For 1402 number of pulses of spark plug successful ignition points were achieved during tests. One of the important results that they concluded is the capability of igniter of producing repeatable ignition pulses over a hundred separate

pulse trains. However, after 1402 pulses, ceramic of the spark plug was broken and test were halted.

Breisacher and Ajmani [15] again tested a LOx/LCH_4 igniter for a main engine. They tested the igniter at near vacuum conditions in a vacuum chamber (1.3 kPa), because of the igniter's future use in lunar ascent engine. 750 ignition tests were conducted to observe the effect of mixture ratio, spark energy level, spark frequency, methane purity, igniter body temperature and igniter geometry. The test variables were chosen to reflect the lunar surface conditions. Also, CFD simulations of different test conditions were performed and the results were compared to test results. They were able to simulate both successful and unsuccessful ignitions with the CFD model. As a result of the tests, they obtained ignition maps versus spark power, energy per spark, spark frequency and methane purity in low pressure environment with a chilled ignitor. They concluded that, they were able to have ignition with the conditions of cold body (144 K) and 1.3 kPa backpressure.

As a part of his master thesis, Roque [16] made some modifications on a previously designed GO_2/GCH_4 ASI according to some design limitations. The previous design was using tangential fuel inlets. In the new design, the iterations made on inlets increased the swirl intensity by 25% with a prediction of greater flame stabilization, however no result is presented in the work about the issue. After testing of equipment separately, the hot tests were concluded at a few different points.

Kleinhenz, Sarmiento and Marshall [17] worked on ignitability of a LOx/LCH_4 ASI versus delivered spark energy, spark timing and repetition rate. They also varied the propellant temperature within the liquid range. It is found out that while higher spark energy creates higher probability of ignition, spark timing and repetition rate also have strong effect on ignitability. It was observed that sparks that are well synchronized with propellant entry and have low energy also can achieve the ignition. They concluded that a high spark rate (200-300 spark per seconds) increases the reliability of igniter, in the optimum time interval.

Flores et al. [18] experimentally evaluated an ASI's ignitability limit with respect to condition of oxidizer and fuel (gaseous or liquid) and mixture ratio of propellants. They used the previously mentioned igniter [16] with a different spark plug due to low reliability of previous spark plug assembly. The first combination that was tested is GCH_4/GO_2. According to their reliability criteria (3 successful ignitions respectively), they concluded that for this combination reliable ignition area lies between the mixture ratio of 2-4. The second combination used colder gaseous methane. Successful ignition range narrowed compared to the previous test case and number of reliable points decreased. This time most ignitions occurred between the mixture ratio of 3-5. The third combination they tried was LCH_4/LO_2. However, they weren't able to have a successful ignition with these inlet conditions. Later, the authors decided to change liquid methane to gaseous methane, and had a few successful points that are scattered in a wide range of mixture ratio.

Sanchez et al. [19] made design iterations on previous igniter [18] to test ignitability limit for liquid methane and liquid oxygen propellant combination. They changed the separate body configuration to one single body and increased the length of injection distance, that is the distance liquid oxygen passes before reaching the fuel, to ensure about the development of oxidizer flow and better mixing. They also changed the ceramic insulation of the spark plug to a thicker ceramic covering. A cavitating venturi is used to fix the mass flow rate of liquid oxygen. However, despite all changes, they were able catch a successful ignition only one time with mixture ratio of 5 and chamber pressure 100 psi. They reported that after this ignition, the igniter melted and the tests were postponed.

To optimize length of mixing zone in GH_2/GO_2 ASI for a scramjet engine Anoop, Assiz and Manu [20] applied a numerical technique. They defined a mixing length ratio which is the ratio of the length between fuel inlet to spark region to the diameter of mixing chamber. The ratio was varied from 0.25 to 0.37. For simplification, chemical reaction wasn't introduced to the numerical model and only cold flow is solved. Using a commercial software, they concluded that none of the designs

achieved a uniform distribution. However, mixing got better as the mixing length ratio increases.

Natale et al. [21] have conducted tests on a GCH_4/GO_2 ASI for LPRE development program, to obtain pressure and temperature data. Also, a CFD model has been developed to compare the results of CFD analyses that utilizes different reaction mechanism and different turbulence chemistry coupling models to temperature and pressure data that they obtained experimentally. The experiment campaign showed an unsymmetrical temperature distribution in the combustion chamber and the combustion chamber pressure reaches almost 15 bar. They observed that the temperature is higher around fuel inlet side, and by doing visual inspection on the ASI they saw the evidence of temperature asymmetry, as an overheated region on the surface of the ASI. They compared four different CFD models with each other and experiments. Two of them utilizes eddy dissipation method with a mono-step pseudo reaction mechanism and with "GRIMECH" mechanism [22]. The other two utilizes laminar finite rate method with "Li Williams" and "REDRAM" mechanisms [23]. While all the combinations estimated the pressure correctly, the last combination was able to capture temperature asymmetry and flame-flapping phenomena in the combustion chamber more accurately. However, authors noted that LFR method converges much slower than the EDM method, therefore EDM is better for design and, LFR is good for further analysis.

Sanchez et al. [24] remodified the igniter of the previous study [18] which melted during the tests, for mapping operability range of the igniter with liquid propellants. After 210 successful tests with gaseous propellants, the igniter was tested with cryogenic propellants. 66 of 100 tests were ignited successfully with different inlet condition and in the mixture ratio range of 1-3. However, during the tests, oxygen couldn't be kept at the saturated state.

Buttay et al. [25] have numerically simulated flow field and combustion downstream of an ASI, where highly under-expanded jet flow occurs. The highly resolved region

consists the flow area just after outlet of the ASI where hot combustion products purges to ambient. The ASI of the study involves a cooling channel around the tube and the coolant is hydrogen gas (some portion of the fuel). The solution region also took into account of this co-flowing colder hydrogen gas inlet around the tube. However, the researches haven't took into consideration the effects of swirl flow structure in the flame tube and the other combustion products which originates from combustion chamber and they have assumed that the flow is unidirectional and consists only hot oxygen and water vapor. They have used massive clusters for calculations on 440,000,000 nodes. After the analysis of this turbulent, compressible and reactive flow, the resulting flow field was examined. It was consisting shock-wave reflections, Mach effects and oblique shocks. It turns out that the ignition of co-flowing hydrogen takes place downstream of the subsonic core that is caused by Mach disk. The ignition was promoted by mixing and hydroperoxyl (HO_2) radicals. The results revealed that reduced kinetic schemes which have been proposed in literature were appropriate to reduce the computational time.

Lately, Marshall, Osborne and Greene [26] used a different style ASI that is designed at NASA. This new style is called "Augmented Spark Impinging Igniter" (Figure 1-9), and its difference from conventional ASIs is that it has a smaller volume before the combustion chamber where some portion of the oxidizer flow is directed and energized by spark plug. Afterwards, the oxidizer in plasma state impinges to combustion chamber and ignites the fuel and remaining oxidizer in the ASI's combustion chamber. Hence, spark plug doesn't face hot environment of combustion chamber. They conducted tests at near vacuum conditions (3.4 kPa), for different fuel feed time lags, O/F ratio and with two different exciter unit: compact and conventional. Test results showed that while both exciter could reach successful ignition, the conventional one was more consistent and amount of oxygen that creates plasma kernel and oxygen feed timing is highly critical in means of ignition.

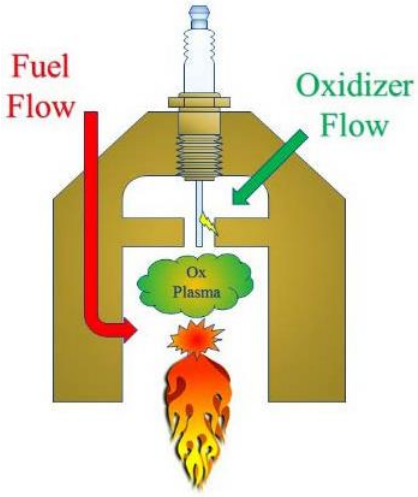

Figure 1-9. Augmented Spark Impinging Igniter [26]

Lastly; Unruh, Hicks and Lineberry [27] designed, manufactured and tested a vacuum chamber for experimenting vacuum ignition of a GO_x-GCH_4 augmented spark igniter. They designed a transparent chamber to capture high speed video of the flame. They conducted twelve test at certain vacuum levels. The results didn't show direct impact of vacuum level on ignitability of the ASI.

As a result, all studies can be subcategorized into three groups. The first group is consisted of studies that research ignitibility and reliability of igniters. The second group tries to optimize the design of an available igniter. The last group focuses on numerical simulation of the physics of the igniter. The classification can be seen from Table 1.1.

Table 1.1. *Classification of ASI Studies*

Type of Work	Reference Numbers
Ignitibility and Reliability	[2], [10],[11], [27], [13]–[15], [17]–[19], [24], [26]
Optimization	[12], [16], [18]–[20], [24], [26]
Numerical Modelling	[15], [20], [21], [25]

Another important outcome of the literature survey is that the ignitibility, especially in systems that utilize methane as fuel, is a problem in igniters. State of propellants

and the configuration of spark system seem to play an important role in this problem. Therefore, researchers try to overcome this issue by optimizing spark plug, mapping ignitibility range and changing the design of the igniter.

1.4. Objectives and Outline of the Thesis

Liquid propellant rocket engines need igniter to initiate combustion, and it is known that ignition failure is responsible for lots of unsuccessful missions [28]. Between different designs, augmented spark igniters outperform alternative designs with their capacity of survival to challenging environments and ability to operate in a broad range. According to ASI's placement in the LPRE structure, too short flame means insufficient energy and ignition failure, while too long flame could mean unnecessary burden, in means of mechanical and thermal strength of the igniter and supportive systems, on rocket's design and local overheated regions. Therefore, to optimize the design of an ASI, the effectivity of the igniter regarding to its operating condition and its location with respect to propellant injectors should be known.

There exist only limited numbers of studies about ASIs in the literature, and most of them deals with ignitability, combustion characteristics and spark plug optimization. None of the studies, to this date, has conducted research on flame length that penetrates the LPRE's combustion chamber or the energy output of the igniter with respect to operating conditions of the igniter.

To understand the effect of O/F ratio of the igniter and total mass flow rate that emanates from the igniter on the characteristics of the resulted plume, experiments should be conducted. In the present study, both numerical and experimental investigations are performed. The main aim of this thesis is to observe the flame characteristics and to validate a numeric model, in order to evaluate performance of each test points. The resulting flame is an invisible reacting flow rather than a pure diffusion flame or premixed flame, thereby an effective flame length definition was made with certain assumptions.

In the experimental study, a previously designed generic ASI is tested at twelve different operating conditions. The flame is observed using schlieren imaging system, temperature data collected from different locations in the plume and pressure of the combustion chamber of the igniter is recorded during experiments.

In the numerical analyses, the flow field and chemical reactions, that take place during combustion, inside the igniter and in the zone where flame spreads are modelled and solved in a three dimensional volume and at steady-state.

Lastly, the experimental and numerical results are discussed and compared in detail and the effective flame length are evaluated for abovementioned test points.

CHAPTER 2

EXPERIMENTAL EVALUATION

2.1. Introduction

Experimental testing of the ASIs are usually done about their ignitability on certain conditions by visual inspection [18], [19], [24], [26],[27]. In the scope of this study, to test the igniter at certain points, to observe and analyze resulting plume characteristics and to validate a numerical model, which will be utilized later in preliminary design of a future ASI, experiments were done with schlieren imaging system, temperature and pressure sensors.

2.2. Test Article

The test article design was originally provided by Prof. Dr. Robert Santoro from Mechanical Engineering Department of Penn State University. Then, it was modified prior to this work. Since it is not a final product, it was designed in a generic manner and highly robust in means of structural strength to perform test in a wide range of operating conditions. The article was manufactured from 303 grade stainless steel to withstand rusting environment of water vapor.

The isometric and section views of the test article can be seen in Figure 2-1 and the main dimensions regarding the flow inside the igniter is shown in Figure 2-2.

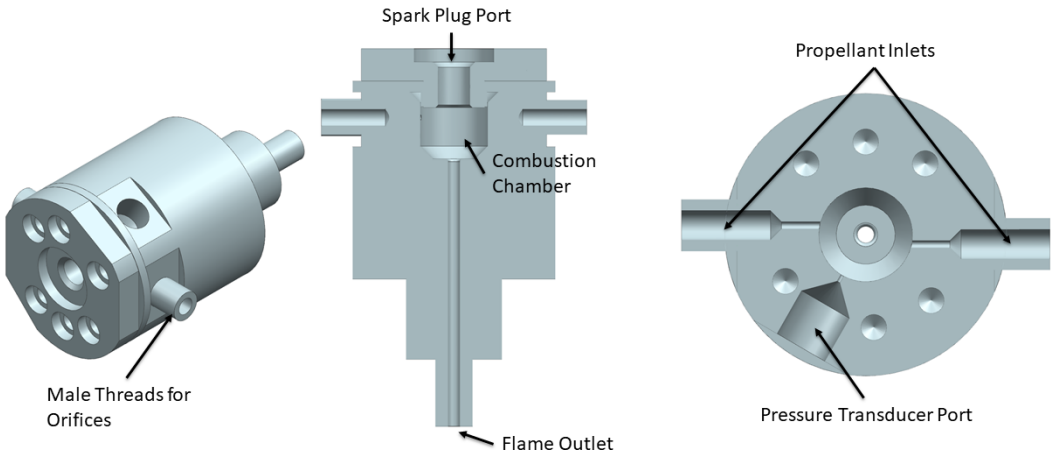

Figure 2-1. Isometric and Section Views of the ASI

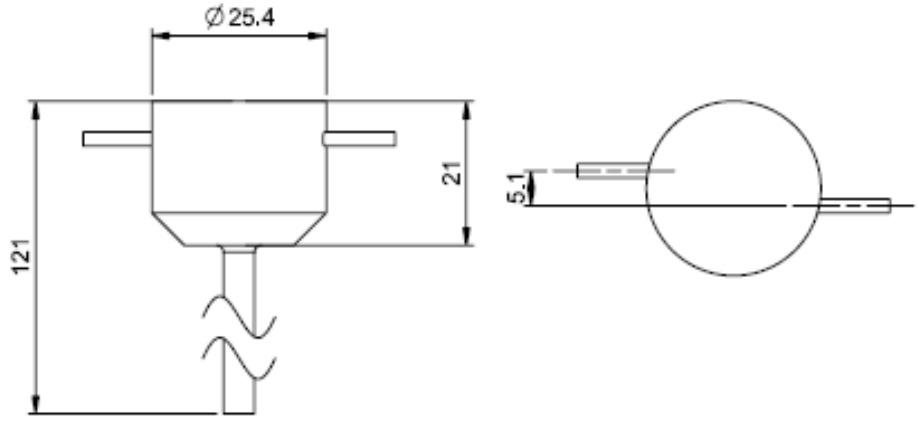

Figure 2-2. Main Dimensions of the ASI (all dimensions are in mm)

After manufacturing, the article is tested up to 50 barg for strength, and tested visually in a water aquarium for any leakage. During the leakage test, the article can be seen in.

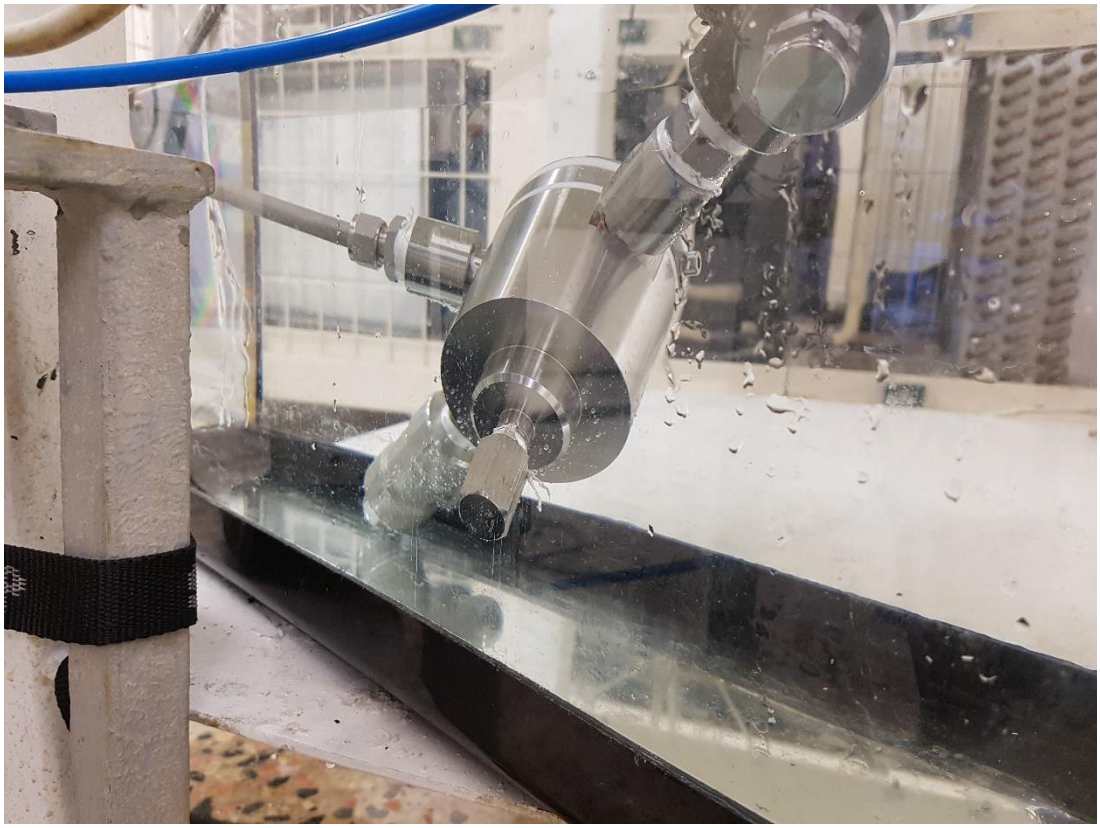

Figure 2-3. Leakage Test of the Test Article

2.2.1. Quenching

Even tough, laminar flame is not expected throughout experiments, igniter is examined in means of flame quenching. According to Kim et al. [29], for low H_2 concentrations in air at 1 atm, the highest quenching diameter is 2 mm. The study also states that addition of steam into the hydrogen/air mixture decreases the quenching diameter. Therefore, the flame tube with a diameter of 4.5 mm is highly safe against quenching.

2.2.2. Spark Plug

A commercially available spark plug is chosen to procure easily and in large numbers. For igniting propellants of the igniter Bosch “Super Plus” spark plug is used. The spark plug has an yttrium enhanced copper core which enhances resistance of spark to erosion. Image of the spark plug can be seen from Figure 2-4.

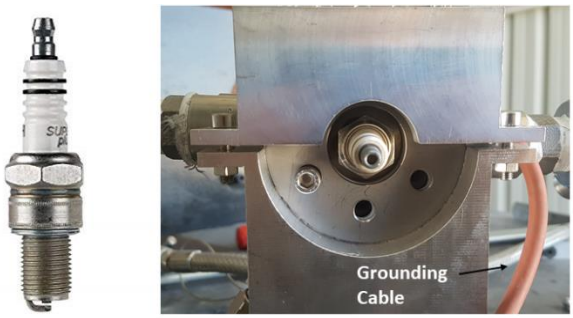

Figure 2-4. Spark Plug of the Test Article

2.3. Experimental Setup

The experiments were carried out in the Spray Combustion Test Facility of the TÜBİTAK-SAGE. Schematic of the related portion of the facility is presented in Figure 2-5.

The setup consists of two lines for gaseous oxygen and gaseous hydrogen. Both lines start from industrial tubes, with their valves, that contain gaseous oxygen or hydrogen at 200 bar in 50 liters. First regulators on the line are attached to tubes. These regulators drop the pressure of the gas from 200 barg to 0-50 barg and are used to adjust supply pressure roughly. After regulators, filters are utilized to stop any contamination that could burn inside the lines or occlude the orifices. Pneumatic valves on the lines are used to control the timing of the flow. The first ones are placed after the first regulators, and the second ones are placed just before the orifices to ensure exact timing of introducing fuel and oxidizer to the igniter. Next to the first pneumatic vanes there are second regulators on the line for fine adjustment. There are pressure sensors at several locations on the line. Two of them are positioned just before the orifices to monitor supply pressure and to have desired pressure level before the orifices, thus obtaining pre-determined mass flow rates. Temperature sensors along the lines are used to record gas temperature before entering the igniter. On both lines there are two check valves. The first one is for directing the purge gas and the second one is for protecting the line from any flashbacks. Between two check valves, purge system is connected to the line. The system uses nitrogen as inert gas, it is operated

after the ignitions to clean the lines, avoid flashbacks, and it is programmed to be activated in case of emergency button is pushed. The abovementioned details can be examined in Figure 2-6.

Whole system is automated and is controlled by user interface from the main PC. Timing of every pneumatic vane and the ignition process can be adjusted.

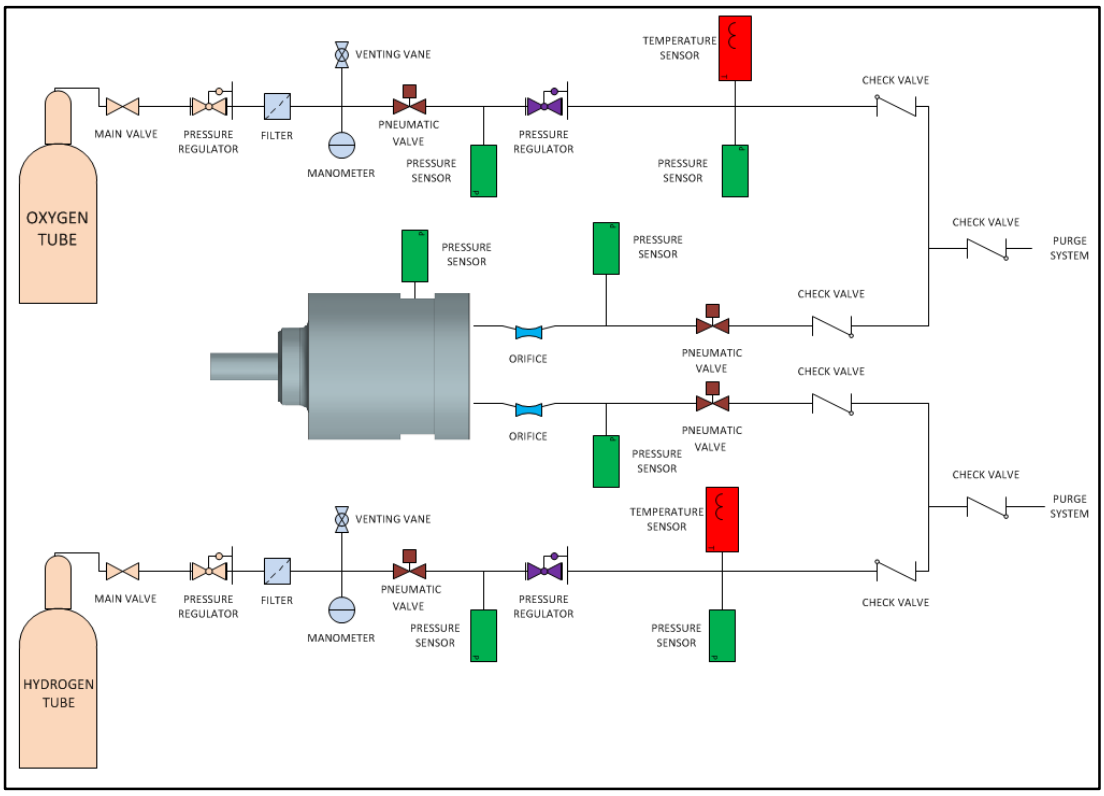

Figure 2-5. Schematic of the Experimental Setup

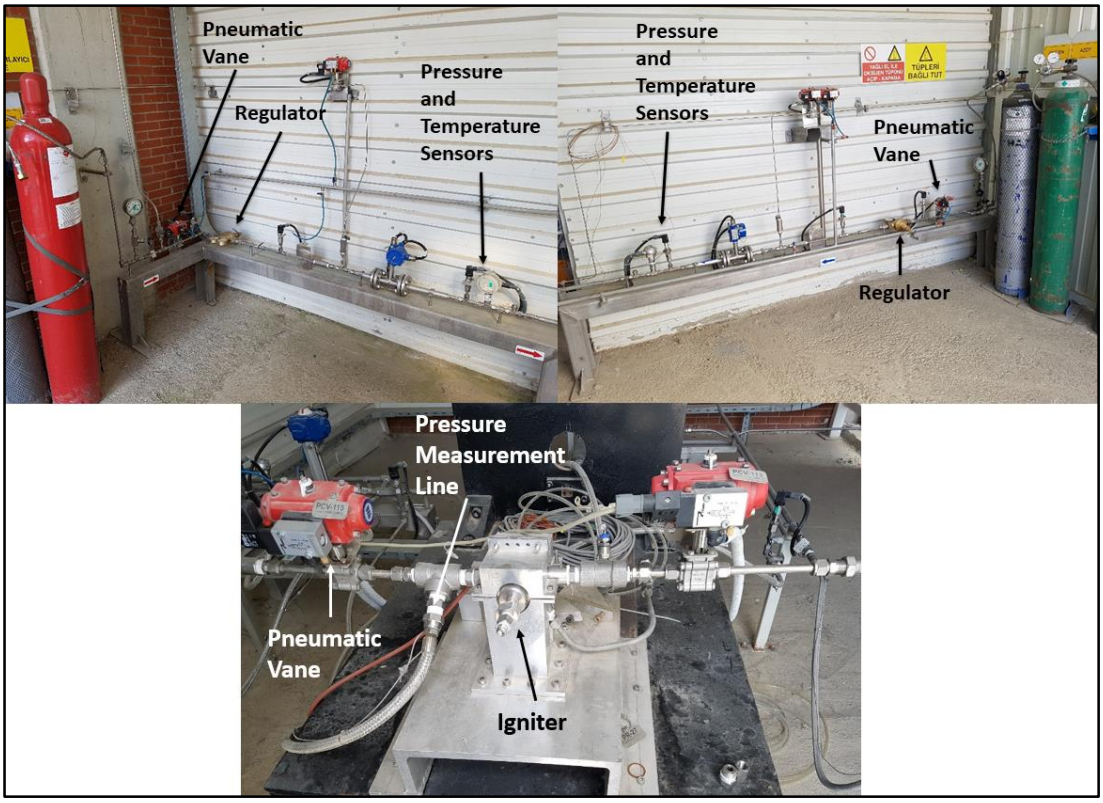

Figure 2-6. Experimental Setup

2.4. Schlieren Imaging

Schlieren imaging (or photography) is a method to visualize flow of fluid which is invisible to human eye by using density variation in transparent media.

Light can't propagate uniformly through inhomogeneous media. Disturbances to homogeneity can be caused by turbulence, thermal convection, shock waves and so on. These disturbances changes density on a big or small scale. Change in density leads to different refractive indices in the transparent media. Refractive index is a dimensionless number which indicates the ratio of the light speed in vacuum to light speed in the medium. This number is usually bigger than one, since light slows when it interacts with matter. Therefore, when light moves through media which has regions with different refractive indices, it refracts at different angles and this refraction can be visualized. In gaseous media, there is linear relationship between the refractive index and the density of gas (2-1).

$$n - 1 = k\rho \tag{2-1}$$

where n is refractive index, ρ is density and k is Gladstone-Dale coefficient [30].

It is known that gradient of refractive index is directly proportional to refraction or bending of light rays [30]. The relation between angular deflection for two-dimensions with a dimensional length of L can be shown as:

$$\varepsilon_x = \frac{L}{n_0}\frac{\partial n}{\partial x} \quad \varepsilon_y = \frac{L}{n_0}\frac{\partial n}{\partial y} \tag{2-2}$$

where n_0 is refractive index of surrounding medium. Since the refractive index is proportional to density, angular deflection is also directly proportional to gradient of density. In other words, schlieren is visualization of first derivative of density.

In traditional application of schlieren, light from a source is directed to a converging lens, then light passes through the region of interest and reaches the second converging lens. Behind the second lens there occurs a focal point where light rays focus. At that point a "knife-edge", which is basically a razor, is placed to increase contrast and to have a meaningful image by filtering. Schematic of this simplest type of schlieren can be seen in Figure 2-7. A famous exemplary schlieren image of a supersonic bullet is shown with Figure 2-8.

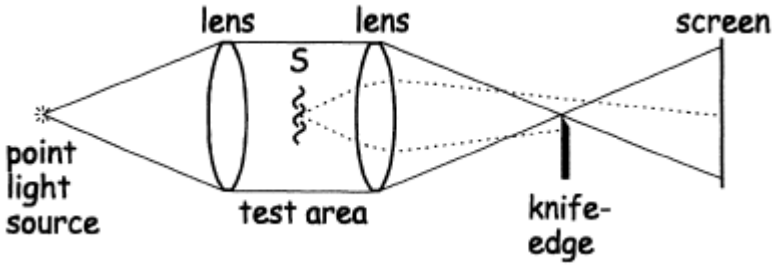

Figure 2-7. Schematic of Simple Schlieren System [30]

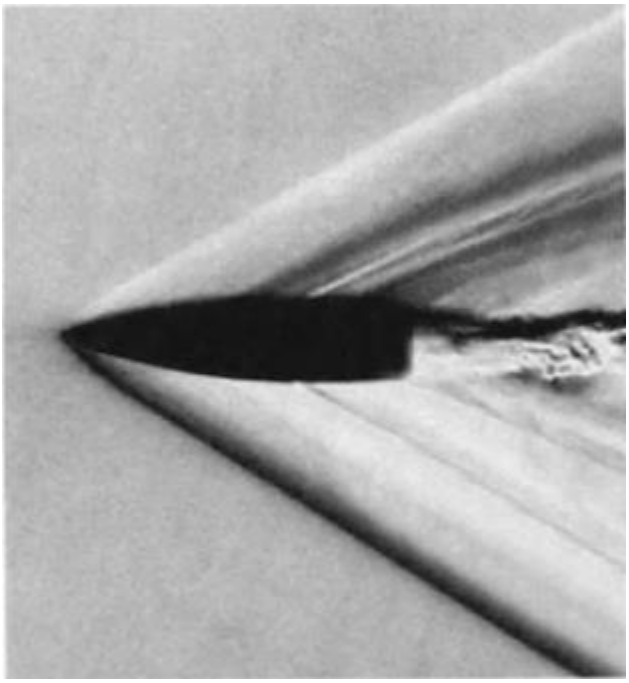

Figure 2-8. Shock Waves Around a Supersonic Bullet [30]

There are several arrangements that use lenses or mirrors alternative to classical system. Today's most popular arrangement is the Z-type 2-mirror schlieren system. This system utilizes two concave mirrors that is placed oppositely. The whole system resembles the shape of letter "Z". When the light leaves the source, it passes through a slit, then hits the first mirror and directs to test region. After test region, rays reach the second mirror and are tilted through the knife edge, later beam is recorded by a camera or image is obtained on a screen. The Z-type arrangement can be examined in Figure 2-9.

In the experiments of this work, AEROLAB Z-type schlieren system, which has focal length of 80 inches and consists of a light source with shot-arc xenon lamp (100-250 VAC, 50/60 Hz) with lens, track-mounted adjustable apparatus, two fine adjustable 10-inch parabolic mirrors, knife edge adjustable in all three axis and angle of inclination with fine adjustment knobs, plain mirror and viewing screen, is used. The three dimensional model of the system is shown in Figure 2-10, the schematic with dimensions can be seen from Figure 2-11.

Schlieren imaging is used to visualize invisible plume of the ASI which burns gaseous hydrogen with gaseous oxygen. The actual flame is occurring inside the chamber, and the resulting plume of the igniter is a mixture of hot vapor and gaseous oxygen, therefore it is invisible.

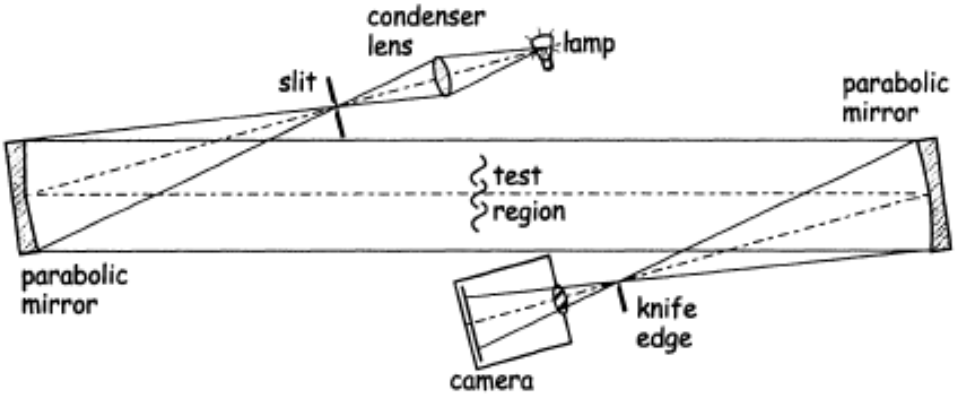

Figure 2-9. Z-type Schlieren System [30]

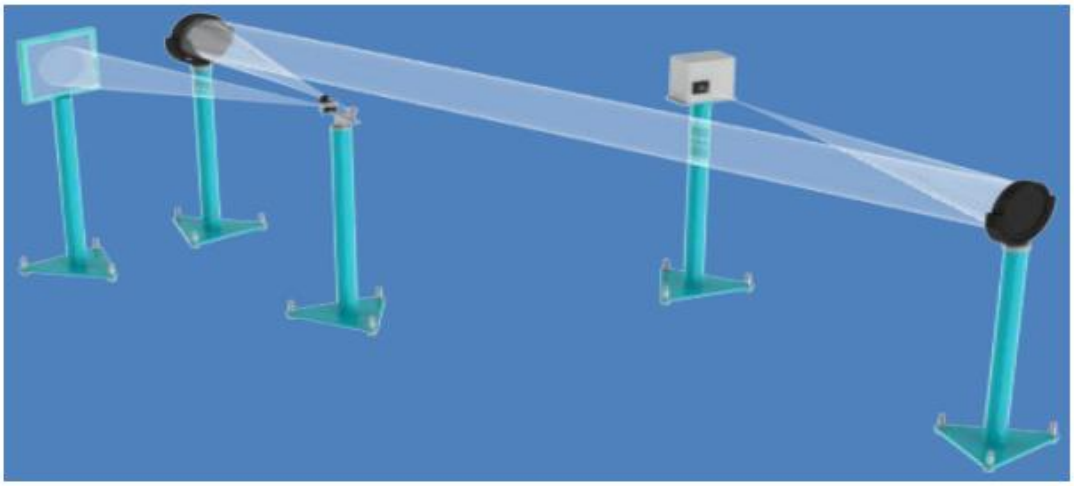

Figure 2-10. AEROLAB Z-type Schlieren System

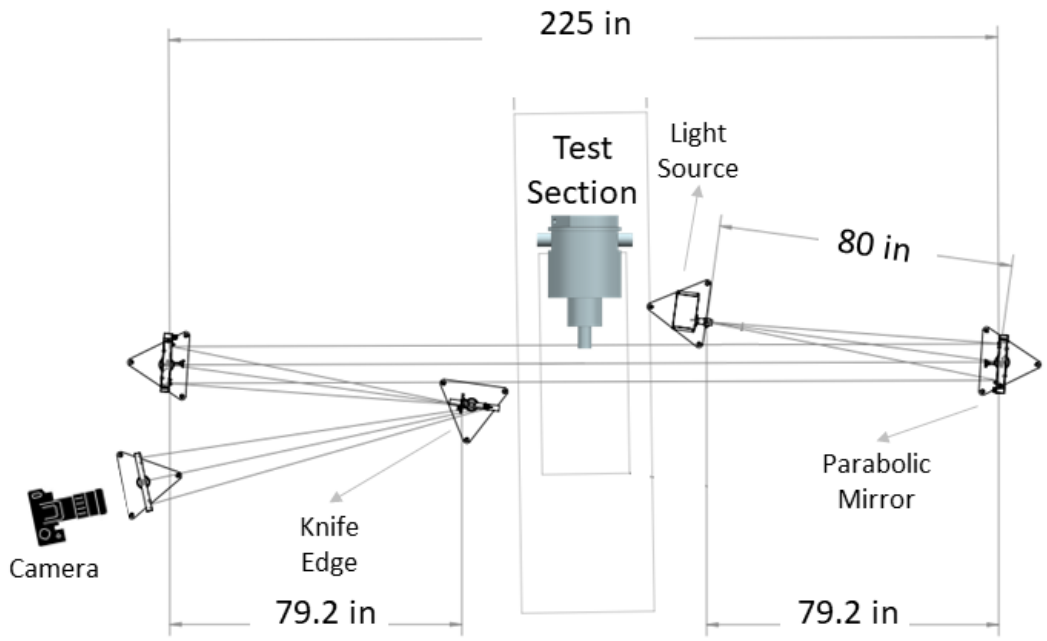

Figure 2-11. Configuration of Schlieren System of the Experiments

2.5. Pressure Recording

In the experiments, pressure value inside the combustion chamber was recorded by KISTLER piezo-resistive 0-10 bar pressure sensor (Figure 2-12). The data is recorded at a rate of 1.5 kHz. The sensor is attached to combustion chamber by a tubing to protect the sensor from hot gases (Figure 2-13).

Figure 2-12. KISTLER Pressure Sensor

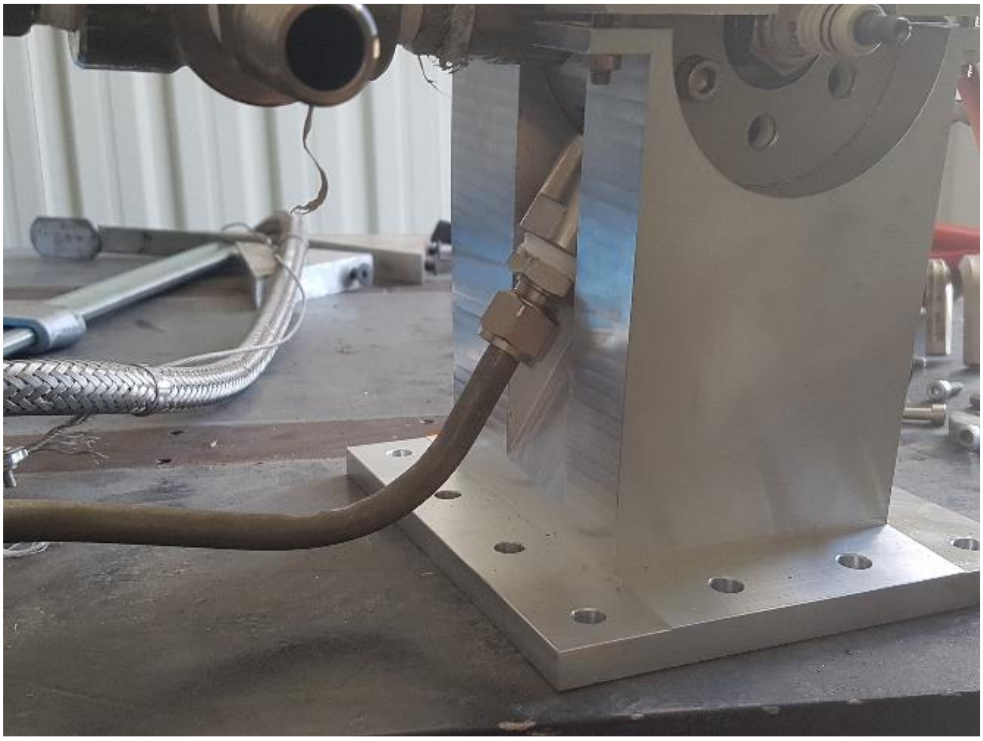

Figure 2-13. Tubing that Assemblies Sensor to Combustion Chamber

2.6. Temperature Recording

Temperature data at certain points in the plume were collected by using five C-type thermocouples. Recording of data was done at a rate of 1.5 kHz. Allocation of the thermocouples in the plume is done between equal spacing and concentric with the flame tube, as can be seen from Figure 2-14. Response time of the thermocouples is about 1.5 s [31], to ensure response time is achieved during the tests, experiments were carried out much more longer than 1.5 s.

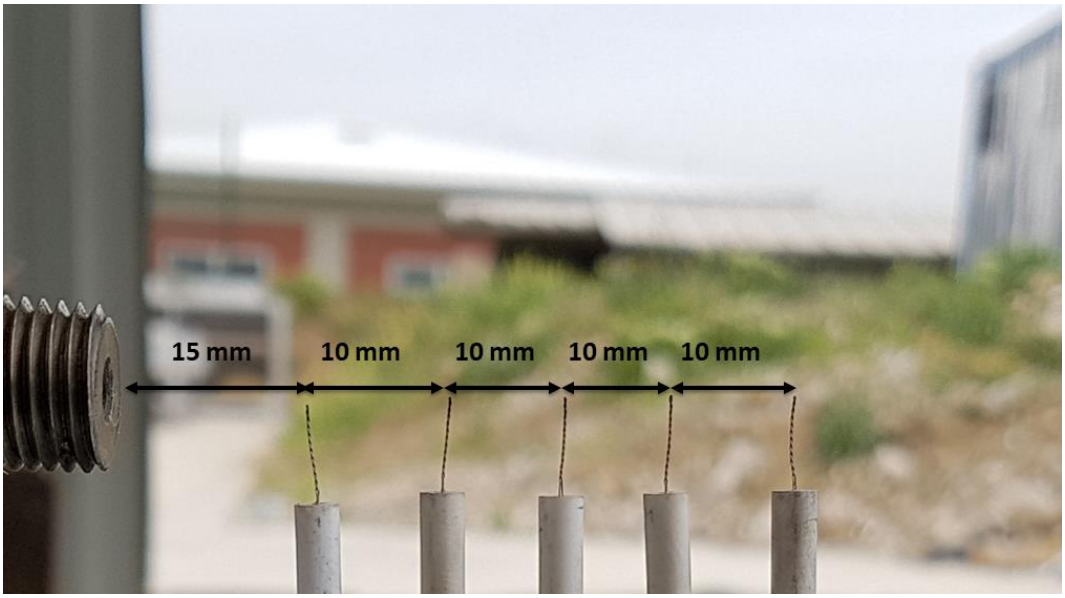

Figure 2-14. Allocation of Thermocouples in the Plume Region

2.7. Experimental Campaign

Oxygen rich combustion in the GO_x/GH_2 ASIs is a settled practice [10, 13]. High O/F ratios provided durable and reliable combustion in the igniter, and eliminated results of high adiabatic flame temperatures (see Figure 2-15 for the adiabatic flame temperatures of hydrogen/oxygen mixtures with respect to O/F ratio at standard conditions), such as sudden detonation and/or necessity for cooling of the igniter. In this extent, O/F ratios of the tests were kept at high values.

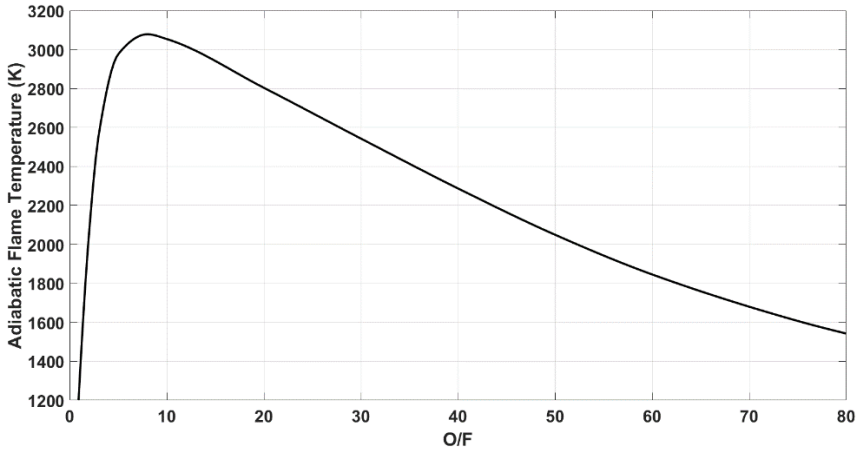

Figure 2-15. Adiabatic Flame Temperature of GO_2/GH_2 mixtures vs. O/F Ratio [32]

Mass flow rates of gaseous oxidizer and gaseous fuel was controlled with orifices. Supply pressure of the inlets of the orifices were regulated, stabilized and observed during the experiments. Since, choked condition is reached at every point by selecting high supply pressure values, stability and independence from downstream pressure of mass flow rates was ensured. Also, total mass flow rates of the campaign were confined at low levels, simply to be on the safe side.

To avoid potential manufacturing faults in tolerances, eccentricity and to have repeatable and fast supply of orifices, in case of any harm to test article, orifices of a self-proven orifice manufacturer were chosen to utilize on test article. The orifice set was provided by O-KEFEE CONTROLS CO., and it was manufactured from 303 grade stainless steel. The set is demonstrated in App. A. The mass flow rates were calculated using the tabulated data of the manufacturer (App. A.).

O/F ratio of 40 was selected as base, and other two conditions were determined such that total mass flow rate was kept nearly constant, while O/F is changed for corresponding supply pressure. O/F ratio was varied to 50 and 75. For each O/F ratio, tests were carried out with a supply pressure of 10, 20, 30 and 40 barg at both inlets. Total of twelve tests were scheduled in 3 sequence with respect to O/F ratio. Overall test matrix can be seen in Table 2-1. Test sequences are summarized in Table 2-2, Table 2-3 and Table 2-4.

Table 2-1. *Test Matrix*

O/F	40	50	75
Supply Pressure (barg)	10-20-30-40	10-20-30-40	10-20-30-40

Table 2-2. *Test Sequence-1*

Test Number	Supply Pressure (barg)	O/F	GO_2 Mass Flow Rate (kg/s)	GH_2 Mass Flow Rate (kg/s)	Total Mass Flow Rate (kg/s)
1	10	~40	0.00088	0.000021	0.000901
2	20	~40	0.00169	0.000041	0.001731
3	30	~40	0.00252	0.000061	0.002581
4	40	~40	0.00335	0.000081	0.003431

Table 2-3. *Test Sequence-2*

Test Number	Supply Pressure (barg)	O/F	GO_2 Mass Flow Rate (kg/s)	GH_2 Mass Flow Rate (kg/s)	Total Mass Flow Rate (kg/s)
5	10	~50	0.00088	0.000017	0.000897
6	20	~50	0.00169	0.000033	0.001723
7	30	~50	0.00252	0.000049	0.002569
8	40	~50	0.00335	0.000065	0.003415

Table 2-4. *Test Sequence-3*

Test Number	Supply Pressure (barg)	O/F	GO_2 Mass Flow Rate (kg/s)	GH_2 Mass Flow Rate (kg/s)	Total Mass Flow Rate (kg/s)
9	10	~75	0.00088	0.000012	0.000892
10	20	~75	0.00169	0.000023	0.001713
11	30	~75	0.00252	0.000034	0.002554
12	40	~75	0.00335	0.000044	0.003394

Before every test, pneumatic vanes were opened and cold flow tests were carried out to regulate flow such that desired supply pressure value before the orifice is reached and stabilized.

In the tests, hydrogen is introduced to system one second after the oxygen, to avoid accumulation of hydrogen without burning inside the combustion chamber. This could have led to explosion.

2.8. Uncertainty Analysis

Every sensor has an uncertainty margin on the measurement that it has made. Apart from other possible source of errors, uncertainty is the deviation from the actual value on the readings [33]. Hence, with a certain confidence level, a measurement can be expressed with the measured value and uncertainty percentage.

Pressure transducer which is used throughout in the experiments, has an accuracy of ±2% at most [34]. This indicates ±2000 Pa error for 1 bar actual value. This error value is acceptable within the range of this work.

Thermocouples that are placed in the plume region to measure temperature of the flame have an accuracy of ±4.5 K up to 450 K, and above 450 K ±1% [35].

Other source of errors in the readings are explained and discussed in the corresponding sections.

CHAPTER 3

NUMERICAL METHODOLOGY

3.1. Introduction

One of the aims of this study is to develop a numeric tool to simulate the physical phenomena and to validate it by comparing with experimental data. If validated, the code will be used later on preliminary design stage of future igniters. Therefore, analyses were done at steady state, to have solutions faster. All the experiments were simulated using this numerical model with the exact mass flow rates and the ambient conditions of the experiments. Model was established in ANSYS Fluent computational fluid dynamics tool environment. This tool utilizes finite volume to discretize governing differential equations. Details are explained in the next title. All computations were done in three-dimensional space with pressure-based solver, and the solution domain consists both the volume of the igniter and the outer region where igniter exhausts.

3.2. Governing Equations

In the numerical analyses, steady state Navier-Stokes equations with turbulence were solved along with compressible flow and combustion in Eularian approach. Reacting species are treated as ideal gas and their thermodynamic and transport properties were taken from built-in library. The velocity vector can be shown as:

$$\vec{V} = \vec{V_x} + \vec{V_y} + \vec{V_z} \qquad (3\text{-}1)$$

where subscripts indicate principal axes. In reacting flows, conservation of mass is defined with the Equation (3-2), Y_i is the mass fraction of each species, J_i is the diffusion flux of each species and R_i is the net rate of production of each species.

$$\nabla\left(\rho\vec{V}Y_i\right) = -\nabla\overline{J_\iota} + R_i \tag{3-2}$$

Diffusion flux can be disintegrated into Equation (3-3). $D_{i,m}$ is the mass diffusion coefficient for the species i in the mixture, μ_t is the turbulent viscosity, Sc_t is the turbulent Schmidt number, T is the temperature and $D_{T,i}$ is the thermal diffusion coefficient. Schmidt number is elaborated with Equation (3-4), where D_t turbulent diffusivity.

$$\overline{J_\iota} = -\left(\rho D_{i,m} + \frac{\mu_t}{S_{ct}}\right)\nabla Y_i - D_{T,i}\,\frac{\nabla T}{T} \tag{3-3}$$

$$Sc_t = \frac{\mu_t}{\rho D_t} \tag{3-4}$$

In viscous flow, conservation of momentum is written as:

$$\nabla\left(\rho\vec{V}.\vec{V}\right) = -\nabla\mathrm{P} + \ \nabla.(\bar{\bar{\tau}}) \tag{3-5}$$

where P is the pressure and $\bar{\bar{\tau}}$ is the stress tensor which is caused by viscous forces and defined by Equation (3-6). μ indicates molecular viscosity and I is the unit tensor.

$$\bar{\bar{\tau}} = \mu\left(\nabla\vec{V} - \frac{2}{3}\nabla\vec{V}I\right) \tag{3-6}$$

Conservation of energy in reacting flows can be expressed as follows:

$$\nabla\left(\vec{V}(\rho E + P)\right) = \nabla.(\mathrm{k}_{eff}\nabla\mathrm{T} - \nabla(\sum_j h_j\overline{J_j}) \ + \bar{\bar{\tau}}.\vec{V}) \ + S_h \tag{3-7}$$

where k_{eff} is the effective conductivity, which is the sum of turbulent thermal conductivity and thermal conductivity, h_j is the sensible enthalpy of each species and S_h is the heat of chemical reaction. The energy term E is:

$$\mathrm{E} = \sum_j h_j Y_j - \frac{\mathrm{P}}{\rho} + \frac{V^2}{2} \tag{3-8}$$

For ideal gases, sensible enthalpy for species "j" can be approached as:

$$h_j = \int_{T_{ref}}^{T} c_{p,j} dT \cong \left(T - T_{ref}\right) c_{p,j} \ (T_{ref} = 298.15) \tag{3-9}$$

Heat of chemical reaction is calculated by:

$$S_h = -\sum_j \frac{h_j^0}{M_j} \mathcal{R}_j \tag{3-10}$$

where h^0 is the enthalpy of formation, M is the molar mass, $\mathcal{R}$ is the volumetric rate of creation. Heat transfer in solid regions are modeled such as:

$$\nabla\left(\vec{V}.\rho h\right) = \nabla(\mathrm{k}\nabla\mathrm{T}) \tag{3-11}$$

where, k is the thermal conductivity of the solid zone. Equation of state for ideal gases is:

$$\rho = \frac{\mathrm{P}}{\frac{R_u}{M_w} T} \tag{3-12}$$

where R_u is the universal gas constant, M_w is the molecular weight. For a perfect gas, in compressible and isentropic flow stagnation temperature (T_0) can be related to static temperature by:

$$\frac{T_0}{T} = 1 + \frac{\gamma - 1}{2} M^2 \tag{3-13}$$

where M is the Mach number. It is the ratio of the velocity of the flow to the sound velocity at that conditions. If the process is assumed to be isentropic, Equation (3-12) and Equation could be combined to obtain the relationship between stagnation pressure (P_0) to static pressure. This relationship is expressed by the following equation:

$$\frac{P_0}{P} = \left(1 + \frac{\gamma - 1}{2} M^2\right)^{\frac{\gamma}{\gamma - 1}} \tag{3-14}$$

3.2.1. Turbulence Modeling

To model turbulence in numerical model "Reynolds-Averaged Navier Stokes" (RANS) equations are utilized. In RANS, vectors and scalar quantities consist of mean and fluctuating components. Symbols with bar on them symbolizes mean, or time-averaged, values, while symbols with dash on them symbolizes fluctuating (deviation from mean) values.

$$\vec{V_x} = \overline{V_x} + V_x' \tag{3-15}$$

$$\emptyset = \overline{\emptyset} + \emptyset' \tag{3-16}$$

Now the conservation of momentum equation in Cartesian tensor from takes the form [36] :

$$\frac{\partial}{\partial x_j}\left(\rho u_i u_j\right) = \frac{\partial \rho}{\partial x_i} + \frac{\partial \rho}{\partial x_j}\left[\mu\left(\frac{\partial u_i}{\partial x_j} + \frac{\partial u_j}{\partial x_i} - \frac{2}{3}\delta_{ij}\frac{\partial u_l}{\partial x_l}\right)\right] + \frac{\partial}{\partial x_j}\left(-\rho\overline{u_i' u_j'}\right) \tag{3-17}$$

The additional term on the right hand side of the equation is called Reynolds stresses [36] and they must be modeled. Throughout the analyses "Boussinesq" approach [36] is utilized.

$$-\rho\overline{u_i' u_j'} = \mu_t\left(\frac{\partial u_i}{\partial x_j} + \frac{\partial u_j}{\partial x_i}\right) - \frac{2}{3}\left(\rho k + \mu\frac{\partial u_k}{\partial x_k}\right)\delta_{ij} \tag{3-18}$$

where k is the turbulent kinetic energy. Low computational cost is the main advantage of this approach. However, additional transport equations should be solved to obtain turbulent kinetic energy and turbulent viscosity. In literature, it is seen that "Realizable k-ε" model is widely used to simulate round jets, recirculating and turbulent reactive flows [37], [38]. In one of these studies [37], experiments took place regarding a combustion chamber and it was shown that the Realizable k-ε model lead compatible results with the experiments. In the same study, LES model was also used to simulate turbulence in numerical analyses that simulate experiments. Even though, the LES model was more compatible with the experiments, it should be noted that it requires higher number of elements and transient solution that could take months to solve. Therefore, Realizable k-ε approach is employed in numerical analyses. "k" resembles turbulent kinetic energy and "ε" stands for turbulent kinetic energy dissipation rate. The modified transport equation for this model are as follows [39]:

$$\frac{\partial}{\partial x_j}(\rho k u_j) = \frac{\partial}{\partial x_j}\left[\left(\mu + \frac{\mu_t}{\sigma_k}\right)\frac{\partial k}{\partial x_j}\right] + G_k + G_b + \rho\varepsilon - Y_M + S_k \tag{3-19}$$

$$\frac{\partial}{\partial x_j}(\rho \varepsilon u_j) = \frac{\partial}{\partial x_j}\left[\left(\mu + \frac{\mu_t}{\sigma_\varepsilon}\right)\frac{\partial \varepsilon}{\partial x_j}\right] + \rho C_1 - \rho C_2 \frac{\varepsilon^2}{k + \sqrt{\nu\varepsilon}} + C_{1\varepsilon}\frac{\varepsilon}{k} C_{3\varepsilon} G_b + S_\varepsilon \tag{3-20}$$

$$C_1 = \max\left(0.43, \frac{\eta}{\eta + 5}\right), \eta = S\frac{k}{\varepsilon}, S = \sqrt{2 S_{ij} S_{ij}} \tag{3-21}$$

$$S_{ij} = \frac{1}{2}\left(\frac{\partial u_i}{\partial x_j} + \frac{\partial u_j}{\partial x_i}\right) \tag{3-22}$$

where, G_k is the generation of turbulence kinetic energy that is caused by the mean velocity gradients, G_b is the generation of turbulent kinetic energy due to buoyancy which is zero in the scope of this thesis, since gravitational effects are neglected. Y_m

contributes the fluctuating dilatation in compressible turbulence with respect to dissipation rate. σ_k and σ_ε are the turbulent Prandtl numbers for k and ε, respectively. C_2 and $C_{1\varepsilon}$ are constants that are obtained empirically. S_k and S_ε are source terms. S is the modulus of the mean rate-of-strain tensor. Turbulent viscosity is calculated by the equations below.

$$\mu_t = \rho C_\mu \frac{k^2}{\varepsilon} \tag{3-23}$$

$$C_\mu = \frac{1}{A_0 + A_s \frac{kU^*}{\varepsilon}} \tag{3-24}$$

$$U^* \equiv \sqrt{S_{ij}S_{ij} + \widetilde{\Omega}_{ij}\Omega_{ij}} \;, \widetilde{\Omega}_{ij} = \Omega_{ij} - 2\varepsilon_{ijk}\omega_k \;, \Omega_{ij} = \overline{\Omega_{ij}} - \varepsilon_{ijk}\omega_k \tag{3-25}$$

where Ω_{ij} is the rate of rotation tensor according to moving reference frame with the angular velocity ω_k .

$$A_s = \sqrt{6}\cos\emptyset \tag{3-26}$$

$$\emptyset = \frac{1}{3}\cos^{-1}\left(\sqrt{6}W\right), W = \frac{S_{ij}S_{jk}S_{ki}}{\left(\frac{S}{\sqrt{2}}\right)^3} \tag{3-27}$$

The constants in the equations are summarized at Table 3-1.

Table 3-1. *Constants in the Turbulence Modelling Equations*

$C_{1\varepsilon}$	C_2	σ_k	σ_ε	A_0
1.44	1.9	1	1.2	4.04

3.2.2. Combustion Modeling

Combustion modeling in turbulent reacting flows starts with the prediction of which turbulence-chemistry interaction model is to be used. The decision is made based on the "Damköhler" number (Da) (Equation) [40]. It is a dimensionless number that defines the ratio of speed of fluid mixing to the chemical reaction rate. Da>> 1 means that flow time scale dominates over the domain and reaction is controlled by turbulent mixing. However, Da<<1 states that chemical time scale is dominant, and reaction rate is controlled by molecular reaction kinetics. Specific to this study, Damköhler number is calculated as suggested by [21], [41]

$$Da = \frac{Characteristic\ Flow\ Time}{Characteristic\ Chemical\ Time} = \frac{\tau_{flow}}{\tau_{chem}} \tag{3-28}$$

$$\tau_{flow} = \frac{Turbulent\ Kinetic\ Energy\ (k)}{Turbulent\ Dissipation\ Rate\ (\varepsilon)} \tag{3-29}$$

Characteristic chemical time scale is computed for different initial temperatures, which are possible to occur inside the combustion chamber (1000-3000 K), by obtaining the time that an isobaric and adiabatic batch reactor, which has the same fuel/oxidizer composition with the Test-1, reaches the 99% of the adiabatic flame temperature, using zero-dimensional kinetic simulations [42]. Characteristic flow time is obtained from cold flow solution of Test-1. Then, with an average value of $\tau_{flow,}$ Damköhler number is obtained (by simply calculating the ratio) and plotted in Figure 3-1. As it can be seen from Figure 3-1, the Damköhler number increases with increasing temperature, since the characteristic chemical time decreases as temperature increases. Another outcome is that the Damköhler number is not significantly high, but also not significantly low. This states that dominance changes between chemical time scale and flow time scale.

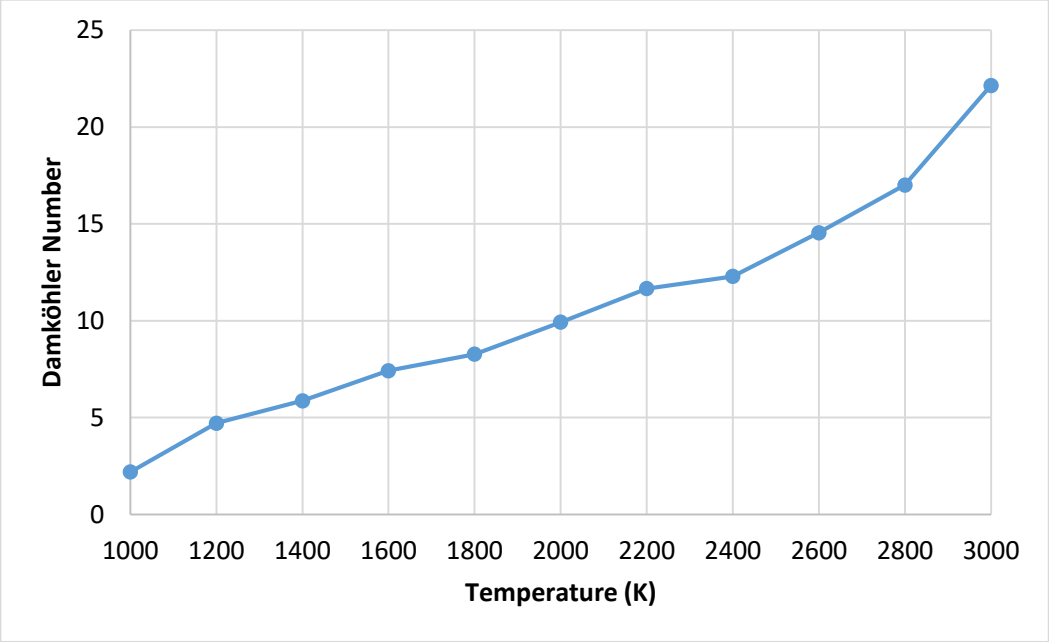

Figure 3-1. Initial Temperature at Ambient Pressure vs. Damköhler Number

As a result, eddy dissipation concept (EDC) model is used in numerical solutions. EDC is turbulence-chemistry interaction model. Unlike laminar finite rate method, it takes turbulence chemistry interaction effects into account and instead of eddy dissipation method it can include detailed chemistry in the solution [43]–[45]. In other words, turbulent flames can be solved along with detailed Arrhenius chemical kinetics. To evaluate hydrogen oxidation, a detailed and verified reaction mechanism [46] (see App. B) is selected. The mechanism consists of 19 reversible reactions and it is verified over a wide range of temperatures, pressures, and equivalence ratios. Modifications to thermodynamic and transport data of the species were done according to aforementioned work [46].

Forward or backward rate constant for a reaction, also production or consumption rate of a species, according to temperature can be expressed in Arrhenius form [40]:

$$k_r = AT^b \exp(-\frac{E_A}{R_u \mathrm{T}}) \tag{3-30}$$

where A is the pre-exponential factor, E_a is the activation energy and b is an empirical constant.

Eddy Dissipation Concept model postulates that chemical reactions happen in small turbulent structures for a given period of time. These little turbulent structures are called fine scales. The governing equations for the Eddy Dissipation Concept model are given:

$$\xi^* = C_\xi \left(\frac{\nu\varepsilon}{k^2}\right)^{\frac{1}{4}} \tag{3-31}$$

where ξ^* represents length fraction of the fine scales, C_ξ is the volume fraction constant (=2.1377), ν is the kinematic viscosity. Time scale that the reactions are assumed to occur is calculated by the following equation:

$$\tau^* = C_\tau \left(\frac{\nu}{\varepsilon}\right)^{\frac{1}{2}} \tag{3-32}$$

where C_τ is the time scale constant (=0.4082). As a result, the source term in mass conservation equation takes the form:

$$R_i = \frac{\rho {\xi^*}^2}{\tau^*\left(1 - {\xi^*}^3\right)} (Y_i^* - Y_i) \tag{3-33}$$

where Y_i^* is the fine scale species mass fraction after reacting over time τ^*.

3.3. Solution Domain

The three dimensional solution domain is shown in in Figure 3-2 and boundary conditions that are applied in numerical analyses are shown in Figure 3-3.

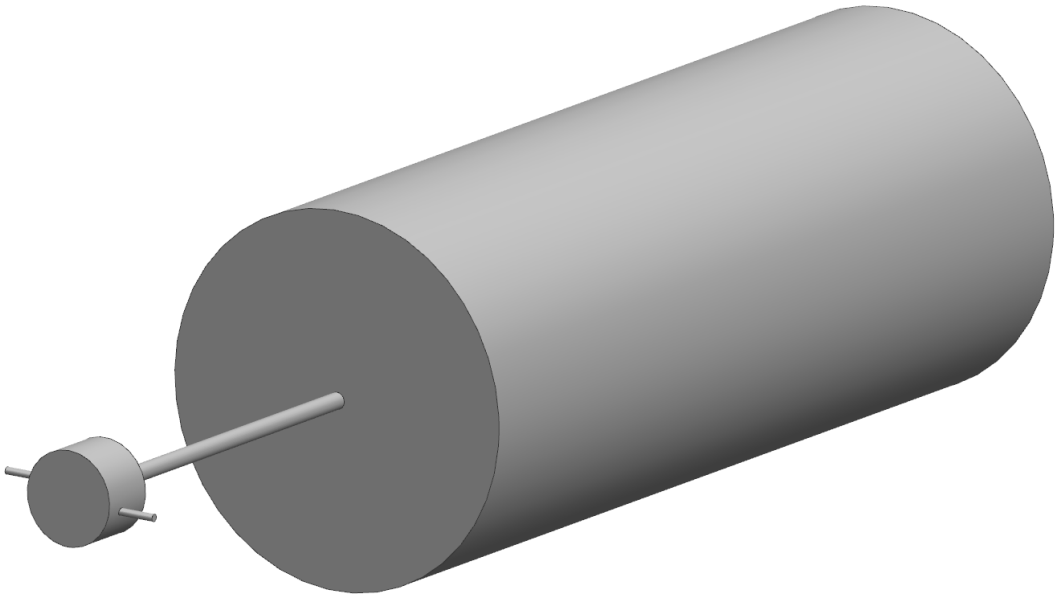

Figure 3-2. Solution Domain

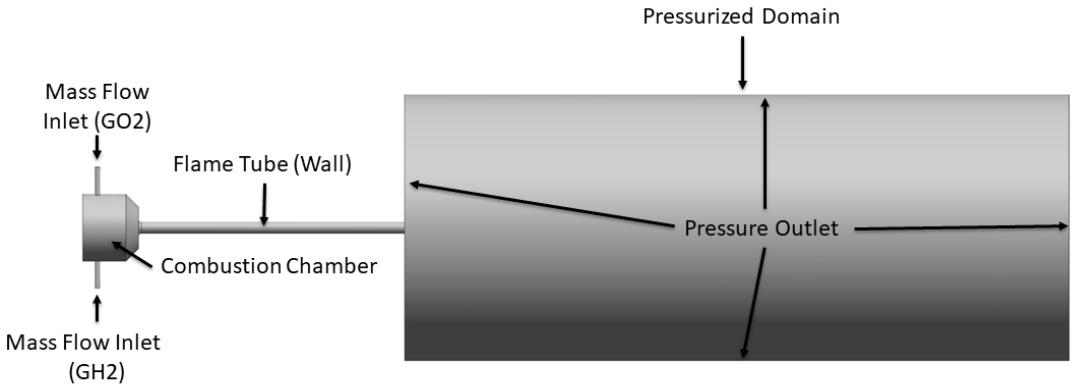

Figure 3-3. Boundary Conditions of Numerical Analyses

Fuel and oxidizer inlets are modeled as mass flow inlet with backpressure value information and mass flow rates that are obtained by the orifices in experimental tests. Surfaces that envelop combustion chamber and flame tube are modeled as wall with corresponding thickness with respect to test article. Zero dimensional heat transfer are solved for these walls with constant surface temperature at the outermost surface of the igniter by inputting solid material's (stainless steel) heat transfer properties. Even tough, flow and reactions in the igniter solved in steady state, it is assumed that heat

transfer in the solid region couldn't achieve steady state throughout the experiment time. That's why, outer surfaces of the igniter, which is modeled by thickness, were kept at constant temperature of the experiment date.

The surfaces of the outer region, where plume exhausts, are modeled as pressure outlet with knowledge of static pressure of the test place and temperature of the experiment date. Pressure outlet boundary conditions also have the knowledge of mass fractions of the ambient air.

3.4. Grid Independence Study

After having solution domain, grid independence study was done. Except first two layers from the outside, Cartesian grid is utilized in the domain with hexahedron. Outside layers were gridded into polyhedral elements. Hence Cartesian grid was obtained in most of the solution domain, while total numbers of elements were kept as small as possible. This meshing technique is called "Poly-Hexcore", and it is seen that it has a faster convergence rate with less number of elements [47] in comparison to conventional techniques.

The grid independence study was carried out by keeping maximum mesh size at 1mm, 0.5 mm and 0.25 mm in the combustion chamber, flame tube and some portion of the pressurized domain for the coarse, medium and fine grids, respectively. The resulting grids are given together in Figure 3-4. The coarse grid has 483,228 elements, the medium grid has 2,371,106 elements and fine grid has 4,747,050 elements.

To test mesh independency, Test-1 is simulated. In order to present the results of the grid sensitivity study temperature, velocity, OH and H_2O mass fractions are plotted along a 0.25 m line, which is extended from the upper surface of the igniter to the flame region, and results can be examined from Figure 3-5, Figure 3-6, Figure 3-7 and Figure 3-8.

As it can be seen from Figure 3-5, Figure 3-6, Figure 3-7 and Figure 3-8, medium and fine grid data almost overlap, and the maximum discrepancy is less than 5%.

Therefore, it is concluded that mesh independence is provided by limiting maximum grid size to 0.5 mm in the combustion chamber, flame tube and some portion of the pressurized domain. Hence, medium grid is used in further analyses.

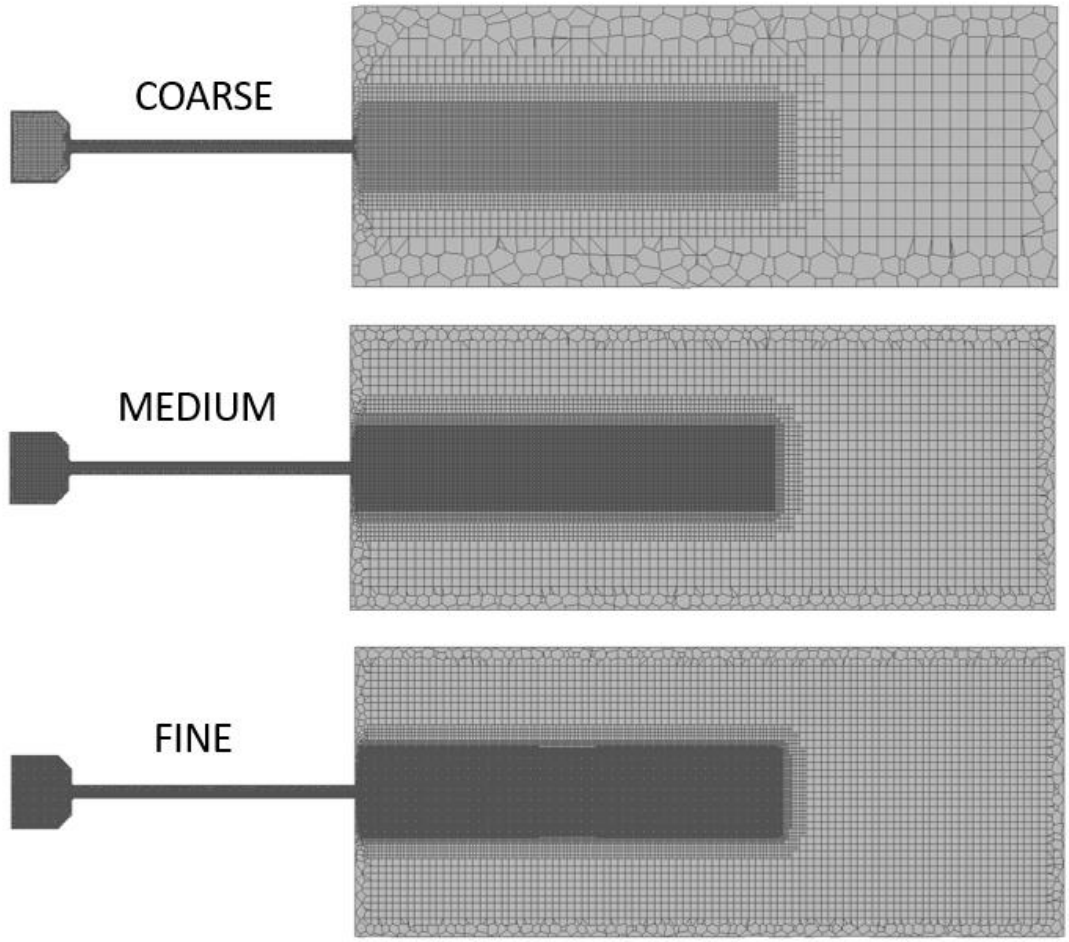

Figure 3-4. Coarse, Medium and Fine Grids

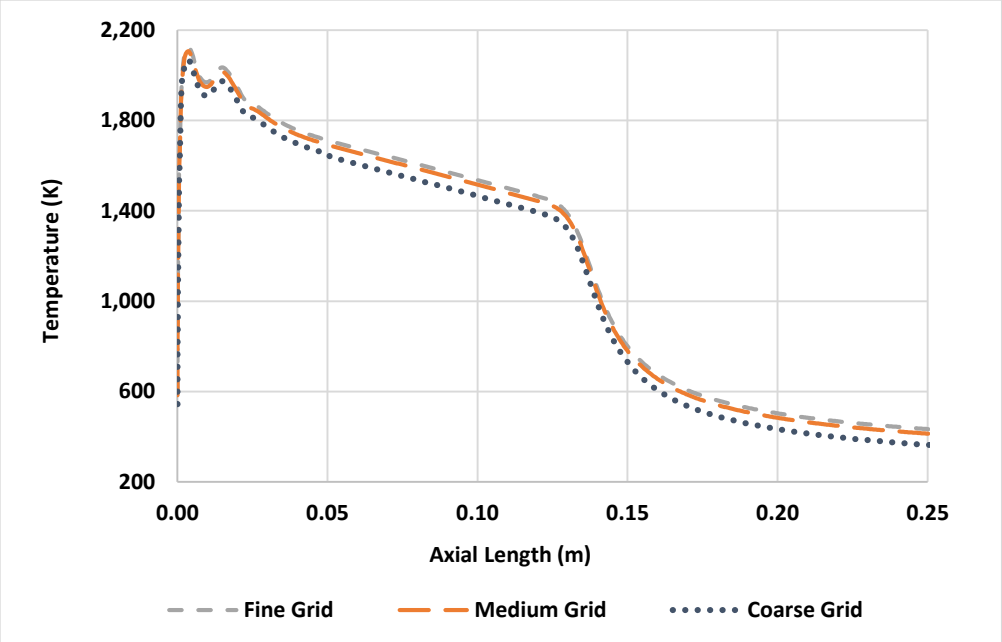

Figure 3-5. Grid Sensitivity Results for Static Temperature

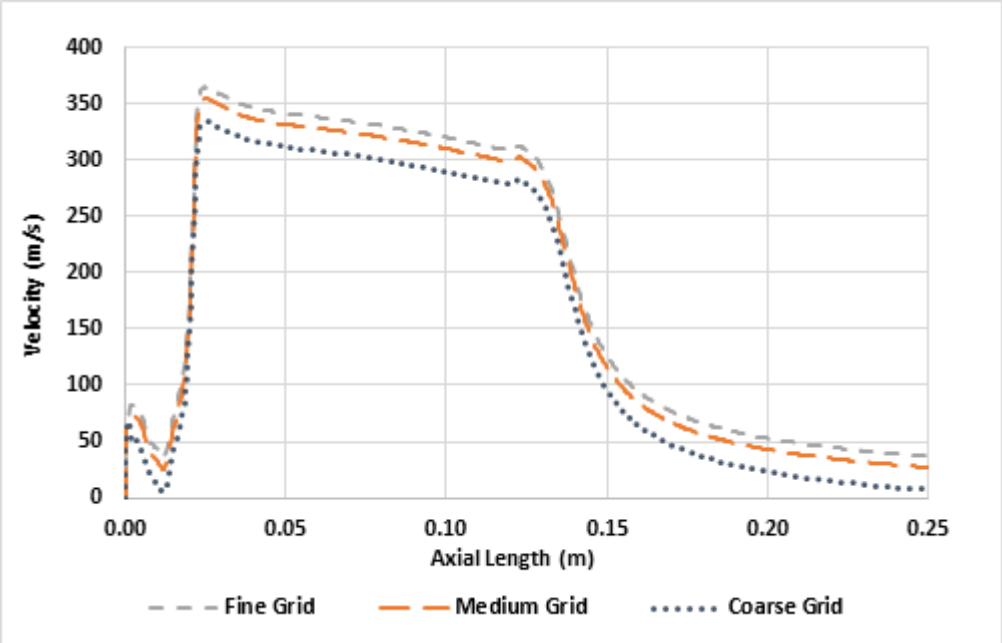

Figure 3-6. Grid Sensitivity Results for Velocity

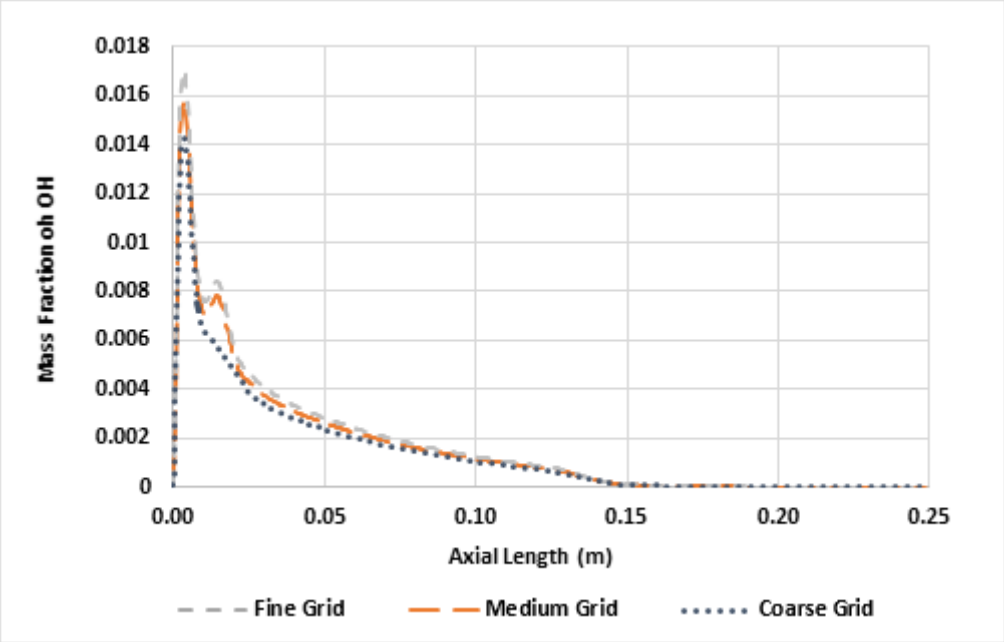

Figure 3-7. Grid Sensitivity Results for OH Mass Fraction

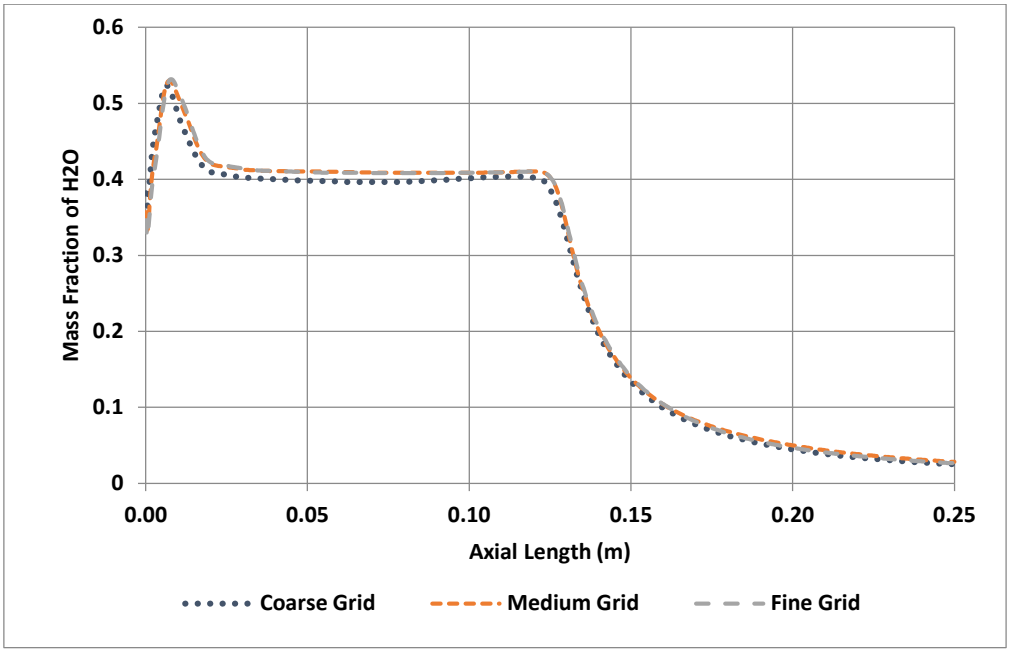

Figure 3-8. Grid Sensitivity Results for H_2O Mass Fraction

CHAPTER 4

COMPARISON OF NUMERICAL AND EXPERIMENTAL RESULTS

4.1. Introduction

Herein, outcomes of numerical analyses are presented and discussed firstly. Then experimental results are given in comparison with numerical analyses. Numerical analyses include contours of temperature, pressure, density, mass fractions of GH_2, GO_2, OH and H_2O. While experimental results contain schlieren images, pressure of the combustion chamber during combustion, and temperature data from plume. Comparison of numerical and experimental results were done in many aspects.

4.2. Numerical Results

All contour plots are drawn on two surfaces. The first one divides whole solution domain into two, while the second one is a plane that contains axis of the inlets and it is perpendicular to first one. These planes are shown on the solution domain model at Figure 4-1.

For all analyses, after cold flow solution without combustion modelling is converged, ignition is achieved by patching a hot cylindrical region inside the combustion chamber and by activating combustion model. Thus, product species start to appear and combustion starts inside the chamber. Later, analyze continues until steady state solution is obtained.

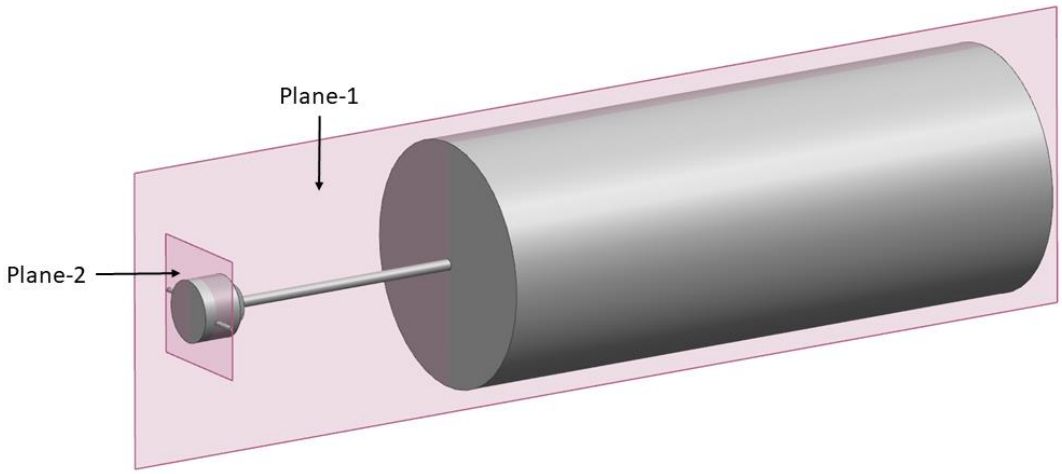

Figure 4-1. Planes of Contour Plots

4.2.1. Temperature

Static temperature values of all test are plotted along a 0.37 m line (centerline axis), which is extended from the upper surface of the igniter to the end of the solution domain, and results can be examined from Figure 4-2. Static temperature contours of the analyses are plotted on two different planes (Figure 4-1) and shown in Figure 4-3, Figure 4-4 and Figure 4-5 for Test-4, Test-8 and Test-12 respectively. Contour plots of all tests can be seen in Appendix D. As it can be observed from the figures, the highest temperature values of the solutions are higher than the adiabatic flame temperatures of the corresponding O/F ratios (Figure 2-15). Hydrogen and oxygen didn't mix well before the combustion, so the combustion didn't show premixed flame properties. Hydrogen molecules that enter the combustion chamber ignite as they come into contact with oxygen molecules. As a consequence, the O/F ratio is not constant throughout the combustion chamber (see App. C). Jet of the hydrogen couldn't penetrate through the chamber as it is repressed by the oxygen jet. Therefore it bends through the chamber wall and ignites at lower O/F ratios. This behavior exposes itself as mass flow rate increases for the same overall O/F ratio. However, this hydrogen richer flame couldn't reach the other side of the combustion chamber, because of the fast and cold oxygen jet. Thus the temperature distribution in whole chamber are highly unsymmetrical. But, this asymmetry decays when the O/F ratio

increases, due to lower temperatures and rapid consumption of lower number of hydrogen molecules don't let flame formation elsewhere and the energy diffuses with rotational flow inside the chamber. Also it is indicated from the results, as the O/F ratio decreases, and/or as the total mass flow rate increases, average temperature of the plume increases, as expected. For all contour images of Plane-2, oxygen flows from left side, and hydrogen enters the combustion from right side.

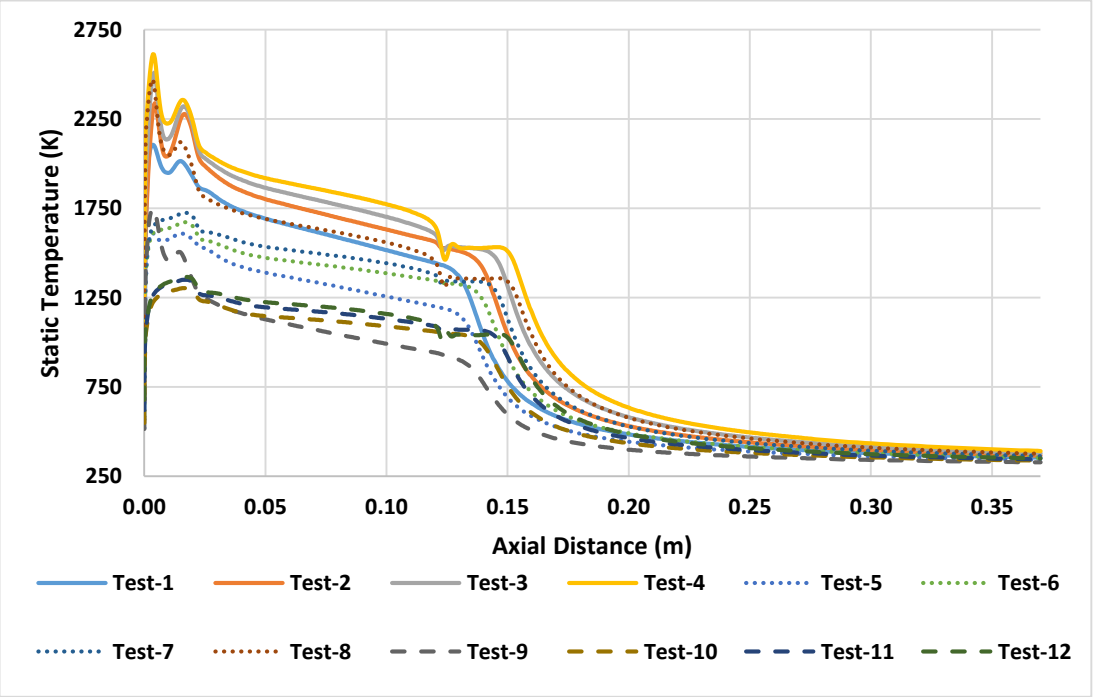

Figure 4-2. Static Temperature Values Along the Centerline of Solution Domain

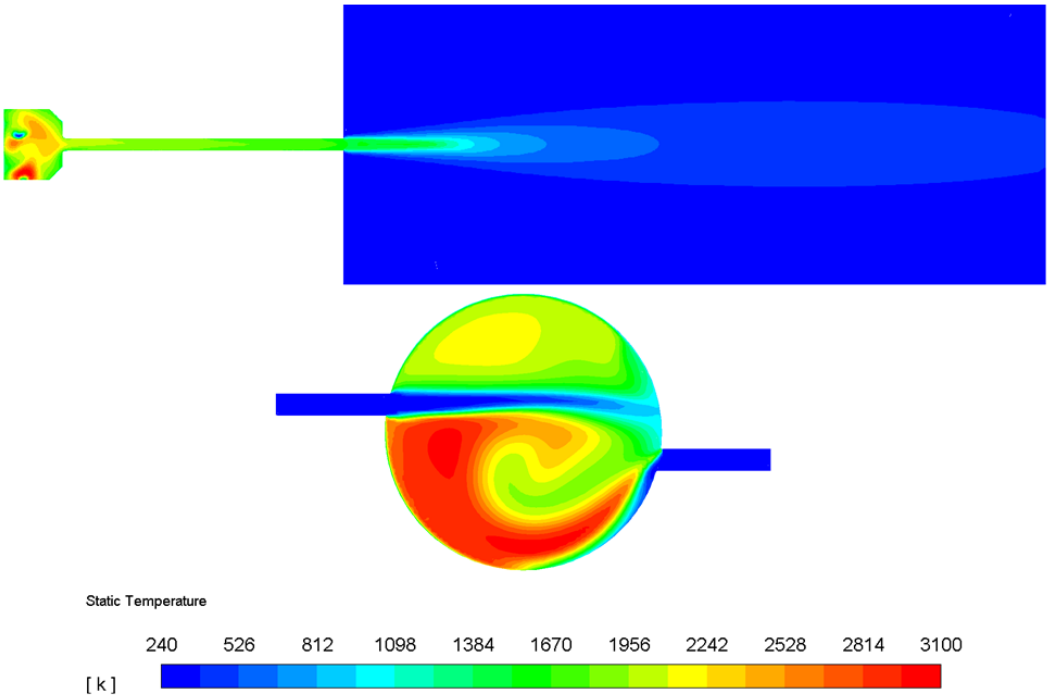

Figure 4-3. Static Temperature Contours on Plane-1 and Plane-2 of Test-4

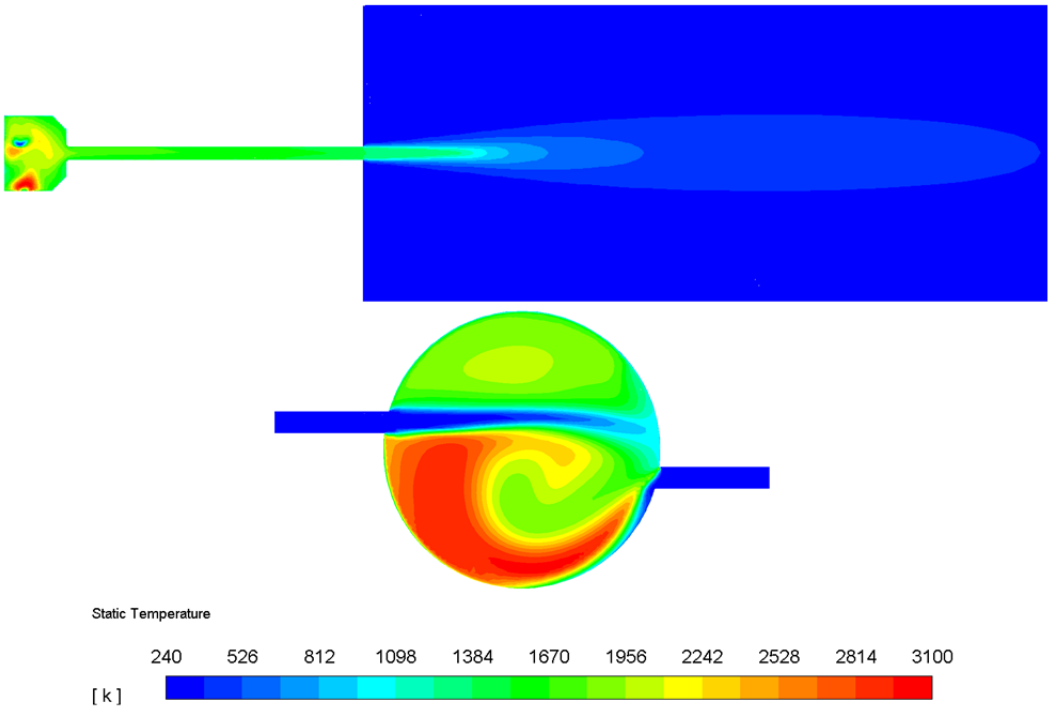

Figure 4-4. Static Temperature Contours on Plane-1 and Plane-2 of Test-8

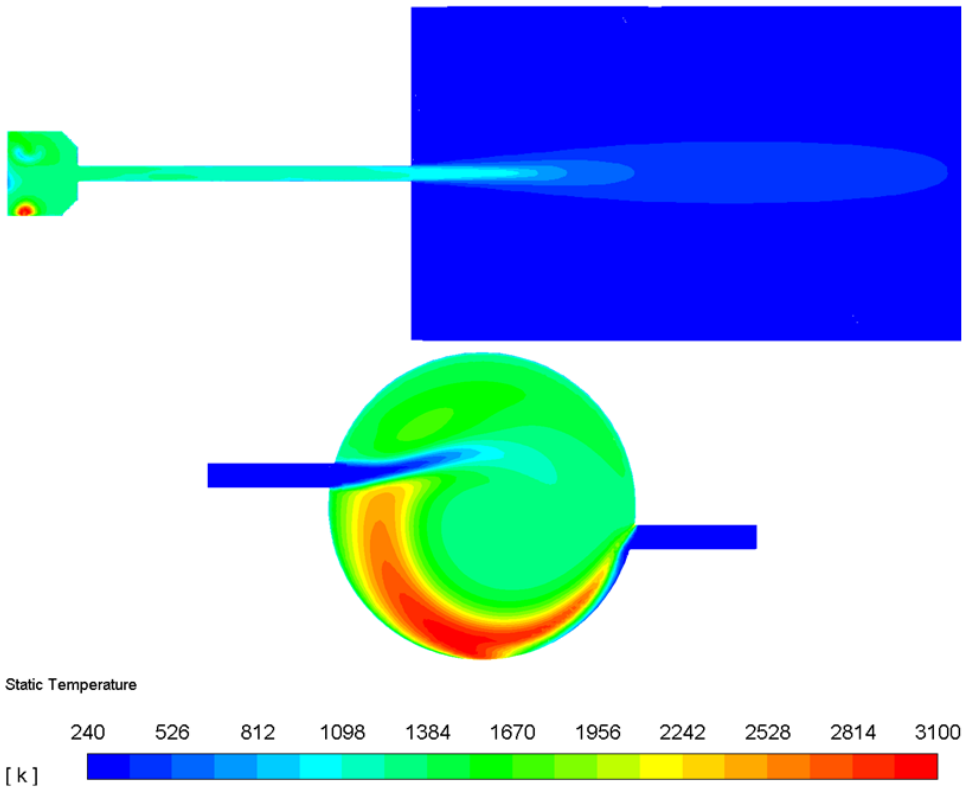

Figure 4-5. Static Temperature Contours on Plane-1 and Plane-2 of Test-12

4.2.2. Pressure

Absolute pressure values of all test are plotted along a 0.37 m line (centerline axis), which is extended from the upper surface of the igniter to the end of the solution domain, and results can be examined from Figure 4-6. Absolute pressure contours of the analyses are plotted on Plane-1 (Figure 4-1) and shown in Figure 4-7, Figure 4-8 and Figure 4-9 for Test-4, Test-8 and Test-12 respectively. Contour plots of all tests can be seen in Appendix E. It is understood that flow is choked for the 30-40 barg analyses. This can be shown by a quick calculation:

$$\frac{P_{cr}}{P} = \left(\frac{2}{\gamma + 1}\right)^{\frac{\gamma}{\gamma - 1}} \tag{4-1}$$

Where P_{cr} is the critic pressure of the downstream for choked flow. Equal to or below this point, flow is choked according to ideal gas law. For 87000 pascal downstream pressure, minimum reservoir (total) pressure:

$$\gamma = 1.4, P \cong 164685\ pascal \tag{4-2}$$

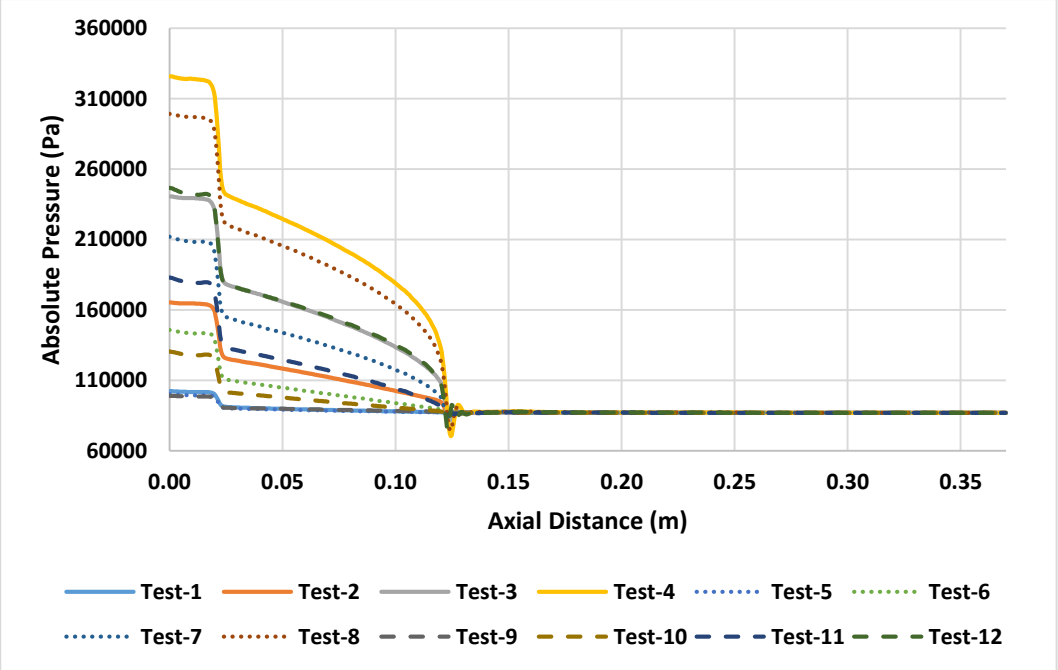

Figure 4-6. Absolute Pressure Values Along the Centerline of Solution Domain

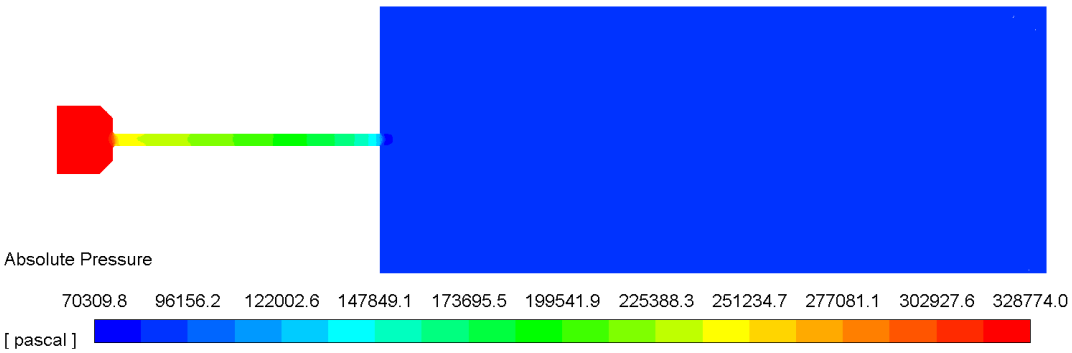

Figure 4-7. Absolute Pressure Contours on Plane-1 (Test-4)

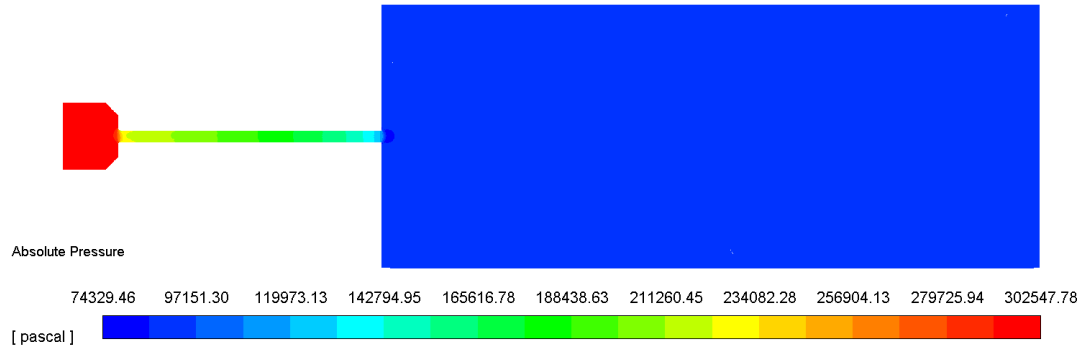

Figure 4-8. Absolute Pressure Contours on Plane-1 (Test-8)

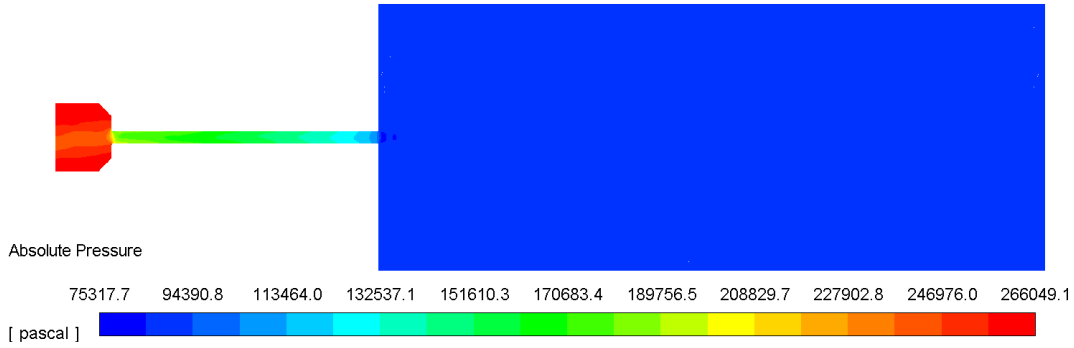

Figure 4-9. Absolute Pressure Contours on Plane-1 (Test-12)

4.2.3. O_2 Mass Fraction

O_2 mass fraction contours of the analyses are plotted on the Plane-2 (Figure 4-1) and shown in shown in Figure 4-10, Figure 4-11 and Figure 4-12 for Test-4, Test-8 and Test-12 respectively. Contour plots of all tests can be seen in Appendix F. Due to high values of O/F ratios, oxygen is dominant in the combustion chamber. When the O/F ratio increases, mass fraction of O_2 ascends through 1. As explained before, oxygen jet pushes the hydrogen jet through the wall, and in that region where hydrogen jet washes the wall, mass fraction of oxygen decays.

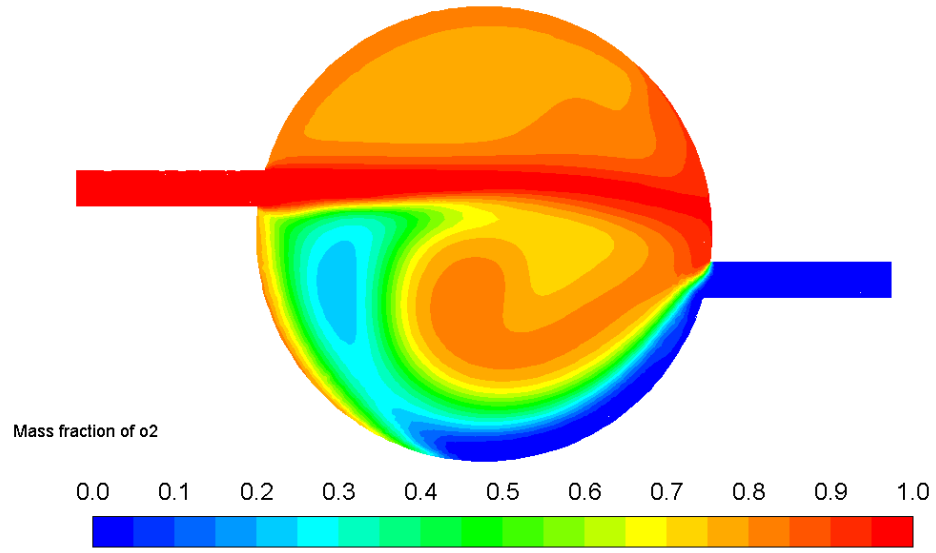

Figure 4-10. O_2 Mass Fraction Contours on Plane-2 (Test-4)

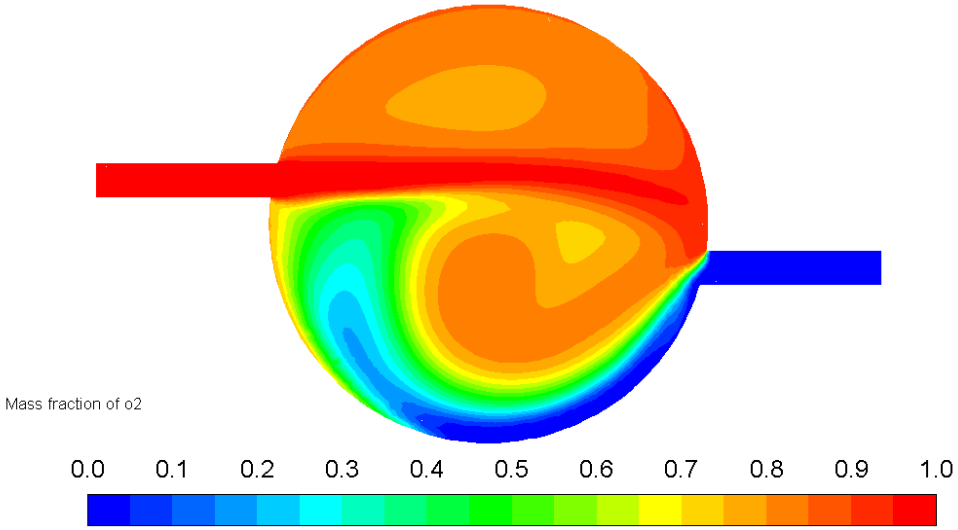

Figure 4-11. O_2 Mass Fraction Contours on Plane-2 (Test-8)

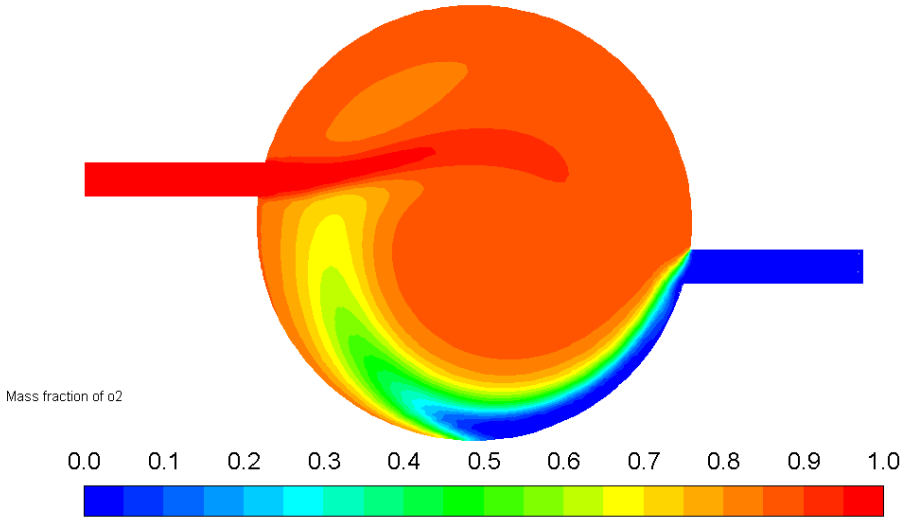

Figure 4-12. O_2 Mass Fraction Contours on Plane-2 (Test-12)

4.2.4. H_2 Mass Fraction

H_2 mass fraction contours of the analyses are plotted on Plane-2 (Figure 4-1) and shown in Figure 4-13, Figure 4-14 and Figure 4-15 for Test-4, Test-8 and Test-12 respectively. Contour plots of all tests can be seen in Appendix G. H_2 molecules disappear quickly, as it is oxidized. As an outcome of high O/F ratio, rapid consumption of H_2 is easily observed.

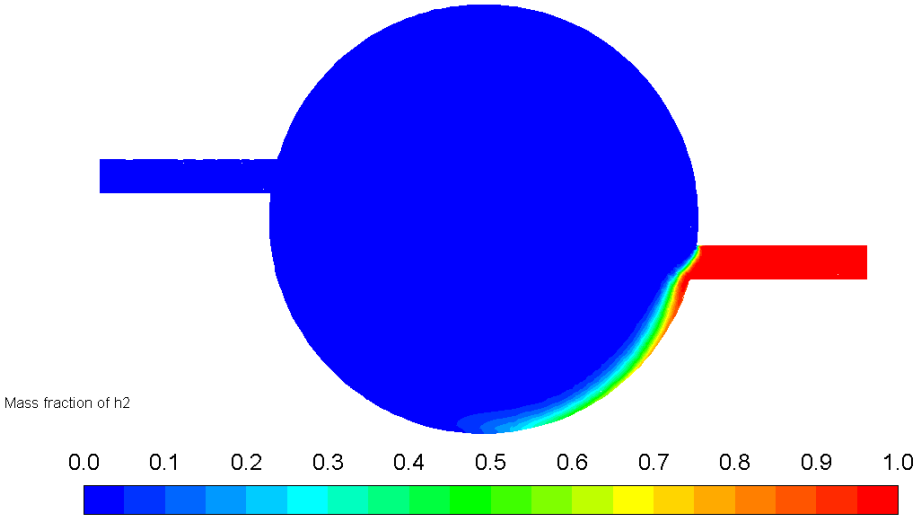

Figure 4-13. H_2 Mass Fraction Contours on Plane-2 (Test-4)

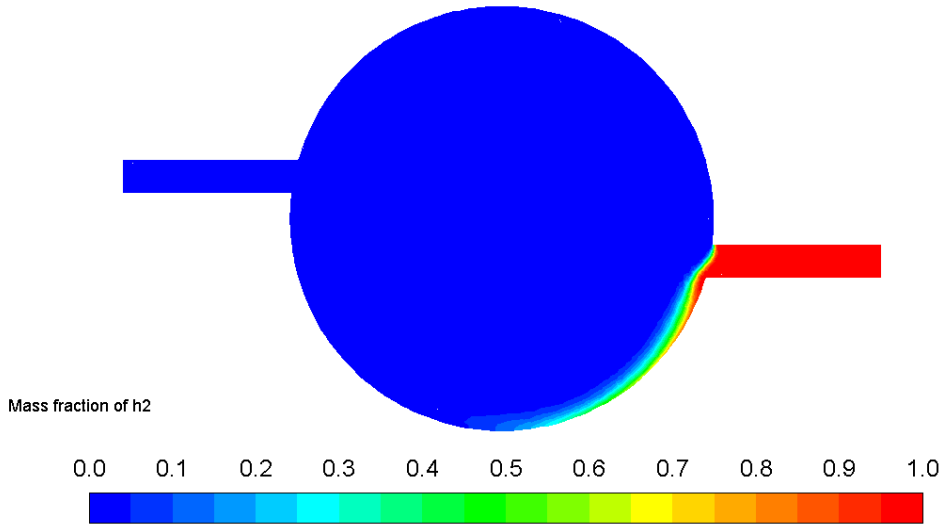

Figure 4-14. H_2 Mass Fraction Contours on Plane-2 (Test-8)

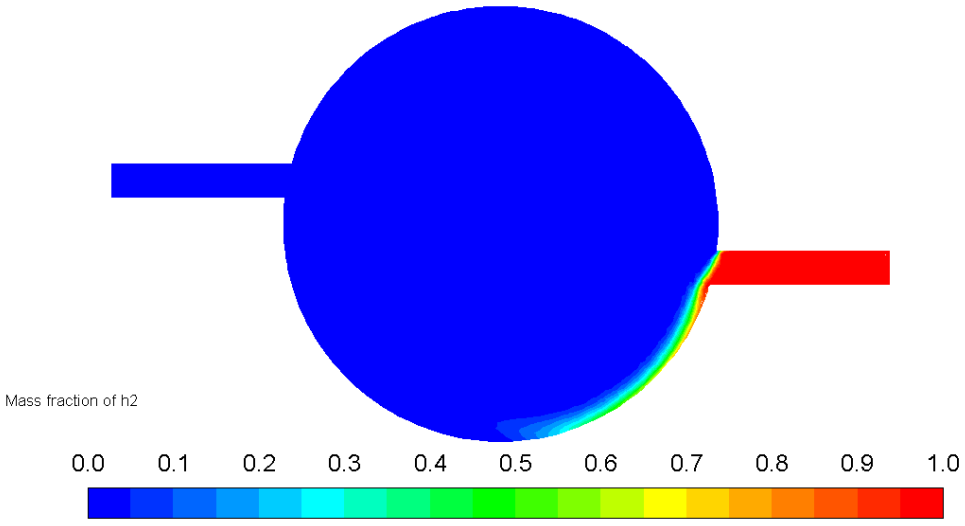

Figure 4-15. H_2 Mass Fraction Contours on Plane-2 (Test-12)

4.2.5. OH Mass Fraction

OH mass fraction contours of the analyses are plotted on the Plane-2 (Figure 4-1) and shown in Figure 4-16, Figure 4-17 and Figure 4-18 for Test-4, Test-8 and Test-12 respectively. Contour plots of all tests can be seen in Appendix H. OH molecule is the indicator and promoting radical of flame formation and ignition of H_2 [46]. Consequently, high values of OH mass fraction are observed in the regions of high

temperatures. Therefore, as the rate of H_2 increases in the combustion chamber, OH molecule constitutes a bigger region. The formation of this molecule, flame at the same time, vanishes quickly when it is introduced to cold oxygen jet. The cold jet inhibits formation of this radical like a cold wall.

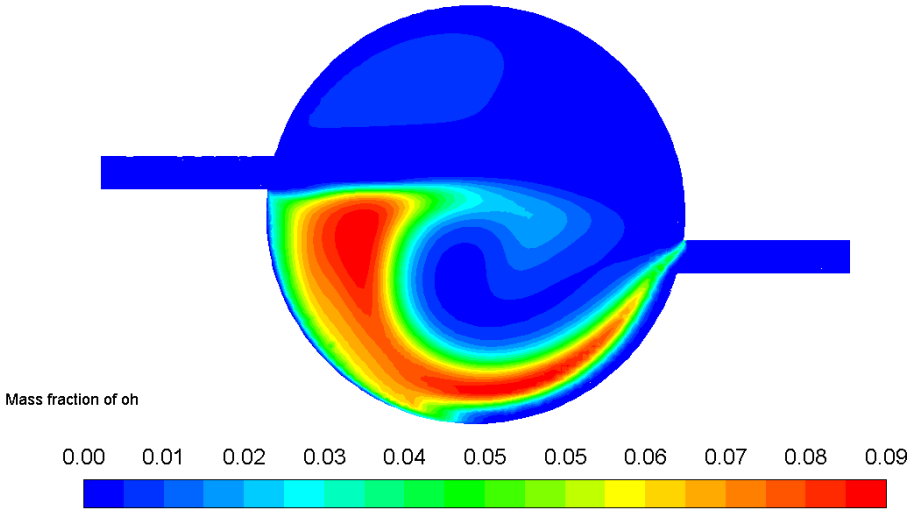

Figure 4-16. OH Mass Fraction Contours on Plane-2 (Test-4)

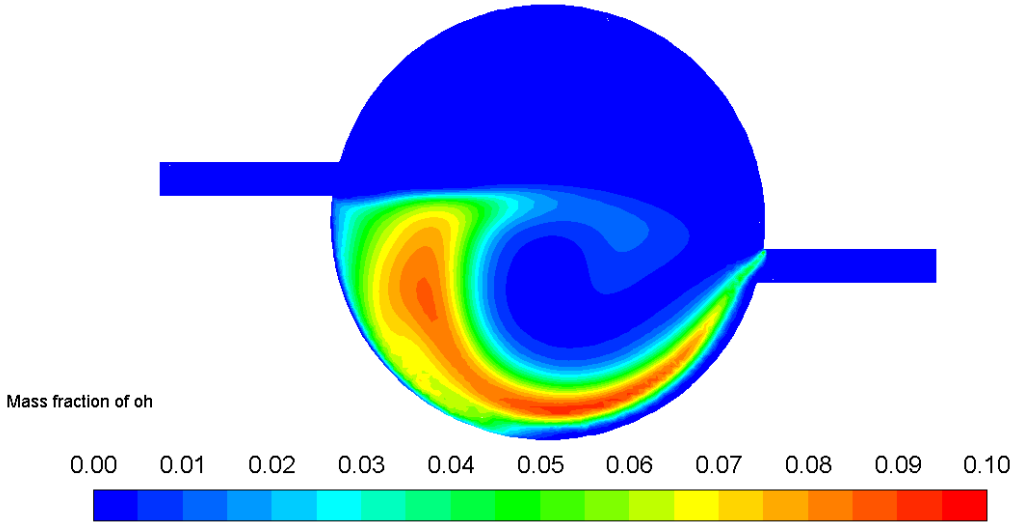

Figure 4-17. OH Mass Fraction Contours on Plane-2 (Test-8)

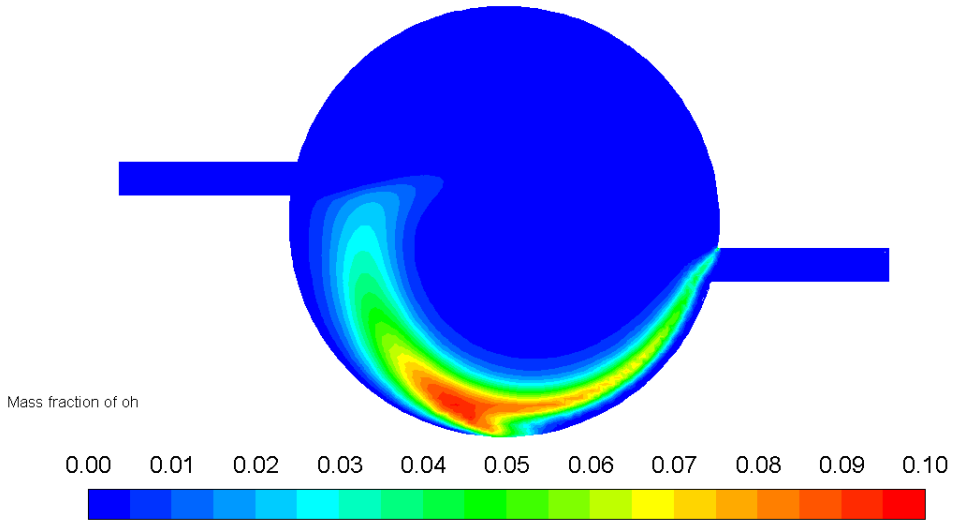

Figure 4-18. OH Mass Fraction Contours on Plane-2 (Test-12)

4.2.6. H_2O Mass Fraction

H_2O mass fraction contours of the analyses are plotted on the Plane-2 (Figure 4-1) and shown in Figure 4-19, Figure 4-20 and Figure 4-21 for Test-4, Test-8 and Test-12 respectively. Contour plots of all tests can be seen in Appendix I. H_2O, basically water vapor, is the final product of hydrogen oxidation. High values of H_2O mass fraction is noticed behind the OH molecule dominant regions that acts like flame front. Behind that region, overall reaction completes mostly and final product shows up. Also the highest rates of vapor are discerned right next to the cold wall. Cold wall extinguishes radical formation and prevents disassociation of H_2O molecule. Dominance of H_2O molecule decreases with increasing O/F value.

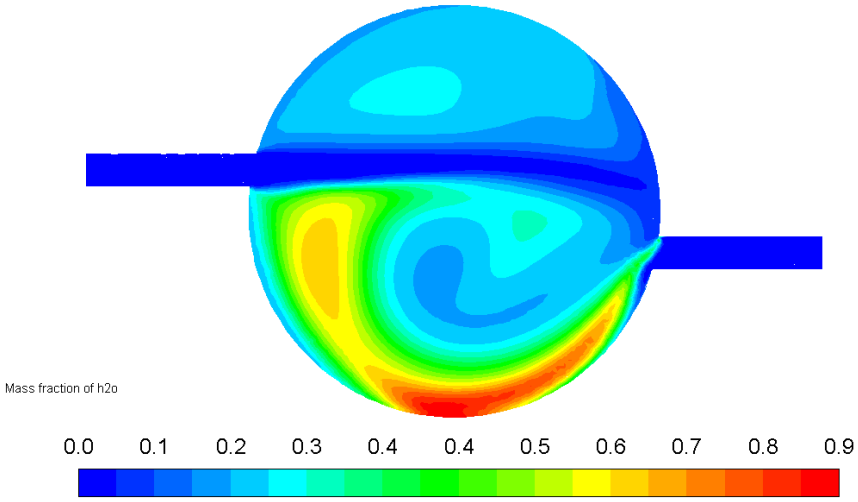

Figure 4-19. H_2O Mass Fraction Contours on Plane-2 (Test-4)

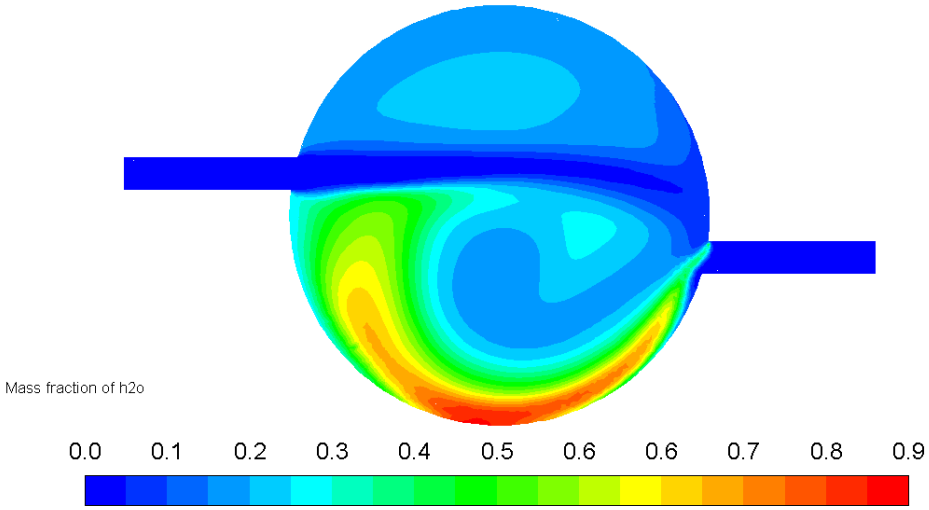

Figure 4-20. H_2O Mass Fraction Contours on Plane-2 (Test-8)

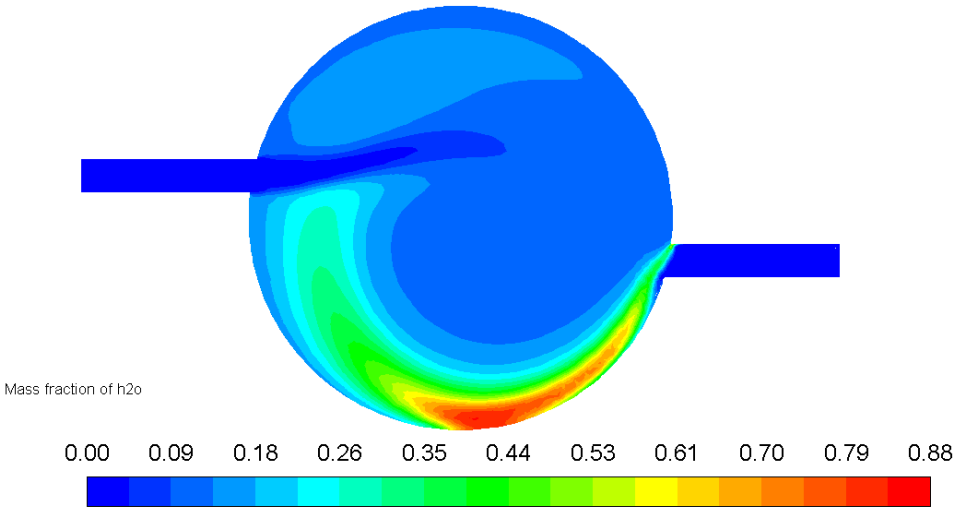

Figure 4-21. H_2O Mass Fraction Contours on Plane-2 (Test-12)

4.3. Experimental Results

In this section, experimental results are presented and compared to numerical results.

4.3.1. Schlieren Imaging

During the ignition experiments, plume of the igniter was examined by using schlieren imaging technique as explained before. An exemplary image series of the experiments, taken from certain instants of Test-1, is shown in Figure 4-22. On this figure, (a) is the instant when there is no flow; (b) is the instant when oxygen flow is started; (c) is the time when the hydrogen rushes into chamber and combustion starts; (d) and (e) is final moments of the ignition and (f) is the ending of the whole process. Instantaneous images from every test during combustion is given in Figure 4-23, Figure 4-24 and Figure 4-25.

As expected, when the supply pressure is increased, recirculation zone moves away, since with increasing pressure total mass flow rate and plume exit velocity increases. However, there is no distinctive difference between 30 barg and 40 barg case (Test-3,4 from Figure 4-23; Test-7,8 from Figure 4-24; Test-11,12 from Figure 4-25), which could be related the fact that at both points the flow is choked at the exit of the ASI. Angle between shear layers decreases slightly with increasing pressure, which can be

observed from figures Figure 4-23, Figure 4-24 and Figure 4-25. This is due to the fact that increasing velocity magnitude in the direction of igniter axis keeps plume directed, and retards widening of the angle.

To resemble with the steady state solutions of the numerical model, all instantaneous frames were unified and averaged by using image processing. Consecutive frames from schlieren imaging of Test-1 at different times are presented in Appendix-J. If the frames are examined, it can be observed that the shear layer angle doesn't change with time. However, recirculation zones seem to jump between upside and downside of the axis, as they break up from the layer. Averaged images smooth this fluctuation.

Comparison between schlieren images of the experiments and numerical analyses is done by creating numerical schlieren images with the density data that is obtained from analyses (Contour plots of density that were obtained from numerical analyses can be examined in Appendix K). Proportional relationship between the deflection of the light rays and first derivative of the density, with respective to corresponding axes, was shown in Chapter 2.4. Therefore resultant deflection of the light rays can be approximated from the density data as follows [48]:

$$\sqrt{\left(\frac{\partial \rho}{\partial x}\right)^2 + \left(\frac{\partial \rho}{\partial y}\right)^2} \tag{4-3}$$

Following this procedure, numerical schlieren images are plotted on the mid-plane of the solution domain. Results are presented with averaged schlieren images in Figure 4-26, Figure 4-27 and Figure 4-28. Then, contrast on the real schlieren and numerical schlieren image was increased and the angle between the shear layer and perpendicular axis was calculated between same locations on both image by using an edge detector image processing code. Method of angle calculation is summarized in Figure 4-29. The results for all tests and the absolute percentage discrepancy between numerical schlieren and measured schlieren images (with respect to measured values) is

tabulated in Table 4-1. Outcomes show good correlation between numerical solution and actual footage of schlieren imaging with an average discrepancy of 1%.

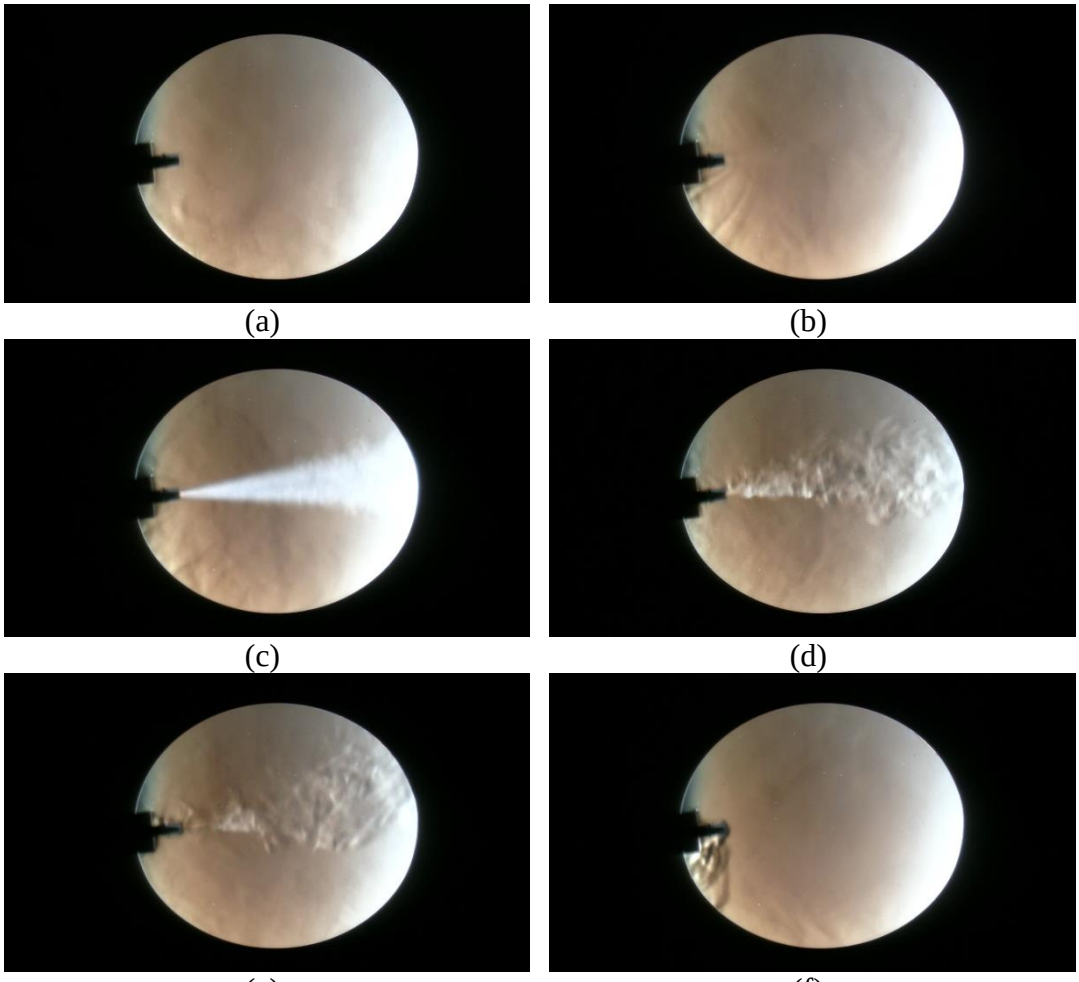

Figure 4-22. Images of Different Instants from Test-1

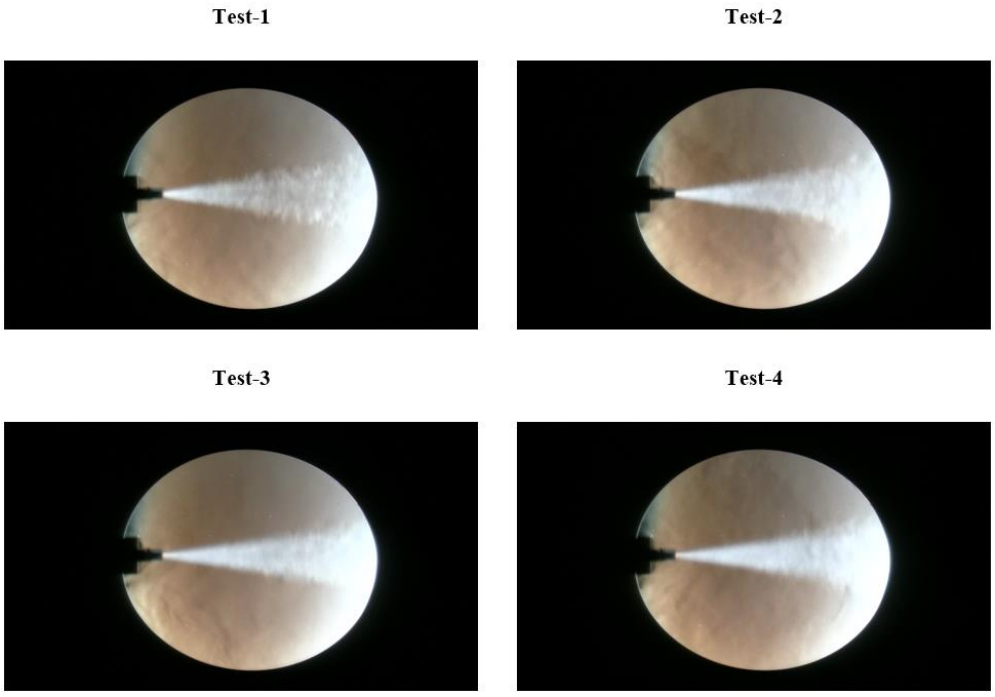

Figure 4-23. Instantaneous Schlieren Images of Test Sequence – 1 (O/F=40)

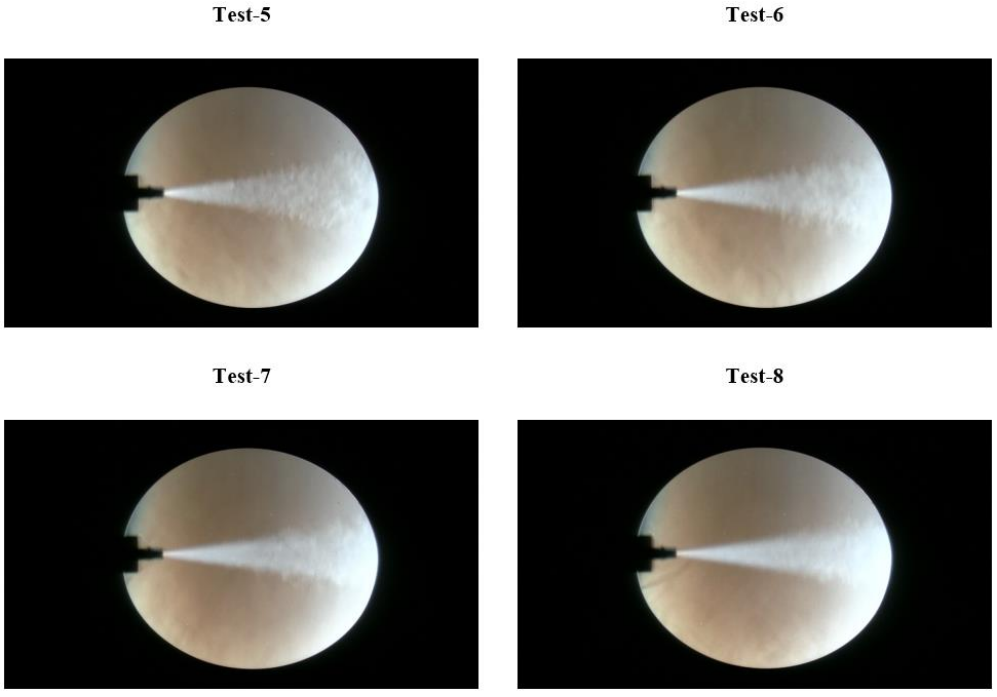

Figure 4-24. Instantaneous Schlieren Images of Test Sequence – 2 (O/F=50)

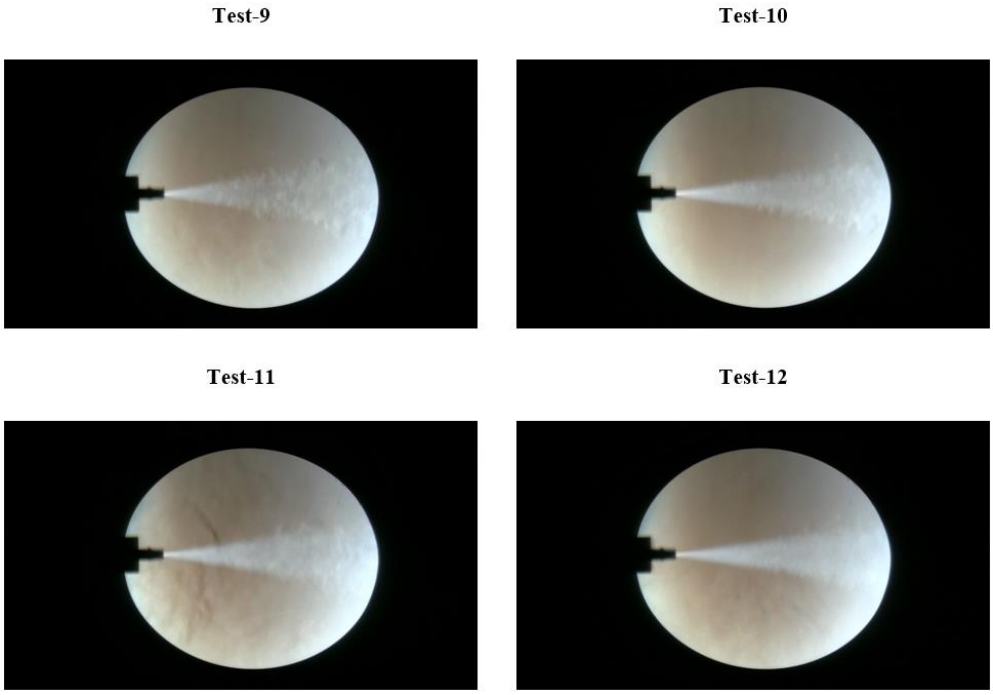

Figure 4-25. Instantaneous Schlieren Images of Test Sequence – 3 (O/F=75)

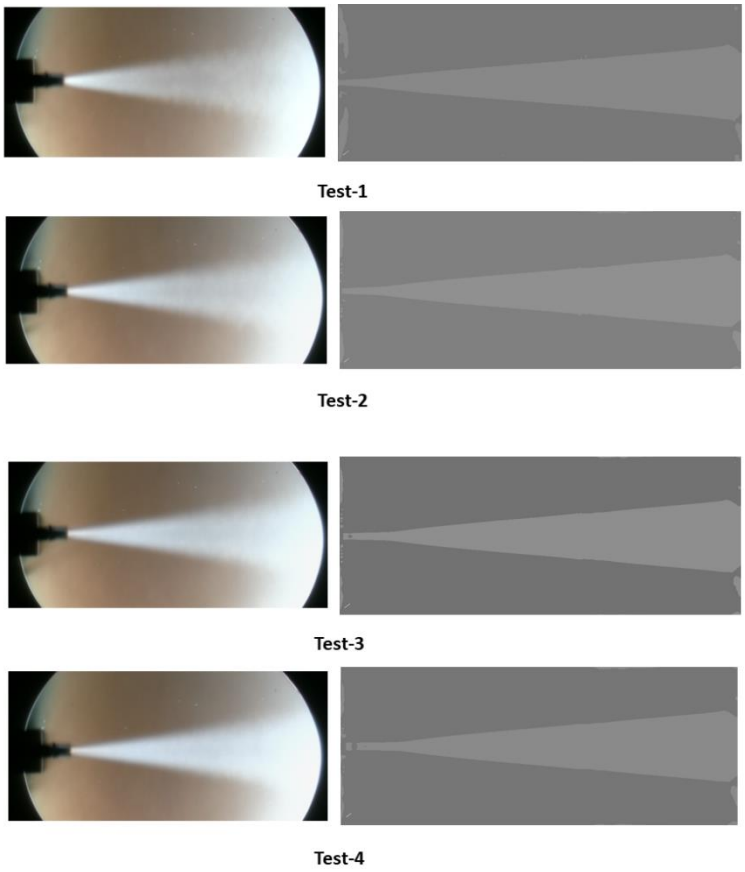

Figure 4-26. Averaged Schlieren Images and Numerical Schlieren Contours of Test Sequence – 1 (O/F=40)

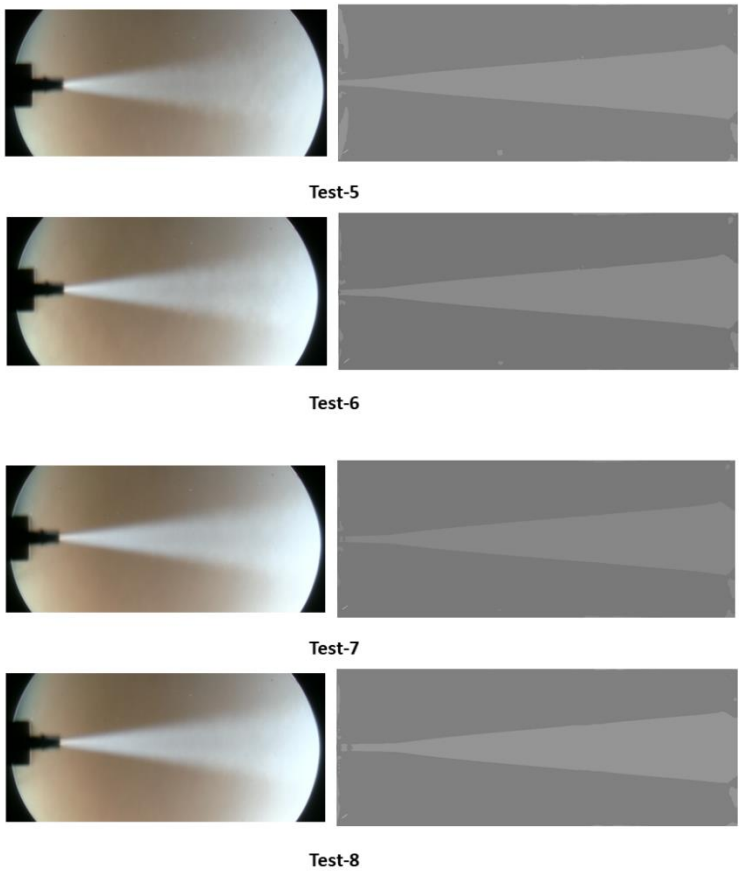

Figure 4-27. Averaged Schlieren Images and Numerical Schlieren Contours of Test Sequence – 2 (O/F=50)

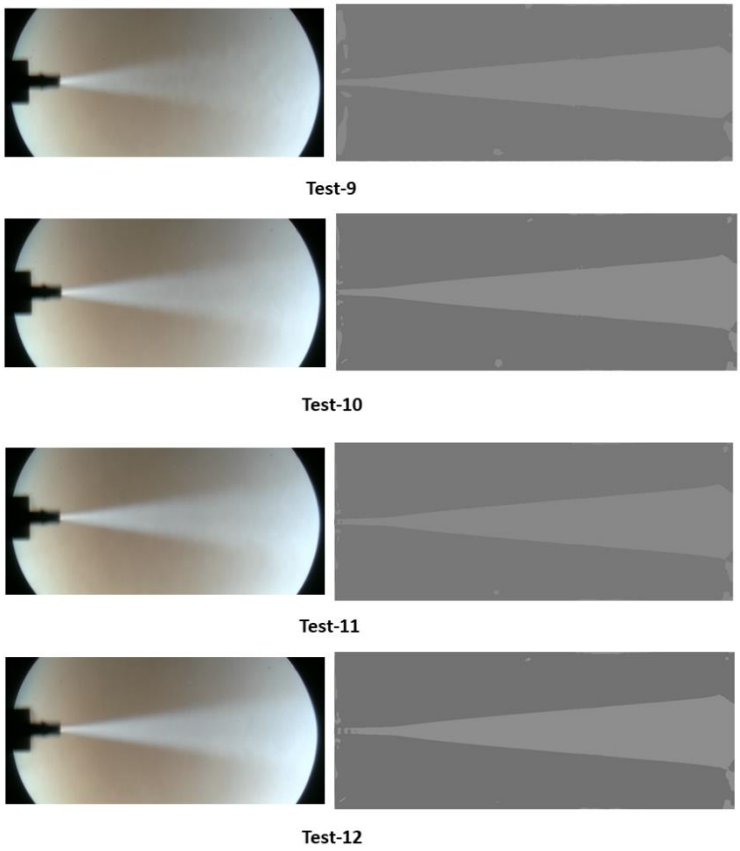

Figure 4-28. Averaged Schlieren Images and Numerical Schlieren Contours of Test Sequence – 3 (O/F=75)

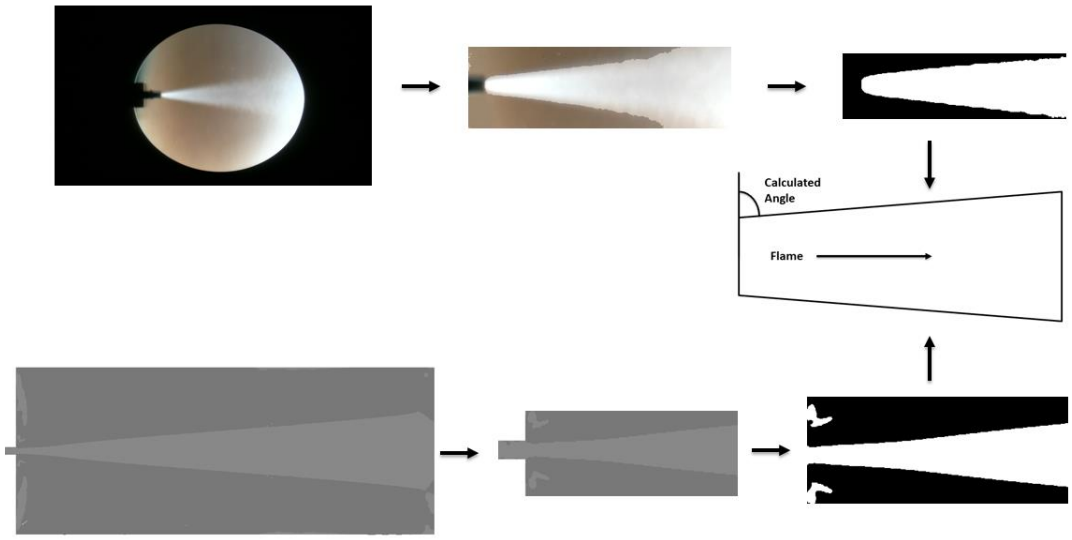

Figure 4-29. Method of Angle Calculation

Table 4-1. *Comparison of Calculated Shear Layer Angles from Numerical and Measured Schlieren Images*

Test	Shear Layer Angle (deg) -Numerical Schlieren	Shear Layer Angle (deg) –Measured Schlieren	Abs. Discrepancy (%)
1	85.16	84.29	1.04
2	87.36	87.71	0.40
3	88.24	88.36	0.14
4	89.08	88.83	0.29
5	84.74	84.29	0.54
6	86.34	86.19	0.18
7	87.71	86.05	1.92
8	89.08	86.19	3.36
9	85.65	84.29	1.62
10	86.57	87.79	1.40
11	87.71	88.09	0.43
12	88.40	88.87	0.54

4.3.2. Pressure Measurements

Pressure in the combustion chamber was recorded during the experiments. All the collected data was filtered by a single-pole low pass frequency filter. This filter

eliminated noise that is caused most probably by spark plug [27]. Also, oscillation in the data could indicate combustion instability at the regarding points, because oscillatory behavior is impotent in Test Sequence-3. This situation needs to be investigated further. Raw data and the filtered data of test sequences are presented in Figure 4-30, Figure 4-31 and Figure 4-32. Even tough filtered data don't seem to capture peaks and sudden decrements, it is done on purpose. The filter algorithm filters the data of low frequency, so it didn't capture peaks and sudden decrements, since they occur rarely. At the last test sequence, the noise of spark plug, or instable combustion behavior, seemed to vanish.

The first peak on the raw data lines indicates the introduction of oxygen gas to the chamber. After one second, when the hydrogen starts to flow inside, combustion starts. However, it takes time to reach steady state pressure value. This phenomenon doesn't appear in 10 barg experiments. In that mass flow rate, introduction of hydrogen and combustion didn't seem to change the pressure much.

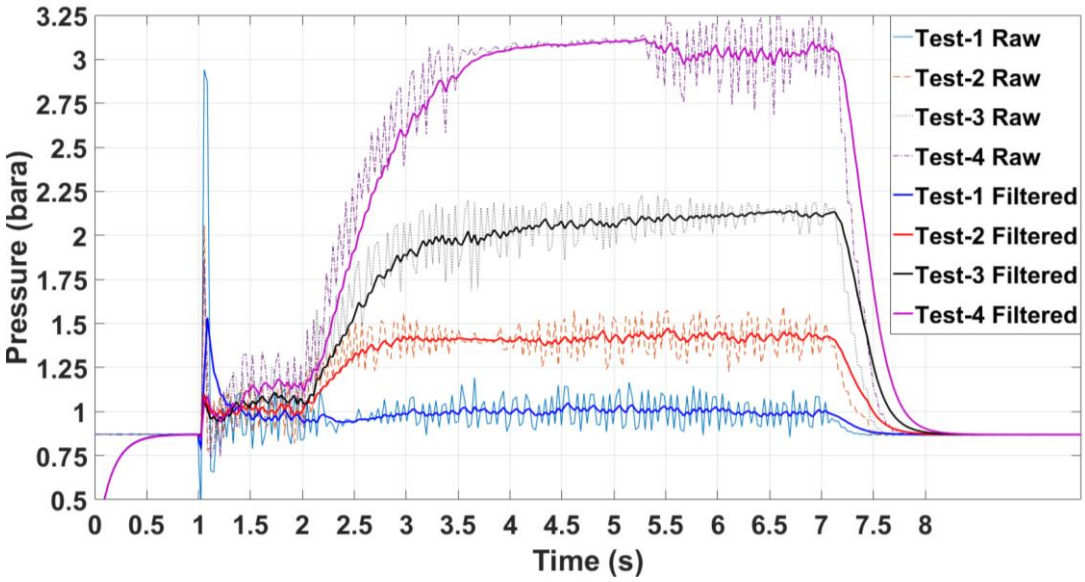

Figure 4-30. Raw and Filtered Pressure Data of Test Sequence-1

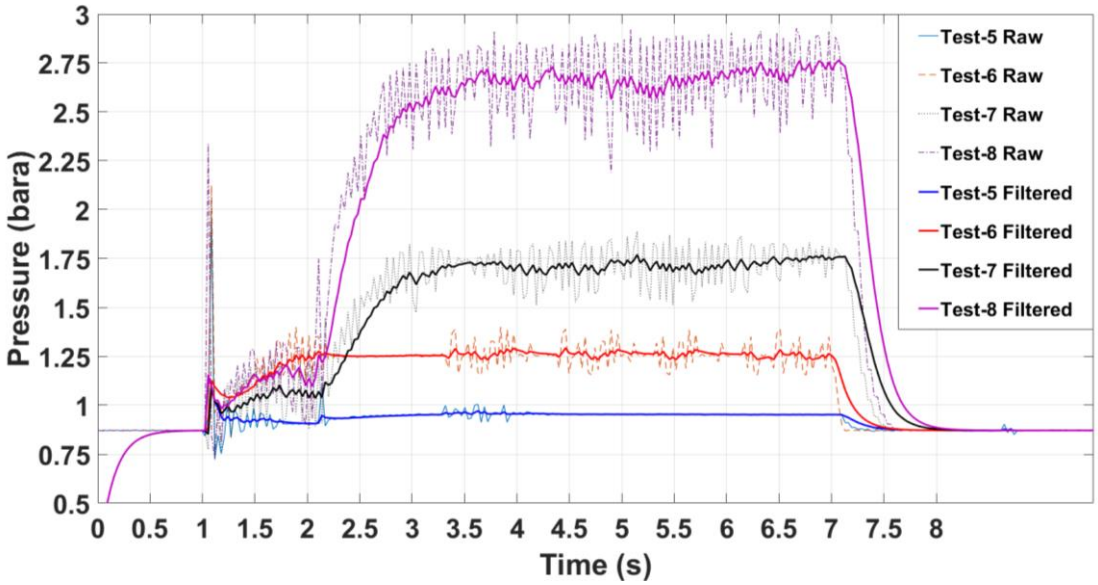

Figure 4-31. Raw and Filtered Pressure Data of Test Sequence-2

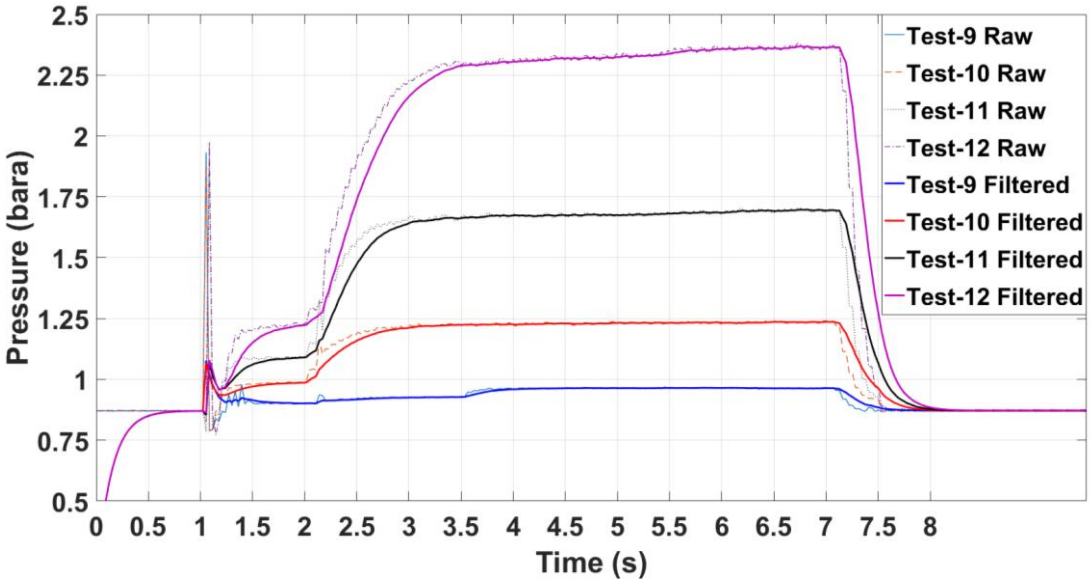

Figure 4-32. Raw and Filtered Pressure Data of Test Sequence-3

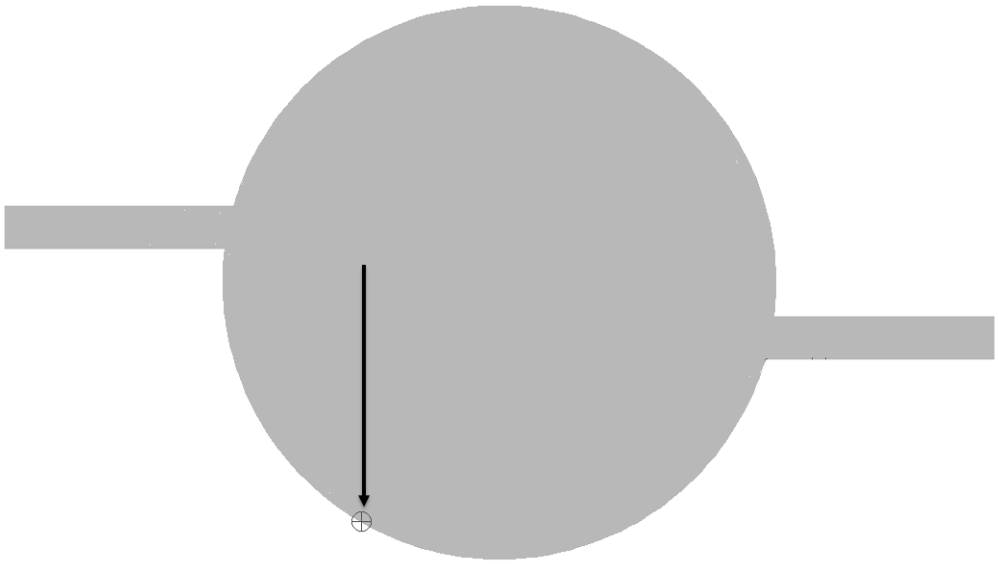

Figure 4-33. Point of Pressure Measurement in the Numerical Analyses

Table 4.2. *Comparison of Steady State Pressure Values in the Combustion Chamber*

Test	Computed Pressure (bar)	Measured Pressure (bar)	Abs. Discrepancy (%)
1	1.032	1.003	2.82
2	1.661	1.420	16.98
3	2.419	2.064	17.20
4	3.277	3.115	5.20
5	1.015	0.958	5.95
6	1.504	1.254	19.99
7	2.199	1.744	26.07
8	3.013	2.655	13.46
9	0.994	0.964	3.07
10	1.372	1.231	11.46
11	1.944	1.693	14.87
12	2.634	2.380	10.66

Pressure values from numerical analyses are obtained from the point (Figure 4-33) that corresponds to pressure transducer port (Figure 2-1) in the domain, and the values are compared to mean values of steady state values (between 4-7 s) of the experiments. It is observed that the numerical solution and experimental data matches promisingly.

The average error is 12.3% with a maximum of %26 and minimum of %2.8. Choked flow results in the 30-40 barg numerical analyses hold in the experiments, too. The highest error is achieved on Test-7. It seems that the measured values are lower than the computed values. This situation gives a clue about source errors. Firstly, average temperature in the combustion chamber may be lower than the analyzes due to several reasons. Secondly, geometric defects inside the flame tube could have enlarged the diameter and changed the choked area. Even 0.5 mm change in diameter could affect backpressure value for a given mass flow rate, drastically (Appendix L).

4.3.2.1. Helmholtz Instability

An analysis was done about Helmholtz instability with respect to operating conditions of Test-1 and geometry of the igniter. The investigation was done to see whether it could be the reason of oscillations in the pressure readings, or not. Helmholtz resonance occurs when fluid flows through a neck from a small volume to atmosphere.

The frequency of the resonance could be calculated as follows [49]:

$$f_{res} = \frac{c}{2\pi}\sqrt{\frac{A_c}{V_c l}} \tag{4-4}$$

Where, "c" is the speed of sound, "A_c" is the cross-sectional area of the hole, "V_c" is the volume of the source and "l" is the length of the neck. The speed of the sound for the conditions of the Test-1 was obtained by CEA [32] software, and the values regarding the geometry were obtained simply from the dimensions of the igniter. The resulting resonance frequency came out to be ≈573 Hz. However, the frequency of the oscillations in the pressure readings is approximately 50 Hz. Therefore, it is understood that the oscillatory behavior in the readings isn't due to Helmholtz instability.

4.3.3. Temperature Measurements

As explained before, from five locations in the plume, temperature data is collected during the experiments. Collected data is filtered by a single-pole low frequency pass filter. Exemplary application of filtering for the Test-1 is given in Figure 4-34 and Figure 4-35. In this case, filtered data and raw data are presented in different figures for virtual clarity.

The temperature data that was collected from thermocouples during the test campaign are compared with the temperature values obtained from numerical solutions at the same locations. To resemble with steady state solutions, mean values between 4-8 s, when the values don't seem to change much, are compared to experimental results. Broadly, results are highly promising. Test data and computed data of temperature values of the Test Sequence-1, Test Sequence-2 and Test Sequence-3 are demonstrated in Figure 4-36, Figure 4-37, Figure 4-38 and tabulated in Table 4.3, Table 4.4, Table 4.5 respectively. Calculated maximum absolute discrepancy, minimum absolute discrepancy and average absolute discrepancy between tests and analyses are tabulated in Table 4.6.

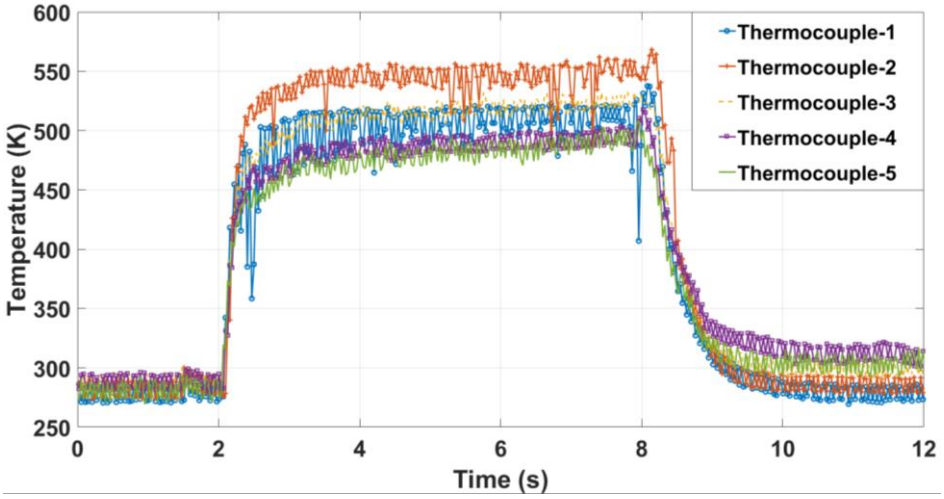

Figure 4-34. Raw Temperature Data from Test-1

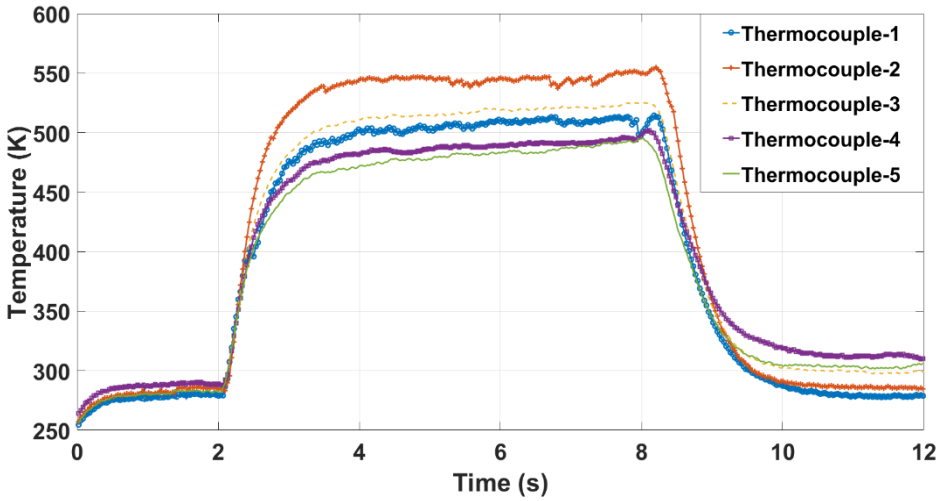

Figure 4-35. Filtered Temperature Data from Test-1

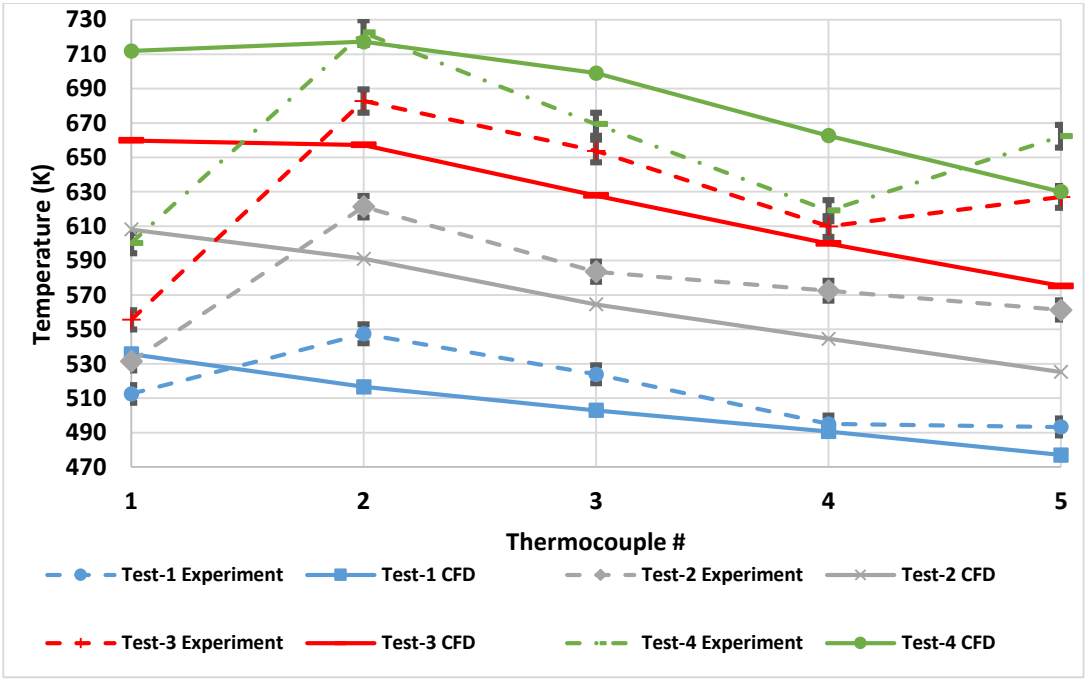

Figure 4-36. Comparison of Measured Temperature Values from Experiments and Computed Temperature Values from Numerical Solutions of Test Sequence-1

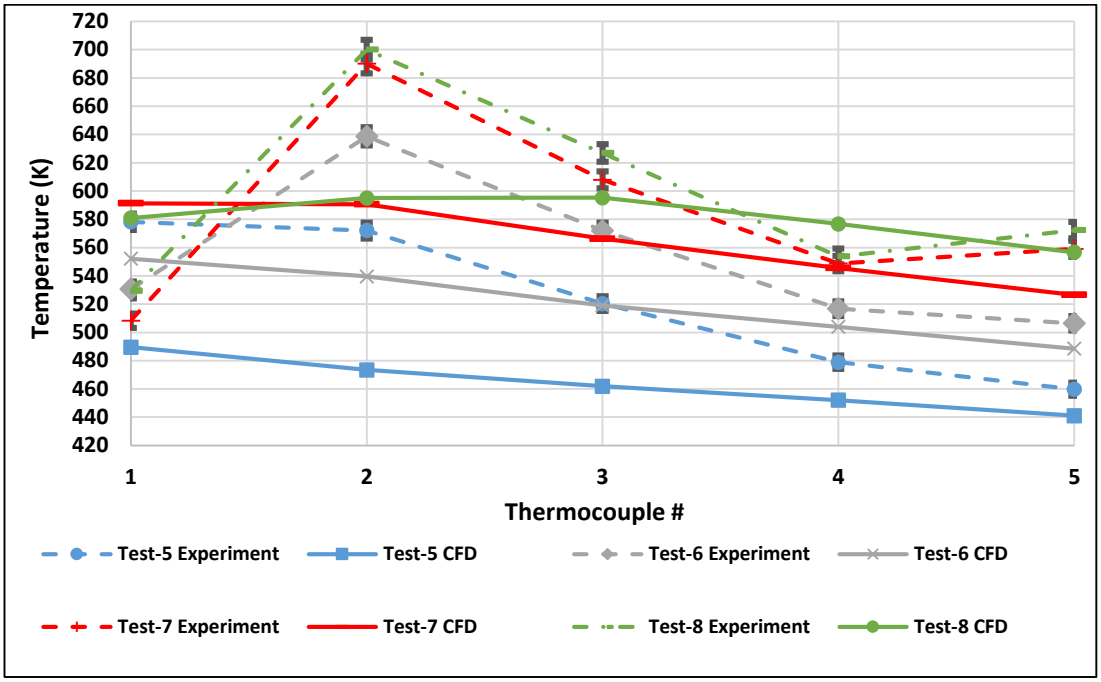

Figure 4-37. Comparison of Measured Temperature Values from Experiments and Computed Temperature Values from Numerical Solutions of Test Sequence-2

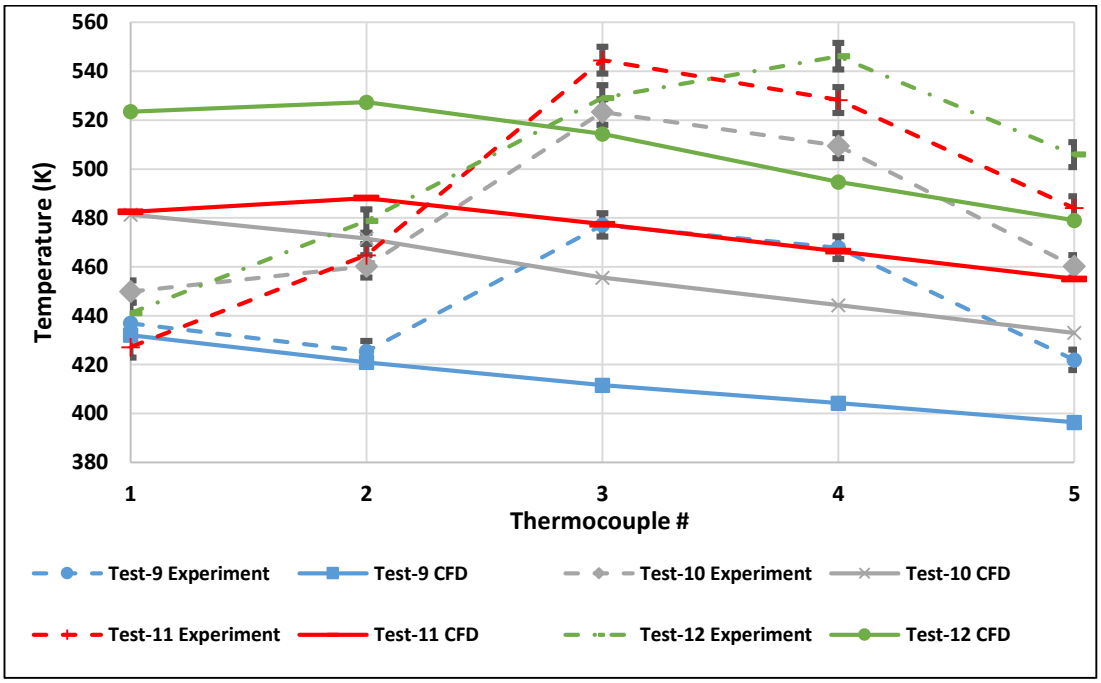

Figure 4-38. Comparison of Measured Temperature Values from Experiments and Computed Temperature Values from Numerical Solutions of Test Sequence-3

Table 4.3. *Comparison of Measured Temperature Values from Experiments and Computed Temperature Values from Numerical Solutions of Test Sequence-1*

	Thermocouple#	**Experimental Result (K)**	**CFD Result (K)**	**Absolute Discrepancy (%)**
Test-1	**1**	512.6	535.7	4.5
	2	547.4	516.6	5.6
	3	523.9	503.0	4.0
	4	495.0	490.6	0.9
	5	493.3	477.0	3.3
Test-2	**1**	531.5	608.1	14.4
	2	621.3	591.1	4.9
	3	583.6	564.6	3.3
	4	572.5	544.5	4.9
	5	561.3	525.3	6.4
Test-3	**1**	555.6	659.8	18.8
	2	682.8	657.2	3.7
	3	653.7	627.8	4.0
	4	609.8	599.9	1.6
	5	627.0	575.2	8.3
Test-4	**1**	600.2	711.8	18.6
	2	722.6	717.2	0.7
	3	669.3	699.0	4.4
	4	619.1	662.6	7.0
	5	662.3	630.0	4.9

Table 4.4. *Comparison of Measured Temperature Values from Experiments and Computed Temperature Values from Numerical Solutions of Test Sequence-2*

	Thermocouple#	**Experimental Result (K)**	**CFD Result (K)**	**Absolute Error (%)**
Test-5	**1**	578.2	489.6	15.3
	2	572.0	473.4	17.2
	3	520.4	461.9	11.2
	4	478.9	452.1	5.6
	5	459.8	441.1	4.1
Test-6	**1**	530.7	552.2	4.1
	2	638.7	539.6	15.5
	3	571.9	519.0	9.3
	4	516.8	503.9	2.5
	5	506.4	488.6	3.5
Test-7	**1**	508.3	591.4	16.3
	2	690.0	590.7	14.4
	3	607.9	566.3	6.8
	4	548.8	545.5	0.6
	5	559.1	526.5	5.8
Test-8	**1**	529.4	580.9	9.7
	2	700.0	595.1	15.0
	3	626.9	595.3	5.0
	4	553.8	576.8	4.2
	5	572.3	556.7	2.7

Table 4.5. *Comparison of Measured Temperature Values from Experiments and Computed Temperature Values from Numerical Solutions of Test Sequence-3*

	Thermocouple#	**Experimental Result (K)**	**CFD Result (K)**	**Absolute Error (%)**
Test-9	**1**	436.9	432.1	1.1
	2	425.4	420.9	1.1
	3	477.1	411.6	13.7
	4	467.8	404.2	13.6
	5	421.9	396.4	6.1
Test-10	**1**	449.9	481.4	7.0
	2	460.2	471.6	2.5
	3	523.4	455.5	13.0
	4	509.5	444.3	12.8
	5	460.2	433.0	5.9
Test-11	**1**	427.1	482.5	13.0
	2	464.8	488.1	5.0
	3	544.5	477.5	12.3
	4	528.3	466.4	11.7
	5	484.0	455.0	6.0
Test-12	**1**	441.0	523.5	18.7
	2	478.8	527.4	10.2
	3	529.1	514.4	2.8
	4	546.2	494.7	9.4
	5	505.9	479.0	5.3

Table 4.6. *Calculated Maximum, Minimum and Average Discrepancies of the Temperature Data Between Experiment Readings and Numerical Solutions*

	Maximum Abs. Error (%)	**Minimum Abs. Error (%)**	**Average Abs. Error (%)**
Test-1	5.6	0.9	3.3
Test-2	14.4	3.3	6.8
Test-3	18.8	1.6	7.3
Test-4	18.6	0.7	7.1
Test-5	17.2	4.1	10.7
Test-6	15.5	2.5	7.0
Test-7	16.3	0.6	8.8
Test-8	15.0	2.7	7.3
Test-9	13.7	1.1	7.1
Test-10	13.0	2.5	8.2
Test-11	13.0	5.0	9.6
Test-12	18.7	2.8	9.3

It is seen that the maximum discrepancy was obtained mostly at Thermocouple-1 (half of the tests). At that point, thermocouples tend to read lower temperatures than the thermocouples after it and values that are obtained from numerical analyses. This error is most probably a measurement error. The reason could be highly chaotic flow field at the exit of the igniter (Figure 4-39). Rotation dominant flow at the exit could introduce error to the readings, and an investigation should be done in that field in terms of turbulence, heat transfer and radiation loss to introduce a recovery factor to readings. Secondly, the flow is supersonic around first thermocouple in some of the experiments. This would also introduce error to readings. Location of thermocouples according to the aforementioned phenomena are shown in Figure 4-40 and Figure 4-41.

Lastly, the thermocouples could have been bent by the momentum of the flow. To test this hypothesis, numerical data is collected from first thermocouple from the analysis

of Test-3, which has the highest error, as if the thermocouple is bent. The thermocouple is bent by five degrees until 20°, then between 20° and 25° it is bent by one degree (Figure 4-42). Results can be seen in Figure 4-45. Parametric study supports the hypothesis. At 24° error drops to 0.9 %, and the experimental reading seems to lay between 24°-25°. For Test-7 and Test-11 at 24° error drops to 0.35% and 4%, respectively. Therefore, it is understood that bending of the thermocouples (especially the first one) introduced error to readings. Nonetheless, 10.7% of maximum average error qualifies numerical model in means of representation of the physical phenomena.

Repeatability of the tests, both for pressure and temperature measurements, are demonstrated in Appendix M, by giving one example from each test sequence. Successive measurements in the given examples show great correlation which leaves no doubt about repeatability.

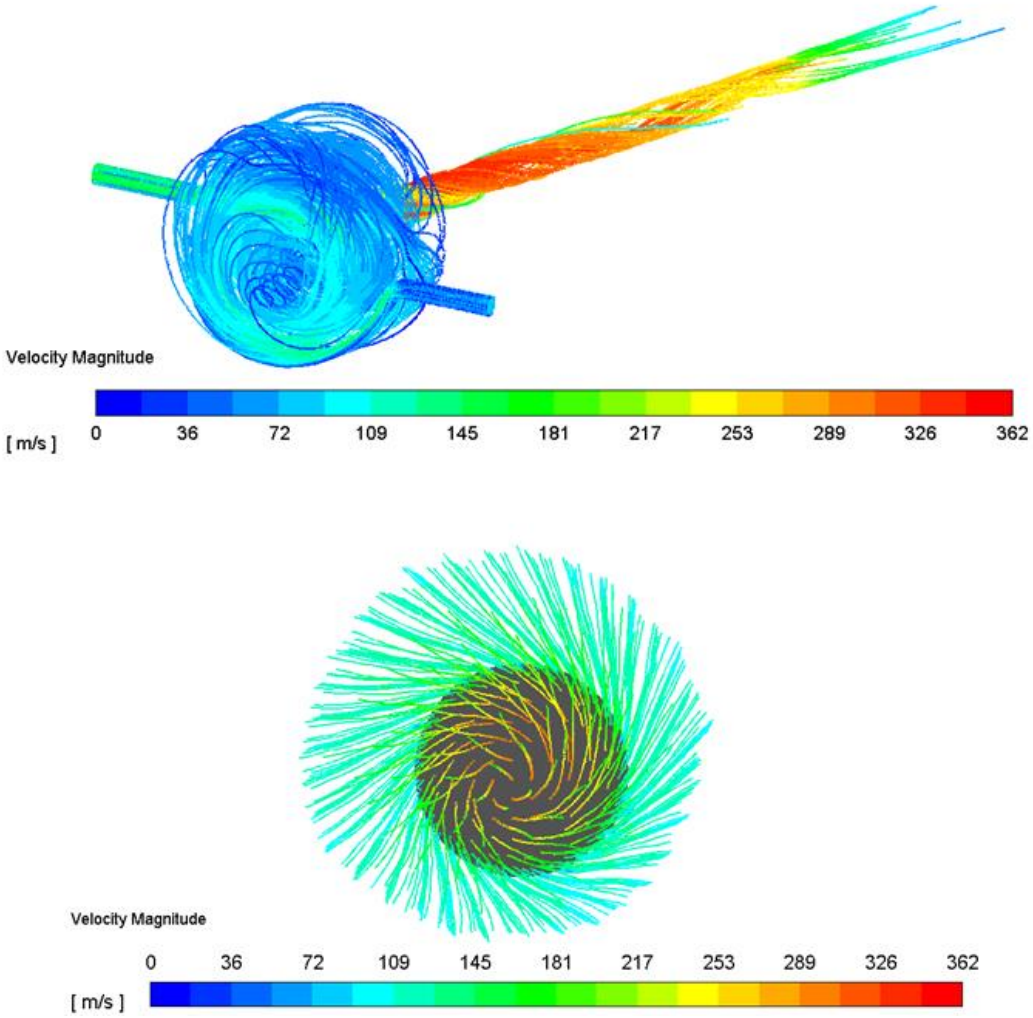

Figure 4-39. Pathlines of Particles Emerging from Inlets and Exit of the Igniter Colored by Velocity Magnitude

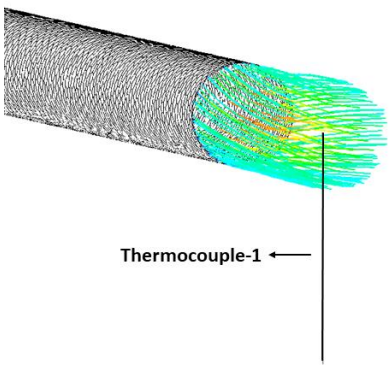

Figure 4-40. Thermocouple-1 Position in the Rotating Flow Exiting the Igniter

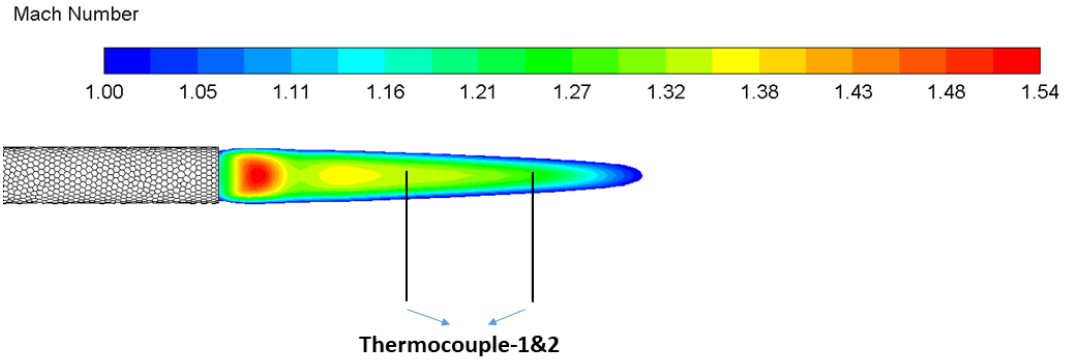

Figure 4-41. Thermocouple-1 and 2 Positions in the Supersonic Flow Exiting the Igniter (Test-4)

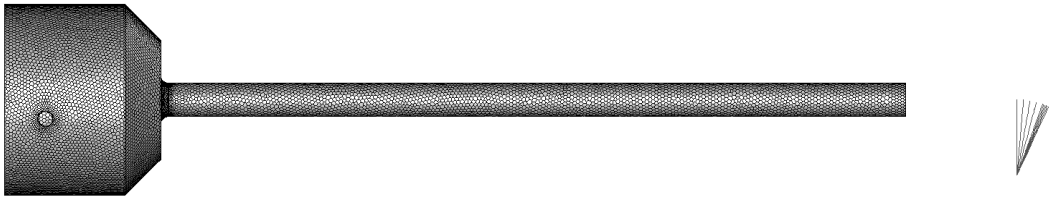

Figure 4-42. Positions of the Bent Thermocouple-1

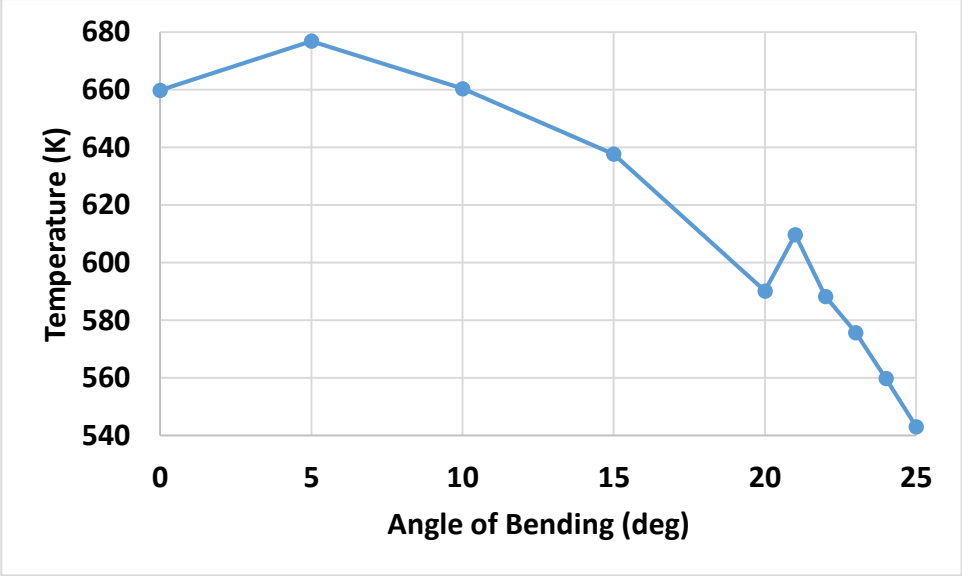

Figure 4-43. Temperature Data of Bent Thermocouple-1 of the Numerical Analysis of Test-3 with respect to Bending Angle

4.3.4. Visual Comparison

Lastly, visual inspection was done on the igniter after the tests. Inspection ensured that numeric model is capable of capturing unsymmetrical temperature distributions inside the combustion chamber. The overheated regions that are detected on the wall of the combustion chamber from numerical solutions were revealed in the combustion chamber, too, by visual inspection. Evidences can be examined in Figure 4-44 and Figure 4-45.

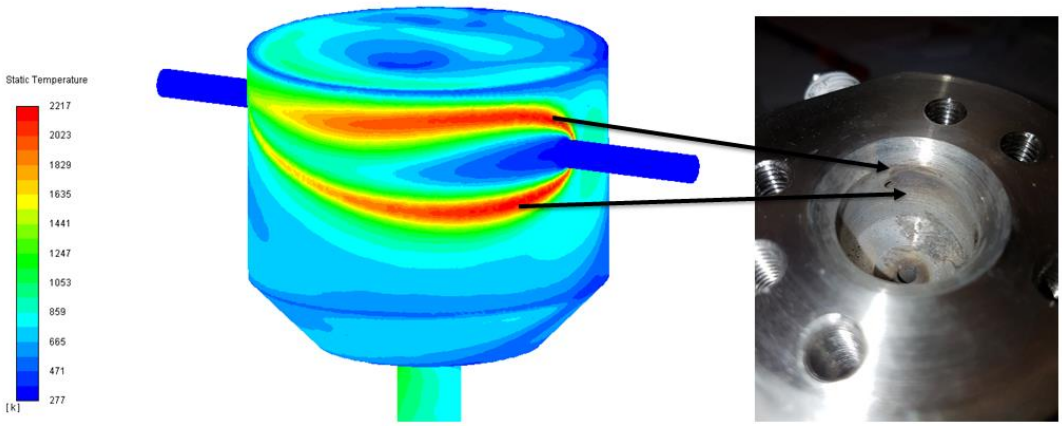

Figure 4-44. Wing-Shaped Overheated Temperature Field Next to Fuel Inlet (Test-1)

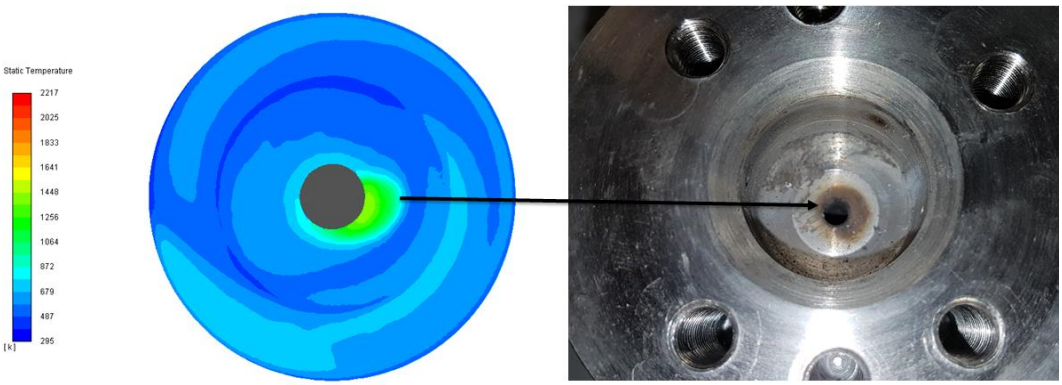

Figure 4-45. Unsymmetrical Temperature Distribution at the Inlet of the Flame Tube (Test-1)

CHAPTER 5

EVALUATION OF PERFORMANCE PARAMETERS

5.1. Definition

LPRE's uses liquid propellants to be able to store more fuel in a unit volume. The liquid propellants (fuel and oxidizer) are injected to the combustion chamber by injectors. Injected liquid forms a spray when it is expanded to the combustion chamber. It takes several forms until it evaporates at the end of the spray structure (Figure 5-1).

To be able to evaluate the performance and to optimize the design of an augmented spark igniter, a performance parameter that is called "effective flame length" is defined. There is no distinctive physical length of the igniter's plume, simply because it is a hot gas ejection. Thus, the definition is made in the light of spray description. Liquid hydrogen and liquid methane are highly efficient and popular fuels. According to researches that were carried out [50], spontaneous ignition temperatures of hydrogen and methane in oxygen at atmospheric conditions are 833 K and 829 K. Consequently, an effective flame must reach the evaporation zone at the aforesaid temperature and ignite the evaporated fuel. Since the parameter is designated to be used in preliminary design, effective flame length is defined as the length of the 800 K iso-surface emanates from the igniter with the assumption of creating a hot surface of 800 K ensures the ignition and atomization is handled well by the injectors. The evaluation of effective flame length is done by the numerical investigation results that is validated through experiments.

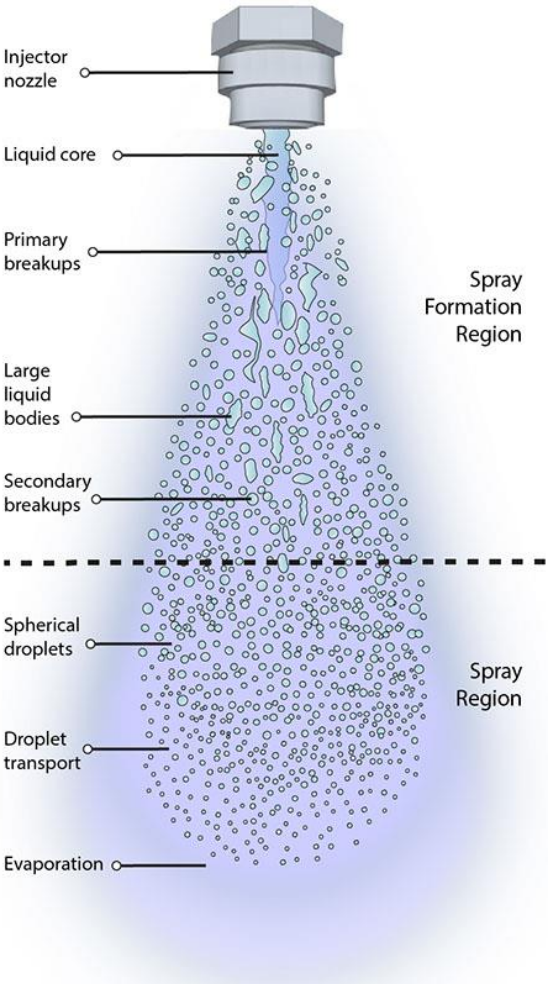

Figure 5-1. Spray Structure [51]

5.2. Evaluation

Evaluation of effective flame length is done by using numerical model that is validated through experimental comparison (Chapter 4). The results are given in Figure 5-2, Figure 5-3, Figure 5-4, and Figure 5-5. Also, to have a different perspective, the internal energy released from the exit of the flame tube, in another words, thermal energy input to the combustion chamber of the LPRE by the igniter is plotted in Figure 5-6, in the same manner with the effective flame length. This parameter simply was obtained by calculating area-weighted average of specific heat at constant volume and temperature at the exit (Equation (5-1)).

$$P = \dot{m} \times c_v \times T_{av} \tag{5-1}$$

Results are highly interesting. It is found that O/F ratio is more effective than the total mass flow rate. The length value that is obtained by 40 barg supply pressure at O/F ratio of 75, is already achieved by 30 barg supply pressure at O/F ratio of 750 and 20 barg supply pressure at O/F ratio of 40. Same trend can be observed in the second graph for energy input. Performance assessments show that, higher adiabatic flame temperature, lower O/F, and higher mass flow rate leads higher energy input and longer effective flame length, as expected. However, rather than increasing mass flow rate, decreasing O/F ratio seems to lead higher energy input to the LPRE's combustion chamber. Therefore, the designer should decide between thermal or structural strength, when designing an igniter system.

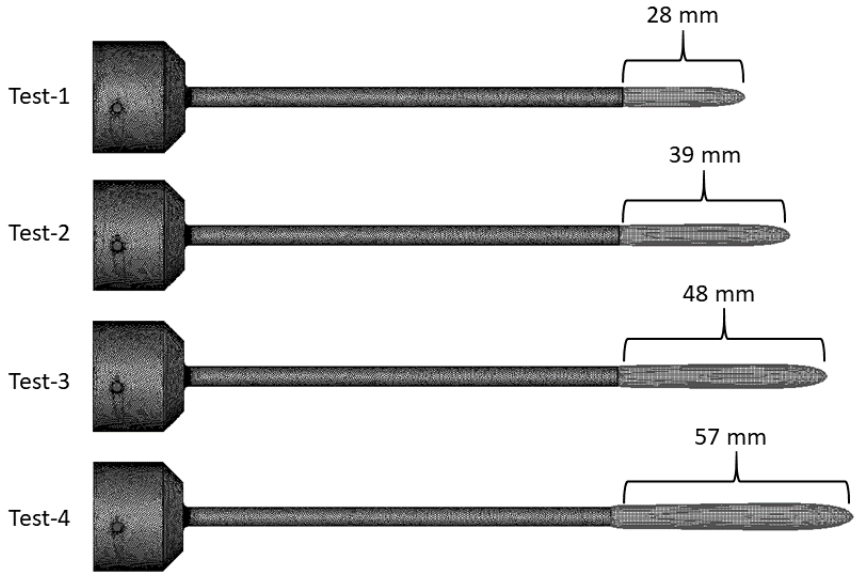

Figure 5-2. Effective Flame Length Evaluation of Test Sequence-1

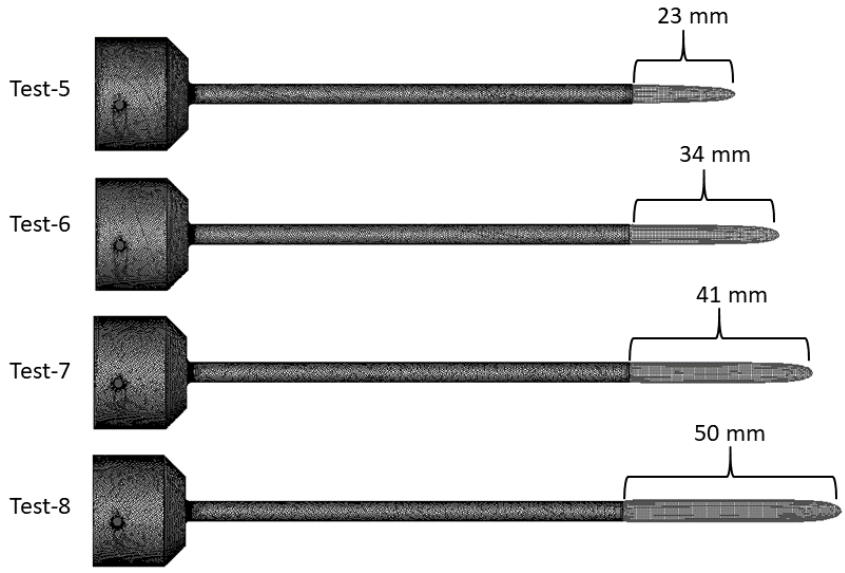

Figure 5-3. Effective Flame Length Evaluation of Test Sequence-2

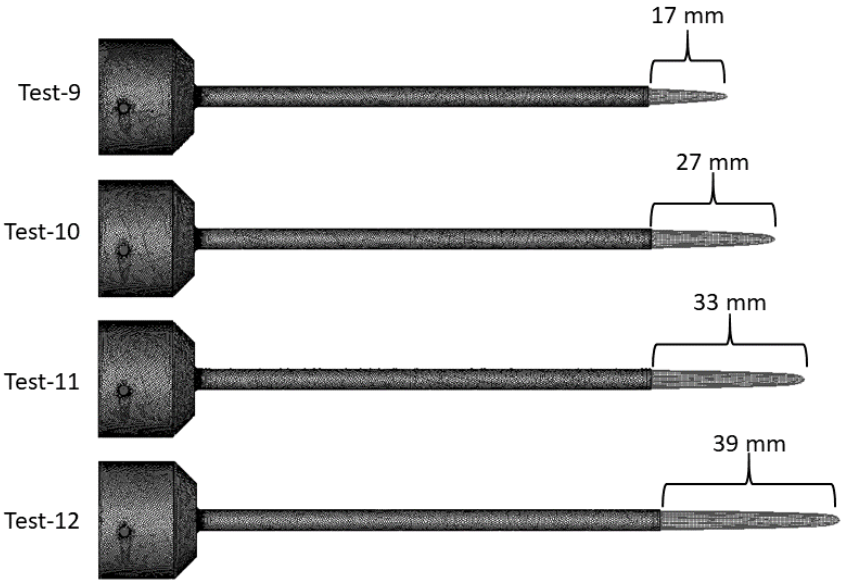

Figure 5-4. Effective Flame Length Evaluation of Test Sequence-3

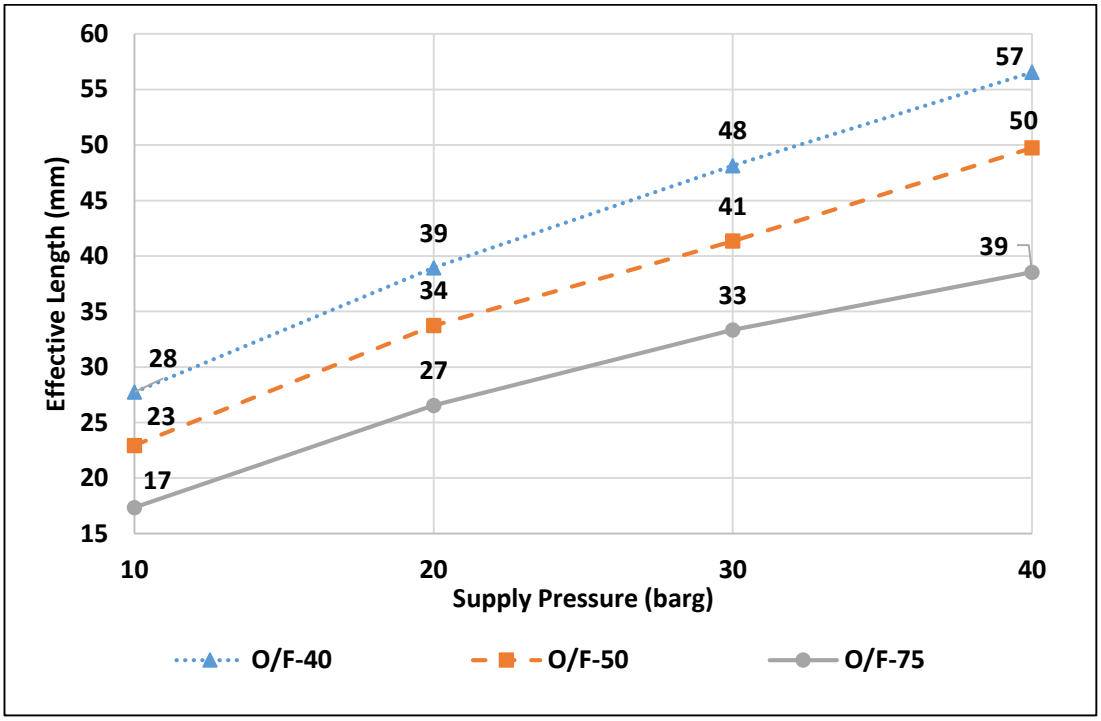

Figure 5-5. Effective Flame Length Evaluation of Operating Conditions of the Igniter

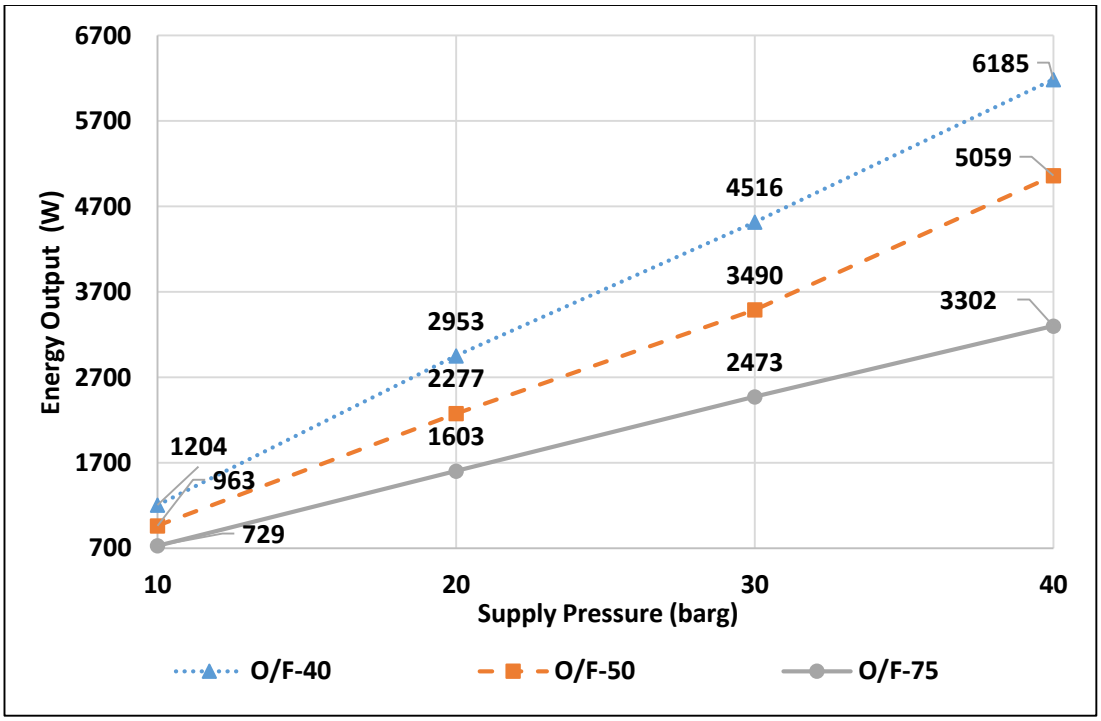

Figure *5-6. Thermal Energy Output of Each Operating Condition of the Igniter*

CHAPTER 6

CONCLUSION

In this thesis, an augmented spark igniter was investigated experimentally and numerically. The igniter was tested for three different O/F ratio at four different total mass flow rate values. During tests temperature data at five different locations from the plume and pressure inside combustion chamber of the ASI was recorded. The plume of the igniter was observed by using schlieren imaging. All points at which igniter is tested, were simulated in a numerical model. Findings of the numerical model and experiments are presented and discussed in regarding chapters.

Comparison between experiments and numerical model was done in four aspects. Firstly, actual schlieren images of the tests were compared to numerical schlieren images that were created by using results of numerical analyses in means of shear angle. Results show tiny differences. Secondly, the pressure data of the experiments were compared to pressure values in the combustion chamber that is obtained by numerical analyses. The maximum error was found out to be 17%, while minimum error is 1%. An average error of 8.8% is well enough to validate model on this comparison. Thirdly, temperature data that is acquired experimentally are compared with findings of numerical results. Experimental temperature data of the first thermocouple was came out to be lower than the findings of the thermocouples behind them. This result shows contrast to physics of the phenomena. Also the maximum error between numerical investigation and experiments occurred at that point, in means of temperature. Therefore, it is concluded that a measurement error is induced to that maximum error values. This measurement fault should be investigated further. Nevertheless, maximum of 10.7% average error indicates that the numerical model is capable of simulating the combustion, conservation of energy and heat transfer well enough. Lastly, the igniter is inspected visually after the tests, and it is understood that the model is able to capture unsymmetrical temperature distribution inside the

combustion chamber by means of resemblance of overheated regions. As a result, numerical model has proved itself in simulating physics of the igniter.

Later, a performance parameter is defined and evaluated to have an optimization parameter for the augmented spark igniters rather than just ignitability which is the major tendency in literature. The defined performance parameter, in the scope of this work, is called “Effective Flame Length”. Assumptions and postulations that is done during the definition of the parameter is explained in the last chapter. Evidences tells that O/F ratio (adiabatic flame temperature of the mixture) is more effective than the total mass flow rate. Doubling mass flow rate and halving (roughly) the O/F ratio lead the same effective flame length. These findings will be useful in preliminary design of an augmented spark igniter.

REFERENCES

[1] G. P. Sutton, *History of Liquid Propellant Rocket Enaines*. 2006.

[2] G. Frenken, E. Vermeulen, F. Bouquet, and B. Sanders, "Development Status of the Ignition System for Vinci," in *38th AIAA/ASME/SAE/ASEE Joint Propulsion Conference & Exhibit*, 2012.

[3] W. M. Marshall, B. Stiegemeier, S. E. Greene, and E. Hurlbert, "Survey of Constellation-Era LOX / Methane Development Activities and Future Development Needs," 2018.

[4] V. Yang, M. Habiballah, J. Hulka, and M. Popp, *Liquid Rocket Engine Thrust Chambers: Aspects of Modelling, Analysis, And Design*, vol. 200. 2004.

[5] D. H. Huang and D. K. Huzel, *Modern Engineering for Design of Liquid-Propellant Rocket Engines*. 1992.

[6] R. L. Zurawski and J. M. Green, "Catalytic Ignition of Hydrogen and Oxygen Propellants," in *24th Joint Propulsion Conference*, 1988.

[7] M. V. Dobrovolskiy, *Liquid Propellant Rocket Engines*. İstanbul: NDL Mühendislik, 2018.

[8] D. Jones, "Reusable Rocket Propulsion for Space Tourism Vehicles," no. July, pp. 1–8, 2012.

[9] Boeing, "Space Shuttle Main Engine Orientation," *Sp. Transp. Syst. Train. Data*, no. June, pp. 1–1105, 1998.

[10] G. A. Repas, "Hydrogen-Oxygen Torch Ignitor," Cleveland, Ohio, 1994.

[11] B. R. Lawver and D. C. Rousar, "Ignition Characterization of the GOX/Ethanol Propellant Combination," in *AIAA/SAE/ASME 20th Joint Propulsion COnference*, 1984.

[12] C. Dexter and T. Mccay, “Space Shuttle Main Engine fuel preburner augmented spark igniter shutdown detonations,” 2013.

[13] B. D. Reed and S. J. Schneider, “Hydroged/Oxygen Auxiliary Propulsion Technology.”

[14] S. Schneider, J. John, and J. Zoeckler, “Design, Fabrication, and Test of a LOX/LCH4 RCS Igniter at NASA,” no. July, pp. 1–11, 2007.

[15] K. Breisacher and K. Ajmani, “LOX / Methane Main Engine Igniter Tests and Modeling,” in *Combustion*, 2008.

[16] J. Betancourt-Roque, “Instrumentation, Control and Torch Ignition Systems Development for Lox/Methane Propulsion Research,” The University of Texas at El Paso, 2012.

[17] J. Kleinhenz, C. Sarmiento, and W. Marshall, “Spark Ignition Characteristics of a LO2/LCH4 Engine at Altitude Conditions,” no. August, pp. 1–14, 2012.

[18] L. E. Sanchez, R. Ellis, V. Dorado, and A. Choudhuri, “An Experimental Investigation of a LOX/CH4 Torch Ignition System for Propulsion Research,” 2014.

[19] J. R. Flores, L. E. Sanchez, R. Ellis, V. Dorado, and A. Choudhuri, “An Experimental Evaluation of a LOX/CH4 Torch Ignition System for Propulsion Research,” 2013.

[20] A. Anoop, M. P. Assiz, and M. J. Manu, “Optimization of Length of Mixing Zone in GH_2-GO_2 Based Torch Igniter, Applying Numerical Techniques,” *Appl. Mech. Mater.*, vol. 592–594, pp. 1692–1696, 2014.

[21] P. Natale, G. Saccone, A. D. French, and F. Battista, “Chemical and CFD modelling of Sub-Scale Bread-Board igniter based on experimental data assessment,” in *51st AIAA/ASME/SAE/ASEE Joint Propulsion Conference*, 2015, pp. 27–29.

[22] Z. Q. Gregory P. Smith, David M. Golden, Michael Frenklach, Nigel W. Moriarty, Boris Eiteneer, Mikhail Goldenberg, C. Thomas Bowman, Ronald K. Hanson, Soonho Song, William C. Gardiner, Jr., Vitali V. Lissianski, "GRI-MECH 3.0." [Online]. Available: http://www.me.berkeley.edu/gri_mech/.

[23] E. L. Petersen and R. K. Hanson, "Reduced kinetics mechanisms for ram accelerator combustion," *J. Propuls. Power*, vol. 15, no. 4, pp. 591–600, 1999.

[24] J. Chaparro, L. E. Sanchez, S. A. Torres, A. R. Choudhuri, and N. D. Love, "Development and Testing of a O2/CH4 Torch Igniter for Propulsion Systems," 2016.

[25] R. Buttay, L. Gomet, G. Lehnasch, and A. Mura, "Highly resolved numerical simulation of combustion downstream of a rocket engine igniter," *Shock Waves*, vol. 27, no. 4, pp. 655–674, 2017.

[26] W. M. Marshall, R. J. Osborne, and S. E. Greene, "Development of Augmented Spark Impinging Igniter System for Methane Engines," pp. 1–23, 2017.

[27] E. C. Unruh, R. D. Hicks, and D. M. Lineberry, "Reduced Pressure Environment Testing of a Torch Augmented Spark Igniter," 2018.

[28] Delta II ARGOS Media Kit, "Delta II Launch Stopped Due to Engine Ignition Failure," 1999. [Online]. Available: https://boeing.mediaroom.com/1999-01-28-Delta-II-Launch-Stopped-Due-to-Engine-Ignition-Failure. [Accessed: 03-Mar-2019].

[29] H. J. Kim, S. . W. Hong, H. D. Kim, S. Y. Yang, and S. H. Chung, "Quenching Distance Measurement for the Control of Hydrogen Explosion," in *Proceedings of the 18th International Colloquium on the Dynamics of Explosion and Reactive Systems*, 2001.

[30] G. S. Settles, *Schlieren and Shadowgraph Techniques: Visualizing Phenomena in Transparent Media*. Springer, 2001.

[31] OMEGA, “Thermocouple Response Time,” 2019. [Online]. Available: https://www.omega.com/en-us/resources/thermocouples-response-time. [Accessed: 25-Sep-2019].

[32] S. Gordon and B. J. McBride, “Computer Program for Calculation of Complex Chemical Equilibrium Compositions and Applications.” NASA Reference Publications 1311, 1996.

[33] S. Bell, “A Beginner’s Guide to Uncertainty of Measurement,” *National Physical Laboratory*, 1999. [Online]. Available: https://www.dit.ie/media/physics/documents/GPG11.pdf.

[34] Kistler, “Absolute Pressure Transmitter Data Sheet,” 2018. [Online]. Available: https://www.kistler.com/?type=669&fid=83437&model=document&callee=frontend. [Accessed: 31-Jul-2019].

[35] N.I.S.T, “Revised Thermocouple Reference Tables - Type C.” [Online]. Available: https://sea.omega.com/temperature/Z/pdf/z239-240.pdf.

[36] F. T. M. Nieuwstadt, B. J. Boersma, and J. Westerweel, *Turbulence: Introduction of Theory and Applications of Turbulent Flows*. Springer Berlin Heidelberg, 2015.

[37] O. C. Kocaman, “Yakıt Enjeksiyonundaki Düzensizliklerin Yanma Odası Çıkış Sıcaklık Profilli Üzerindeki Etkilerinin Büyük Burgaç Benzetimi İle İncelenmesi,” TOBB Ekonomi ve Teknoloji Üniversitesi, 2018.

[38] M. P. Bulat and P. V. Bulat, “Comparison of turbulence models in the calculation of supersonic separated flows,” *World Appl. Sci. J.*, vol. 27, no. 10, pp. 1263–1266, 2013.

[39] D. C. Wilcox, *Turbulence Modeling for CFD*, 3rd ed. DCW Industries, 2006.

[40] S. R. Turns, *An Introduction to Combustion Concepts and Applications*, 3rd ed. McGraw Hill, 2012.

[41] B. Ivancic and W. Mayer, “Time- and Length Scales of Combustion in Liquid Rocket Thrust Chambers,” *J. Propuls. Power*, vol. 18, no. 2, pp. 247–253, 2008.

[42] W. C. R. R. J. Kee, F. M. Rupley, J. A. Miller, M. E. Coltrin, J. F. Grcar, E. Meeks, H. K. Moffat, A. E. Lutz, G. DixonLewis, M. D. Smooke, J. Warnatz, G. H. Evans, R. S. Larson, R. E. Mitchell, L. R. Petzold, C. W. M. Caracotsios, W. E. Stewart, P. Glarborg, and O. Adigun, “CHEMKIN COLLECTION.” Reaction Design, Inc., San Diego, 2000.

[43] I. R. Gran and B. F. Magnussen, “A numerical study of a bluff-body stabilized diffusion flame. Part 1. Influence of turbulence modeling and boundary conditions,” *Combust. Sci. Technol.*, vol. 119, no. 1–6, pp. 171–190, 1996.

[44] I. R. Gran and B. F. Magnussen, “A numerical study of a bluff-body stabilized diffusion flame. Part 2. Influence of combustion modeling and finite-rate chemistry,” *Combust. Sci. Technol.*, vol. 119, no. 1–6, pp. 191–217, 1996.

[45] B. F. Magnussen, “THE EDDY DISSIPATION CONCEPT A BRIDGE BETWEEN SCIENCE AND TECHNOLOGY,” in *ECCOMAS Thematic Conference on Computational Combustion*, 2005.

[46] M. Ó Conaire, H. J. Curran, J. M. Simmie, W. J. Pitz, and C. K. Westbrook, “A comprehensive modeling study of hydrogen oxidation,” *Int. J. Chem. Kinet.*, vol. 36, no. 11, pp. 603–622, 2004.

[47] H. Mendis, “Better meshing using ANSYS Fluent Meshing.” [Online]. Available: https://www.linkedin.com/pulse/better-meshing-using-ansys-fluent-hashan-mendis/. [Accessed: 03-Mar-2019].

[48] J. J. Quirk, “A Contribution to the Great Riemann solver debate,” *J. Numer. Methods Fluids*, vol. 18, no. November 1992, pp. 555–574, 1994.

[49] E. S. Webster and C. E. Davies, “The Use of Helmholtz Resonance for Measuring the Volume of Liquids and Solids,” *Sensors*, vol. 10, no. 12, pp. 10663–10672, 2010.

[50] I. Glassman and R. A. Yetter, *Combustion*, Fourth. Elsevier, 2008.

[51] Spray Imaging Group, “Spray Description.” [Online]. Available: https://spray-imaging.com/spray-description.html. [Accessed: 03-Mar-2019].

APPENDICES

A. Orifice Catalog

Metal Orifice Assemblies

8

Description

One-piece construction of solid metal is employed. Orifices are accurately machined, thoroughly cleaned, and flow tested to exacting standards. Sizes range from .004" to .125" orifice diameter. Special sizes can be made to order. Type DEL is a two-piece construction.

Applications

- Precision Flow Control – Gases or Liquids
- Speed Controls – Cylinders and Actuators
- Accurate Timing in Pneumatic or Hydraulic Circuits
- Flow Restriction
- Accurate Throttling
- Snubbers - Gages and Instruments
- Ultrasonic Sound Sources

Advantages

- High Pressure Capability
- Bi-directional Flow Compatibility
- Economical Precision Orifice
- Repeatable Orifice Size and Shape
- Predictable Flow Rate

Flow Direction

Metal Orifice Assemblies can be used for flow in either direction. The data on pages 20 and 21 is for a flow direction as shown in the right column on this page.

Kits

See pages 30-31 for kit selection.

General Specifications

Maximum Operating Pressure –
Brass 2000 psig
303 SS 4000 psig
Type DEL
Brass 200 psig

Flow – See flow chart for air on pages 20 and 21.
Orifice Diameters – .004" to .125" standard. Consult factory for other sizes.
Orifice Diameter Accuracy – ±.0005"
C_v Range – .00035 to .37 See pages 20 and 21.
Fluid Media – Air, Water, Gases and Liquids compatible with materials of construction.
Dimensions – See drawings on page 9.

NPT CONNECTIONS

Size Number	Orifice Dia. In.	Size Number Range
4	.0039	
5	.0051	
6	.0059	
7	.0071	
8	.0079	
9	.0091	
10	.0102	
11	.0110	
12	.0122	
13	.0130	Type B, E or V
14	.0142	Brass 4-125
15	.0150	303SS 4-125
16	.016	
17	.017	
18	.018	
19	.019	Type D, G, H or VV
20	.020	Brass 4-125
21	.021	303SS 4-125
22	.022	
23	.023	
24	.024	
25	.025	Type BM or EM
26	.026	Brass 4-125
27	.027	303SS 4-125
28	.028	
29	.029	
31	.031	
32	.032	Type BH or EH
33	.033	Brass 4-125
35	.035	303SS 4-125
37	.037	
38	.038	
39	.039	
40	.040	Type BMM
41	.041	Brass 4-125
42	.042	303SS 4-125
43	.043	
47	.047	
52	.052	
55	.055	Type DEL
60	.060	Brass 4-63
63	.063	
67	.067	
70	.070	
73	.073	
76	.076	
79	.079	
81	.081	
86	.086	
89	.089	
94	.094	
96	.096	
100	.100	
104	.104	
109	.109	
113	.113	
120	.120	
125	.125	

Construction

Type B, E or V

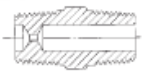

Orifice diameter .021" or larger

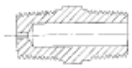

Orifice diameter .020" or smaller

Type D, G, H or VV

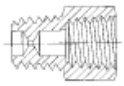

Orifice diameter .021" or larger

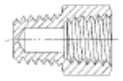

Orifice diameter .020" or smaller

Type BM or EM

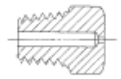

Type BH or EH

Type BMM

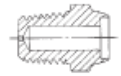

Type DEL

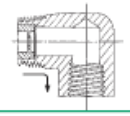

Part Numbers

The complete part number for an orifice assembly includes Type, Size Number, Body Material and Options.

EXAMPLES

Type	Size Number	Body Material	Options	Part Number
B	10 (.010")	Brass	–	B-10-BR
G	15 (.015")	Brass	–	G-15-BR
D	20 (.020")	SS	–	D-20-SS

O'Keefe Controls Co. P.O. BOX Q • TRUMBULL, CT 06611 • CT PHONE (203) 261-6711 • TOLL FREE PHONE (800) 533-3285 • FAX (203) 261-8331
e-mail ca@okcc.com • website www.okcc.com

Metal Orifice Air Flow – SLPM

	Orifice Diameter Inches	0.004	0.005	0.006	0.007	0.008	0.009	0.010	0.011	0.012	0.013	0.014	0.015	0.016	0.017	0.018	0.019	0.020	0.021	0.022	0.023	0.024	0.025	0.026	0.027	0.028	0.029	0.031	0.032	0.033
	Size Number	4	5	6	7	8	9	10	11	12	13	14	15	16	17	18	19	20	21	22	23	24	25	26	27	28	29	31	32	33
	C_v	0.00035	0.00061	0.00086	0.0012	0.0015	0.0019	0.0025	0.0028	0.0034	0.0038	0.0043	0.0050	0.0055	0.0067	0.0073	0.0080	0.0088	0.0096	0.011	0.012	0.013	0.014	0.016	0.017	0.018	0.019	0.022	0.024	0.025
Supply Pressure – psig	1	0.035	0.064	0.086	0.127	0.170	0.226	0.280	0.308	0.398	0.45	0.52	0.61	0.66	0.77	0.86	0.96	1.05	1.13	1.29	1.41	1.54	1.67	1.91	1.95	2.21	2.39	2.65	2.88	3.03
	5	0.09	0.16	0.21	0.30	0.40	0.52	0.65	0.71	0.92	1.06	1.21	1.41	1.54	1.76	1.98	2.22	2.47	2.65	2.97	3.24	3.53	3.83	4.34	4.44	4.94	5.31	5.86	6.42	6.80
	10	0.12	0.22	0.31	0.43	0.57	0.74	0.93	1.01	1.29	1.48	1.68	1.95	2.01	2.26	2.54	2.83	3.16	3.53	4.33	4.75	5.18	5.55	6.15	6.43	7.18	7.83	8.63	9.40	9.98
	15	0.16	0.28	0.39	0.54	0.72	0.93	1.17	1.26	1.62	1.85	2.10	2.44	2.50	2.85	3.23	3.57	4.01	4.41	5.35	5.93	6.43	6.95	7.58	7.95	8.78	9.58	10.6	11.6	12.3
	20	0.19	0.33	0.46	0.65	0.85	1.10	1.38	1.49	1.92	2.19	2.49	2.87	2.97	3.40	3.86	4.26	4.84	5.22	6.35	6.95	7.58	8.15	8.90	9.28	10.3	11.2	12.4	13.5	14.3
	25	0.22	0.39	0.53	0.75	0.98	1.27	1.59	1.71	2.20	2.50	2.86	3.28	3.42	3.92	4.45	4.91	5.59	6.01	7.30	7.95	8.65	9.38	10.2	10.7	11.7	12.8	14.2	15.4	16.3
	30	0.25	0.44	0.60	0.85	1.12	1.43	1.80	1.93	2.47	2.82	3.21	3.69	3.87	4.43	5.03	5.56	6.33	6.81	8.23	8.98	9.75	10.6	11.5	12.0	13.2	14.4	15.9	17.3	18.4
	40	0.30	0.54	0.74	1.05	1.38	1.77	2.21	2.37	3.04	3.45	3.93	4.51	4.78	5.47	6.21	6.85	7.81	8.42	10.1	11.0	12.0	13.0	14.1	14.7	16.1	17.5	19.4	21.1	22.5
	50	0.36	0.65	0.88	1.26	1.65	2.10	2.62	2.80	3.58	4.07	4.64	5.31	5.70	6.51	7.40	8.15	9.26	10.0	11.9	13.0	14.2	15.4	16.6	17.3	19.0	20.7	22.9	25.0	26.6
	60	0.42	0.75	1.02	1.46	1.91	2.42	3.02	3.23	4.13	4.70	5.34	6.13	6.61	7.56	8.58	9.46	10.7	11.6	13.8	15.0	16.4	17.7	19.2	20.0	21.9	23.8	26.4	28.8	30.7
	70	0.48	0.86	1.16	1.67	2.17	2.75	3.43	3.66	4.68	5.32	6.05	6.96	7.53	8.61	9.77	10.8	12.2	13.2	15.6	17.0	18.5	20.1	21.7	22.7	24.8	27.0	30.0	32.7	34.9
	80	0.54	0.96	1.30	1.87	2.43	3.08	3.83	4.09	5.23	5.95	6.77	7.79	8.46	9.67	11.0	12.1	13.7	14.9	17.5	19.0	20.7	22.5	24.2	25.3	27.7	30.2	33.6	36.7	39.0
	90	0.60	1.07	1.44	2.08	2.69	3.40	4.23	4.51	5.78	6.58	7.49	8.62	9.38	10.7	12.2	13.4	15.2	16.5	19.3	21.0	22.9	24.9	26.8	28.0	30.7	33.5	37.2	40.6	43.2
	100	0.66	1.17	1.58	2.28	2.95	3.72	4.63	4.94	6.33	7.22	8.21	9.46	10.3	11.8	13.4	14.7	16.6	18.0	21.1	23.0	25.1	27.4	29.4	30.8	33.7	36.8	40.9	44.6	47.5
Vacuum Level In. Hg.	5	0.053	0.096	0.129	0.191	0.253	0.332	0.406	0.450	0.582	0.661	0.773	0.899	0.977	1.14	1.28	1.41	1.55	1.70	1.90	2.10	2.30	2.48	2.74	2.83	3.16	3.41	3.78	4.12	4.32
	10	0.069	0.124	0.168	0.246	0.324	0.421	0.519	0.564	0.730	0.834	0.972	1.12	1.24	1.41	1.58	1.79	1.96	2.18	2.44	2.68	2.89	3.13	3.44	3.58	4.00	4.30	4.77	5.16	5.43
	15 (Choked Flow)	0.075	0.134	0.185	0.268	0.351	0.455	0.566	0.614	0.792	0.902	1.07	1.22	1.35	1.55	1.75	1.94	2.19	2.32	2.61	2.85	3.12	3.34	3.65	3.78	4.20	4.51	5.05	5.45	5.72
	20 (Choked Flow)	0.075	0.134	0.185	0.268	0.351	0.455	0.566	0.614	0.792	0.902	1.07	1.22	1.35	1.55	1.75	1.94	2.19	2.32	2.61	2.85	3.12	3.34	3.65	3.78	4.20	4.51	5.05	5.45	5.72
	30 (Choked Flow)	0.075	0.134	0.185	0.268	0.351	0.455	0.566	0.614	0.792	0.902	1.07	1.22	1.35	1.55	1.75	1.94	2.19	2.32	2.61	2.85	3.12	3.34	3.65	3.78	4.20	4.51	5.05	5.45	5.72

	Orifice Diameter Inches	0.035	0.037	0.038	0.039	0.04	0.041	0.042	0.043	0.047	0.052	0.055	0.06	0.063	0.067	0.07	0.073	0.076	0.079	0.081	0.086	0.089	0.094	0.096	0.1	0.104	0.109	0.113	0.12	0.125
	Size Number	35	37	38	39	40	41	42	43	47	52	55	60	63	67	70	73	76	79	81	86	89	94	96	100	104	109	113	120	125
	C_v	0.028	0.031	0.032	0.033	0.036	0.038	0.039	0.041	0.048	0.059	0.068	0.081	0.088	0.1	0.11	0.12	0.13	0.14	0.15	0.17	0.18	0.2	0.21	0.23	0.25	0.27	0.31	0.34	0.37
Supply Pressure – psig	1	3.48	3.83	4.13	4.46	4.6	4.67	4.99	5.36	6.43	8.04	9.4	11.2	12.2	14.2	15.9	16.9	18.5	20.3	21.7	23.5	25.4	28.4	30.1	32.9	35.5	39.6	43.1	47.8	50.1
	5	7.67	8.48	9.09	9.7	10.2	10.6	11.3	12.1	14.2	17.6	20.3	23.9	26.1	30.3	33.8	36.1	39.4	43.1	46	51.1	54.9	61.9	65	70.8	76.6	84.8	92.1	102	108
	10	10.6	11.8	12.5	13.6	14.4	14.8	15.6	16.8	19.4	24.5	27.1	32.2	35.2	40.7	45.6	48.5	52.9	57.3	61.6	67.9	72.3	81	85.5	92.3	102	112	118	135	148
	15	13.1	14.5	15.4	16.7	17.7	18.2	19.1	20.4	23.6	29.7	32.9	39	42.6	49.3	55.3	58.8	64	69.4	74.5	82.1	87.3	97.8	103	111	123	135	143	163	178
	20	15.3	17	18.1	19.6	20.9	21.4	22.5	24	27.7	35	38.7	45.9	50.1	58	65	69	75.3	81.4	87.3	95.6	102	114	121	130	144	158	167	190	210
	25	17.7	19.6	20.8	22.6	24	24.7	25.9	27.6	31.9	40.3	44.6	52.8	57.7	66.7	74.7	79.3	86.4	93.5	100	110	117	131	138	149	164	180	191	219	241
	30	20	22.2	23.6	25.6	27.2	28	29.4	31.3	36	45.6	50.4	59.7	65.2	75.4	84.3	89.5	97.4	105	113	125	132	148	156	168	185	204	216	248	273
	40	24.8	27.4	31.7	31.6	33.6	34.6	36.3	38.7	44.5	56.3	62.2	73.6	80.3	92.7	104	110	120	129	139	153	162	181	191	207	228	251	267	306	337
	50	29.5	32.6	34.8	37.6	40.1	41.3	43.3	46	52.9	66.9	74	87.4	95.4	110	123	131	142	153	164	181	192	215	227	247	272	299	317	364	401
	60	34.3	38	40.6	43.8	46.7	48.1	50.3	53.5	61.5	77.7	85.8	101	110	127	142	151	164	177	189	210	223	250	264	286	315	347	368	422	465
	70	39.2	43.3	46.3	50	53.3	55	57.4	61	70	88.4	97.6	115	126	145	162	171	186	202	216	240	254	285	301	327	360	398	421	482	531
	80	44	48.7	52.1	56.2	60	61.9	64.5	68.5	78.6	99.1	109	129	141	162	181	191	209	227	242	269	285	320	338	367	404	445	472	541	596
	90	50	54.2	57.8	62.4	66.7	68.9	71.5	76	87.2	109	121	143	156	179	200	211	231	251	268	298	316	354	374	406	447	492	522	598	660
	100	53.9	59.6	63.7	68.7	73.5	77.3	78.6	83.5	95.8	120	133	156	171	196	221	234	255	277	296	329	349	392	413	449	494	544	578	662	729
Vacuum Level In. Hg.	5	4.92	5.4	5.81	6.29	6.76	6.82	7.29	7.67	9.08	11.3	12.4	14.8	17.1	20	22.5	23.9	26	28.3	30.2	33.2	35.9	40.1	41.8	45.3	49	53.9	57.9	65.3	70.9
	10	6.18	6.78	7.29	7.85	8.31	8.5	9.08	9.58	11.1	13.9	15.4	18.2	21.2	24.4	27.2	29.9	32.5	35.3	37.7	41.5	44.8	50	52.1	56.6	61.2	67.2	72.2	81.4	88.4
	15 (Choked Flow)	6.5	7.17	7.63	8.22	8.66	8.87	9.46	10	11.6	14.4	15.9	18.6	22.1	25.5	28.4	31.2	33.9	36.8	39.4	43.3	46.7	52.1	54.4	59	63.8	70.1	75.3	84.9	92.2
	20 (Choked Flow)	6.5	7.17	7.63	8.22	8.66	8.87	9.46	10	11.6	14.4	15.9	18.6	22.1	25.5	28.4	31.2	33.9	36.8	39.4	43.3	46.7	52.1	54.4	59	63.8	70.1	75.3	84.9	92.2
	30 (Choked Flow)	6.5	7.17	7.63	8.22	8.66	8.87	9.46	10	11.6	14.4	15.9	18.6	22.1	25.5	28.4	31.2	33.9	36.8	39.4	43.3	46.7	52.1	54.4	59	63.8	70.1	75.3	84.9	92.2

Standard Conditions 70°F, 14.7 psia

SCFH – Standard Cu. Ft. Per Hour
SLPM – Standard Liters Per Minute

Above data obtained with Type B restrictor. Flow rates for other metal restrictors are essentially the same as for Type B. Above data supercedes previous publications.

O'Keefe Controls Co. P.O. BOX Q • TRUMBULL, CONNECTICUT 06611 • CT PHONE (203) 261-6711 • TOLL FREE PHONE (800) 533-3285 • FAX (203) 261-8331

B. H_2-O_2 Reaction Mechanism

H_2/O_2 Reaction Mechanism (units: cm^3, mol, s, kcal, K)

	Reaction	A	n	E_a
		H_2/O_2 chain reactions		
1	$\dot{H} + O_2 = \dot{O} + \dot{O}H$	1.91×10^{14}	0.00	16.44
2	$\dot{O} + H_2 = \dot{H} + \dot{O}H$	5.08×10^{4}	2.67	6.292
3	$\dot{O}H + H_2 = \dot{H} + H_2O$	2.16×10^{8}	1.51	3.43
4	$\dot{O} + H_2O = \dot{O}H + \dot{O}H$	2.97×10^{6}	2.02	13.4
		H_2/O_2 dissociation/recombination reactions		
5[a]	$H_2 + M = \dot{H} + \dot{H} + M$	4.57×10^{19}	−1.40	105.1
6[b]	$\dot{O} + \dot{O} + M = O_2 + M$	6.17×10^{15}	−0.50	0.00
7[c]	$\dot{O} + \dot{H} + M = O\dot{H} + M$	4.72×10^{18}	−1.00	0.00
8[d,e]	$\dot{H} + \dot{O}H + M = H_2O + M$	4.50×10^{22}	−2.00	0.00
		Formation and consumption of $H\dot{O}_2$		
9[f,g]	$\dot{H} + O_2 + M = H\dot{O}_2 + M$	3.48×10^{16}	−0.41	−1.12
	$\dot{H} + O_2 = H\dot{O}_2$	1.48×10^{12}	0.60	0.00
10	$H\dot{O}_2 + \dot{H} = H_2 + O_2$	1.66×10^{13}	0.00	0.82
11	$H\dot{O}_2 + \dot{H} = \dot{O}H + \dot{O}H$	7.08×10^{13}	0.00	0.30
12	$H\dot{O}_2 + \dot{O} = \dot{O}H + O_2$	3.25×10^{13}	0.00	0.00
13	$H\dot{O}_2 + \dot{O}H = H_2O + O_2$	2.89×10^{13}	0.00	−0.50
		Formation and consumption of H_2O_2		
14[h]	$H\dot{O}_2 + H\dot{O}_2 = H_2O_2 + O_2$	4.2×10^{14}	0.00	11.98
	$H\dot{O}_2 + H\dot{O}_2 = H_2O_2 + O_2$	1.3×10^{11}	0.00	−1.629
15[i,f]	$H_2O_2 + M = \dot{O}H + O\dot{H} + M$	1.27×10^{17}	0.00	45.5
	$H_2O_2 = \dot{O}H + O\dot{H}$	2.95×10^{14}	0.00	48.4
16	$H_2O_2 + \dot{H} = H_2O + \dot{O}H$	2.41×10^{13}	0.00	3.97
17	$H_2O_2 + \dot{H} = H_2 + H\dot{O}_2$	6.03×10^{13}	0.00	7.95
18	$H_2O_2 + \dot{O} = \dot{O}H + H\dot{O}_2$	9.55×10^{06}	2.00	3.97
19[h]	$H_2O_2 + \dot{O}H = H_2O + H\dot{O}_2$	1.0×10^{12}	0.00	0.00
	$H_2O_2 + \dot{O}H = H_2O + H\dot{O}_2$	5.8×10^{14}	0.00	9.56

[a] Efficiency factors are $H_2O = 12.0$; $H_2 = 2.5$.
[b] Efficiency factors are $H_2O = 12$; $H_2 = 2.5$; Ar = 0.83; He = 0.83.
[c] Efficiency factors are $H_2O = 12$; $H_2 = 2.5$; Ar = 0.75; He = 0.75.
[d] Original pre-exponential A factor is multiplied by 2 here.
[e] Efficiency factors are $H_2O = 12$; $H_2 = 0.73$; Ar = 0.38; He = 0.38.
[f] Troe parameters: reaction 9, $a = 0.5$, $T^{***} = 1.0 \times {}^{-30}$, $T^{*} = 1.0 \times 10^{+30}$, $T^{**} = 1.0 \times 10^{+100}$; reaction 15, $a = 0.5$, $T^{*} = 1.0 \times 10^{+30}$, $T^{***} = 1.0 \times {}^{-30}$.
[g] Efficiency factors are $H_2 = 1.3$; $H_2O = 14$; Ar = 0.67; He = 0.67.
[h] Reactions 14 and 19 are expressed as the sum of the two rate expressions.
[i] Efficiency factors are $H_2O = 12$; $H_2 = 2.5$; Ar = 0.45; He = 0.45;

C. Contour of O/F Ratio in the Combustion Chamber of Test-1 Numerical Simulation

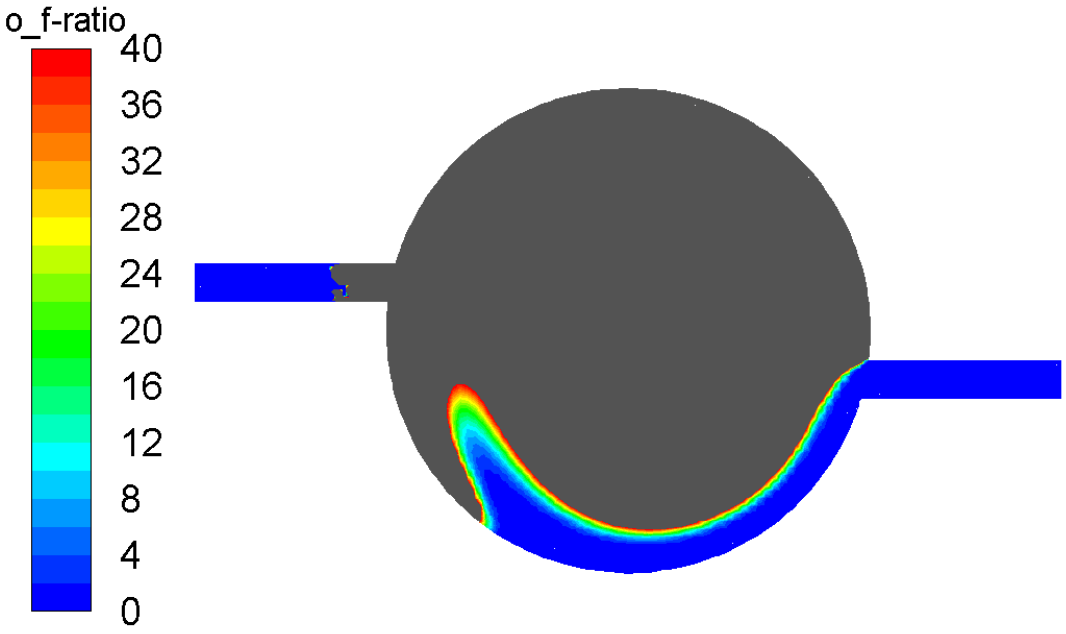

D. Static Temperature Contours

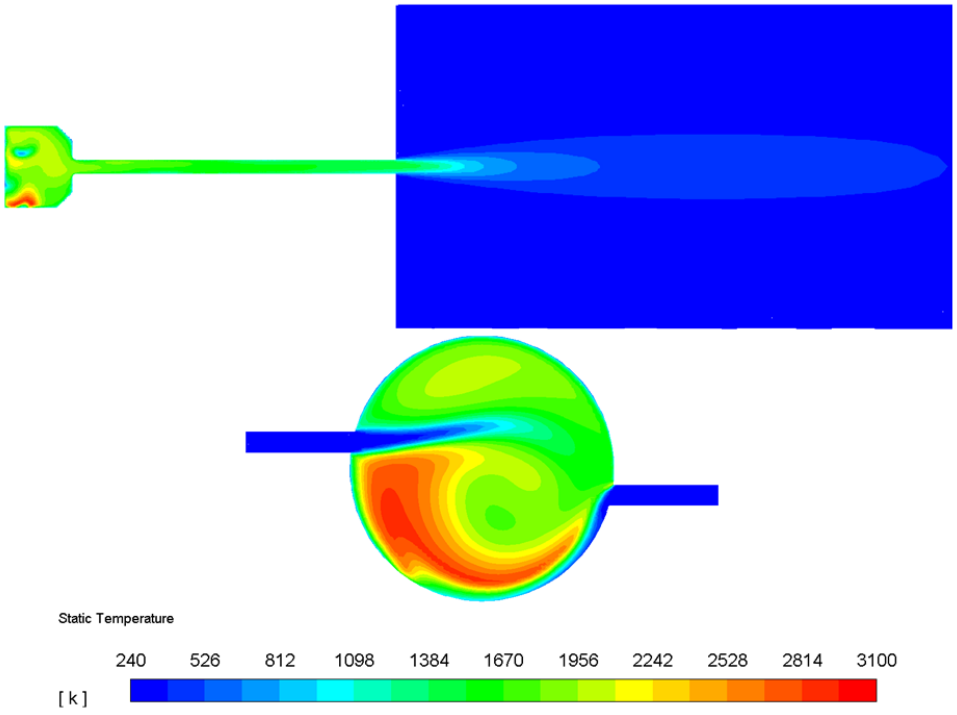

Figure D-1. Static Temperature Contours for Test-1 on Plane-1 and Plane-2

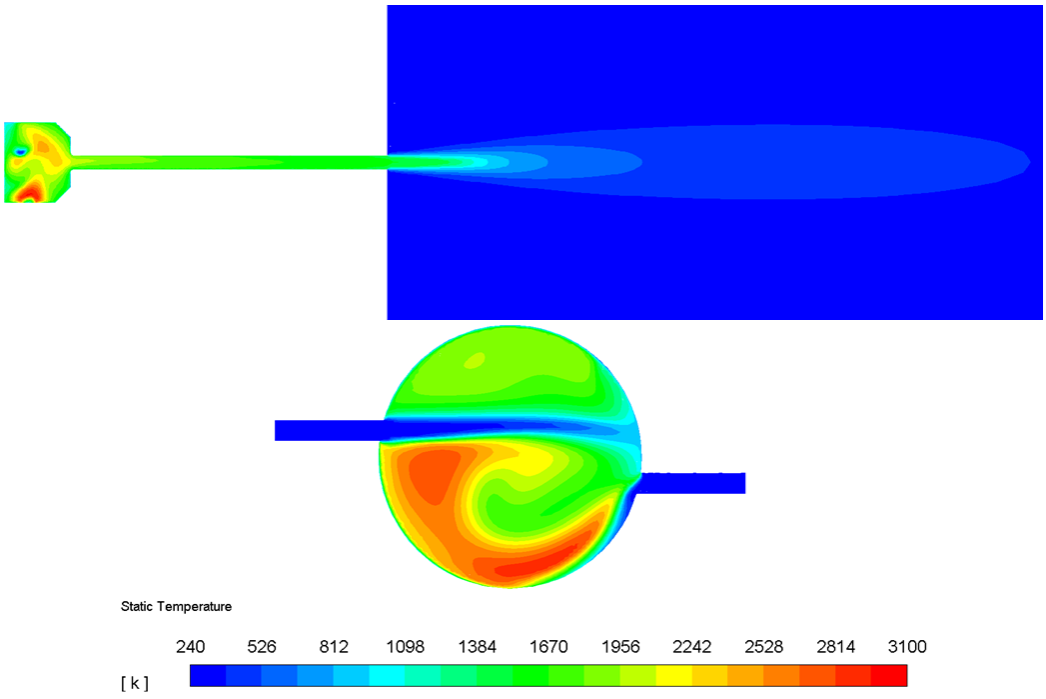

Figure D-2. Static Temperature Contours for Test-2 on Plane-1 and Plane-2

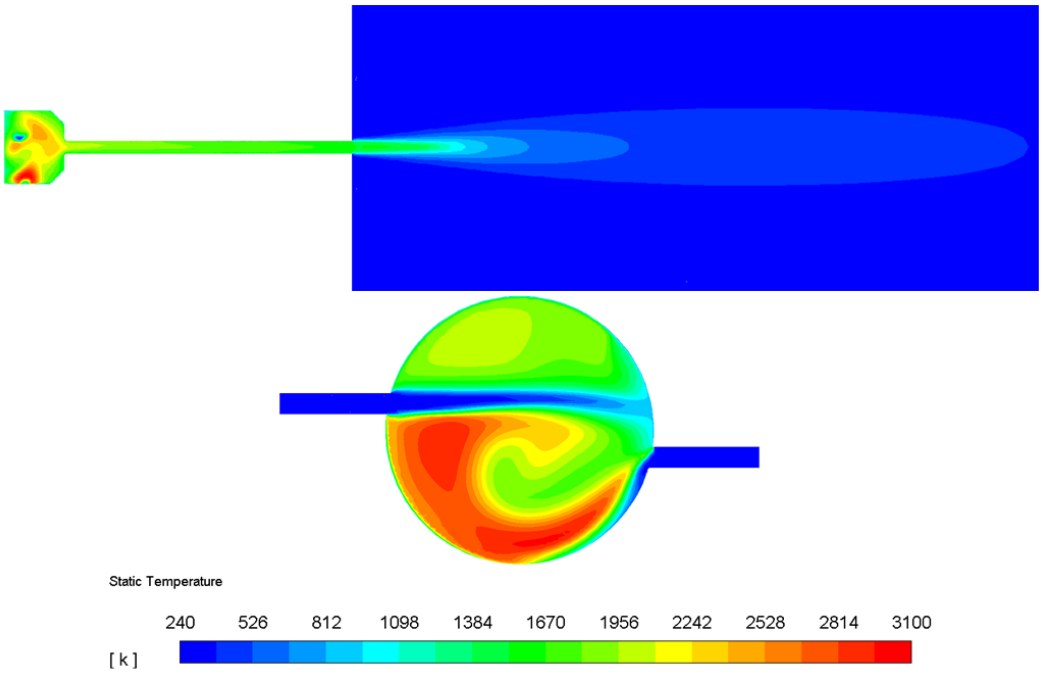

Figure D-3. Static Temperature Contours for Test-3 on Plane-1 and Plane-2

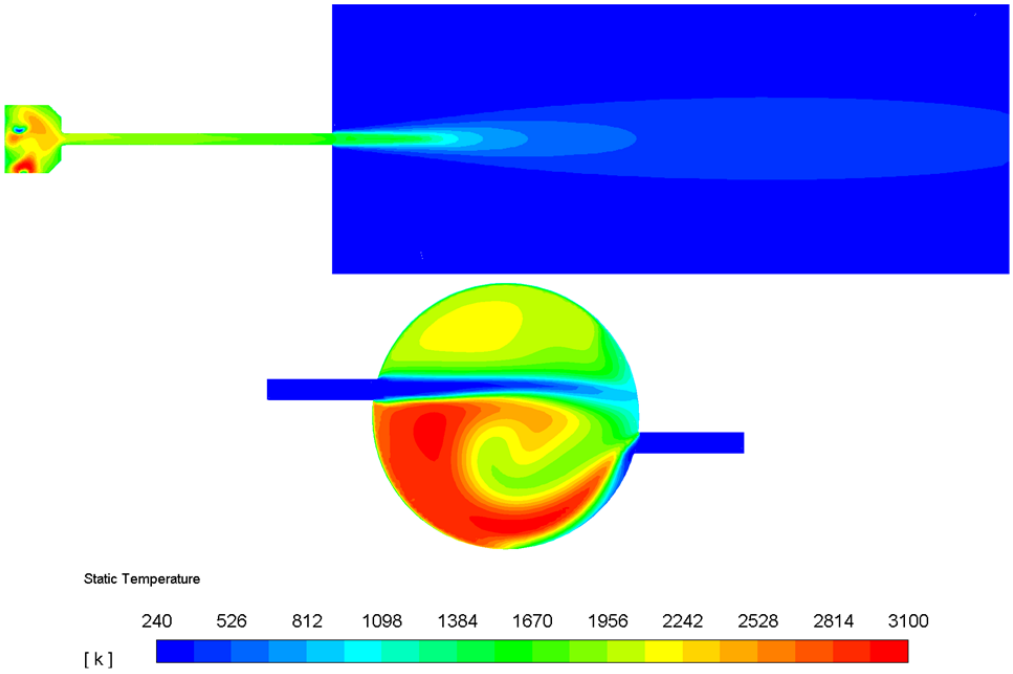

Figure D-4. Static Temperature Contours for Test-4 on Plane-1 and Plane-2

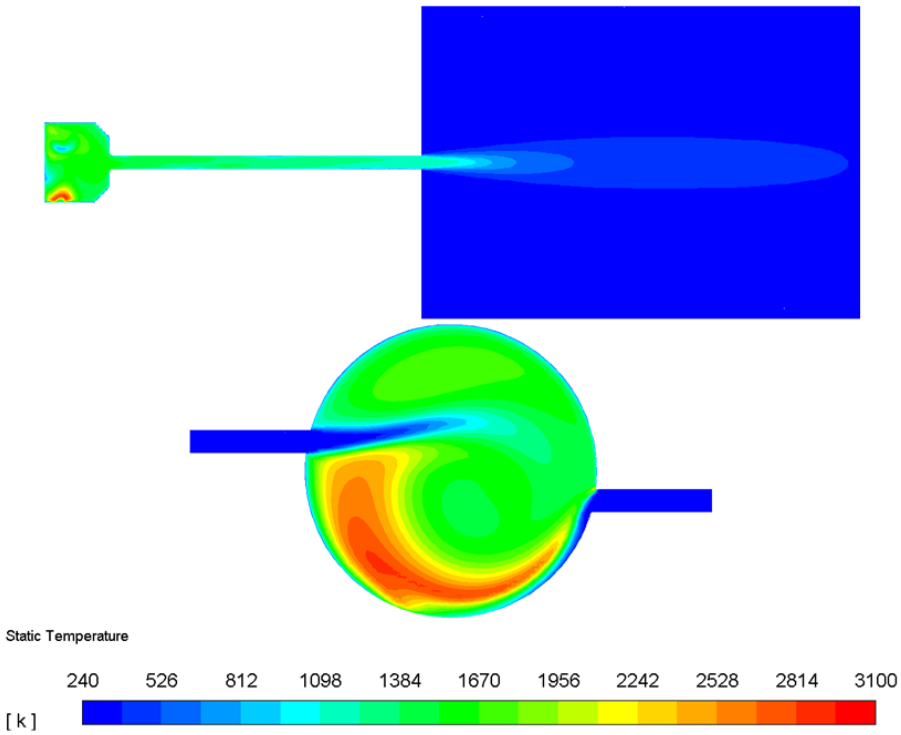

Figure D-5. Static Temperature Contours for Test-5 on Plane-1 and Plane-2

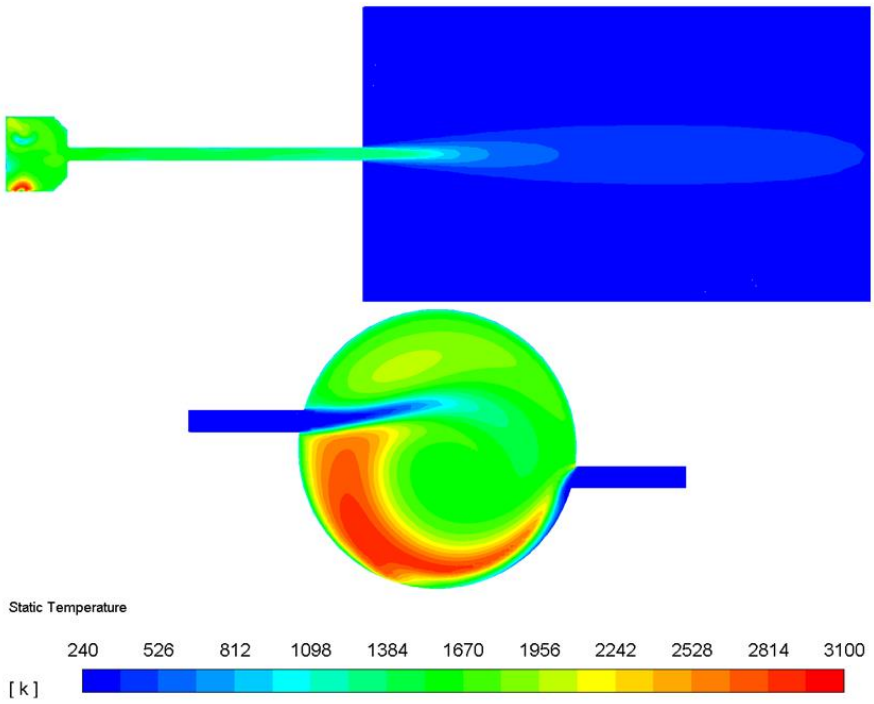

Figure D-6. Static Temperature Contours for Test-6 on Plane-1 and Plane-2

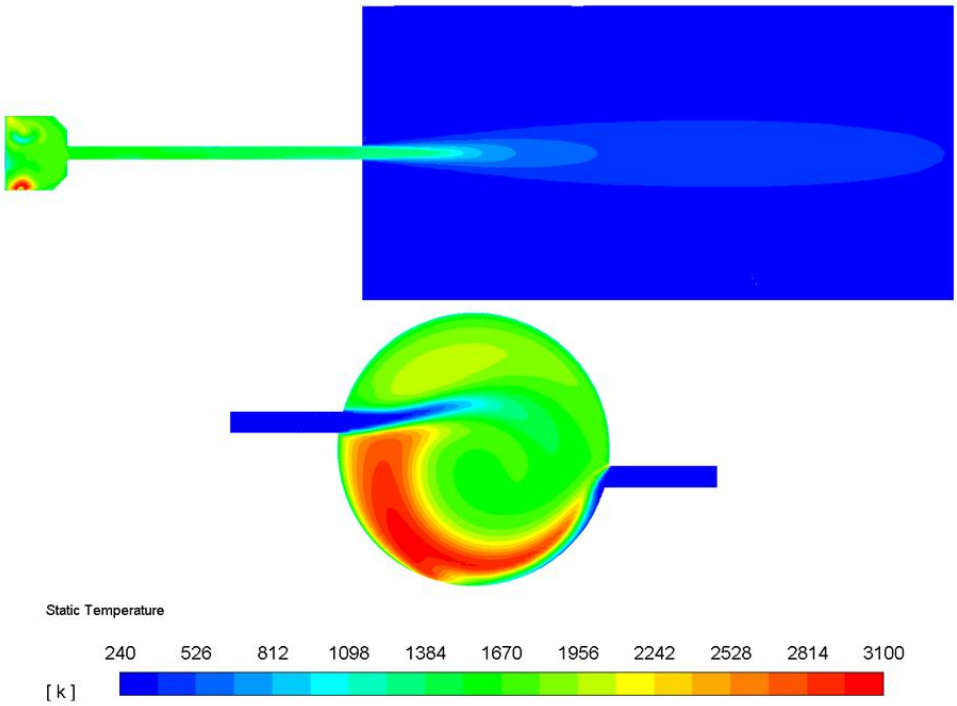

Figure D-7. Static Temperature Contours for Test-7 on Plane-1 and Plane-2

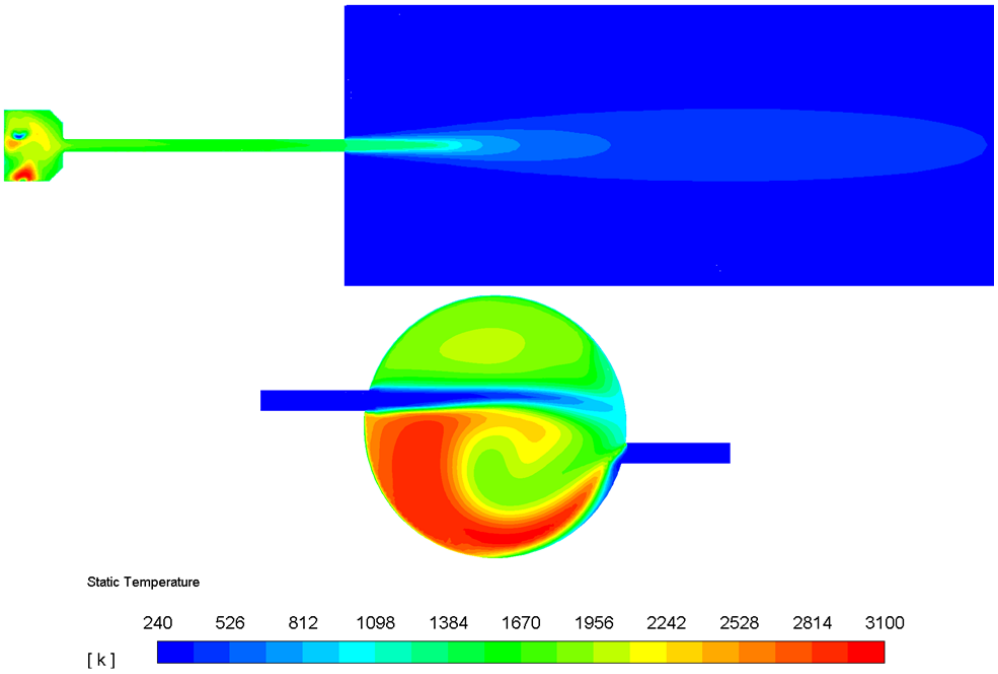

Figure D-8. Static Temperature Contours for Test-8 on Plane-1 and Plane-2

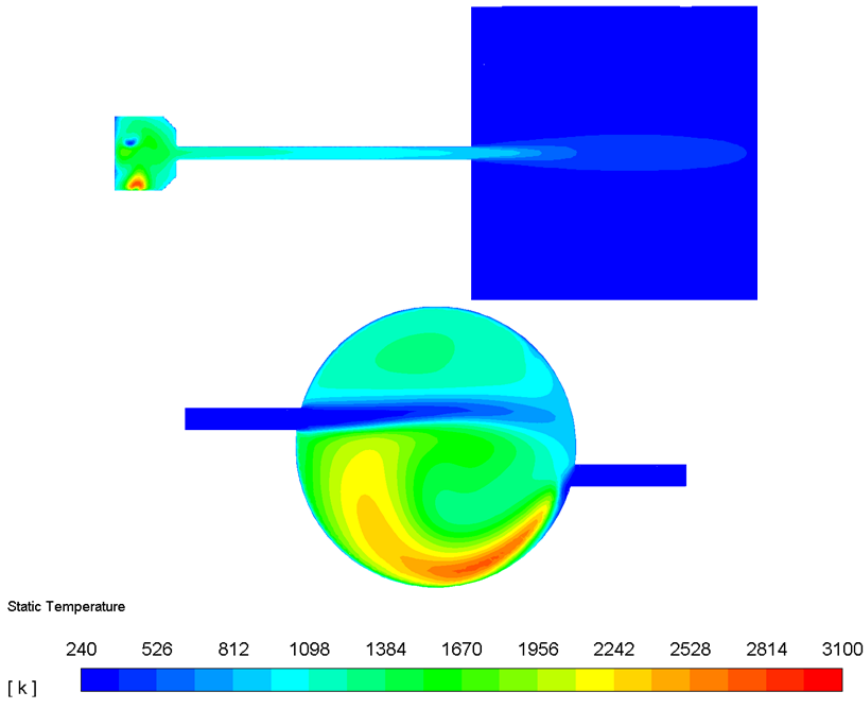

Figure D-9. Static Temperature Contours for Test-9 on Plane-1 and Plane-2

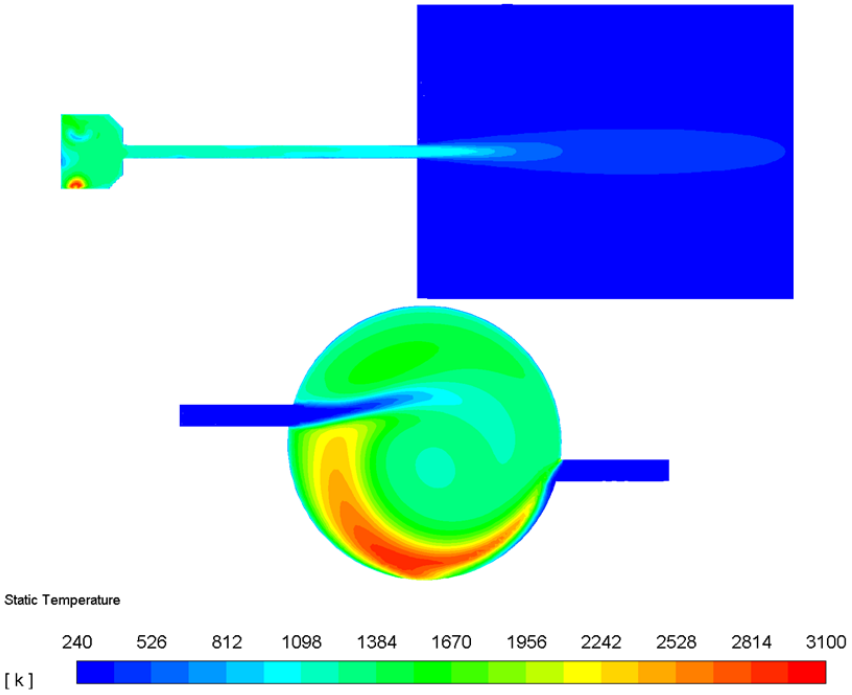

Figure D-10. Static Temperature Contours for Test-10 on Plane-1 and Plane-2

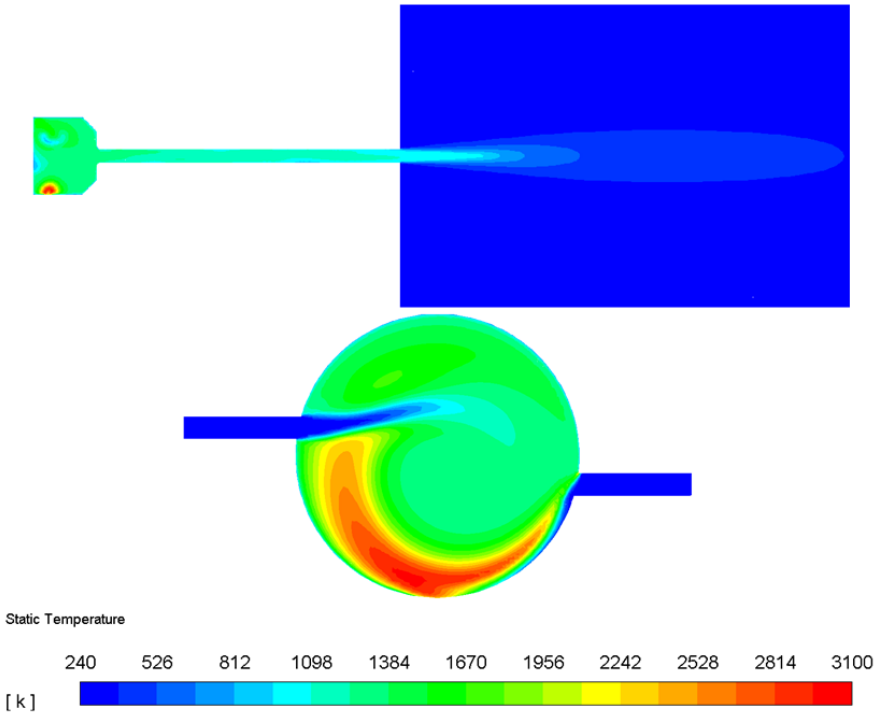

Figure D-11. Static Temperature Contours for Test-11 on Plane-1 and Plane-2

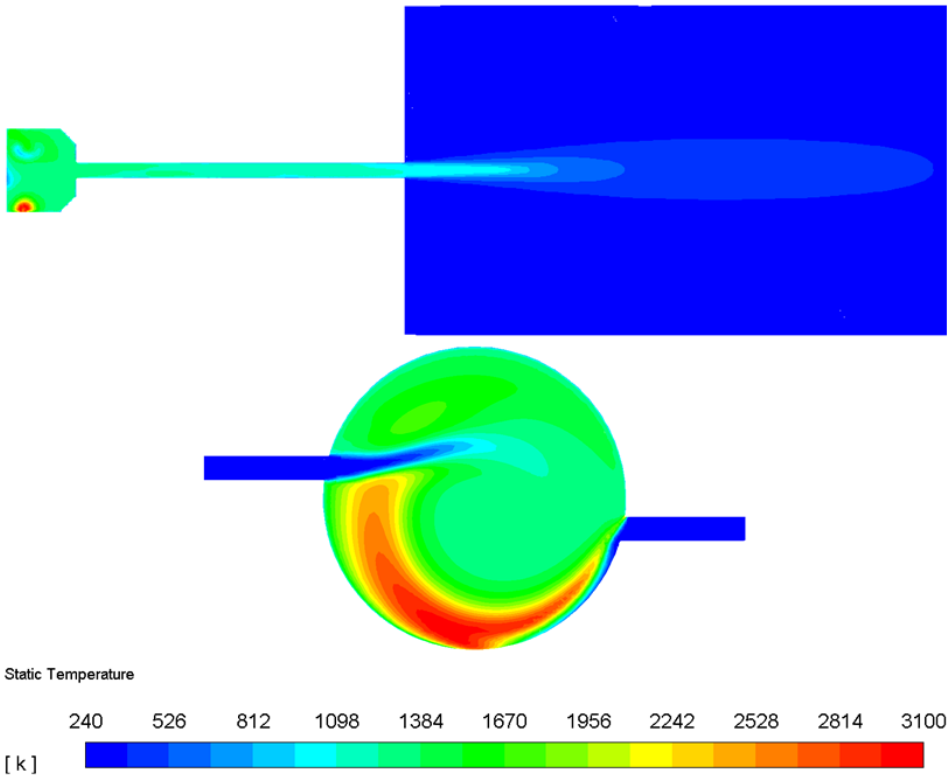

Figure D-12. Static Temperature Contours for Test-12 on Plane-1 and Plane-2

E. Pressure Contours

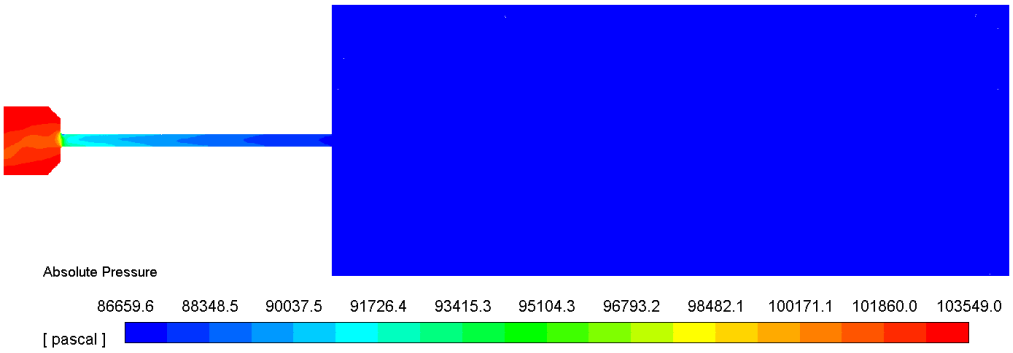

Figure E-13. Absolute Pressure Contours for Test-1 on Plane-2

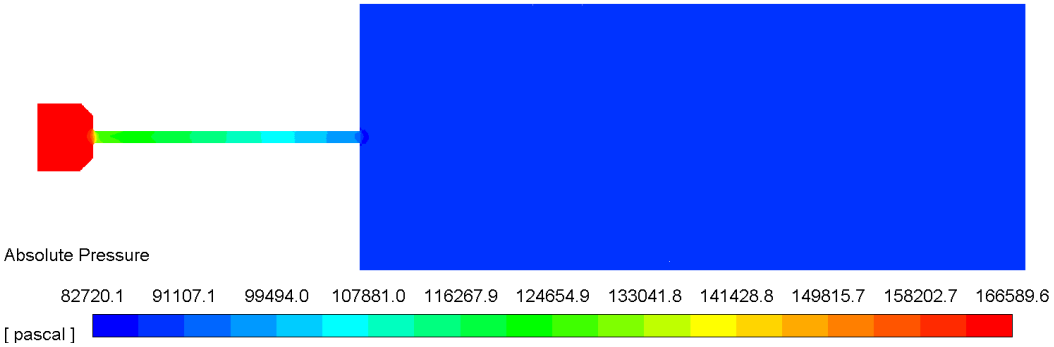

Figure E-2. Absolute Pressure Contours for Test-2 on Plane-2

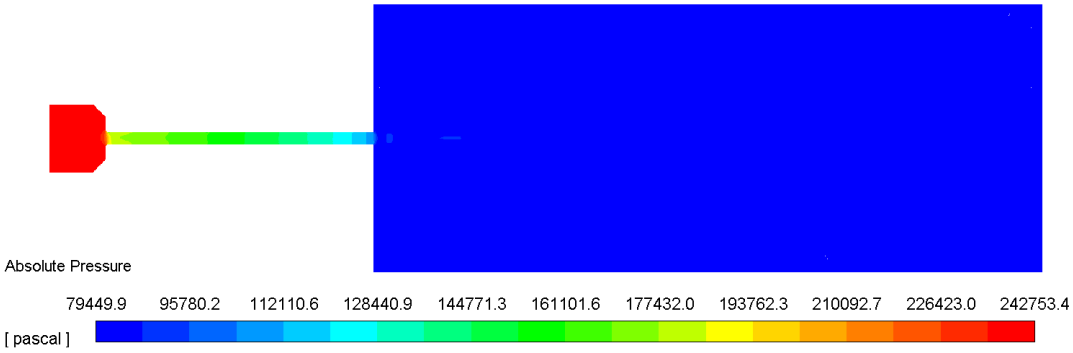

Figure E-3. Absolute Pressure Contours for Test-3 on Plane-2

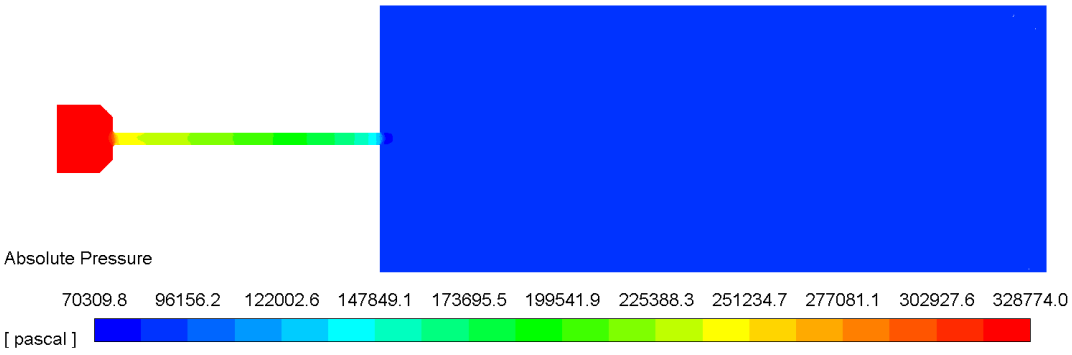

Figure E-4. Absolute Pressure Contours for Test-4 on Plane-2

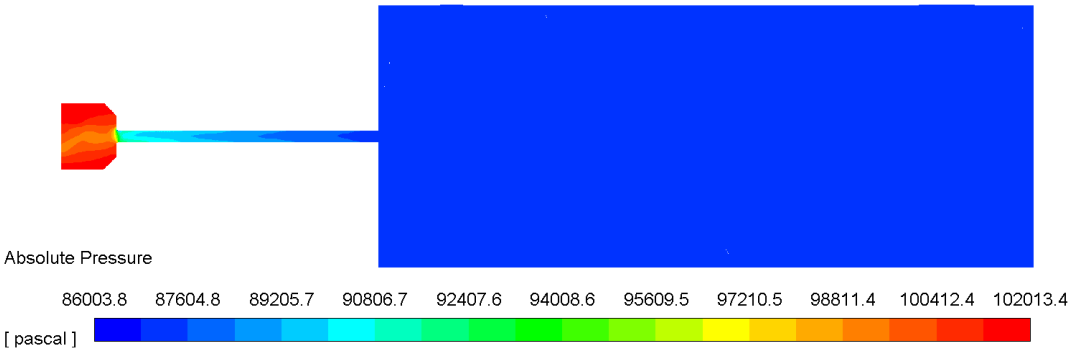

Figure E-5. Absolute Pressure Contours for Test-5 on Plane-2

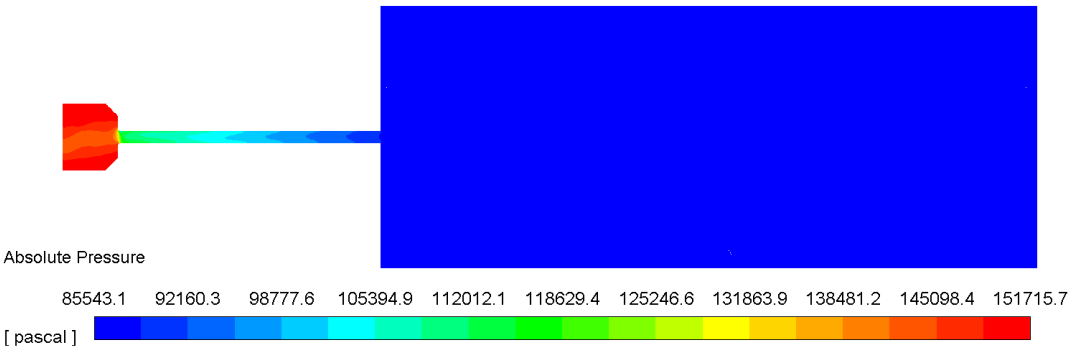

Figure E-6. Absolute Pressure Contours for Test-6 on Plane-2

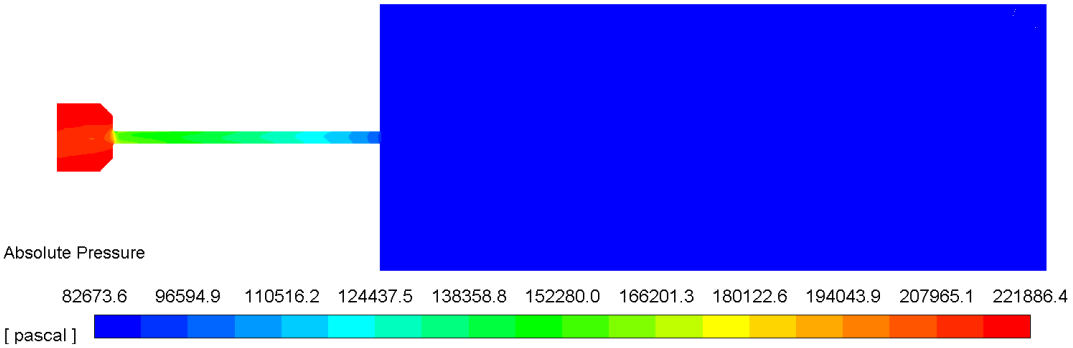

Figure E-7. Absolute Pressure Contours for Test-7 on Plane-2

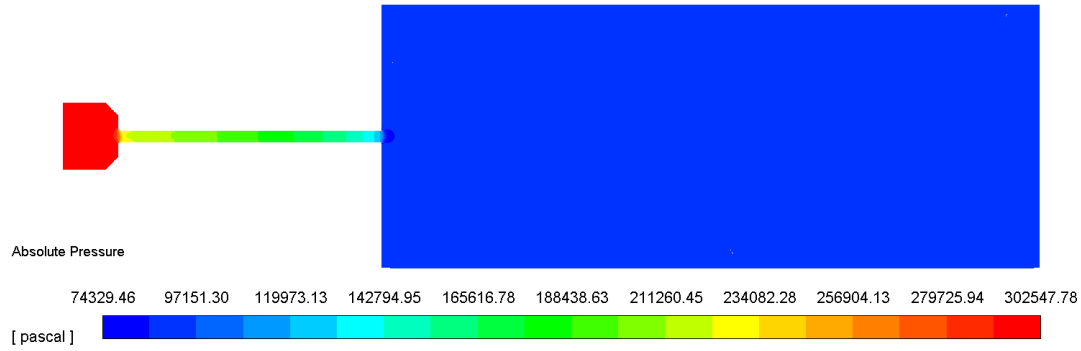

Figure E-8. Absolute Pressure Contours for Test-8 on Plane-2

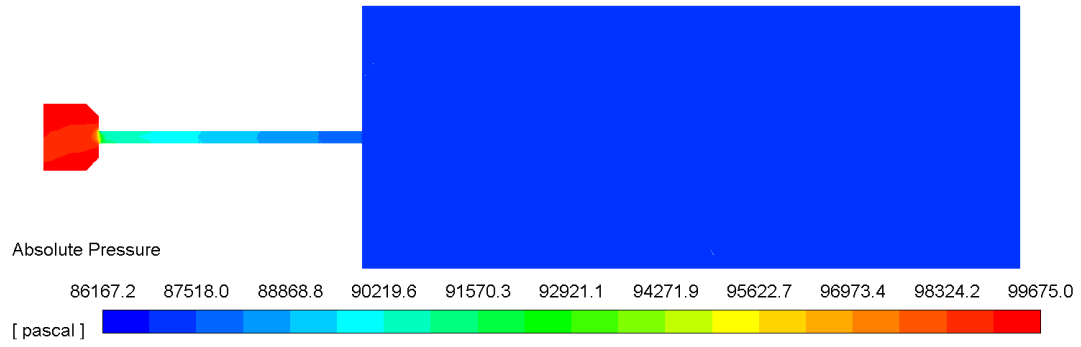

Figure E-9. Absolute Pressure Contours for Test-9 on Plane-2

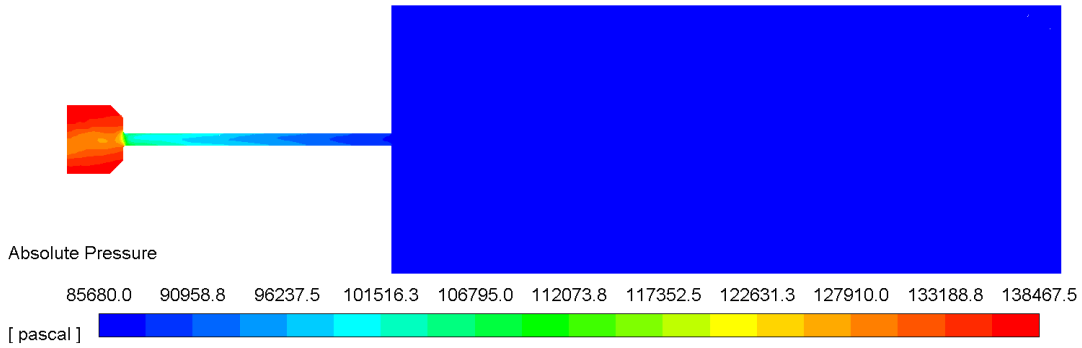

Figure E-10. Absolute Pressure Contours for Test-10 on Plane-2

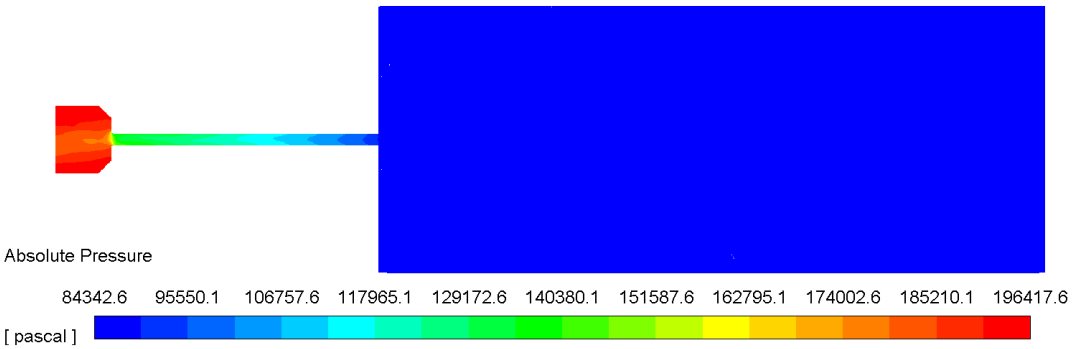

Figure E-11. Absolute Pressure Contours for Test-11 on Plane-2

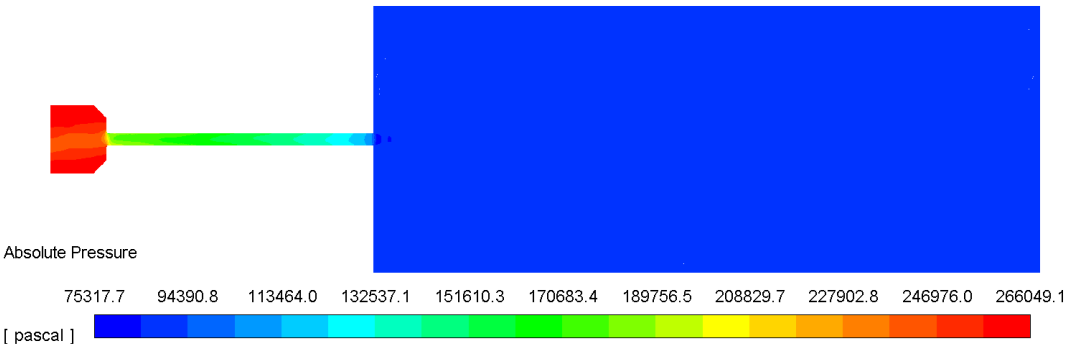

Figure E-12. Absolute Pressure Contours for Test-12 on Plane-2

F. O_2 Mass Fraction Contours

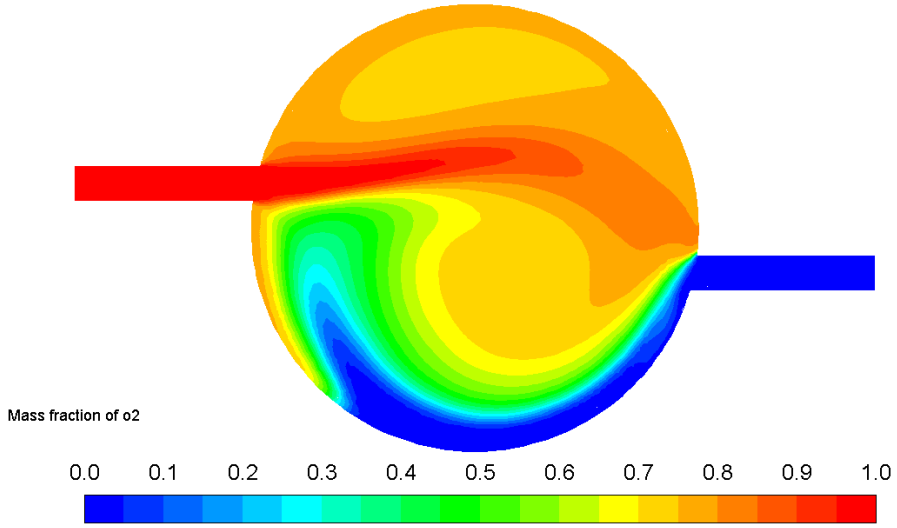

Figure F-1. O_2 Mass Fraction Contours for Test-1 on Plane-2

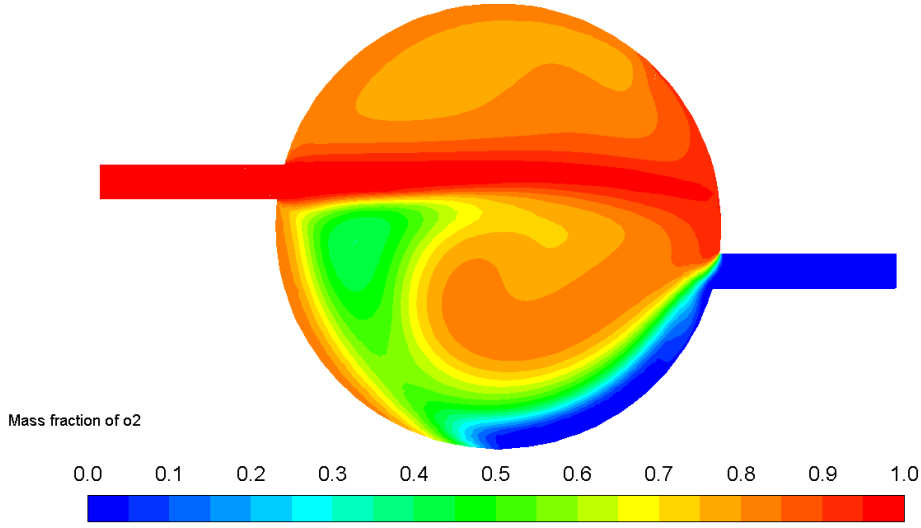

Figure F-2. O_2 Mass Fraction Contours for Test-2 on Plane-2

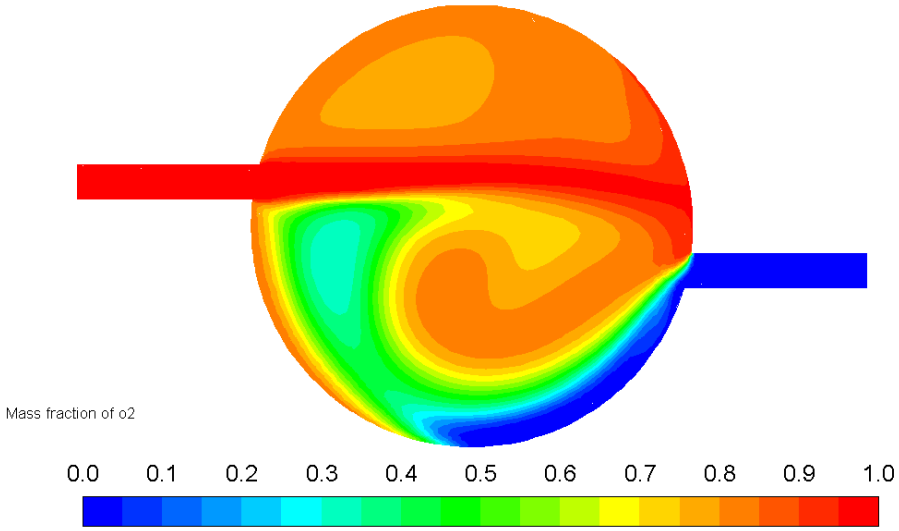

Figure F-3. O_2 Mass Fraction Contours for Test-3 on Plane-2

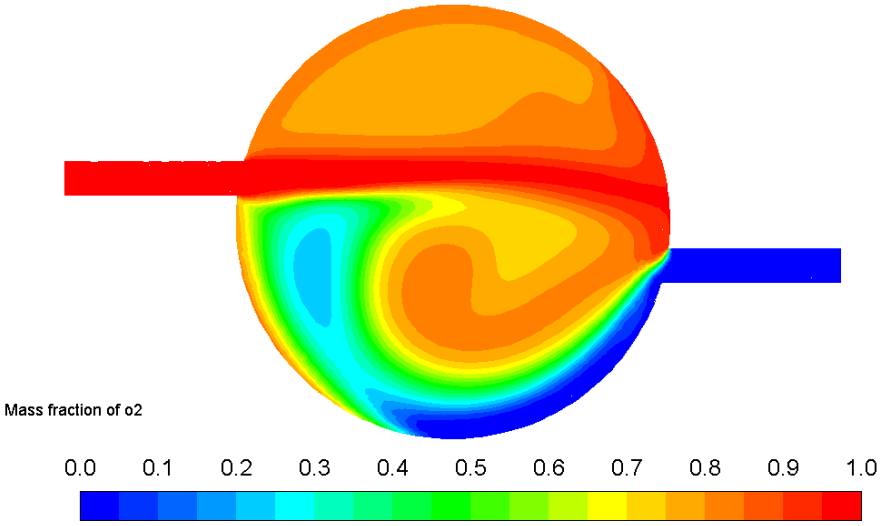

Figure F-4. O_2 Mass Fraction Contours for Test-4 on Plane-2

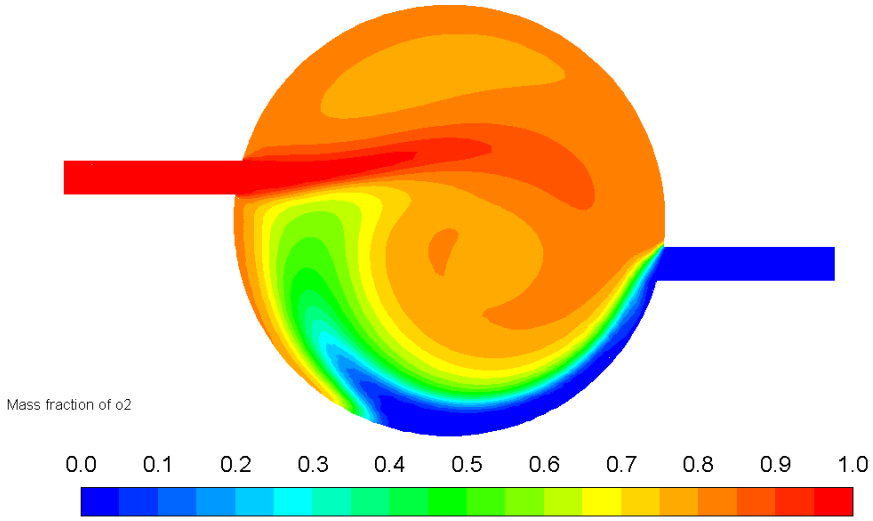

Figure F-5. O_2 Mass Fraction Contours for Test-5 on Plane-2

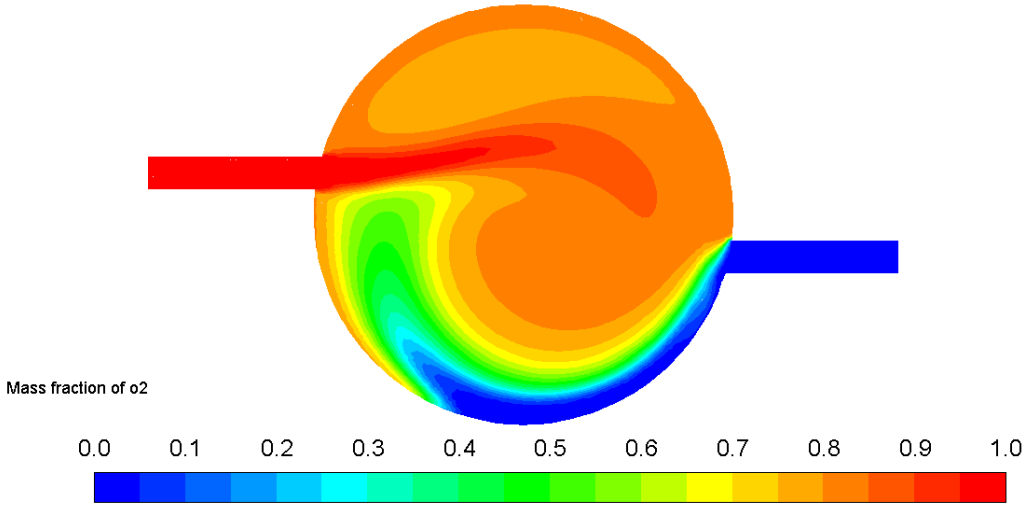

Figure F-6. O_2 Mass Fraction Contours for Test-6 on Plane-2

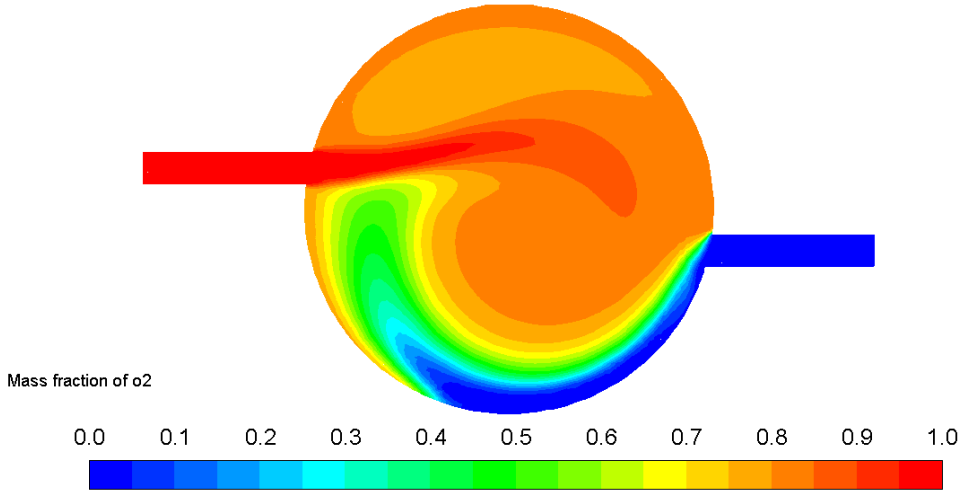

Figure F-7. O_2 Mass Fraction Contours for Test-7 on Plane-2

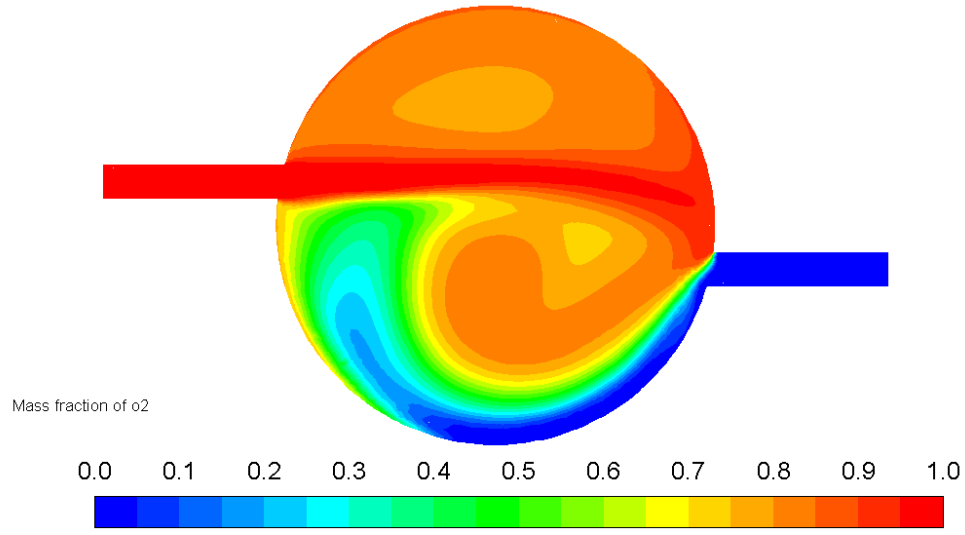

Figure F-8. O_2 Mass Fraction Contours for Test-8 on Plane-2

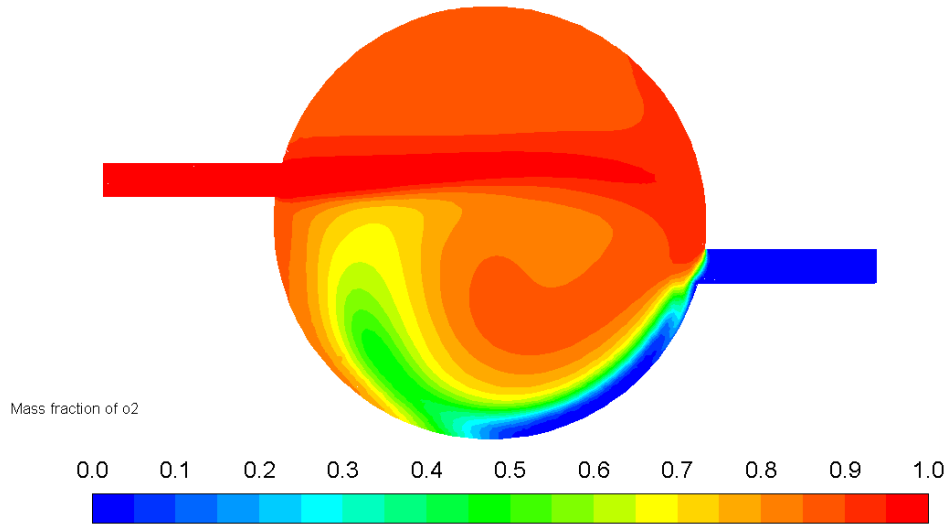

Figure F-9. O_2 Mass Fraction Contours for Test-9 on Plane-2

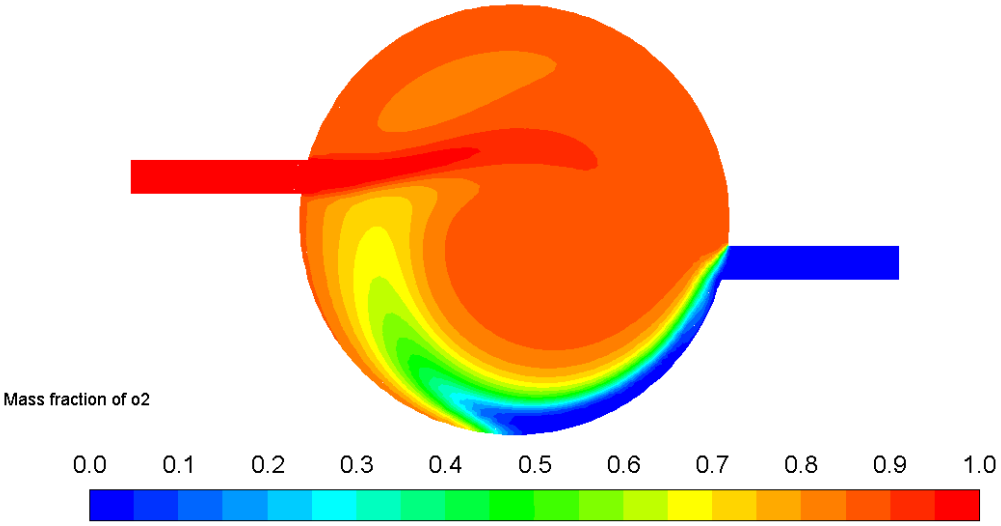

Figure F-10. O_2 Mass Fraction Contours for Test-10 on Plane-2

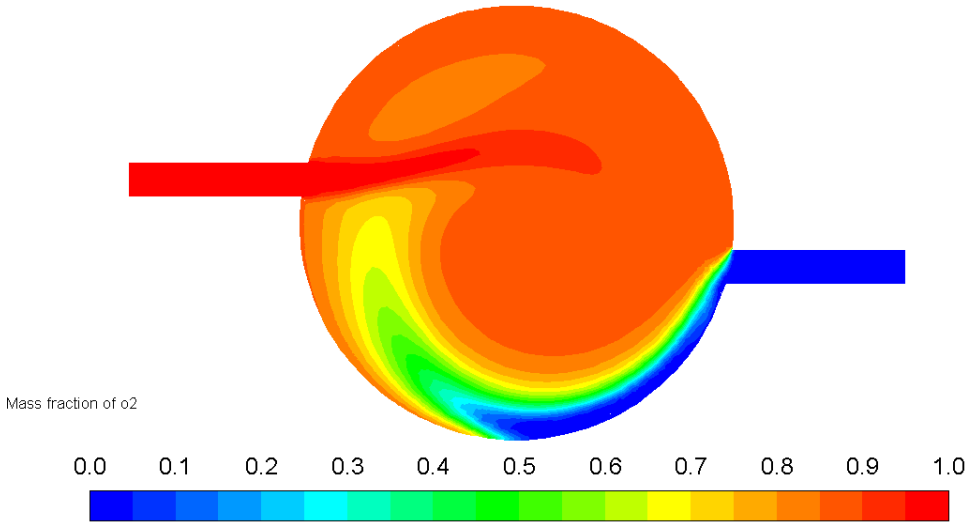

Figure F-11. O_2 Mass Fraction Contours for Test-11 on Plane-2

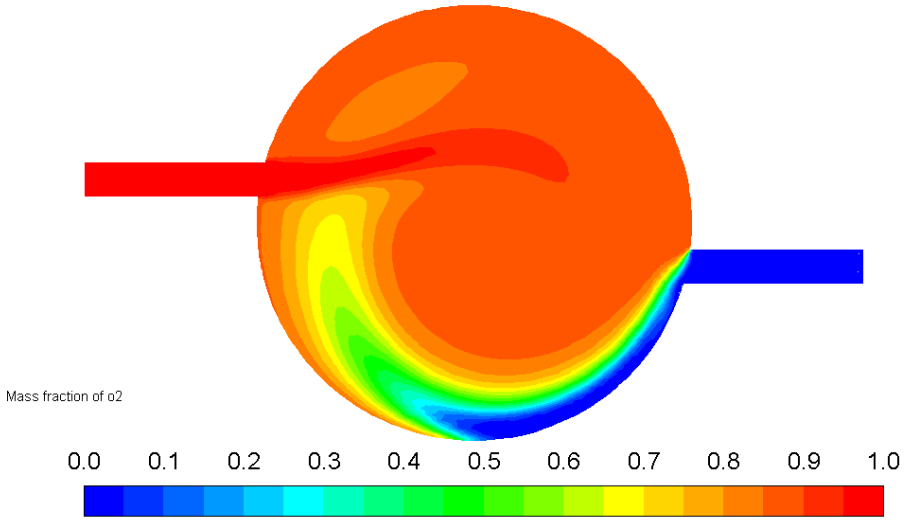

Figure F-12. O_2 Mass Fraction Contours for Test-12 on Plane-2

G. H_2 Mass Fraction Contours

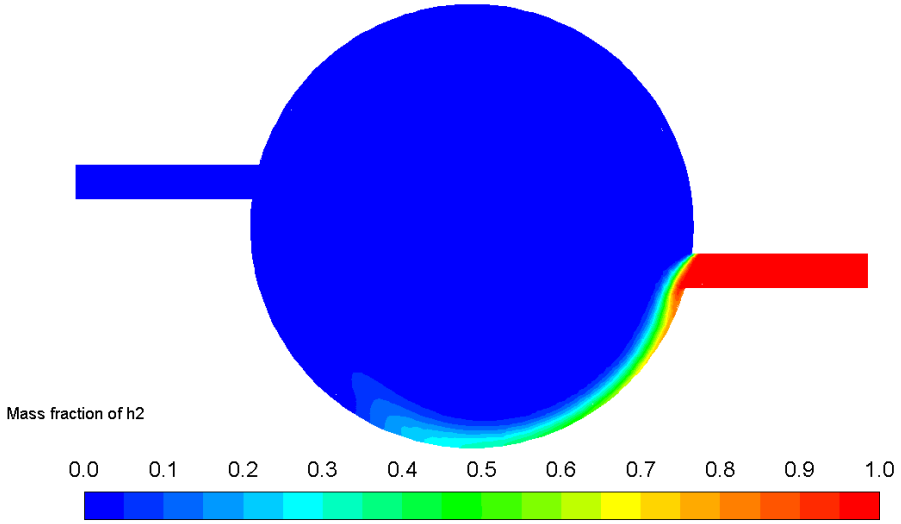

Figure G-1. H_2 Mass Fraction Contours for Test-1 on Plane-2

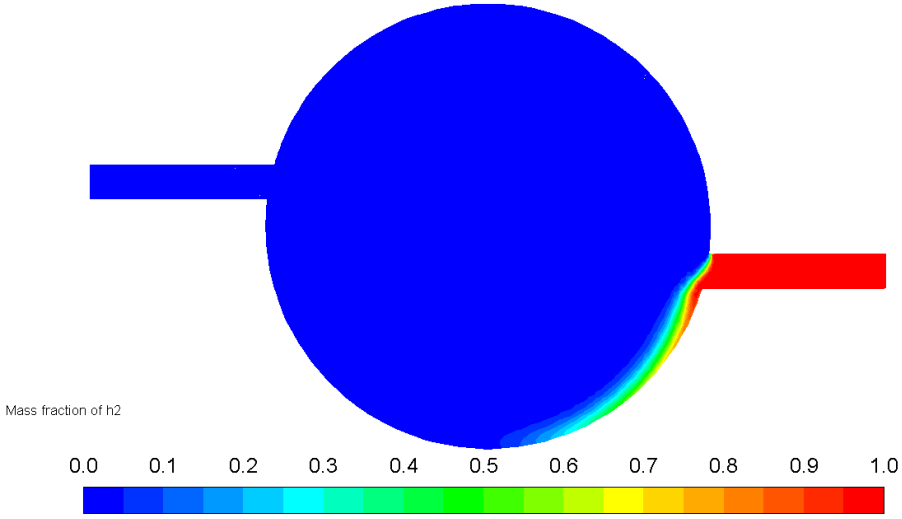

Figure G-2. H_2 Mass Fraction Contours for Test-2 on Plane-2

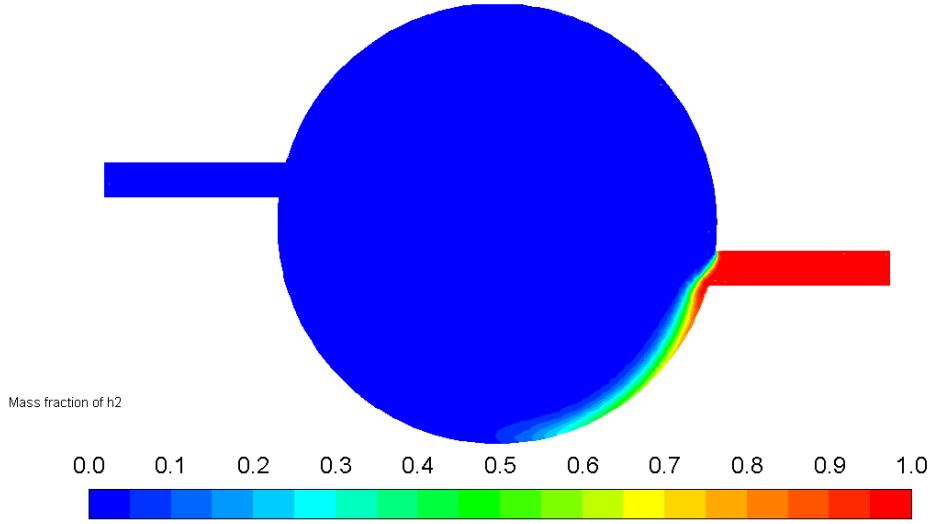

Figure G-3. H_2 Mass Fraction Contours for Test-3 on Plane-2

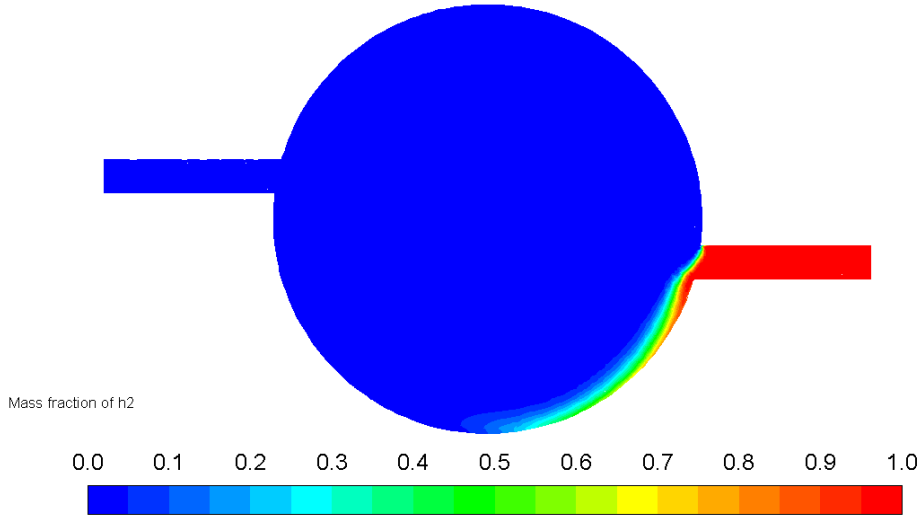

Figure G-4. H_2 Mass Fraction Contours for Test-4 on Plane-2

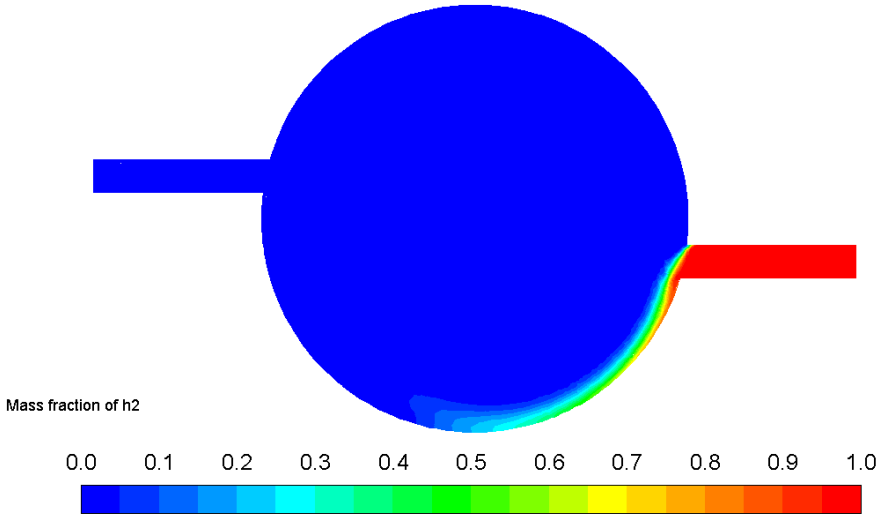

Figure G-5. H_2 Mass Fraction Contours for Test-5 on Plane-2

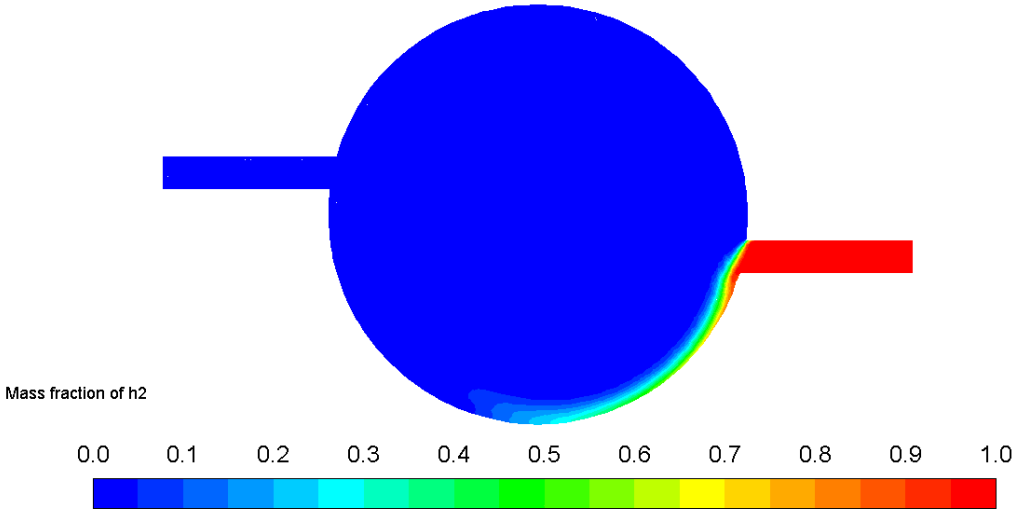

Figure G-6. H_2 Mass Fraction Contours for Test-6 on Plane-2

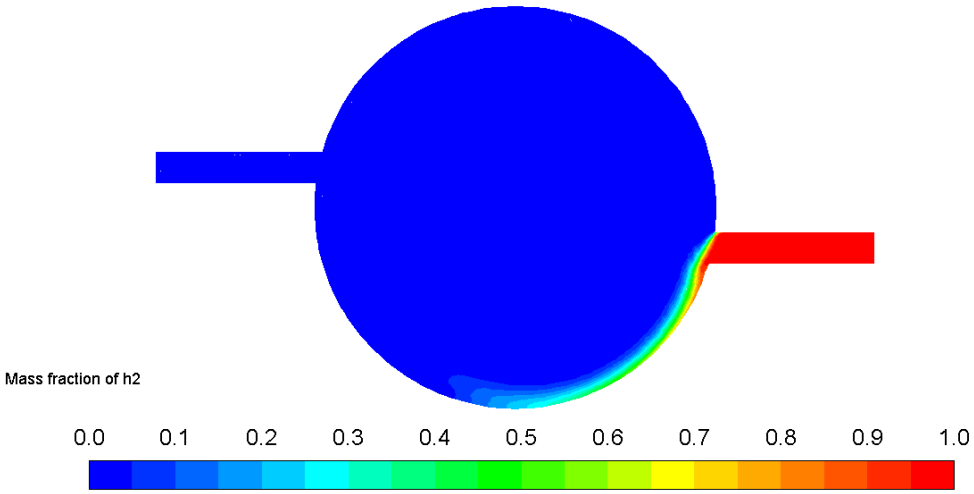

Figure G-7. H_2 Mass Fraction Contours for Test-7 on Plane-2

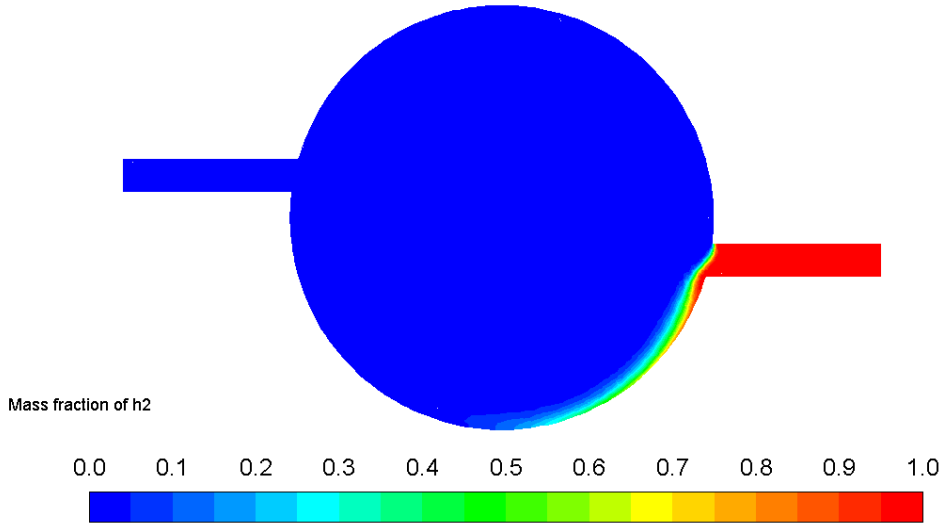

Figure G-8. H_2 Mass Fraction Contours for Test-8 on Plane-2

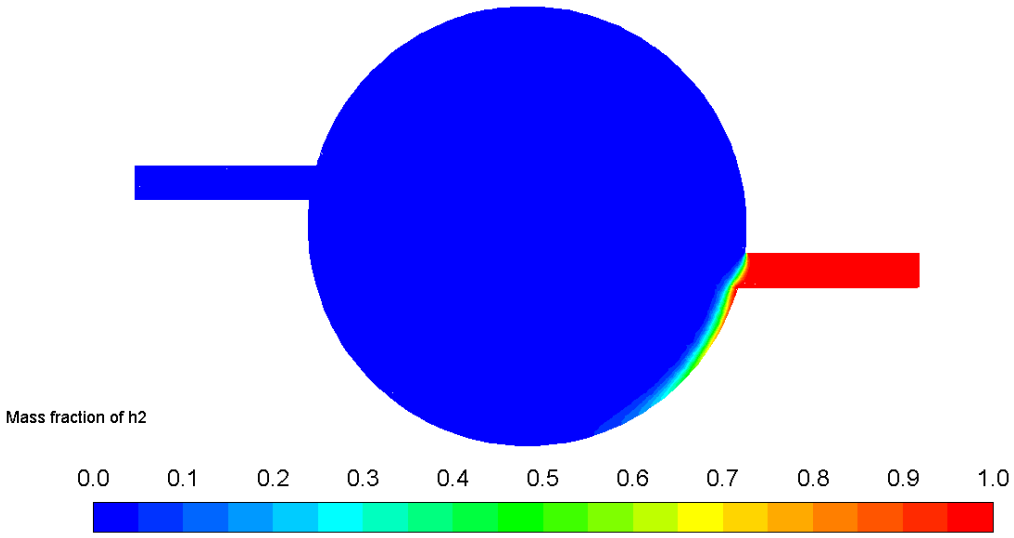

Figure G-9. H_2 Mass Fraction Contours for Test-9 on Plane-2

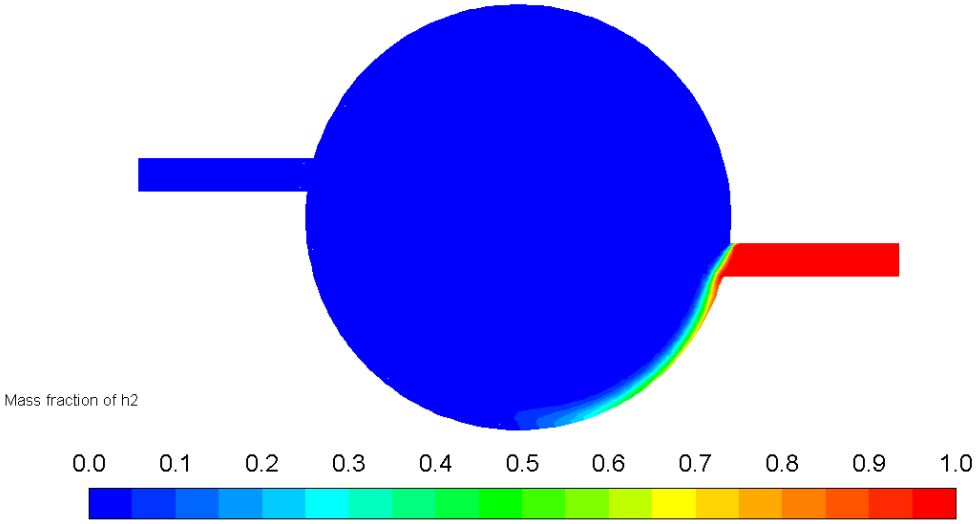

Figure G-10. H_2 Mass Fraction Contours for Test-10 on Plane-2

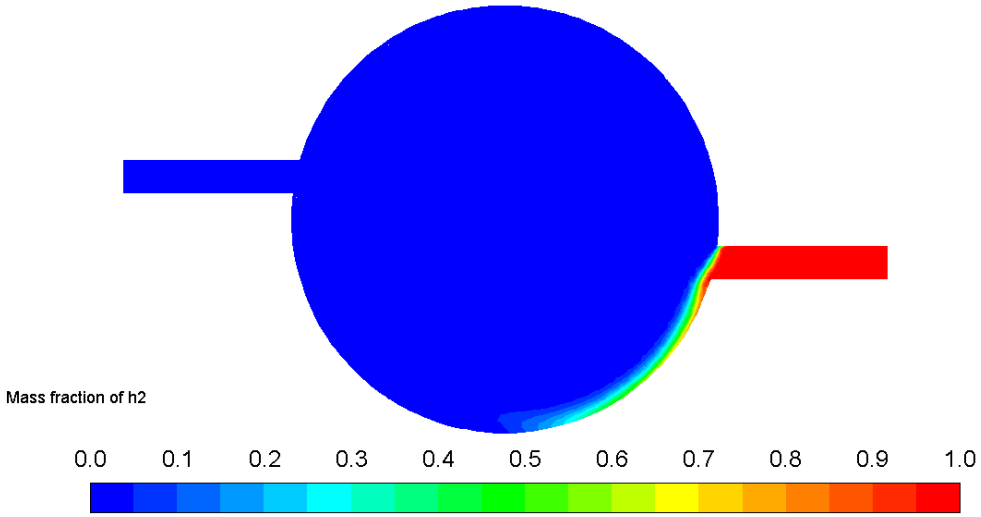

Figure G-11. H_2 Mass Fraction Contours for Test-11 on Plane-2

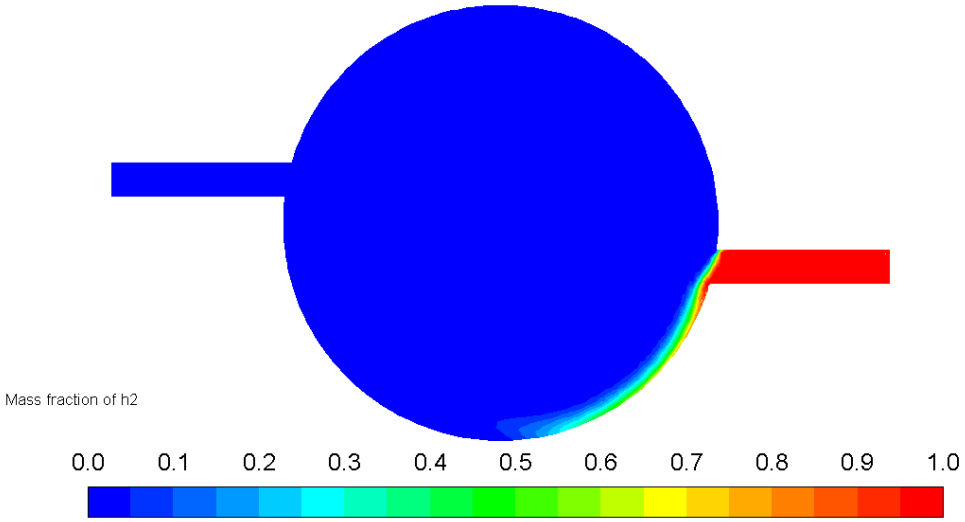

Figure G-12. H_2 Mass Fraction Contours for Test-12 on Plane-2

H. OH Mass Fraction Contours

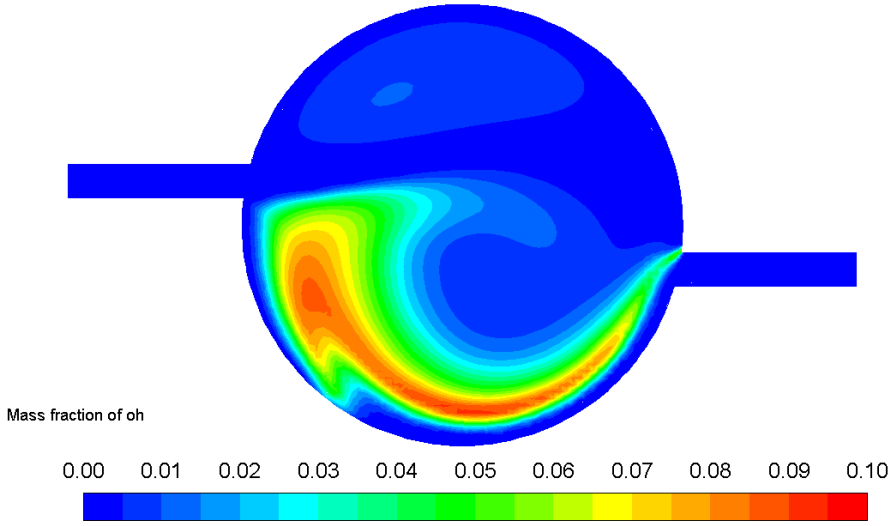

Figure H-1. OH Mass Fraction Contours for Test-1 on Plane-2

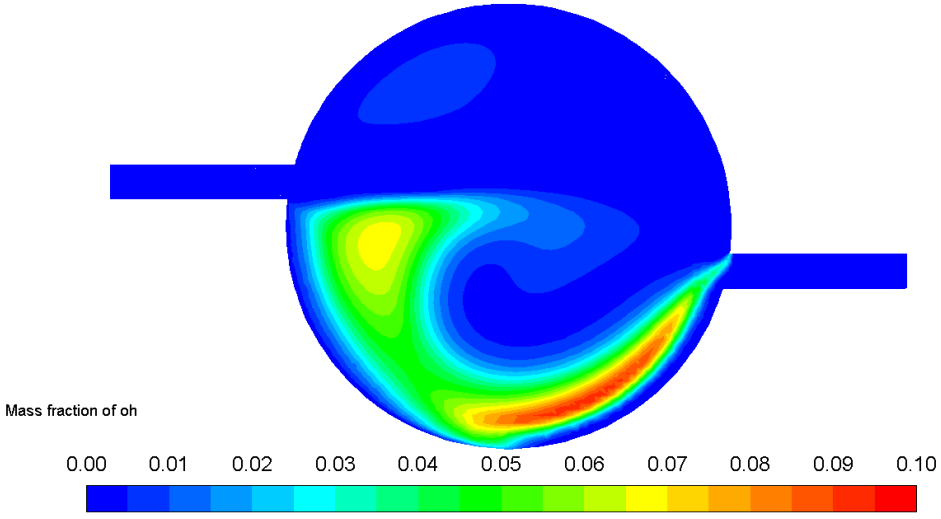

Figure H-2. OH Mass Fraction Contours for Test-2 on Plane-2

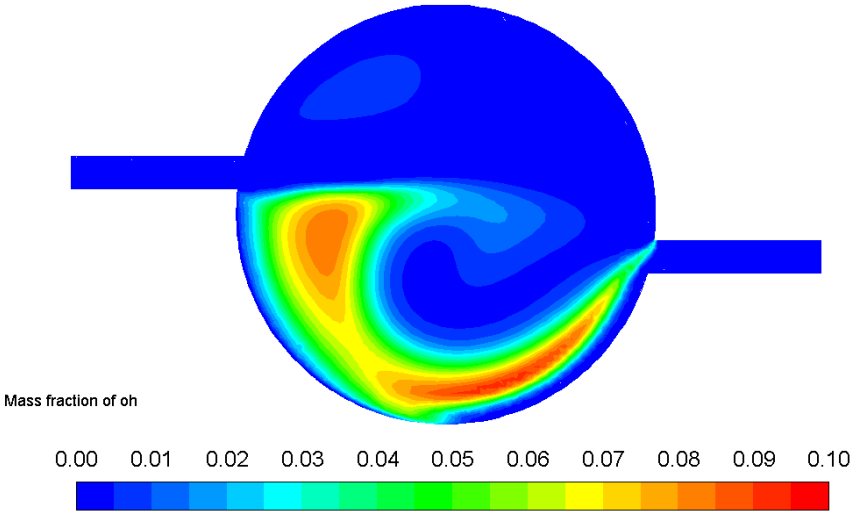

Figure H-3. OH Mass Fraction Contours for Test-3 on Plane-2

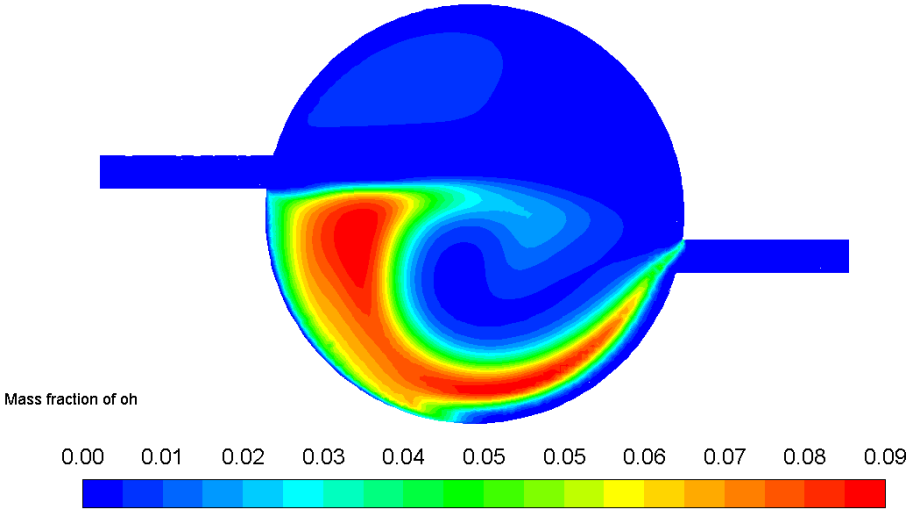

Figure H-4. OH Mass Fraction Contours for Test-4 on Plane-2

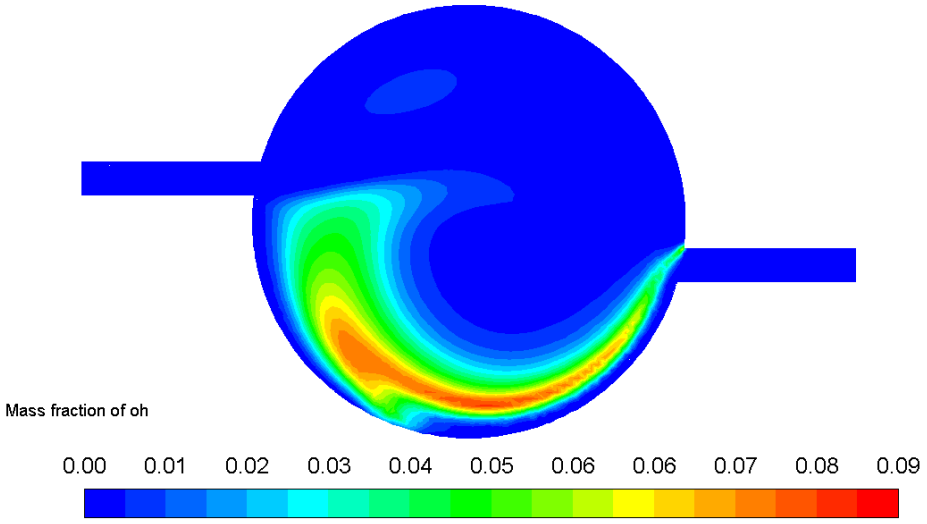

Figure H-5. OH Mass Fraction Contours for Test-5 on Plane-2

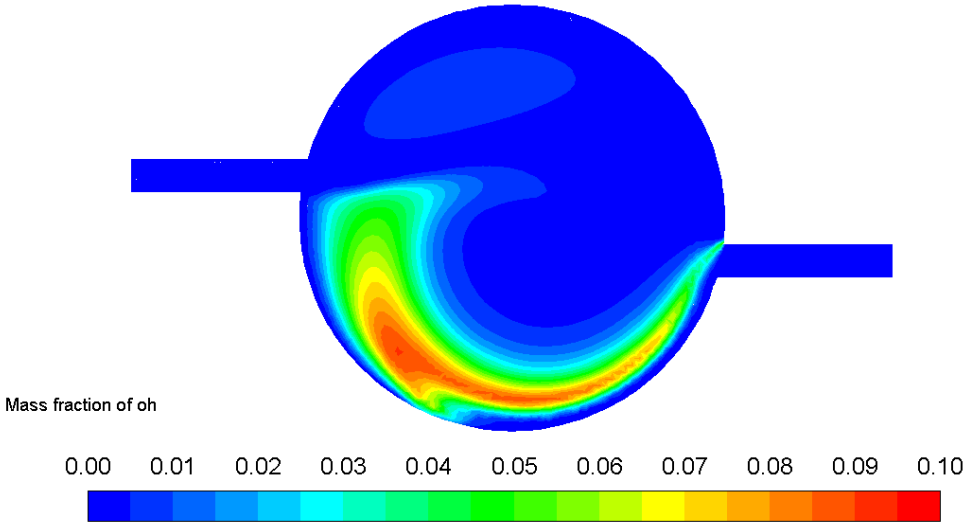

Figure H-6. OH Mass Fraction Contours for Test-6 on Plane-2

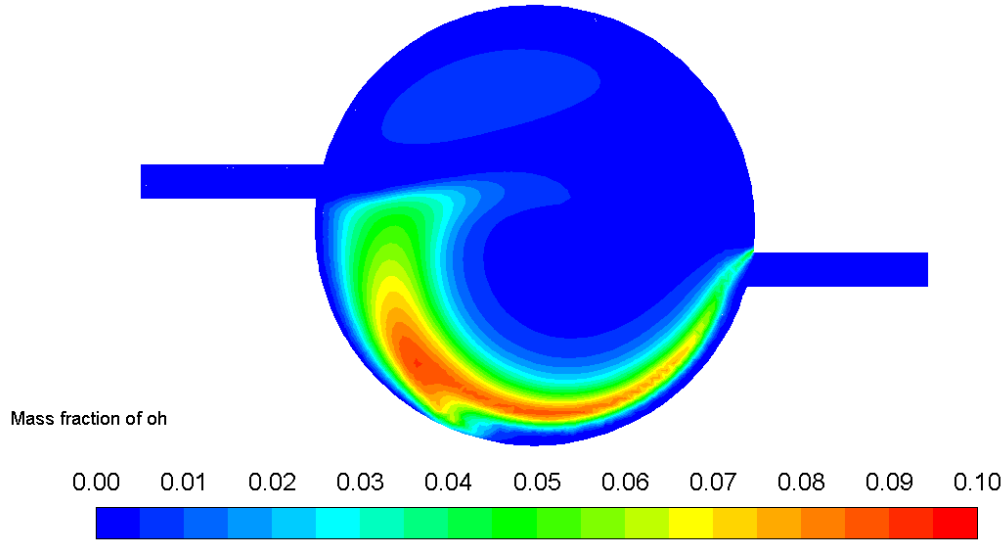

Figure H-7. OH Mass Fraction Contours for Test-7 on Plane-2

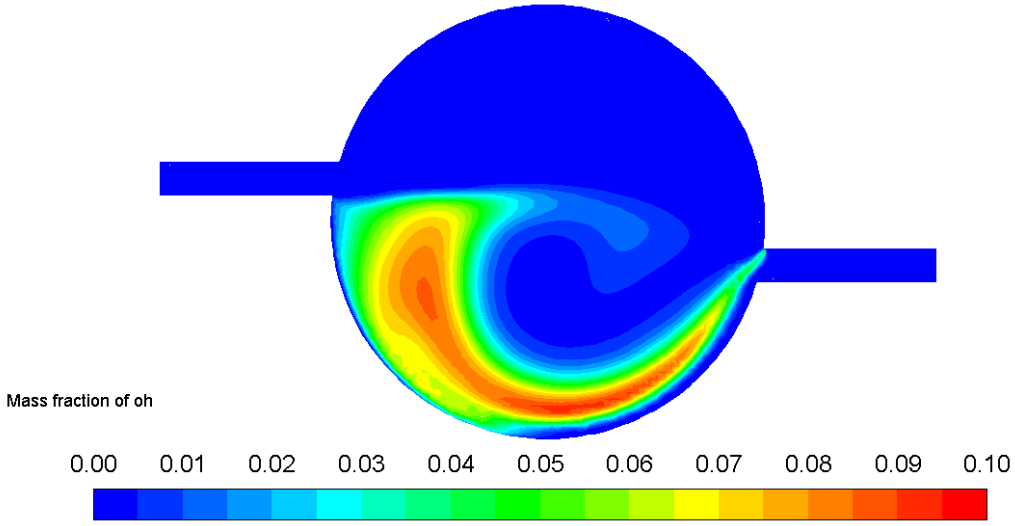

Figure H-8. OH Mass Fraction Contours for Test-8 on Plane-2

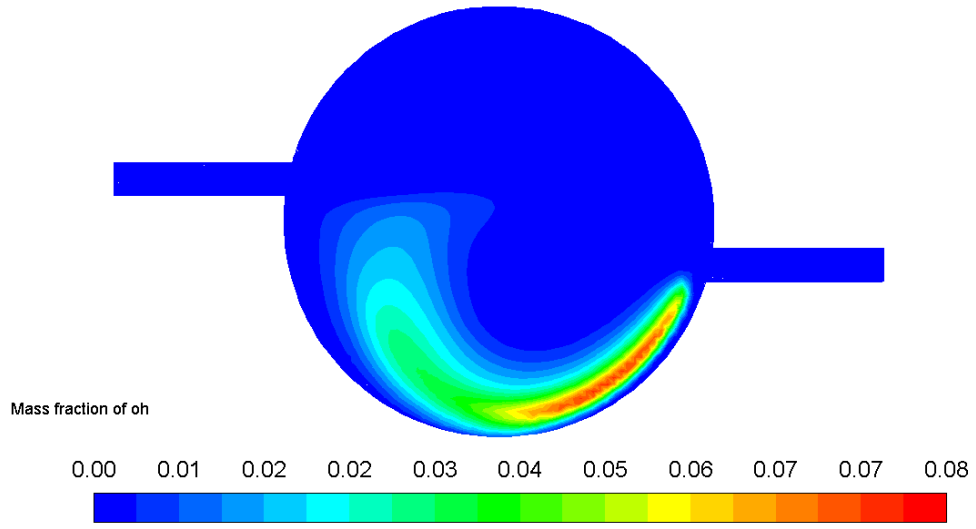

Figure H-9. OH Mass Fraction Contours for Test-9 on Plane-2

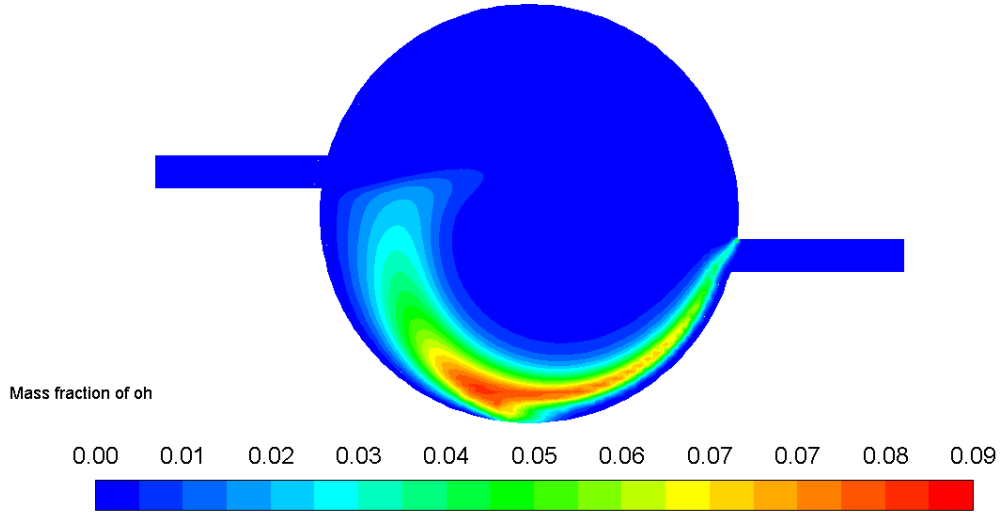

Figure H-10. OH Mass Fraction Contours for Test-10 on Plane-2

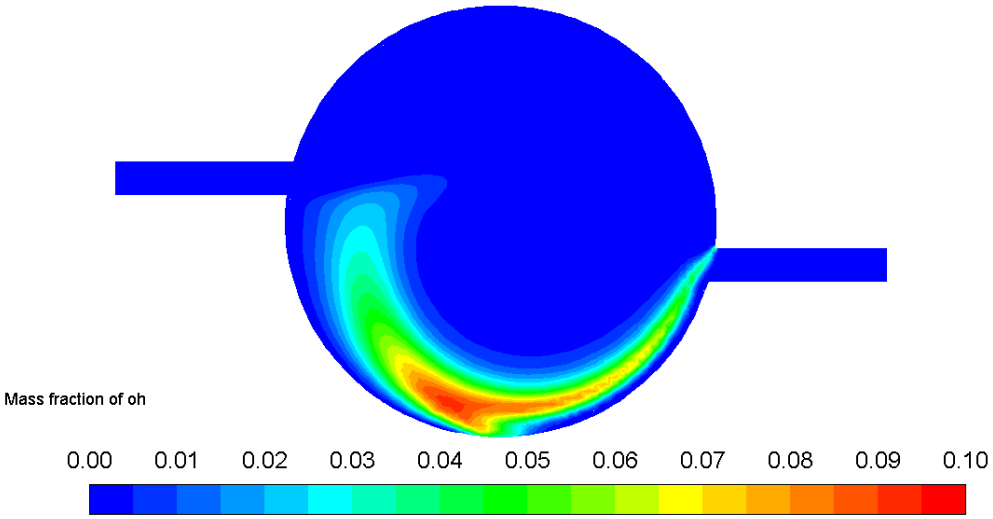

Figure H-11. OH Mass Fraction Contours for Test-11 on Plane-2

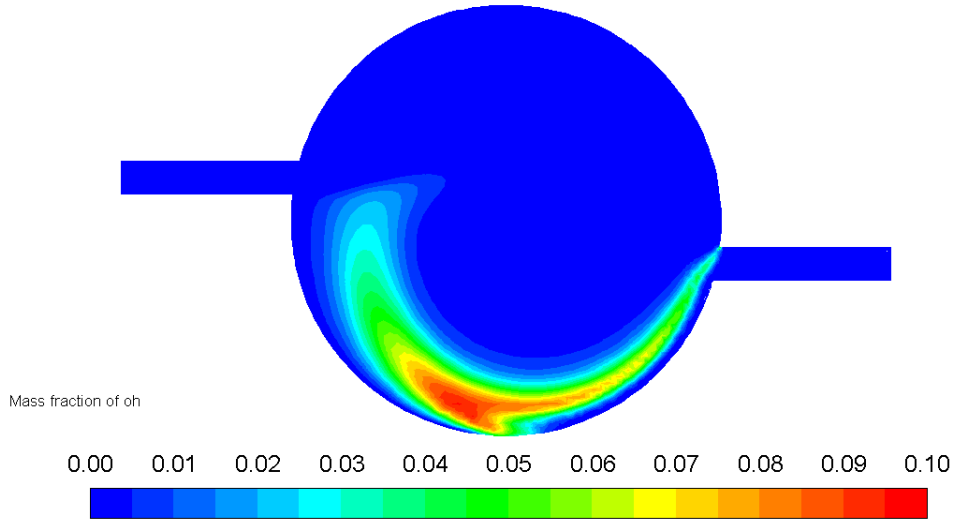

Figure H-12. OH Mass Fraction Contours for Test-12 on Plane-2

I. H_2O Mass Fraction Contours

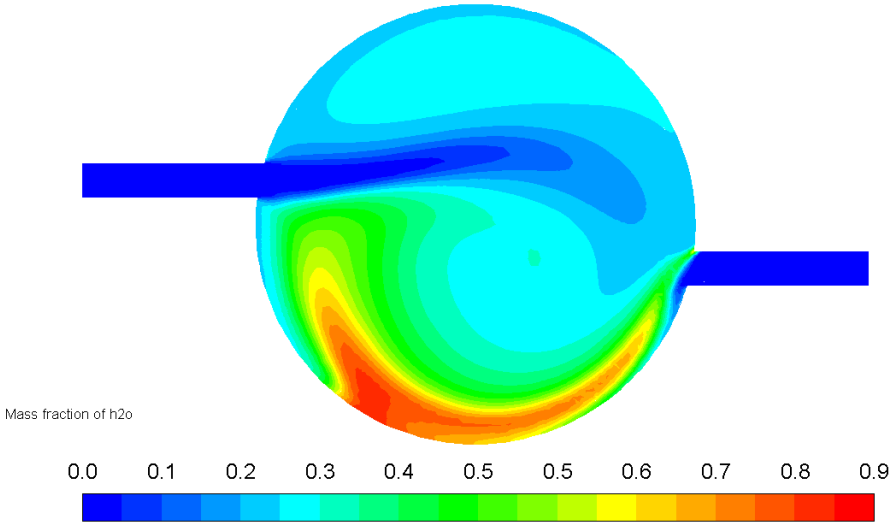

Figure I-1. H_2O Mass Fraction Contours for Test-1 on Plane-2

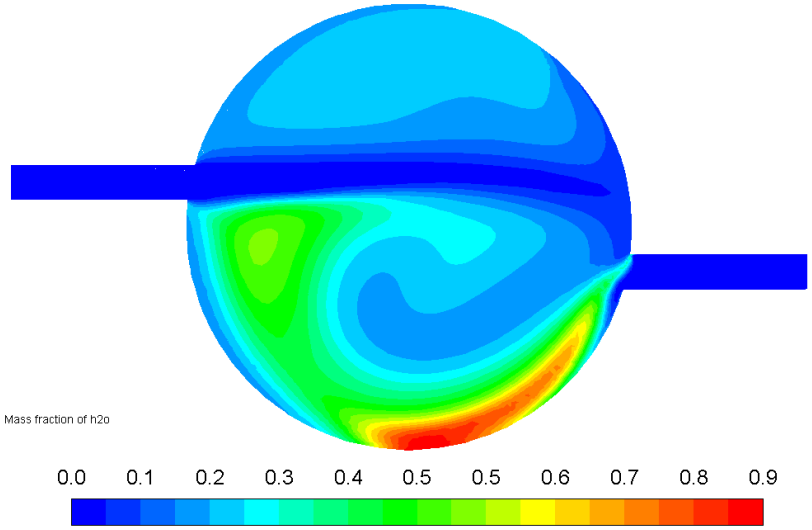

Figure I-2. H_2O Mass Fraction Contours for Test-2 on Plane-2

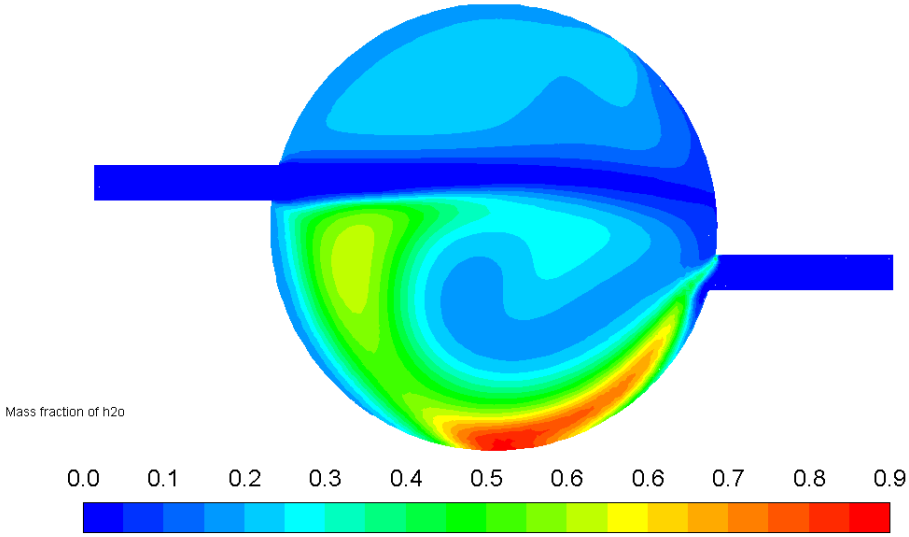

Figure I-3. H_2O Mass Fraction Contours for Test-3 on Plane-2

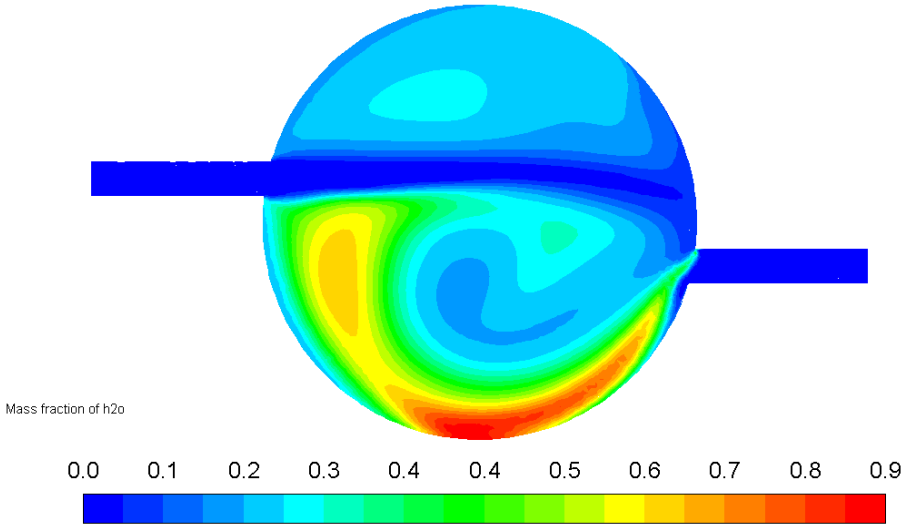

Figure I-4. H_2O Mass Fraction Contours for Test-4 on Plane-2

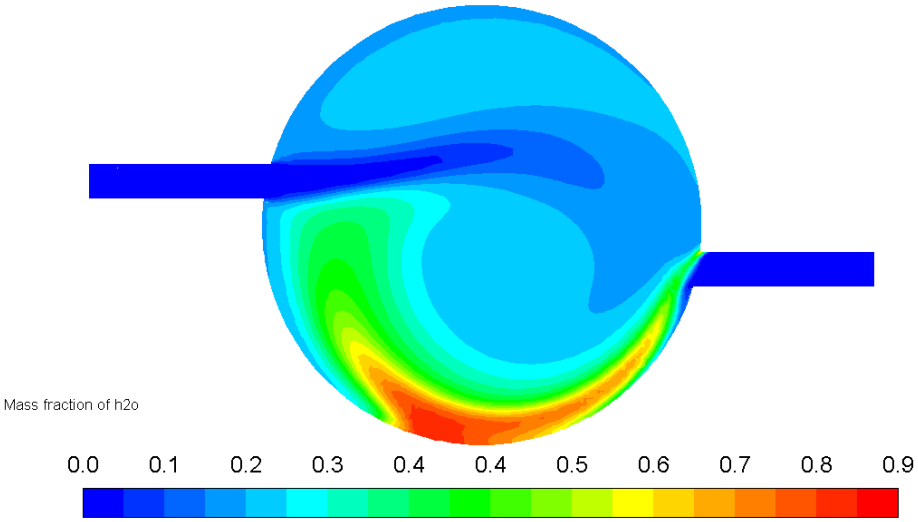

Figure I-5. H_2O Mass Fraction Contours for Test-5 on Plane-2

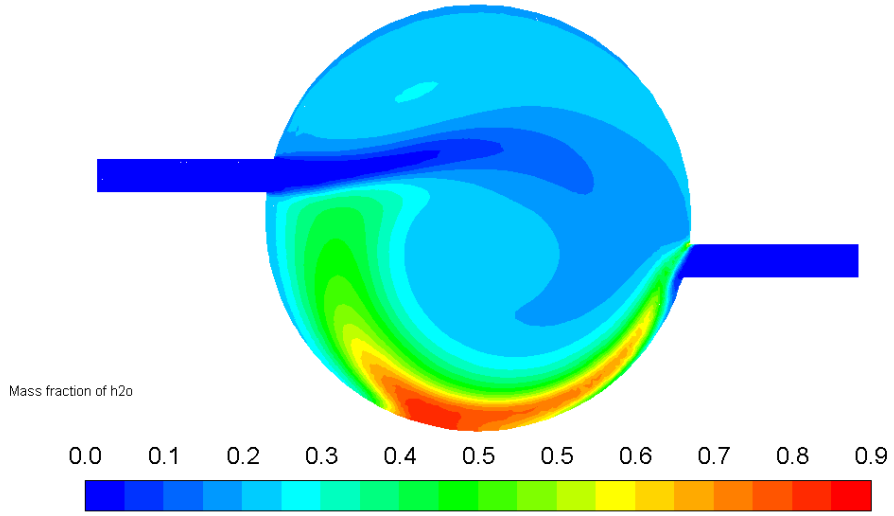

Figure I-6. H_2O Mass Fraction Contours for Test-6 on Plane-2

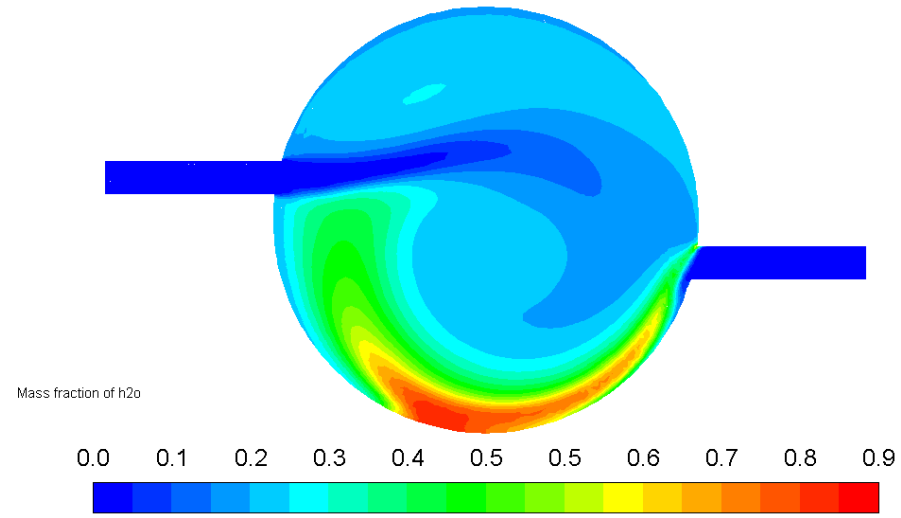

Figure I-7. H_2O Mass Fraction Contours for Test-7 on Plane-2

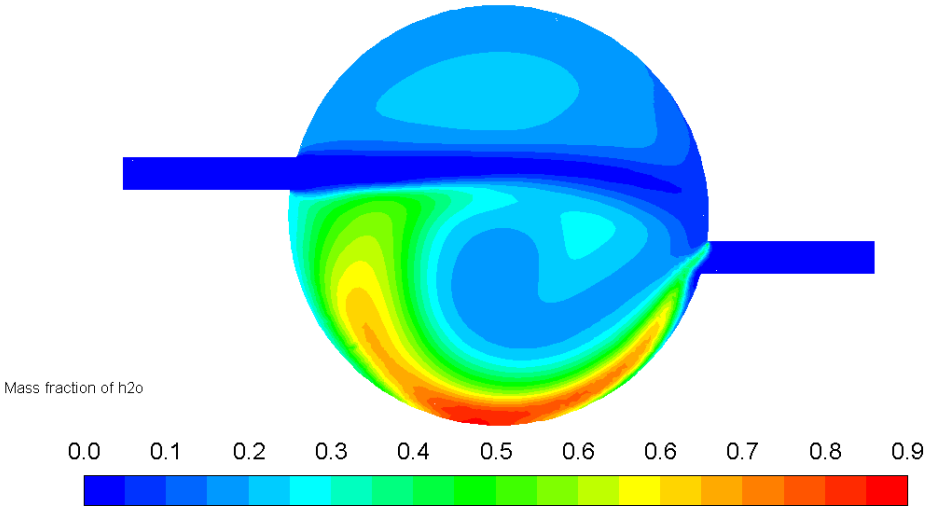

Figure I-8. H_2O Mass Fraction Contours for Test-8 on Plane-2

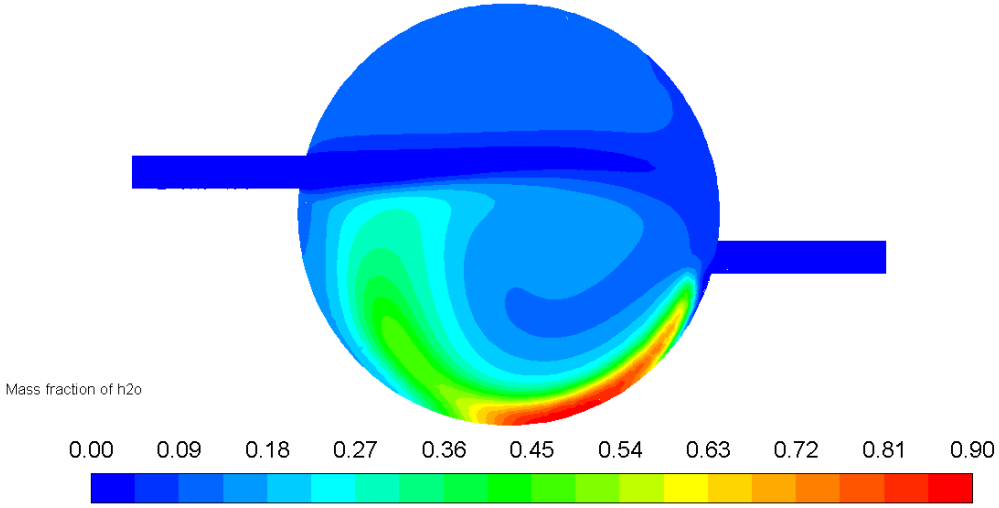

Figure I-9. H_2O Mass Fraction Contours for Test-9 on Plane-2

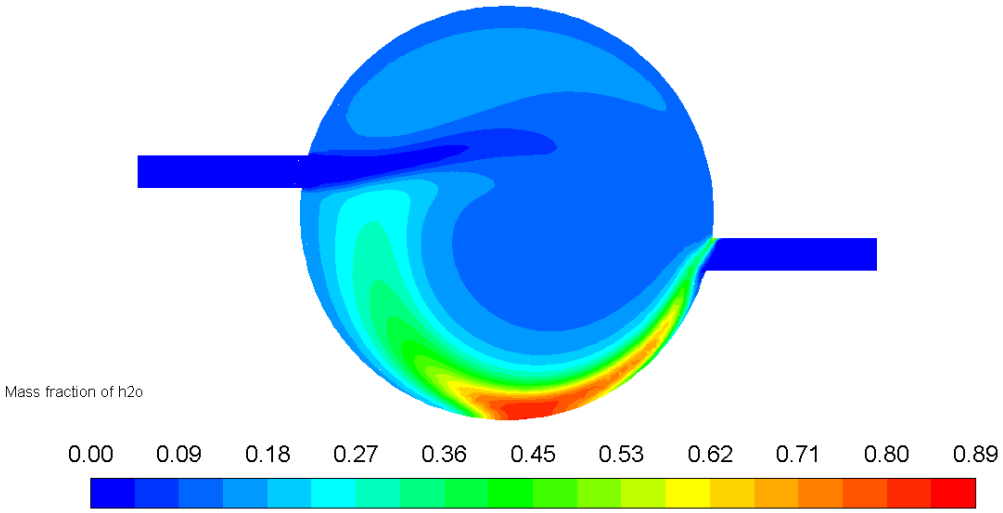

Figure I-10. H_2O Mass Fraction Contours for Test-10 on Plane-2

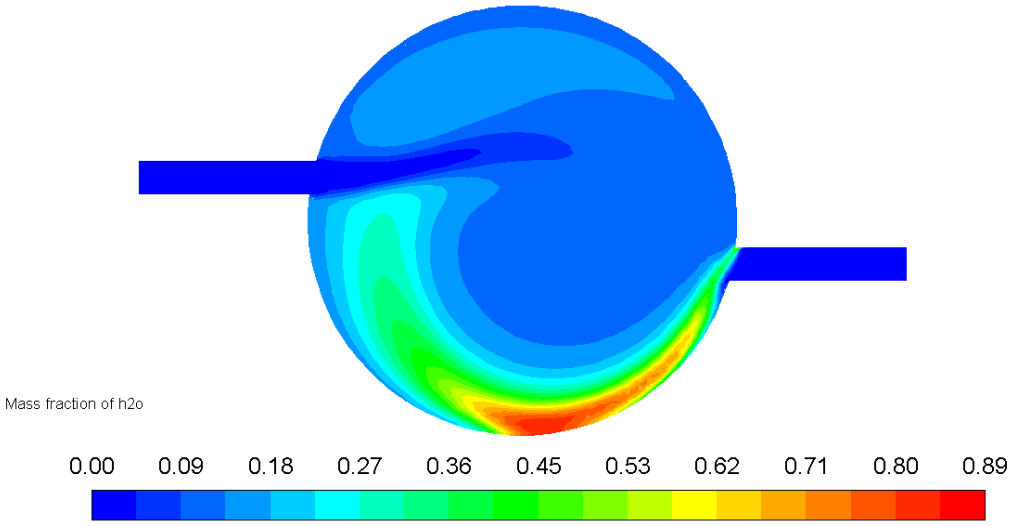

Figure I-11. H_2O Mass Fraction Contours for Test-11 on Plane-2

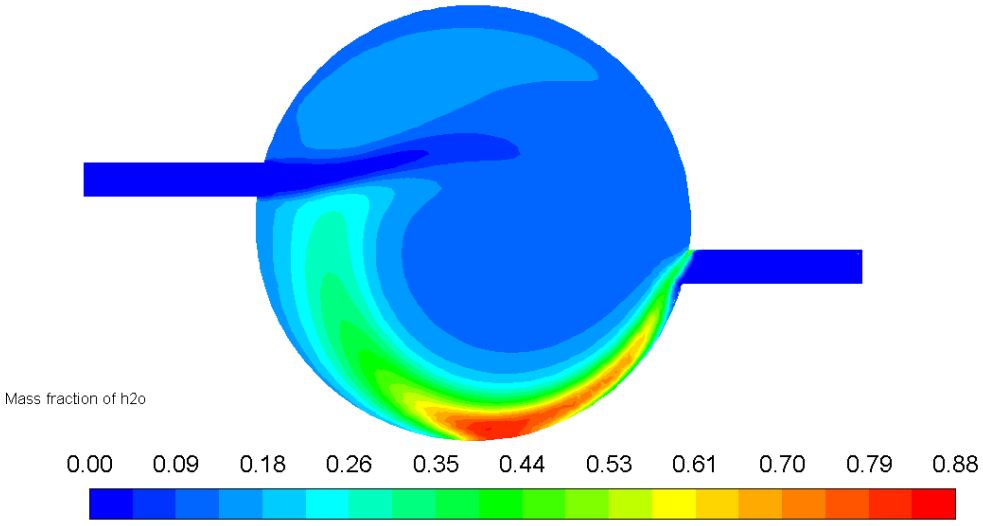

Figure I-12. H_2O Mass Fraction Contours for Test-12 on Plane-2

J. Consecutive Frames from Test-1

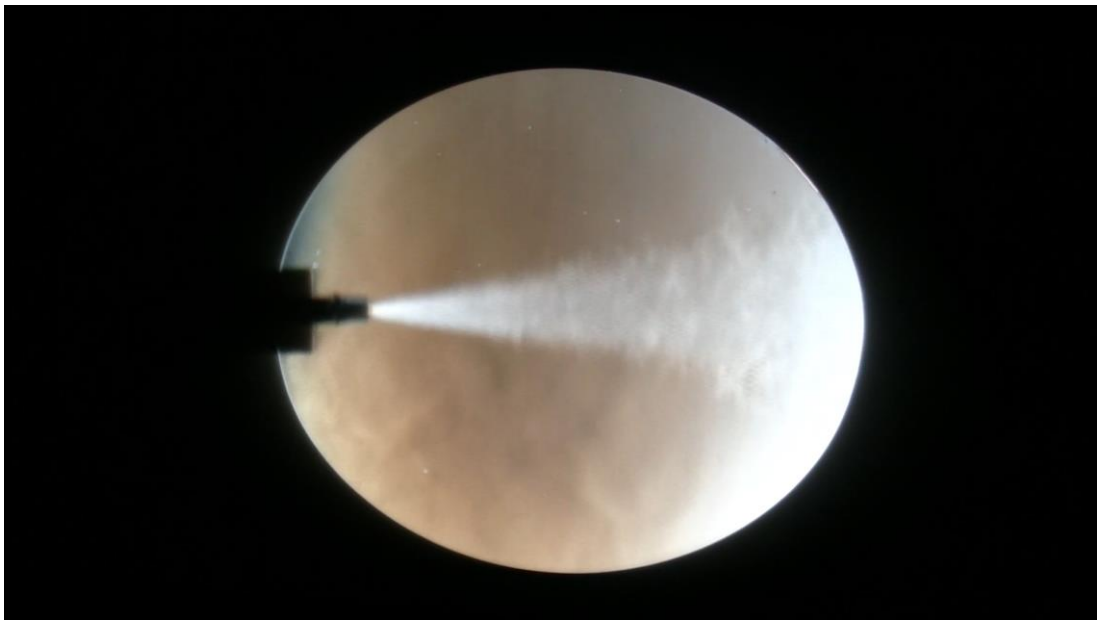

(a)

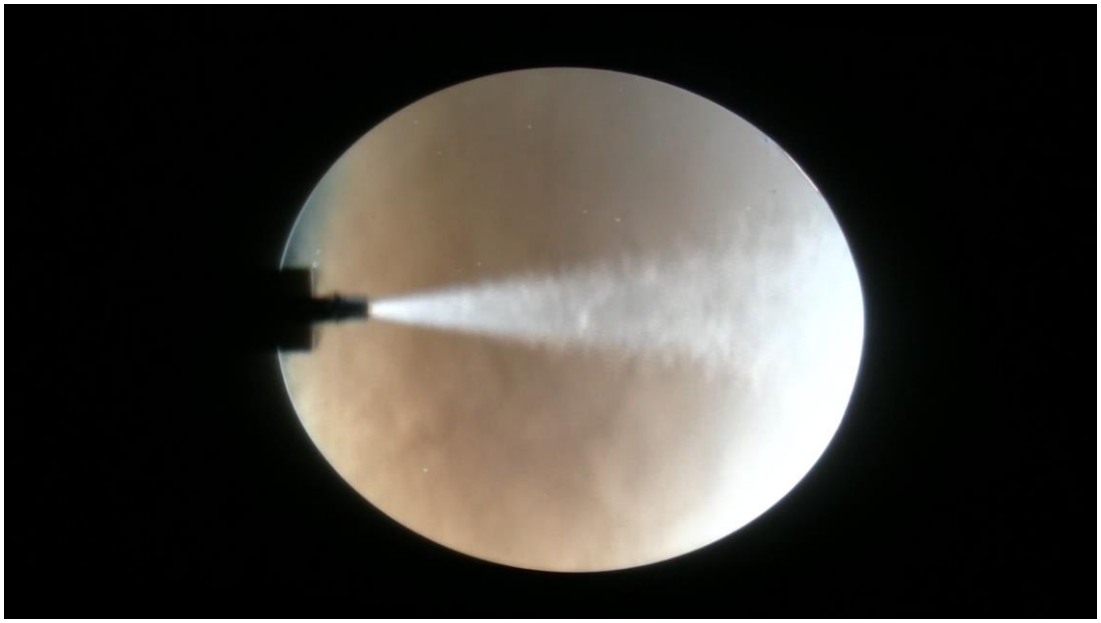

(b)

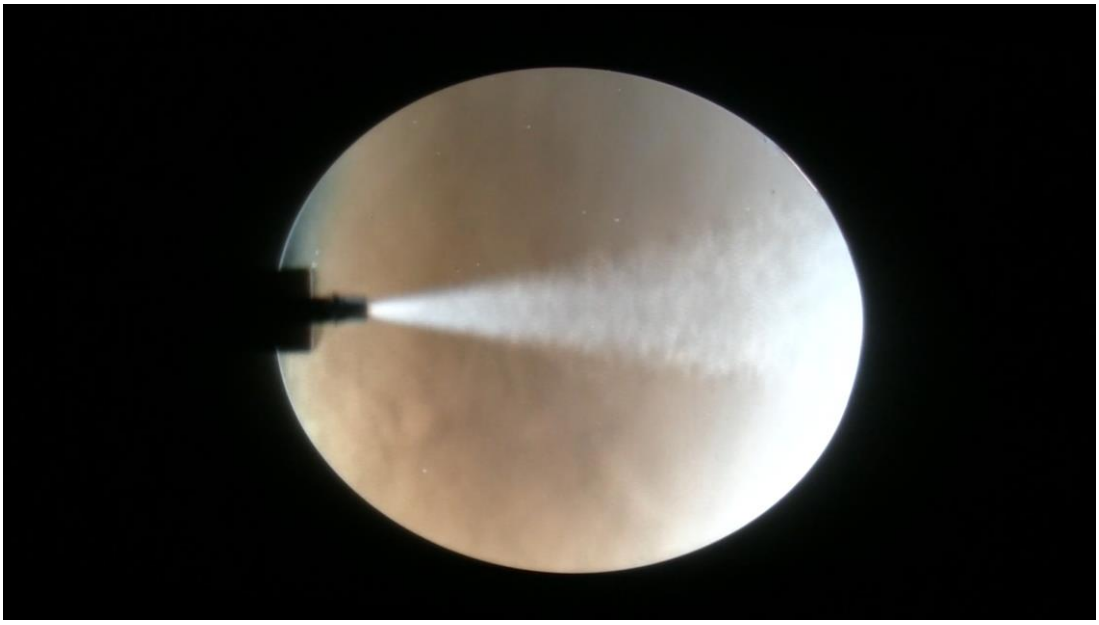

(c)

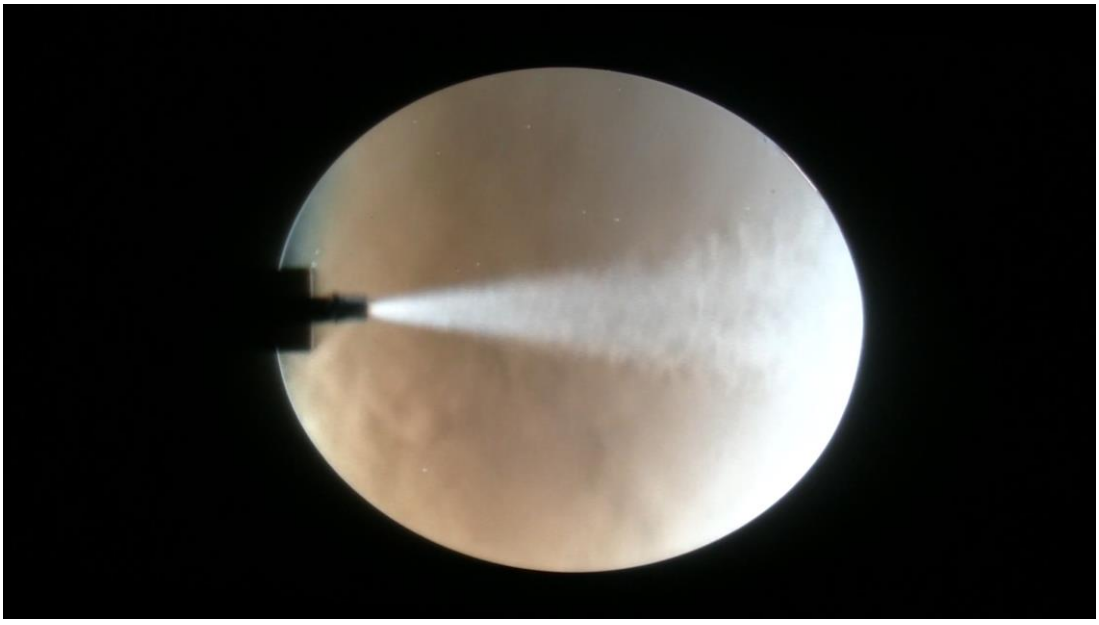

(d)

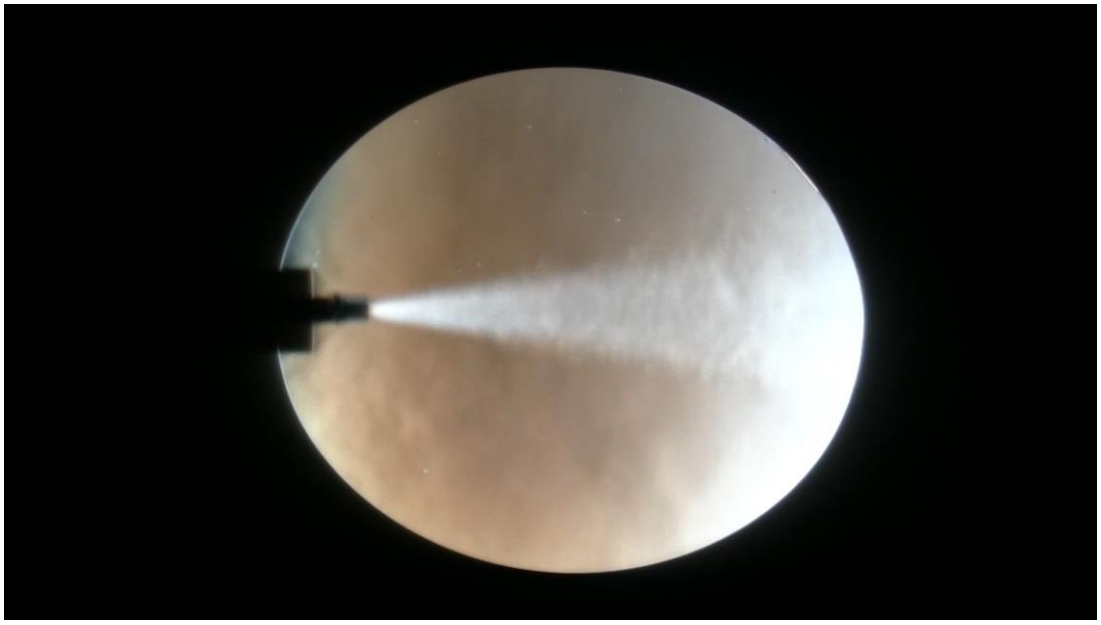

(e)

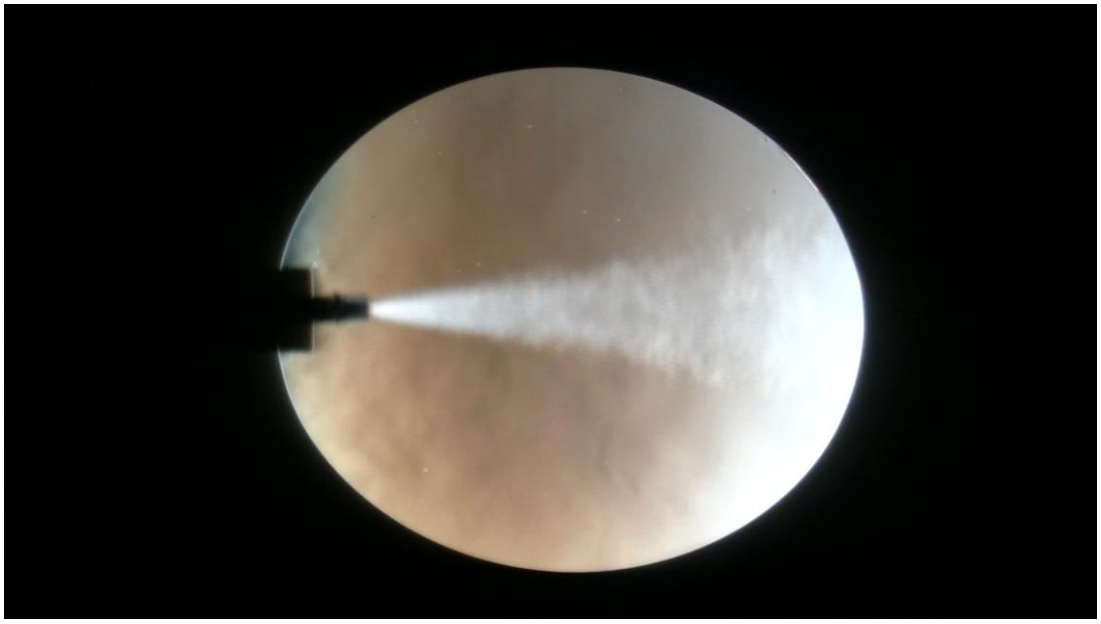

(f)

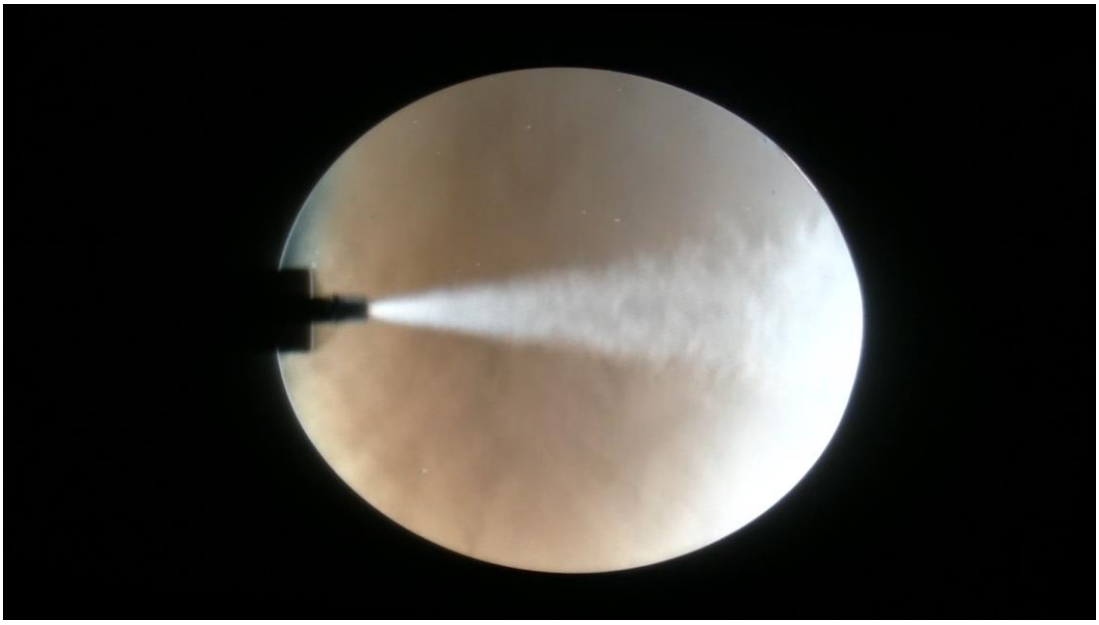

(g)

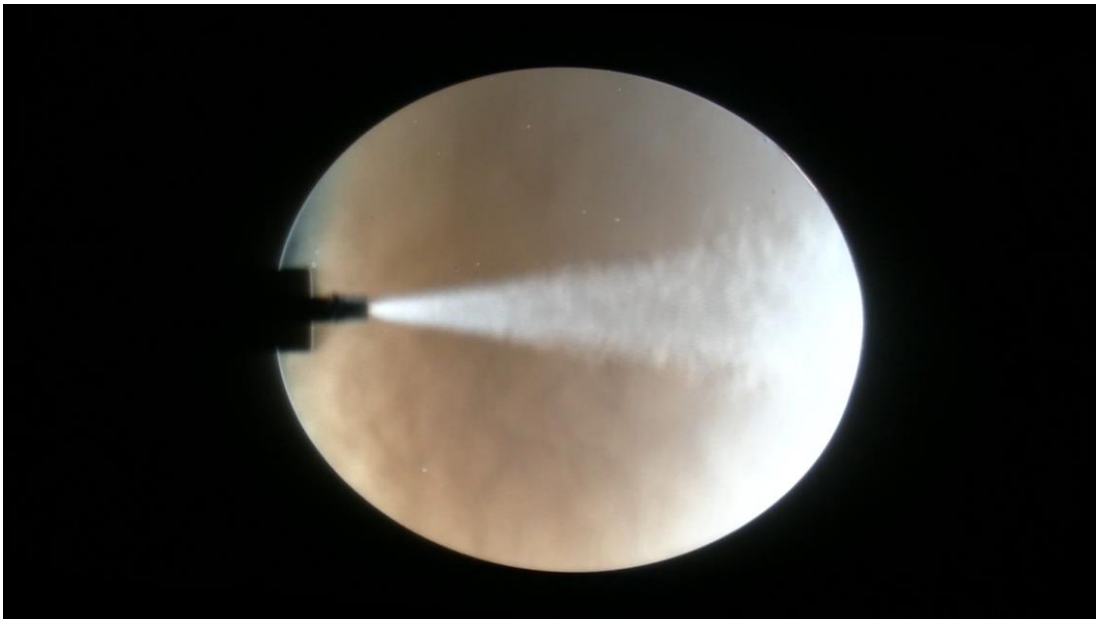

(h)

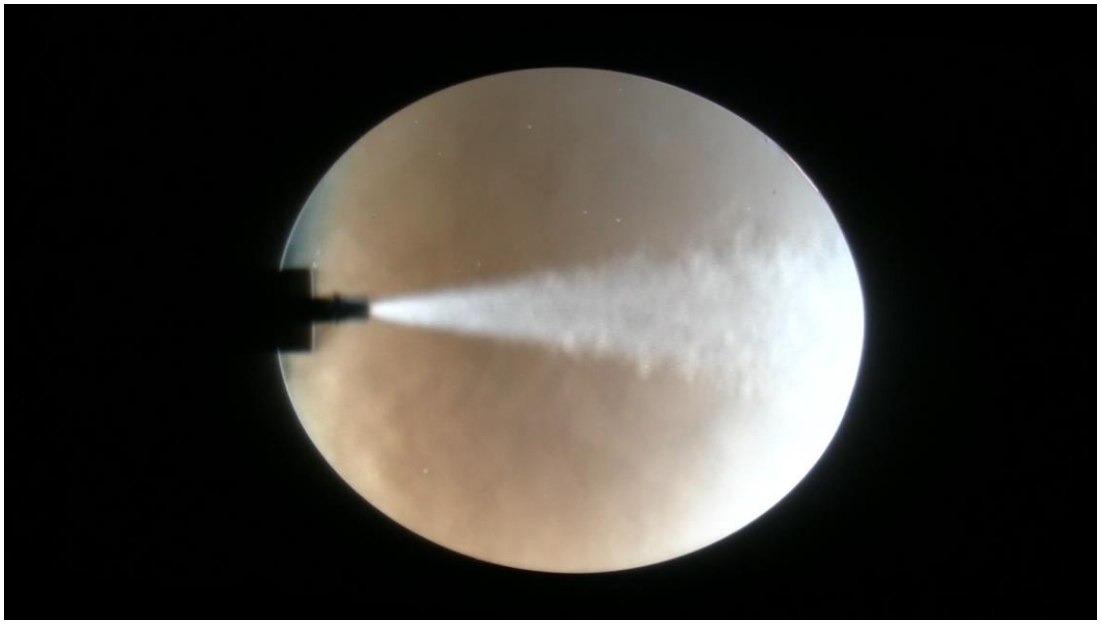

(i)

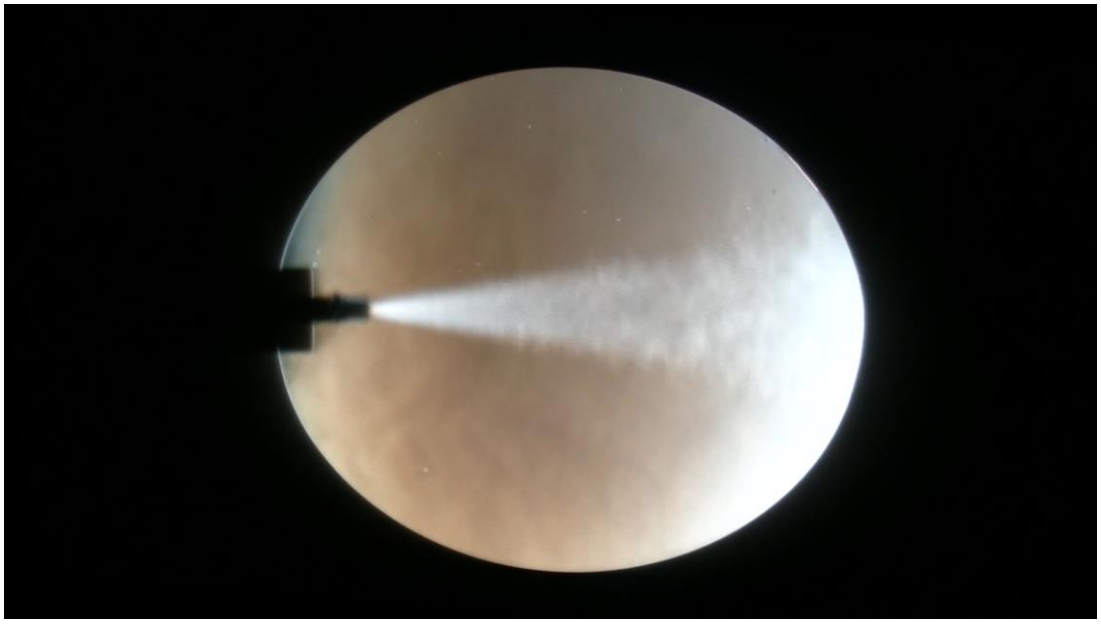

(j)

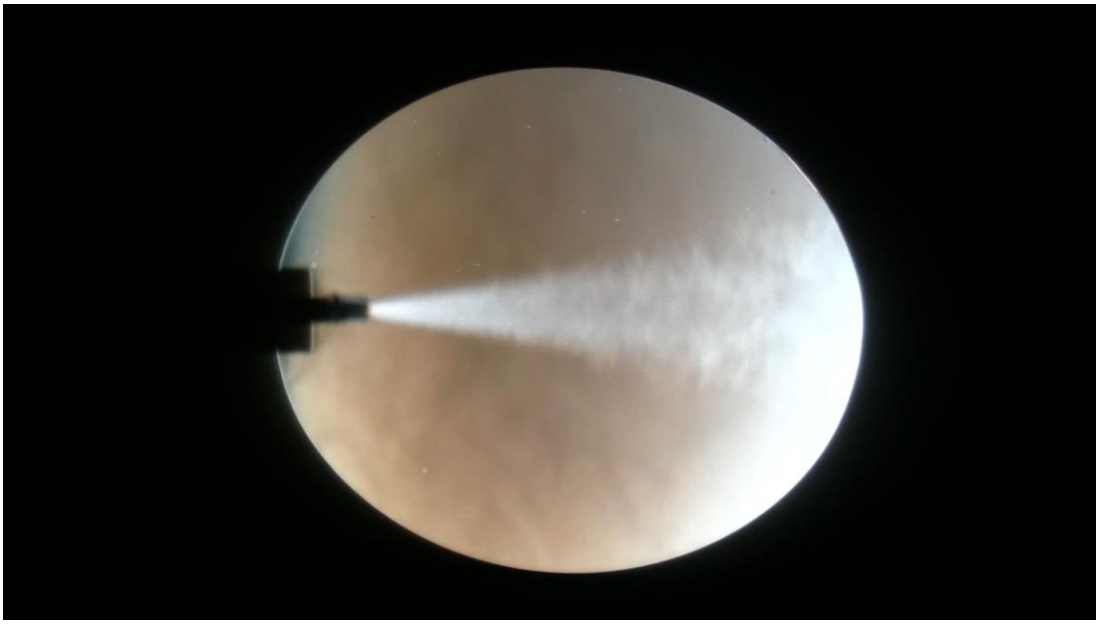

(k)

Figure J-1. Frames from Schlieren Imaging of Test-1 at Different Times: (a) t_0, (b) t_0+40 ms, (c) t_0+80 ms, (d) t_0+120 ms, (e) t_0+160 ms, (f) t_0+200 ms, (g) t_0+240 ms, (h) t_0+280 ms, (i) t_0+320 ms, (j) t_0+360 ms, (k) t_0+400 ms

K. Density Contours

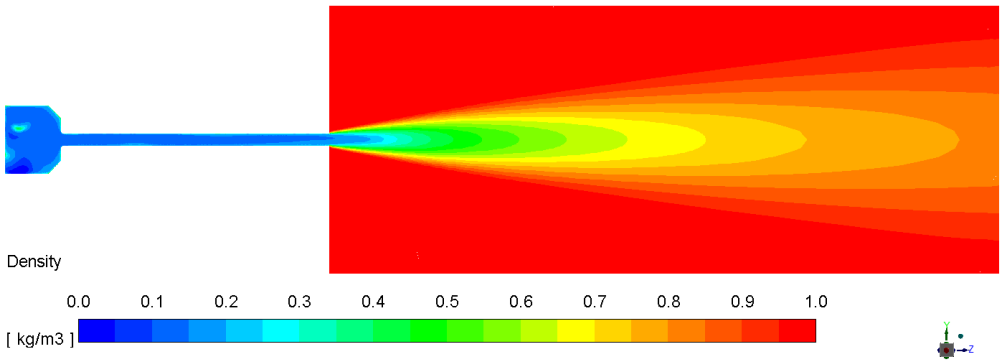

Figure K-1. Density Contours on Plane-1 for Test-1 on Plane-1

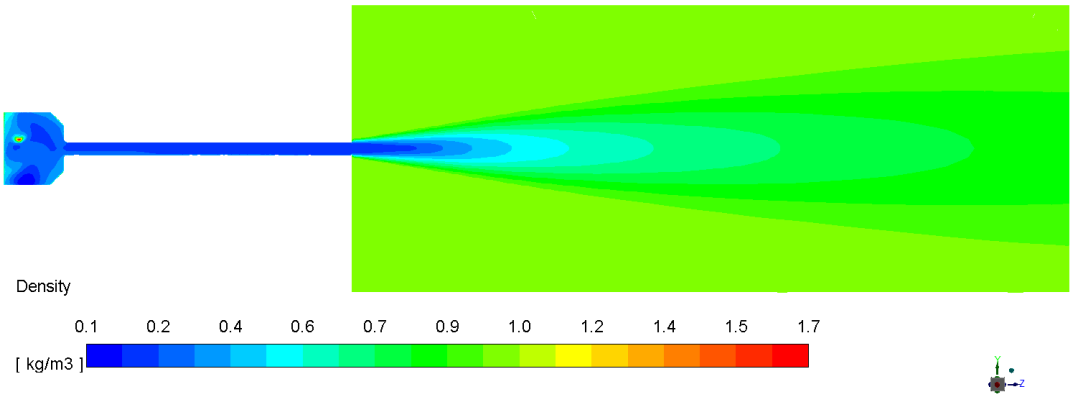

Figure K-2. Density Contours on Plane-1 for Test-2 on Plane-1

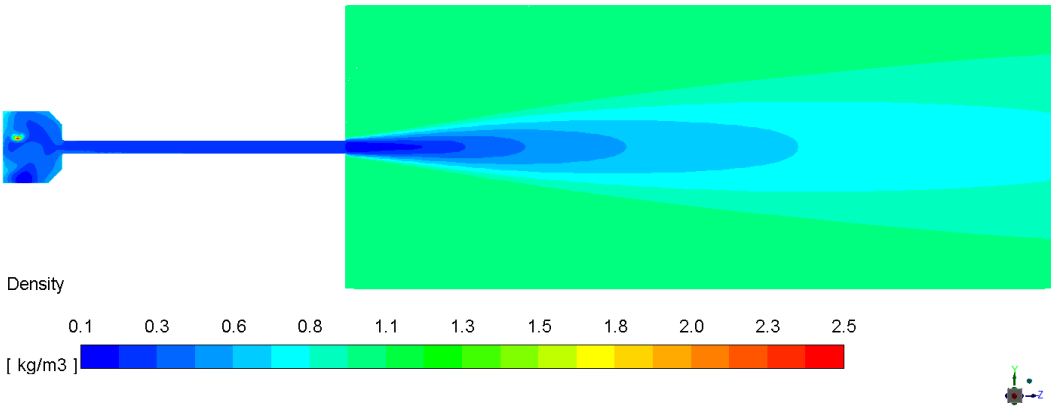

Figure K-3. Density Contours on Plane-1 for Test-3 on Plane-1

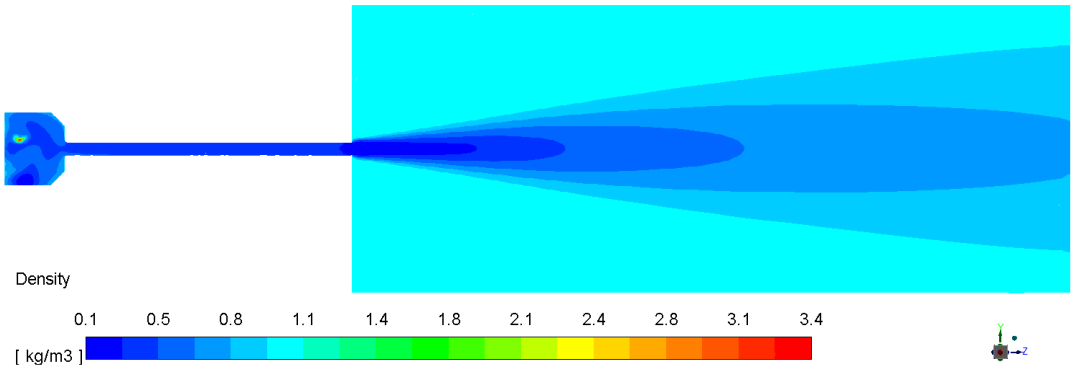

Figure K-4. Density Contours on Plane-1 for Test-4 on Plane-1

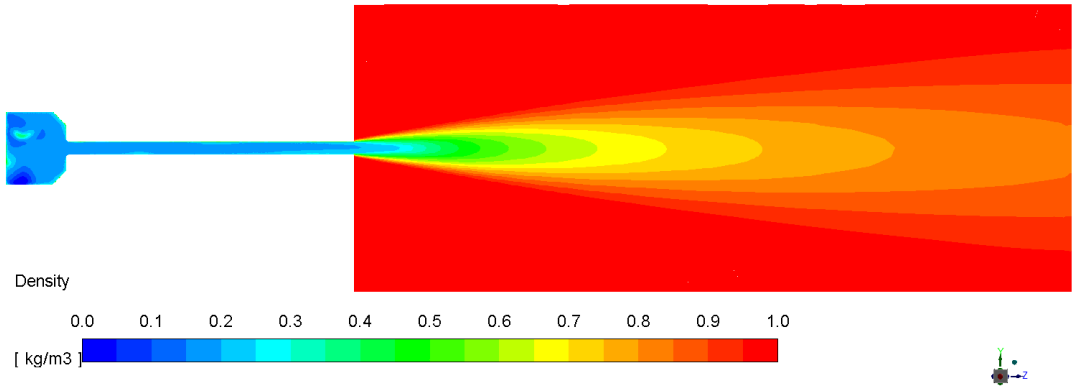

Figure K-5. Density Contours on Plane-1 for Test-5 on Plane-1

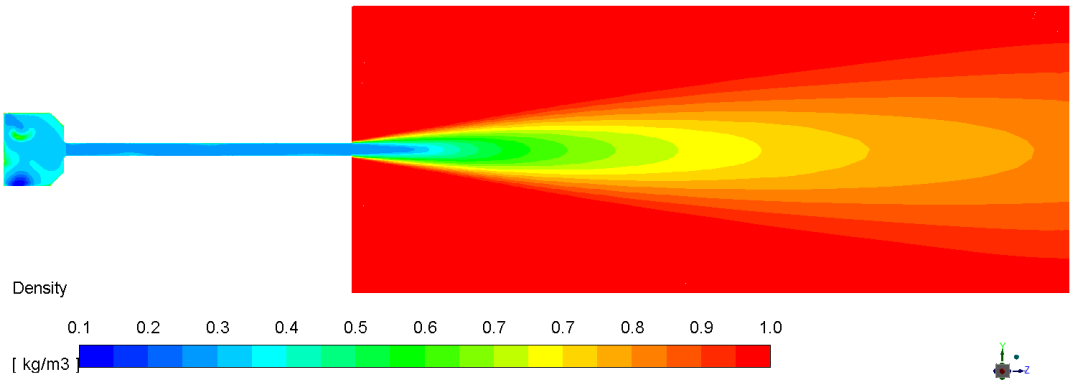

Figure K-6. Density Contours on Plane-1 for Test-6 on Plane-1

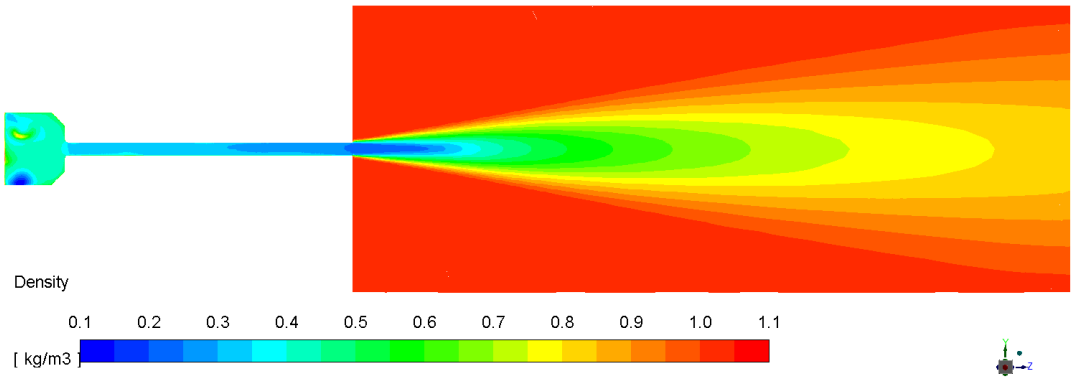

Figure K-7. Density Contours on Plane-1 for Test-7 on Plane-1

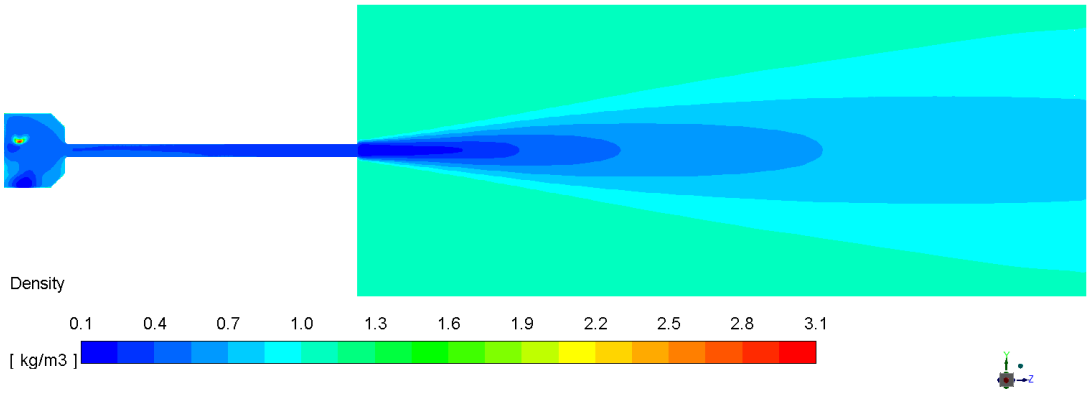

Figure K-8. Density Contours on Plane-1 for Test-8 on Plane-1

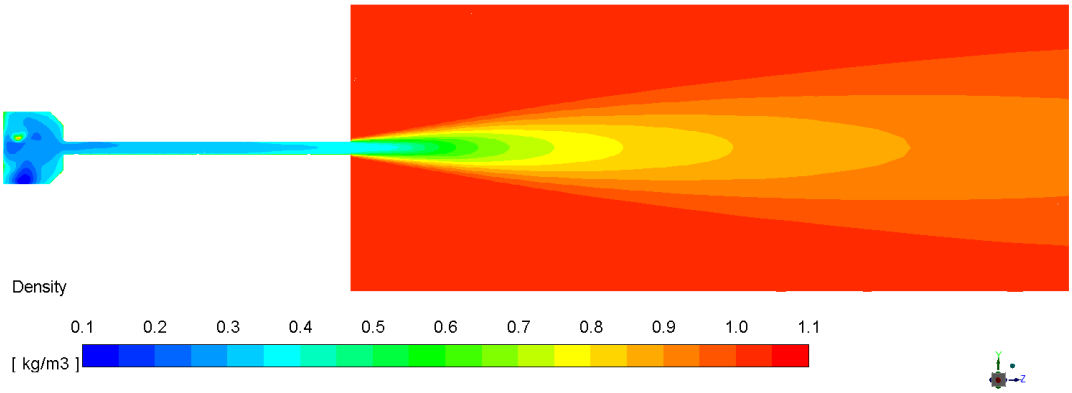

Figure K-9. Density Contours on Plane-1 for Test-9 on Plane-1

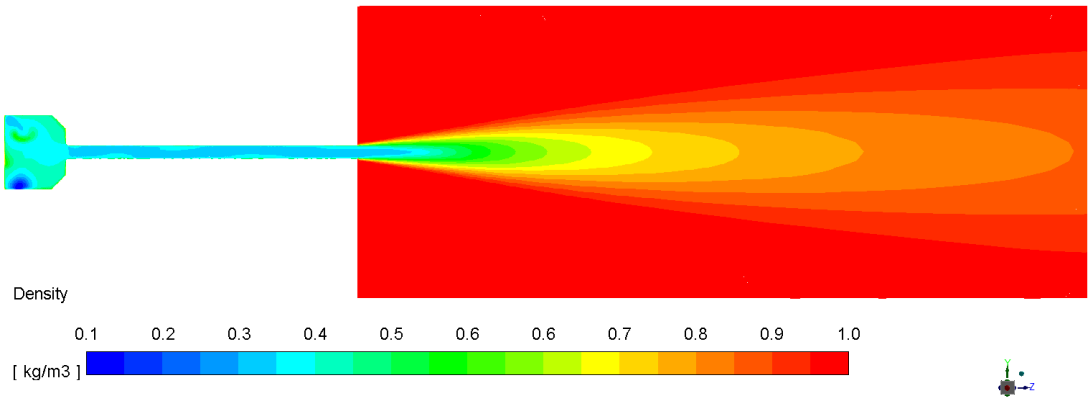

Figure K-10. Density Contours on Plane-1 for Test-10 on Plane-1

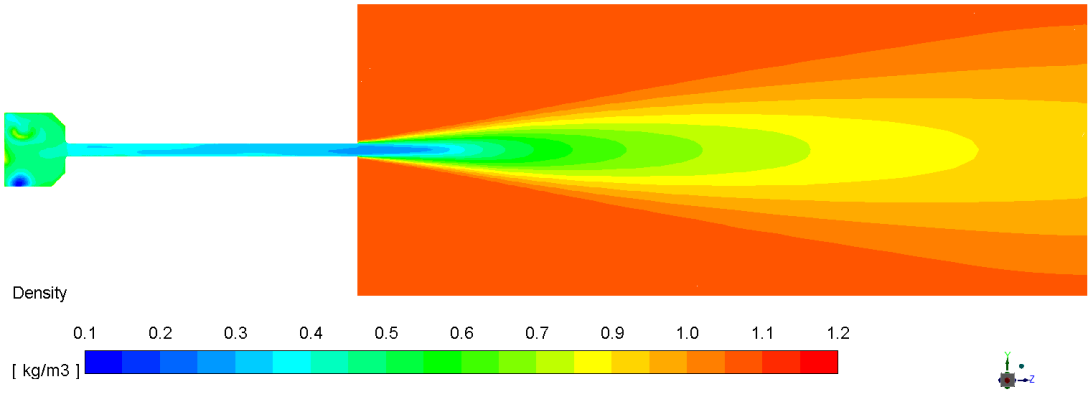

Figure K-11. Density Contours on Plane-1 for Test-11 on Plane-1

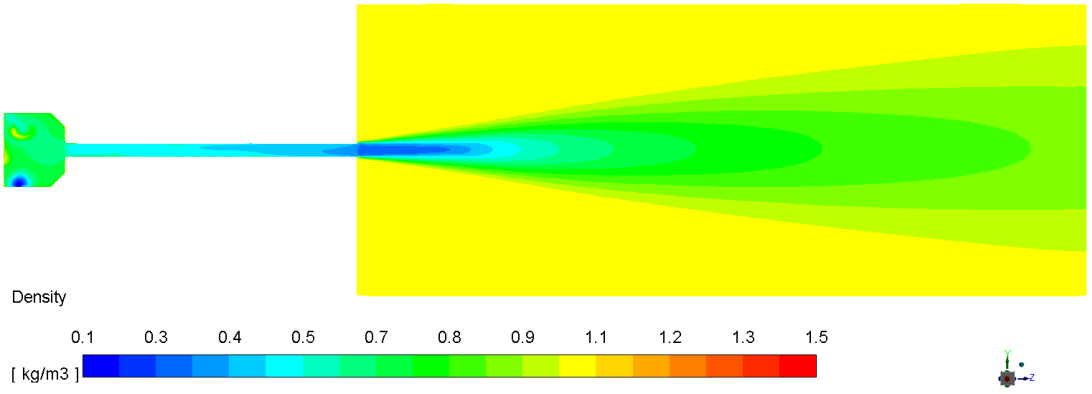

Figure K-12. Density Contours on Plane-1 for Test-12 on Plane-1

L. Effect of Diameter on Backpressure Value for Choked Flow

For a choked flow, backpressure can be calculated as;

$$P_t = \frac{m \times \sqrt{\dot{T_t \times R}}}{A \times \sqrt{\gamma} \times \left(\frac{\gamma+1}{2}\right)^{-\left(\frac{\gamma+1}{2(\gamma-1)}\right)}}$$

To understand the effect of diameter on the backpressure value, calculation is done for air with a stagnation temperature of 2000 K and for 0.003 kg/s.

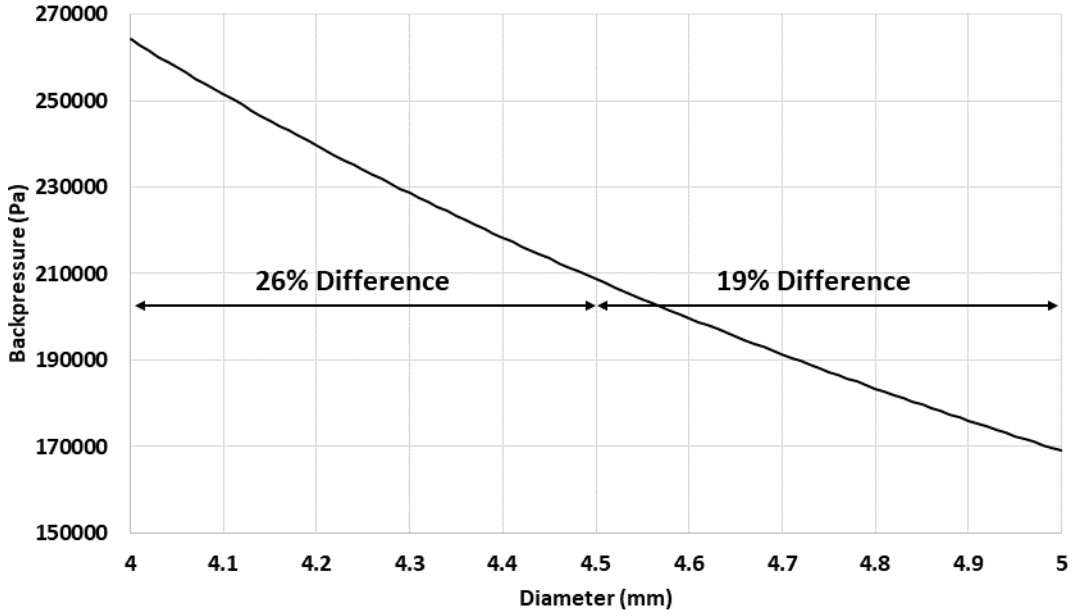

Figure L-1. Effect of Diameter on Backpressure Value for Choked Flow

M. Repeatability Demonstration of the Tests

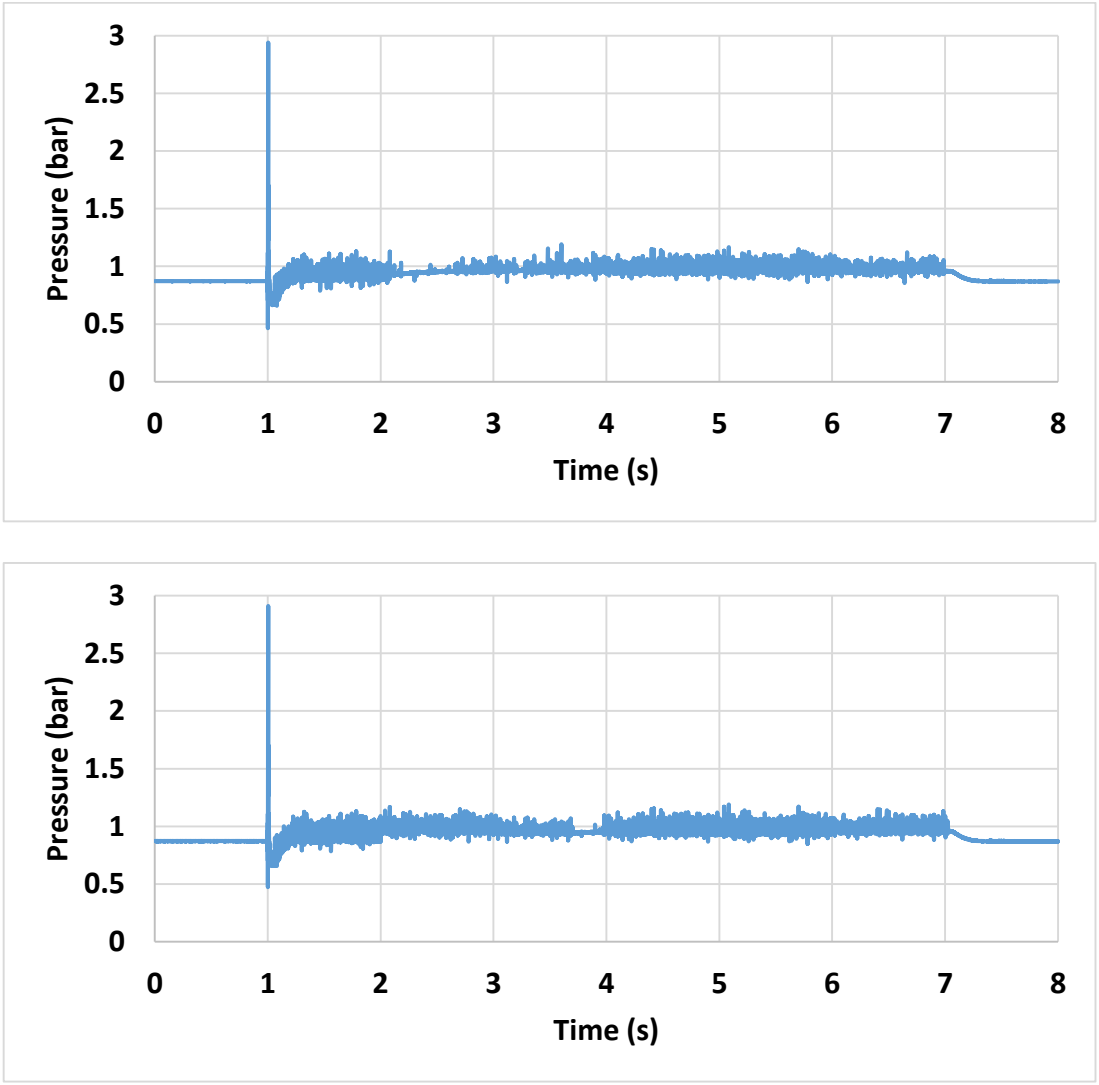

Figure M-1. Pressure Measurements of Test-1

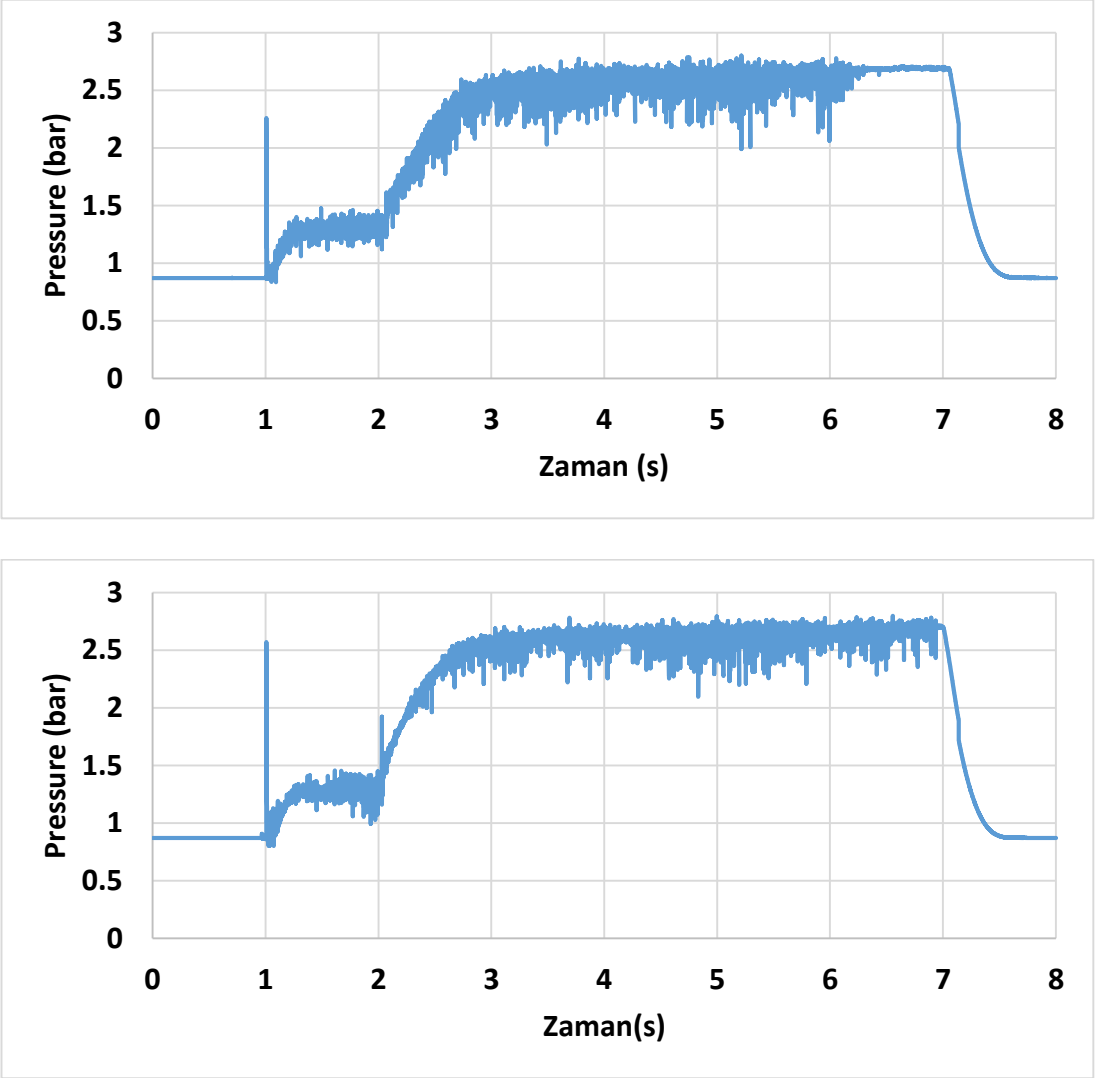

Figure M-*2*. Pressure Measurements of Test-8

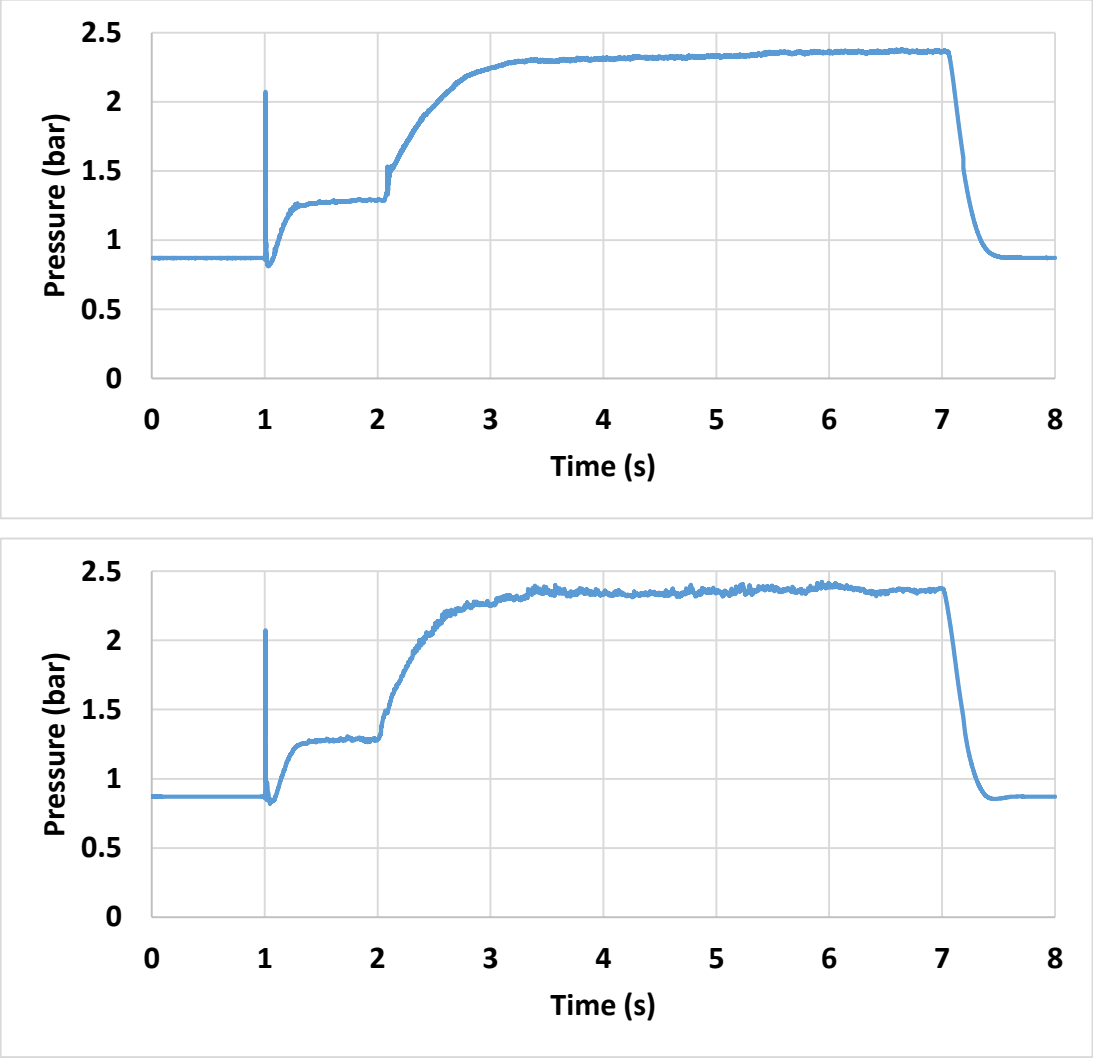

Figure M-3. Pressure Measurements of Test-12

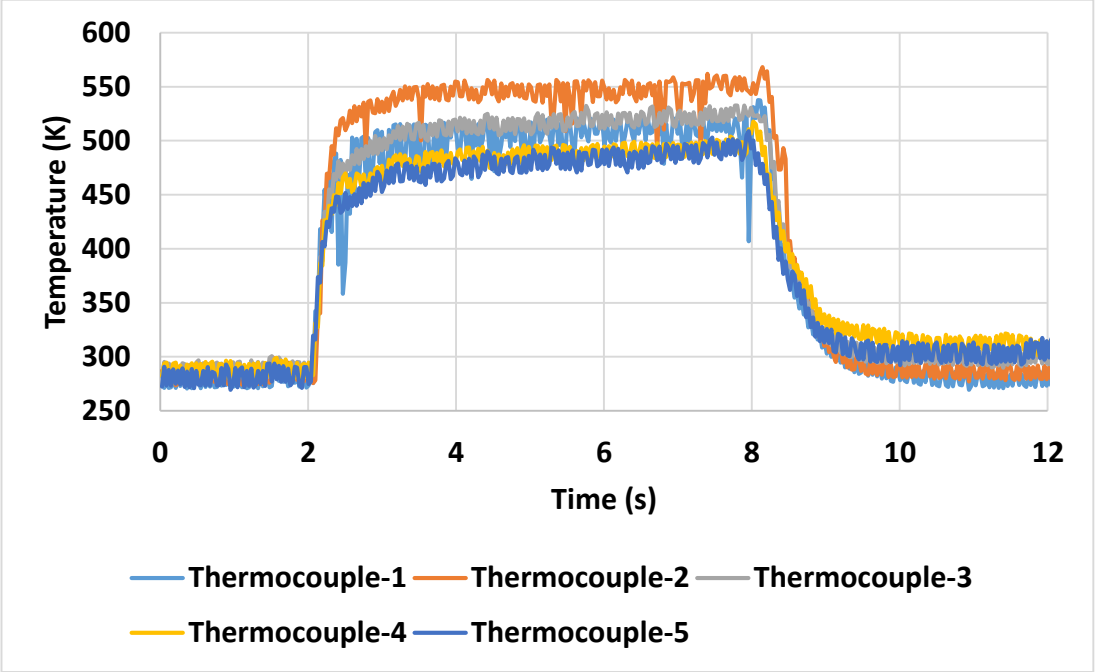

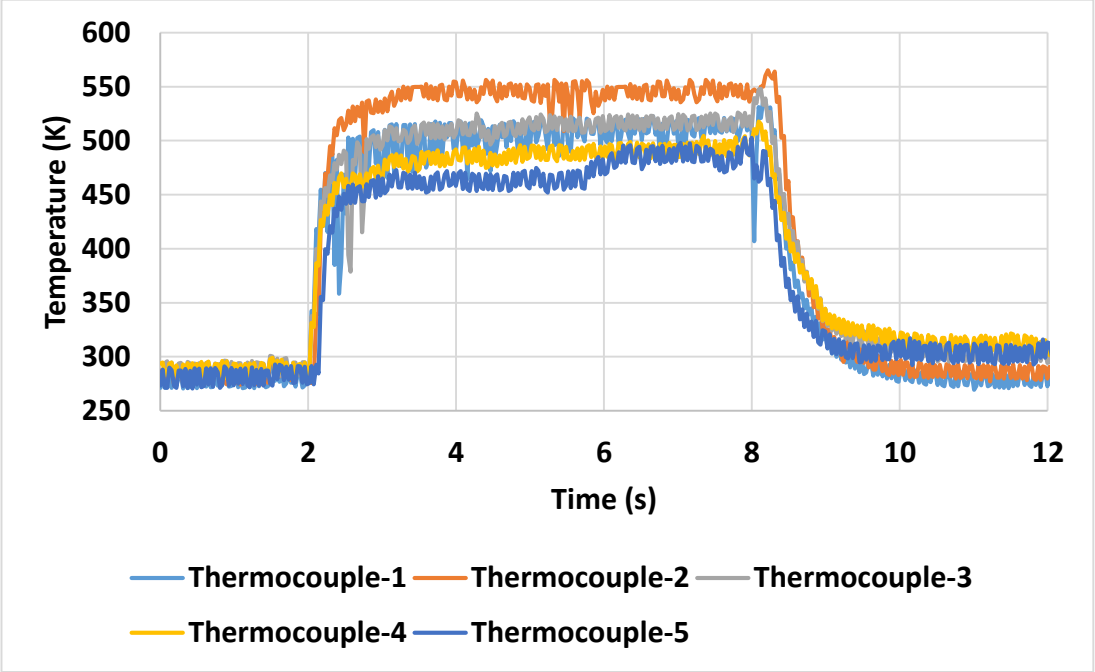

Figure M-4. Temperature Measurements of Test-1

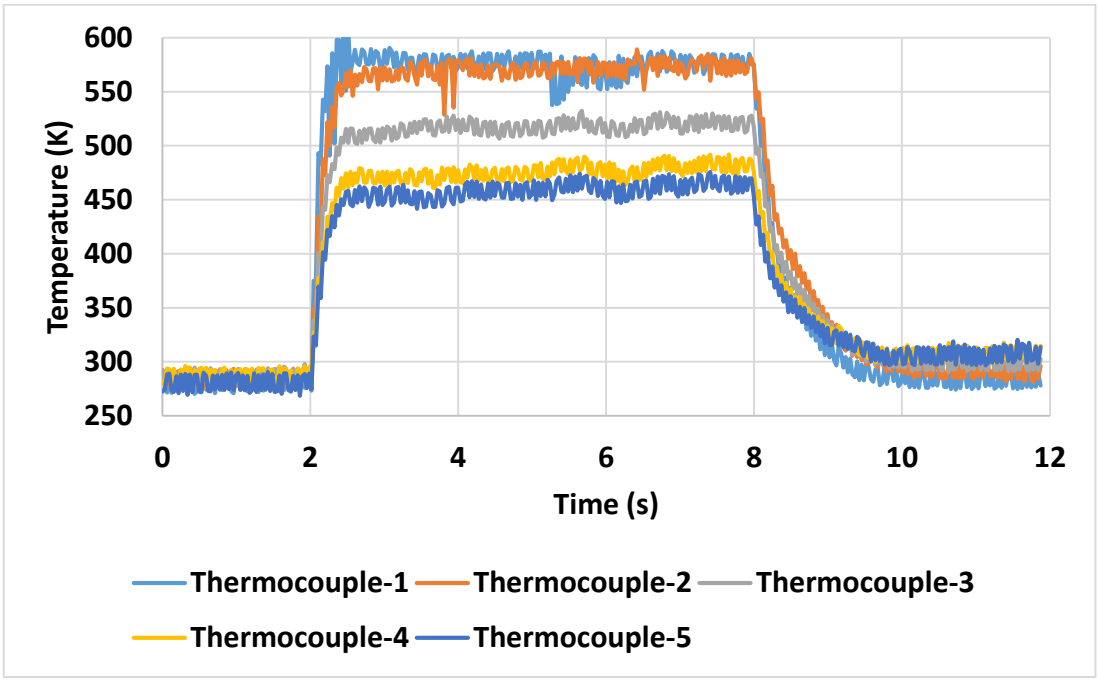

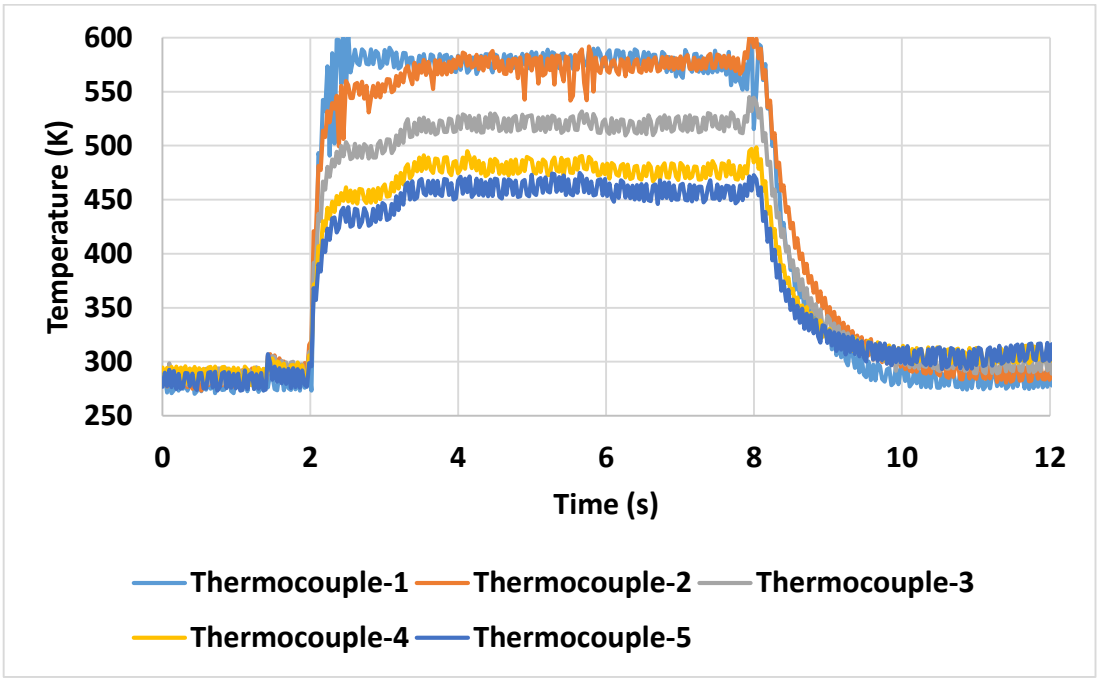

Figure M-5. Temperature Measurements of Test-5

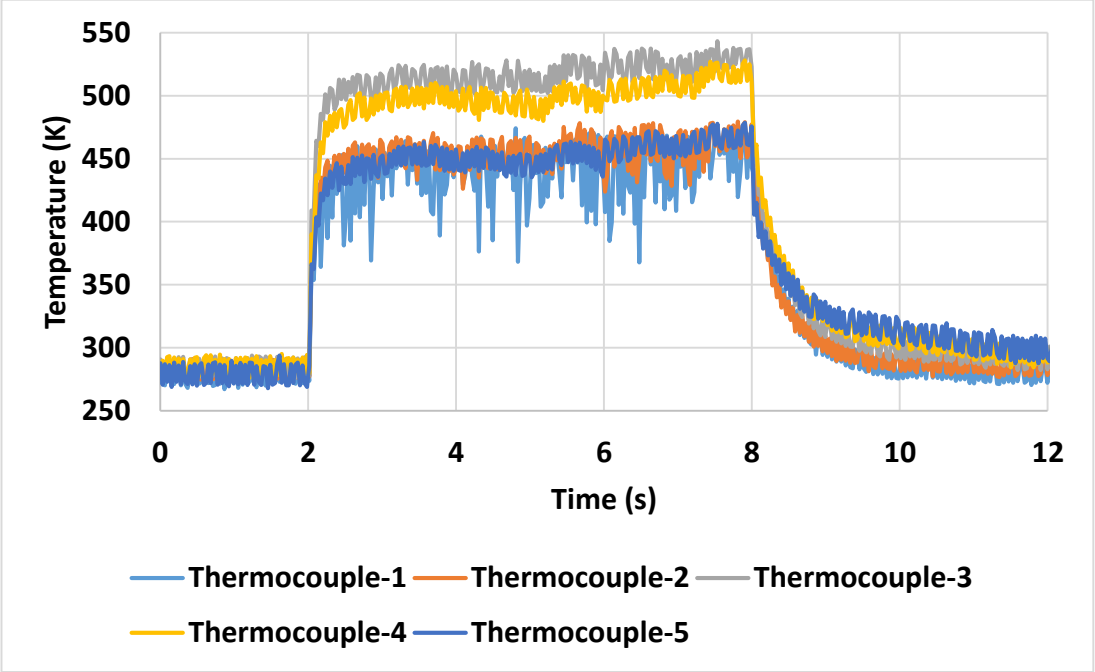

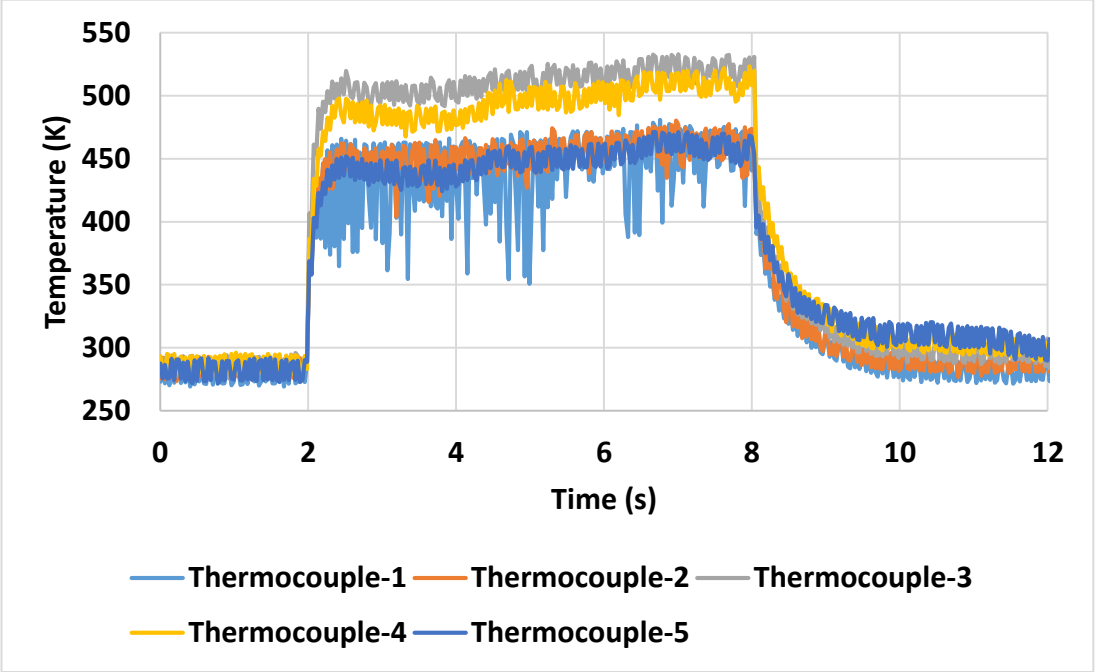

Figure M-*6.* Temperature Measurements of Test-10